

Generalized harmonic modeling technique for 2D electromagnetic problems : applied to the design of a direct-drive active suspension system

Citation for published version (APA):

Gysen, B. L. J. (2011). *Generalized harmonic modeling technique for 2D electromagnetic problems : applied to the design of a direct-drive active suspension system*. [Phd Thesis 1 (Research TU/e / Graduation TU/e), Electrical Engineering]. Technische Universiteit Eindhoven. <https://doi.org/10.6100/IR719773>

DOI:

[10.6100/IR719773](https://doi.org/10.6100/IR719773)

Document status and date:

Published: 01/01/2011

Document Version:

Publisher's PDF, also known as Version of Record (includes final page, issue and volume numbers)

Please check the document version of this publication:

- A submitted manuscript is the version of the article upon submission and before peer-review. There can be important differences between the submitted version and the official published version of record. People interested in the research are advised to contact the author for the final version of the publication, or visit the DOI to the publisher's website.
- The final author version and the galley proof are versions of the publication after peer review.
- The final published version features the final layout of the paper including the volume, issue and page numbers.

[Link to publication](#)

General rights

Copyright and moral rights for the publications made accessible in the public portal are retained by the authors and/or other copyright owners and it is a condition of accessing publications that users recognise and abide by the legal requirements associated with these rights.

- Users may download and print one copy of any publication from the public portal for the purpose of private study or research.
- You may not further distribute the material or use it for any profit-making activity or commercial gain
- You may freely distribute the URL identifying the publication in the public portal.

If the publication is distributed under the terms of Article 25fa of the Dutch Copyright Act, indicated by the "Taverne" license above, please follow below link for the End User Agreement:

www.tue.nl/taverne

Take down policy

If you believe that this document breaches copyright please contact us at:

openaccess@tue.nl

providing details and we will investigate your claim.

Generalized Harmonic Modeling Technique for 2D Electromagnetic Problems

Applied to the Design of a Direct-Drive
Active Suspension System

PROEFSCHRIFT

ter verkrijging van de graad van doctor
aan de Technische Universiteit Eindhoven,
op gezag van de rector magnificus, prof.dr.ir. C.J. van Duijn,
voor een commissie aangewezen door het College voor Promoties
in het openbaar te verdedigen
op dinsdag 20 december 2011 om 16.00 uur

door

Bart Ludo Jozef Gysen

geboren te Bilzen, België

Dit proefschrift is goedgekeurd door de promotor:

prof.dr. E. Lomonova MSc

Copromotor:

dr. J.J.H. Paulides MPhil



This research is supported by the Svenska Kullagerfabriken Automotive Development Center in Nieuwegein, The Netherlands.

A catalogue record is available from the Eindhoven University of Technology Library.
ISBN: 978-90-386-2970-4

Reproduction: Ipskamp Drukkers B.V., Enschede, The Netherlands.

Copyright © 2011 by B.L.J. Gysen. All rights reserved.

*To my parents
Aan mijn ouders*

Summary

Generalized Harmonic Modeling Technique for 2D Electromagnetic Problems

Applied to the Design of a Direct-Drive Active Suspension System

The introduction of permanent magnets has significantly improved the performance and efficiency of advanced actuation systems. The demand for these systems in the industry is increasing and the specifications are becoming more challenging. Accurate and fast modeling of the electromagnetic phenomena is therefore required during the design stage to allow for multi-objective optimization of various topologies.

This thesis presents a generalized technique to design and analyze 2D electromagnetic problems based on harmonic modeling. Therefore, the prior art is extended and unified to create a methodology which can be applied to almost any problem in the Cartesian, polar and axisymmetric coordinate system. This generalization allows for the automatic solving of complicated boundary value problems within a very short computation time. This method can be applied to a broad class of classical machines, however, more advanced and complex electromagnetic actuation systems can be designed or analyzed as well.

The newly developed framework, based on the generalized harmonic modeling technique, is extensively demonstrated on slotted tubular permanent magnet actuators. As such, numerous tubular topologies, magnetization and winding configurations are analyzed. Additionally, force profiles, emf waveforms and synchronous inductances are accurately predicted. The results are within approximately 5 % of the non-linear finite element analysis including the slotted stator effects.

A unique passive damping solution is integrated within the tubular permanent magnet actuator using eddy current damping. This is achieved by inserting conductive rings in the stator slot openings to provide a passive damping force without compromising the tubular actuator's performance. This novel idea of integrating conductive rings is secured in a patent. A method to calculate the damping ratio due to these conductive rings is presented where the position, velocity and temperature dependencies are shown.

The developed framework is applied to the design and optimization of a direct-drive electromagnetic active suspension system for passenger cars. This innovative solution is an alternative for currently applied active hydraulic or pneumatic suspension systems for improvement of the comfort and handling of a vehicle. The electromagnetic system provides an improved bandwidth which is typically 20 times higher together with a power consumption which is approximately five times lower. As such, the proposed system eliminates two of the major drawbacks that prevented the widespread commercial breakthrough of active suspension systems.

The direct-drive electromagnetic suspension system is composed of a coil spring in parallel with a tubular permanent magnet actuator with integrated eddy current damping. The coil spring supports the sprung mass while the tubular actuator either consumes, by applying direct-drive vertical forces, or regenerates energy. The applied tubular actuator is designed using a non-linear constrained optimization algorithm in combination with the developed analytical framework. This ensured the design with the highest force density together with low power consumption. In case of a power breakdown, the integrated eddy current damping in the slot openings of this tubular actuator, together with the passive coil spring, creates a passive suspension system to guarantee fail-safe operation.

To validate the performance of the novel proof-of-concept electromagnetic suspension system, a prototype is constructed and a full-scale quarter car test setup is developed which mimics the vehicle corner of a BMW 530i. Consequently, controllers are designed for the active suspension strut for improvement of either comfort or handling. Finally, the suspension system is installed as a front suspension in a BMW 530i test vehicle. Both the extensive experimental laboratory and on-road tests prove the capability of the novel direct-drive electromagnetic active suspension system. Furthermore, it demonstrates the applicability of the developed modeling technique for design and optimization of electromagnetic actuators and devices.

Contents

Summary	v
List of symbols	xiii
1 Introduction	1
1.1 The magnetization direction of society	1
1.2 Towards extensive electromagnetic modeling	2
1.2.1 Analytical models	2
1.2.2 Numerical models	4
1.2.3 Transformation techniques	5
1.2.4 Semi-analytical models	5
1.3 The journey of a car driver	6
1.4 A short overview of suspension systems	8
1.4.1 Passive suspension systems	9
1.4.2 Semi-active suspension systems	10
1.4.3 Active suspension systems	11
1.4.4 The direct-drive electromagnetic suspension system	14
1.5 Thesis outline	15
I Electromagnetic modeling techniques	17
2 Generalized harmonic modeling technique	19
2.1 Literature overview	21
2.2 Assumptions	23
2.3 Division in regions	24
2.4 Magnetostatic Maxwell equations	26
2.5 Source term description	28
2.6 Semi-analytical solution	29
2.6.1 Cartesian coordinate system	31
2.6.2 Polar coordinate system	31
2.6.3 Axisymmetric coordinate system	33
2.7 Boundary conditions	34
2.7.1 Neumann boundary condition	34
2.7.2 Dirichlet boundary condition	35
2.7.3 Continuous boundary condition	36

2.7.4	Combined Neumann and continuous boundary condition . . .	37
2.7.5	Conservation of magnetic flux	41
2.7.6	Ampère's law	43
2.8	Numerical implementation	44
2.9	Finite element verification	45
2.9.1	Cartesian coordinate system	46
2.9.2	Polar coordinate system	48
2.9.3	Axisymmetric coordinate system	49
2.10	Summary and conclusions	52
3	Modeling of tubular permanent magnet actuators	53
3.1	Topologies and configurations	55
3.1.1	Translator configurations	55
3.1.2	Stator tooth geometry	57
3.1.3	Slot, pole and winding configurations	58
3.2	Application of the generic modeling technique	60
3.2.1	Assumptions and simplifications	60
3.2.2	Division in regions for tubular actuators	63
3.2.3	Assignment of the boundary conditions	63
3.2.4	Finite element verification	65
3.3	Flux density inside the soft-magnetic regions	65
3.3.1	Stator teeth and stator back-iron	68
3.3.2	Translator back-iron	70
3.3.3	Pole pieces	71
3.4	Electromotive force	73
3.5	Synchronous inductance	75
3.6	Force profile	76
3.6.1	Calculation methods	77
3.6.2	Force calculation and separation of components	79
3.6.3	End-effects	82
3.7	Copper losses	84
3.8	Thermal model	85
3.9	Summary and conclusions	89
4	Integrated electromagnetic passive damping	91
4.1	Electromagnetic damping	93
4.1.1	Hysteresis	93
4.1.2	Eddy currents	95
4.1.3	Excess loss	96
4.1.4	Solid steel versus laminations	96
4.2	Enhancing damping using conductive materials	98
4.2.1	Conductive layer on the stator bore	100
4.2.2	Conductive rings in the slot openings	100
4.2.3	Conductive discs in the slots	101
4.2.4	Conductive rings within the stator teeth	101
4.2.5	Conductive rings within the stator back-iron	101

4.3	Prediction of the enhanced damping constant	101
4.3.1	Dynamic modeling techniques	101
4.3.2	Induced flux linkage in the conductive rings	104
4.3.3	Impedance of the conductive rings	106
4.3.4	Eddy currents in the conductive rings	110
4.3.5	Dissipated power, damping force and constant	112
4.4	Influence on the actuator performance	114
4.5	Summary and conclusions	118

II Design of a direct-drive active suspension system 119

5	System topology and specifications	121
5.1	The benchmark vehicle	123
5.2	The passive suspension system of the benchmark vehicle	123
5.3	The active suspension system	126
5.3.1	Spring characteristic	126
5.3.2	Direct-drive actuation	127
5.3.3	Damping characteristic	128
5.4	Power electronics	133
5.5	Two degrees of freedom quarter car model	134
5.6	Road vibrations	136
5.7	Objectives and specifications	139
5.7.1	Suspension stroke and velocity	139
5.7.2	Comfort and human sensitivity	140
5.7.3	Handling	142
5.8	Sensors	144
5.9	System integration	145
5.10	Summary and conclusions	146
6	Automated optimization and design	149
6.1	The optimization algorithm	151
6.2	Coilover integration and mechanical design	152
6.3	Material selection	155
6.4	Thermal constraints	156
6.5	Design criteria and strategy	157
6.6	Force optimization	158
6.6.1	Problem formulation	158
6.6.2	Implementation aspects	160
6.6.3	Comparison of the optimized force densities	161
6.7	Loss minimization	162
6.7.1	Number of periodic sections	162
6.7.2	Problem formulation	165
6.7.3	Comparison of the optimized copper losses	166
6.8	Electromagnetic damping	167
6.8.1	Fail-safe damping versus power consumption	168
6.8.2	Design of the conductive rings	169

6.9	End-effects	171
6.10	Number of turns	172
6.11	Final design	173
6.12	Summary and conclusions	175
7	Control and experimental verification	177
7.1	Realization of the prototype	179
7.1.1	Permanent magnet array	179
7.1.2	Stator assembly	180
7.1.3	Strut assembly	182
7.2	Experimental verification of the active suspension strut	183
7.2.1	The electromotive force	184
7.2.2	The cogging and end-effect force	184
7.2.3	The damping force	186
7.2.4	The active force	188
7.3	Quarter car test setup	189
7.3.1	Description of the setup	189
7.3.2	Control of road actuation	191
7.3.3	Identification	192
7.4	Robust control of the vehicle corner	194
7.4.1	Parameter variation	195
7.4.2	Robust control structure	195
7.4.3	Weighting functions	196
7.4.4	Controller synthesis	198
7.5	Experimental verification on the quarter car test setup	200
7.5.1	Performance on a stochastic road	201
7.5.2	Force and power consumption	202
7.5.3	Performance on a deterministic road profile	204
7.6	Experimental verification on the BMW 530i	206
7.6.1	Comfort	206
7.6.2	Handling	208
7.7	Summary and conclusions	209
III	Closing	211
8	Conclusions and Recommendations	213
8.1	Conclusions of Part I	213
8.1.1	Generic harmonic modeling technique	213
8.1.2	Modeling of slotted TPMA's	214
8.1.3	Integration of eddy current damping	215
8.2	Conclusions of Part II	215
8.2.1	Direct-drive fail-safe active suspension system	215
8.2.2	Automated optimization and design	216
8.2.3	Control and experimental verification	216
8.3	Thesis contributions	217
8.4	Recommendations for future work	218

8.4.1	Harmonic modeling including high permeability regions . .	218
8.4.2	Harmonic modeling of 3D problems	219
8.4.3	Revision of specifications for the active suspension system .	219
8.4.4	Full vehicle control	219
8.4.5	Alternative functionalities or applications	220
A	Correlation functions	221
B	Boundary condition matrices for TPMAs	223
B.1	Radial magnetization	224
B.2	Quasi-Halbach magnetization	227
B.3	Axial magnetization	229
B.4	Continuity of the magnetic vector potential	232
C	Controllers and weighting filters	235
C.1	Road actuation	235
C.2	Weighting filters	236
	Bibliography	237
	Samenvatting	251
	Acknowledgements	253
	Curriculum Vitae	255

List of symbols

Symbol	Quantity	Unit
α_m	Temperature coefficient of the remanence of the PMs	-
α_p	Radial magnet width to pole pitch ratio	-
α_r	Temperature coefficient of the conductive rings	-
β	Wavelength distribution of the road profile	1/m
γ	Front to rear mass distribution	-
Δ	Offset in the tangential direction	m or rad
Δ_z	Relative displacement	m
ε	Correlation function	-
ζ	Correlation function	-
η	Correlation function	-
θ	Polar or cylindrical coordinate	rad
θ_e	Relative displacement	rad or deg
κ	Correlation function	-
Λ	Flux linkage	Wb
μ	Permeability	H/m
μ_0	Permeability of vacuum ($4\pi 10^{-7}$)	H/m
μ_r	Relative permeability	-
ν	Subregion index	-
π	Mathematical constant (3.1415)	-
ϕ	Flux	Wb
ϕ_r	Roll angle	rad
φ_c	Commutation angle	rad
φ_m	Magnetic scalar potential	A
ρ	Resistivity	Ωm
ρ_m	Magnetic charge density	A/m ²
σ	Conductivity	S/m
τ	Tangential width or pitch	m or rad
χ	Magnetic susceptibility	-
ω	Angular frequency	rad/s
\vec{A}	Magnetic vector potential	Wb/m
Ω	Spatial frequency	1/m

a	Field coefficient, acceleration	(*), m/s ²
\vec{B}	Magnetic flux density vector	T
B_{rem}	Remanent flux density	T
b	Field coefficient	(*)
C_0	Hysteresis loss coefficient	J/kg
C_1	Classical loss coefficient	Js/kg
C_2	Excess loss coefficient	Js ^{1/2} /kg
C_{ph}	Number of coils per phase per periodic section	-
C_r	General roughness of the road profile	m
c	Field coefficient	(*)
d	Field coefficient	(*)
d_a	Damping of the active suspension	Ns/m
d_{fe}	Damping due to the iron losses	Ns/m
d_p	Damping of the passive suspension	Ns/m
d_r	Damping due to the conductive rings	Ns/m
\vec{E}	Electrical field strength vector	V/m
\vec{e}	Unit vector	-
e_{ph}	Electromotive force (emf)	V
\vec{F}	Force vector	N
\mathcal{F}	Function of Bessel integrals	-
f	Frequency	Hz
$f(\mathbf{x})$	Objective function	(*)
f_c	Correction function	-
f_d	Force density	N/m ³
G	Transfer function	(*)
\mathcal{G}	Source term function	T
$g(\mathbf{x})$	Inequality constraints	-
\vec{H}	Magnetic field strength vector	A/m
$h(\mathbf{x})$	Equality constraints	-
h	Height	m
I	Constant current	A
\mathcal{I}_o	Modified Bessel function of first kind of order o	-
i	Instantaneous current	A
\vec{J}	Current density vector	A/m ²
j	Region index, imaginary unit	-
K_e	Emf constant	Vs/m
$K_{e,0}$	Emf constant at zero velocity	Vs/m
$K_{e,v}$	Decrement of the emf constant per velocity	s/m
$K_{ph,v}$	Phase shift of the emf constant per velocity	rad s/m
\mathcal{K}_o	Modified Bessel function of second kind of order o	-
k	Region index, thermal conductivity	- , W/(mK)
k_f	Filling factor	-
k_p	Stiffness of the passive suspension	N/m
k_a	Stiffness of the active suspension	N/m

(*) Unit depends on the context

k_t	Tire stiffness	N/m
L	Length	m
L	Inductance	H
l	General coordinate	m or rad
\vec{M}	Magnetization vector	A/m
\vec{M}_0	Residual magnetization vector	A/m
M	Mass	kg
m	Harmonic number	-
N	Maximum number of harmonics	-
N_t	Number of turns per coil	-
N_{pa}	Number of active periodic sections	-
N_{px}	Number of extra periodic sections	-
n	Harmonic number	-
P	Number of poles per periodic section, power	- , W
P_r	Power spectral density of the road profile	m ² /Hz
p	General coordinate	m
q	General coordinate	m or rad
R	Radius	m
R	Resistance	Ω
r	Polar or cylindrical coordinate	m
S	Number of slots per periodic section, surface	- , m
s	Coefficient	-
T	Temperature	$^{\circ}\text{C}$
\mathbb{T}	Magnetic stress tensor	T^2
t	Time	s
W	Weighting function	-
w	Spatial frequency	(*)
\vec{x}	Position vector	m
\mathbf{x}	Variable vector	(*)
x	Cartesian coordinate	m
y	Cartesian coordinate	m
V	Volume	m ³
\mathcal{V}	Number of subregions	-
v	Velocity	m/s
Z	Impedance	Ω
z	Cartesian, polar or cylindrical coordinate	m

(*) Unit depends on the context

Abbreviation	Description
1D	One-dimensional
2D	Two-dimensional
3D	Three-dimensional
ABC	Active Body Control
ABS	Anti-lock Braking System
ac	Alternating current
AOD	Automated Optimization and Design
ARC	Anti Roll Control
ASR	Anti Slip Regulation
BEM	Boundary Element Method
BMW	Bayerische Motoren Werke
CLD	California Linear Drives
dc	Direct current
DoF	Degree-of-Freedom
ELMASP	Electromagnetic Spring
emf	Electromotive Force
EMT	External Magnet Topology
ESP	Electronic Stability Program
FDM	Finite Difference Method
FEA	Finite Element Analysis
FEM	Finite Element Method
FSPM	Flux Switching Permanent Magnet
IMT	Internal Magnet Topology
LQG	Linear Quadratic Gaussian
LQR	Linear Quadratic Regulator
MEC	Magnetic Equivalent Circuit
MIMO	Multi-Input-Multi-Output
mmf	Magnetomotive Force
PM	Permanent Magnet
PSD	Power Spectral Density
PTFE	Poly-Tetra-Fluor-Etheen
PWM	Pulse Width Modulation
RMS	Root Mean Square
SKF	Svenska Kullagerfabriken
TEC	Thermal Equivalent Circuit
TIA	Tubular Induction Actuator
TPFSA	Tubular Parallel Flux Switching Actuator
TPMA	Tubular Permanent Magnet Actuator
VDA	Verband Der Automobilindustrie

Chapter 1

Introduction

“The upward spiral of investing money, effort and time to create systems that make things cheaper, easier and faster.”

1.1 The magnetization direction of society

The discovery of electromagnetism and its applicability in energy generation, conversion and consumption has tremendously changed the society as we experience today. In 1831, the experiment of Michael Faraday, in which he proved that a moving wire in a magnetic field produces a current, has led to his creation of the first electric motor. In parallel, Joseph Henry developed a similar type of motor which is now classified to be a direct current (dc) electric motor. Later, in 1887, Nikola Tesla introduced the alternating current (ac) motor which is the most commonly used motor today. The introduction of permanent magnets and development of neodymium-iron-boron (NdFeB) in the early 1980s [125] led to more efficient, powerful and smaller motors. Permanent magnets allow for more creativity and design freedom which, together with electromagnets, lead to complex actuation systems as presently existing in the industry. From rotary, linear, multi-degree of freedom (DoF) and planar actuators to passive gravity compensation systems and magnetic gears, the list of applications is endless. Even more, these efficient motors have recently made their introduction in the automotive industry. Initially, the alternator and starter motor were the only electric generator and motor in the car. Later, more functionalities like electric windows, adjustable seats and power steering are using electric motors. Currently, the ongoing transition to electric traction [25] even including electric variable transmission [26] and introduction of steer-by-wire [19], brake-by-wire and even suspension-by-wire systems, requires more advanced, efficient and powerful electromagnetic solutions.

1.2 Towards extensive electromagnetic modeling

Permanent magnets allow for more variety in topologies of motors, actuators and motion systems due to the various shapes, magnetization directions and combinations of different patterns. However, compared to electrically excited machines or actuators, several key differences should be addressed. Firstly, the magnetic flux originated from the permanent magnet travels through the magnet itself, compared to the flux generated by an electromagnet which travels through a ferromagnetic core. Therefore, permanent magnet machines tend to have a larger equivalent airgap compared to wound field machines. This leads to more leakage flux which requires more accurate modeling techniques. Secondly, the magnetic flux of the permanent magnets cannot be altered, leading to intrinsic (passive) attraction or repulsion forces or cogging forces with regard to machines. These passive forces may be undesirable and have to be minimized, however the existence of passive forces may be desirable as for example in fail-safe devices [57] or gravity compensation [46]. Thirdly, demagnetization due to high operating temperatures or external magnetic fields should be taken into account to guarantee satisfactory performance under these conditions.

Rare earth materials are still relatively expensive and during the design of electromagnetic components, it is crucial to make optimal use of them. Therefore, in addition to the presence of more leakage flux, extensive modeling of the electromagnetic field distribution has become a crucial step in the design process for developing electromagnetic devices, machines and actuators which have improved position accuracy, acceleration and force density.

Quasi-static (low frequency) electromagnetic modeling methods can be classified either as analytical, semi-analytical or numerical. Analytical models give a direct mathematical expression of the magnitude or distribution of the magnetic field. Semi-analytical models require the numerical integration or summation of an analytical formula and numerical methods require the full discretization of the geometry and/or boundaries.

1.2.1 Analytical models

Magnetic Equivalent Circuit

The most commonly used analytical model is known as the magnetic equivalent circuit (MEC). This method simplifies the flux distribution of a geometry in predefined flux tubes with constant flux. The magnetic flux density is then obtained as a product of the given magnetomotive force (mmf) due to a permanent magnet or a coil and the permeance of these flux tubes. Examples of this method are given in [114, 124]. The advantage of this method is its simplicity, low computational time and ability to include the saturation of each permeance. However, this

method has the disadvantage that prior knowledge of the flux distribution is necessary to construct an accurate model. Although a good accuracy can be achieved for a certain topology, this accuracy can be lost due to parameter variation or relative motion especially in structures including permanent magnets which have a relatively large airgap and hence suffer from leakage flux.

Current model

To obtain the field distribution in two- or three-dimensions (2D or 3D), the direct solution of the magnetostatic Maxwell's equations in terms of the magnetic vector potential, \vec{A} , is given by [52]

$$\vec{A}(\vec{x}) = \frac{\mu}{4\pi} \int_V \frac{\vec{J}(\vec{x}')}{|\vec{x} - \vec{x}'|} dV', \quad (1.1)$$

for a current density \vec{J} of the source (coil or wire), μ the permeability and \vec{x} and \vec{x}' the observation and source vector, respectively. This equation is known as the Biot-Savart law and it can be used to calculate the field distribution of current filaments, current sheets or current densities [70]. To find the field distribution due to a permanent magnet, the magnet is described as an equivalent current distribution [135] and consequently, equation (1.1) is solved, referred to as the current (sheet) model for permanent magnets.

Charge model

Alternatively, the permanent magnets can be described using an equivalent magnetic charge distribution ρ_m . The magnetic scalar potential (φ_m), is obtained as

$$\varphi_m(\vec{x}) = \frac{1}{4\pi} \int_V \frac{\rho_m(\vec{x}')}{|\vec{x} - \vec{x}'|} dV', \quad (1.2)$$

Consequently, the magnetic field strength (\vec{H}) is derived from the magnetic scalar potential using $\vec{H} = -\nabla\varphi_m$ [2]. Both the current and charge model assume a unity relative permeability of the permanent magnets. Furthermore, their applicability is still limited to regular magnet shapes, although an irregular shape can be approximated by a finite number of triangular shapes [86]. Each individual magnet has to be modeled separately which results in a relatively large computation time for systems including a large number of magnets. This method and the current model are especially beneficial for 3D geometries in the absence of soft-magnetic material where numerical methods suffer from a large computational time.

1.2.2 Numerical models

Numerical models discretize the geometry in finite mesh elements which are generally triangular for 2D and tetrahedral for 3D problems. The field solution for each element is approximated by a first or second order polynomial. Consequently, the energy function is described in terms of the field solution. The coefficients of the polynomials are obtained by minimizing the total energy of the problem taking into account interface conditions between each element and the boundary conditions at the border of the model space. This technique is referred as the finite element method (FEM) or analysis (FEA) [131]. In case only the boundaries are meshed it is referred as the boundary element method (BEM).

The oldest numerical method is the finite difference method (FDM) which describes the partial differential equations for each node in terms of a finite difference equation relating the field solution at each node to its neighboring nodes. The total field solution is then obtained by solving the total algebraic matrix of interface conditions. However, this method requires an orthogonal discretization of the geometry which is difficult to realize in problems involving curvilinear boundaries [35]. Therefore, FEM is more applicable and more popular nowadays.

For each numerical method holds that an increased mesh density improves the accuracy until numerical instability is reached, however it also increases the computational time. Numerical methods are considered to be the most generic approach to analyze electromagnetic problems since they apply to the most common industrial components and systems with the least amount of assumptions. They have the ability to handle complex geometries, include non-linear material parameters and couple to various physical domains like magnetic/thermal, magnetic/mechanical, electrical/thermal [72]. Furthermore, the capability of analyzing transient phenomenon and the coupling with electrical circuits or power electronics made these methods very popular in research and engineering.

Although these methods are computationally expensive, it is successfully applied to automated optimal design (AOD) of electromagnetic motors [71]. However, these optimization algorithms might still run in the order of hours to optimize a single geometry with three variables [117]. Therefore, more hybrid modeling techniques are employed combining FEM with analytical methods, even together with a mapping function as for example in space-mapping optimization [47].

However, correct geometry discretization requires prior knowledge of the field distribution to get a reliable solution. In ironless structures without concentrated magnetic fields [81], or machines with a small airgap and a large outer size, or devices with a very small stroke compared to their size [84], these methods become even more problematic due to the necessity of a high mesh density and/or size. Although the models can be parameterized in sizes, the variation in number of poles and slots in an electrical machine is still difficult and/or time consuming. Therefore, an (semi-)analytical method is often still desirable during the design stage where FEA is generally used as a verification method.

1.2.3 Transformation techniques

Transformation techniques are applied to the previous mentioned methods in order to apply certain boundary conditions, even with complicated shapes. The application of these transformation techniques can result in analytical methods becoming semi-analytical or even numerical. One example is the imaging method used to include soft-magnetic boundaries within the geometry [70]. The soft-magnetic boundaries are replaced by an equivalent 'imaged' source. In the case of two or more boundaries, the number of included images becomes infinite and a truncation is necessary, resulting in the analytical description becoming semi-analytical.

Another form of transformation technique is the (Schwarz-Christoffel) conformal mapping [38] in which the geometry is mapped into a less complex domain, allowing the use of analytical methods. Consequently, the solution is mapped back to the original domain. This mapping function is analytic in the case of a geometry with a maximum of four corner points however in case more points are considered, the mapping function has to be calculated numerically [38].

1.2.4 Semi-analytical models

Semi-analytical models consider the direct solution of Maxwell's equations as for the analytical models described in Sections 1.2.1 and 1.2.1. However, the solution includes a numerical summation or integration. A modeling technique belonging to this group is given by harmonic or Fourier modeling using transfer relations, or sometimes referred to as sub-domain modeling [16, 169]. The total geometry is divided into orthogonal regions (regions whose boundaries are parallel with the axes of the coordinate system) based upon material properties or/and boundary conditions. The sources (permanent magnet and coils) are described using a Fourier series. For each region, the Maxwell equations are solved in terms of the magnetic vector potential or magnetic scalar potential which leads to a Laplace or Poisson equation. The resulting field solution is obtained using separation of variables [21] and is again written in the form of a Fourier series. Finally, a set of unknown coefficients of the field solution is solved with the given boundary conditions between the various regions. This modeling technique has a limited discretization of the geometry and a discretization in the (spatial) frequency domain. Due to the use of Fourier analysis, this modeling technique is particularly useful for periodic geometries, as in the case of rotary machines or long stroke linear actuators. Since long stroke actuation systems generally consist of 'periodic sections', the analysis is restricted to one periodic section with periodic boundary conditions. Therefore, it is assumed that the end-effects of the long stroke actuator are negligible or can be dealt with separately. Furthermore, the relative permeability of each region is included and rectangular soft-magnetic boundaries can be incorporated. However, the soft-magnetic materials are generally considered to have infinite permeability, although this is not necessary for certain cases.

For example, when a region is periodic, a finite permeability can be addressed. With the use of iterative solving, the non-linear B-H curve of the soft-magnetic material can be included.

In general, each type of problem has its own suitable modeling technique, since not always a high accuracy is preferred but a low computational time could be more important. For almost every technique, these requirements are a trade-off, although the increased computational capability of microprocessors enhanced the preference use of numerical methods. For analytical or numerical calculation of secondary parameters, like force, electromotive force or inductance, only a local field solution at a predetermined point or line is necessary. Numerical methods require the solution for the total meshed geometry in order to obtain these secondary parameters [24, 28, 29]. Therefore, a mesh-free solution is preferred since the computational time is reduced. In certain problems, it even allows for analytical expressions which provide for direct means to illustrate the dependencies of the geometric parameters and material properties.

The origin of the harmonic modeling technique dates back to the beginning of the 20th century. To date many applications were considered in various coordinate systems. However, some dearth in the literature is still apparent, especially with respect to the inclusion of irregular soft-magnetic boundaries. This thesis presents a generic form, unifies and integrates all previous work into a single framework. This framework allows for implementation and automatic generation of complex analytical models for a high number of regions for the 2D Cartesian, polar and axisymmetric coordinate system. It creates a platform for extensive simulation and research for a wide class of 2D electromagnetic problems. Consequently, these models provide a tool for fast optimization and design of electromagnetic motors (inductance, synchronous and reluctance), actuators and devices. With this respect, more advanced, complex and efficient actuation systems can be developed for industrial, commercial and automotive applications. This thesis demonstrates the applicability of the generic modeling technique for the automated optimization and design of an electromagnetic active suspension system for passenger cars.

1.3 The journey of a car driver

The invention of the wheel around 4000 BC caused a revolution in transportation of humans and cargo. The horse drawn vehicle appeared which, for a while, was the standard way of transportation around the world. These carts (two-wheeled) or wagons (four-wheeled) initially had wooden wheels. The invention of the spoked wheel came around 2000 BC where a steel rim was added another thousand years later, see Fig. 1.1. This was the standard for a long period of time until in 1870 AD the first pneumatic tire was invented. This significantly improved the comfort and quality of transportation and is still used to date. The cargo was generally fixed directly to the wheel axle until the first suspension



Figure 1.1: Horse carriage with wooden and steel leaf springs.

system in the form of wooden leaf springs appeared around the time of the early Egyptians. The steel variant, (Fig. 1.1), appeared later on and was the first type of suspension system on early passenger cars.

Ever since, the comfort, controllability and safety of the suspension systems is increasing. It is of significant importance regarding the daily number of passenger cars on the road. Taking the Netherlands as an example, the number rose from 200 cars around the year 1900 up to 7.8 million in the year 2011, resulting in an average of 1 car per 2.1 inhabitants [139]. Each of them is traveling around 12.000 km per year on the Dutch road network which spans around 130.000 km. Among the 720 traffic accidents of the Netherlands in the year 2009, 296 involved passenger cars [139]. The best accident prevention is changing the populations driving attitude. However, people rely more and more on technologies that make cars inherently safer. Several technologies have proved to reduce the number of accidents, for example the anti-lock braking system (ABS), the anti-slip regulation (ASR) and the electronic stability program (ESP). The ABS system is the most popular one and is integrated in almost 100% of all the top 50 best selling cars since 2006 [139]. The system even became compulsory for all new vehicles in de European Union.

In addition to the previously mentioned active safety systems, an electronically controlled suspension system or (semi-)active suspension system can provide an additional form of safety. These suspension systems have the capability of dynamically altering their characteristics dependent on road conditions and driver inputs [89]. Such a system can respond to a sudden steering command during the well-known 'moose'- or 'elk'-test and prevent the car from roll-over. An active suspension system has furthermore the capability of responding to road vibrations and isolate the driver and passengers from any disturbance. It might, for example, be implemented in ambulances, where this system provides a faster and comfortable transportation of patients. Current research focuses on an active suspension between the ambulance and the stretcher [122]. Although these systems proved to be effective, active suspension applied at the four wheels of the ambulance eliminates the source of vibrations for the whole ambulance, including medical equipment and personnel. Furthermore, a bulky system within the ambulance is removed, resulting in additional space for medical equipment.



Figure 1.2: (a) In-wheel motor of Michelin and (b) Autonomous vehicle of GM.

The introduction of active suspensions is however, still limited, mainly due to the additional power consumption, mass and complexity. However, several reasons will enhance the introduction of active suspension systems. Due to the ever increasing oil price, political and environmental reasons, electrical vehicles will become a significant portion in everyday traffic. The ultimate degree of freedom and efficiency is achieved using in-wheel motors, Fig. 1.2(a), however this results in a reduced comfort since the unsprung mass is increased [76]. In [151], the effect of increasing the unsprung mass has been investigated experimentally on a VW Lupo 3L. It has been shown that an addition of 7.5 kg to the sprung and unsprung mass decreases ride comfort up to 25 % and 8 % in the front and rear, respectively. An increase in sprung mass of 160 kg due to the battery pack compensates for this, however, it increases the dynamic tire load up to 40 %. Therefore, it might be necessary to integrate an active suspension within the in-wheel motors as already can be observed in the design of Michelin shown in Fig. 1.2(a). Additionally, the power consumption of active suspension systems can be reduced considering electromagnetic solutions over currently used hydraulic systems.

The future generation of vehicles will become more efficient, intelligent and independent of the driver. Car-to-car and car-to-infrastructure communication will lead to autonomous vehicles, as for example shown in Fig. 1.2(b) [7], and cooperative driving where the driver is extracted from the loop. Given the fact such vehicles might ever appear in traffic, these vehicles will need active systems to act on the vehicle dynamics in critical or accident avoidant situations.

1.4 A short overview of suspension systems

The function of a suspension system is three-fold. Firstly, a suspension system fixes the location of the wheel axle in lateral and longitudinal direction. Secondly, it provides a better wheel to road contact since the wheels become independent of each other and have the possibility to follow an imperfect road profile, assuring stability and control. Thirdly, it isolates the driver, passenger, cargo and vehicle from the road disturbances, assuring a comfortable drive, even for the vehicle,

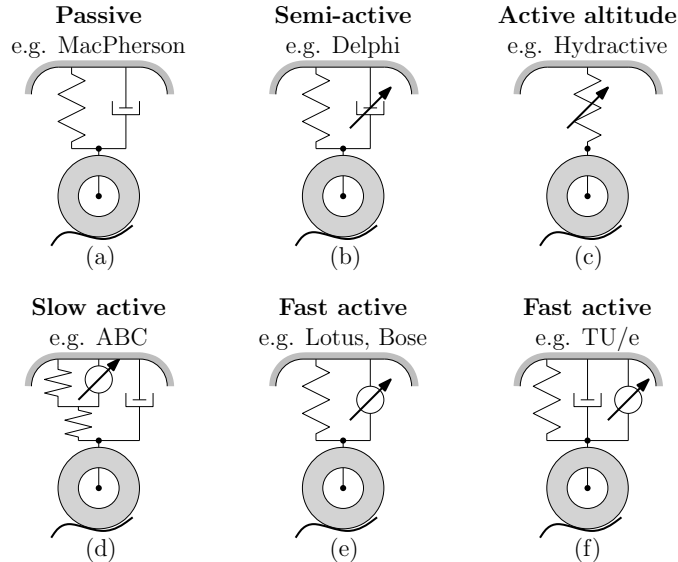


Figure 1.3: Schematic representation of various suspension topologies.

increasing its durability. Depending on the functionality, suspension systems can generally be classified as passive, semi-active or active. A schematic representation of different suspension topologies is presented in Fig. 1.3, the different geometries are discussed in the next subsections.

1.4.1 Passive suspension systems

The first (passive) suspension systems consisted only of a set of leaf springs. Leaf springs are easy to manufacture and provide wheel axle location next to a springing medium. However, due to their space requirements, coil springs appeared on the scene since they provide a very compact frictionless springing medium. Furthermore, they can be combined with telescopic hydraulic dampers creating a single unit called coil-over-damper or coilover which can be preassembled. All passive suspension systems nowadays consist of such a coil spring and a hydraulic or pneumatic damper, as schematically shown in Fig. 1.3(a). The difference in classification results from how the suspension arms, springs and dampers are configured.

One of the most commonly used front suspension is the MacPherson suspension, which was invented around 1947 [103]. This system consists of a single wishbone connecting the knuckle to the chassis, hereby fixing the position of the wheel in the longitudinal and lateral direction, see Fig. 1.4(a). Generally, a coilover connects the knuckle with the top chassis while providing a pivot point at the top for steering. This coilover resists moments about the lateral and longitudinal axis. Finally, a toe control link is used for fixing the rotation of the wheel about its

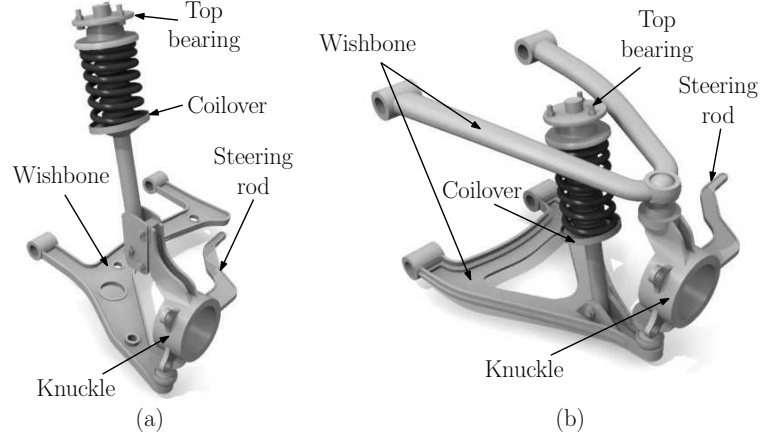


Figure 1.4: Typical independent front suspension systems: (a) MacPherson and (b) double wishbone.

vertical axis. In front suspension systems, this link is used as the steering rod. To complete the suspension, generally, an anti-roll bar is used which connects the left and right knuckles with a torsional spring, thereby reducing roll during cornering. The advantage of this topology is that it offers more space on the top than the double wishbone suspension shown in Fig. 1.4(b). This results in more space for the engine, particularly when mounted transversely. Furthermore, the low cost and simple construction make this topology very popular as a front suspension. One disadvantage of this suspension topology compared to double wishbone systems is that noise and vibration from the road is directly transmitted to the chassis and more isolation is necessary. Furthermore, vertical movement of the tire results in a larger change in camber angle leading to a lower handling performance than the double wishbone system. Although these passive suspensions are simple, economic and fail-safe, their characteristics are fixed and designers still struggle to find the perfect compromise between a comfortable ride and sufficient handling.

1.4.2 Semi-active suspension systems

Semi-active or adaptive damping suspension systems appeared around 1980 and have the ability to alter the damping characteristic with minimal amount of energy, Fig. 1.3(b). Semi-active suspension systems can be hydraulic based, in which the orifice opening is varied to alter the damping behavior [79, 92]. Alternatively, they can be based on magnetorheological fluid, in which a magnetic field varies the viscosity of the hydraulic fluid mixed with ferromagnetic particles, again altering the damping characteristic [14, 56]. This technology is developed by Delphi Corporation [31] under the name 'MagneRide' shown in Fig. 1.5. Compared to passive systems, they can vary the dissipation rate of energy with minimal power requirements as indicated in Fig. 1.6. The previous examples however, both dis-

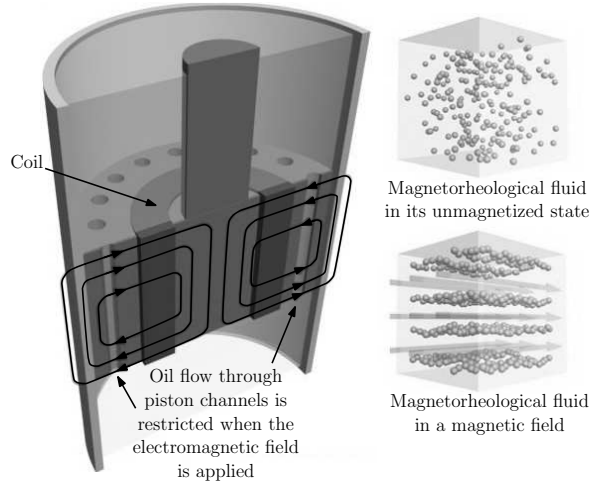


Figure 1.5: Magnetorheological damper, MagneRide of Delphi Corporation.

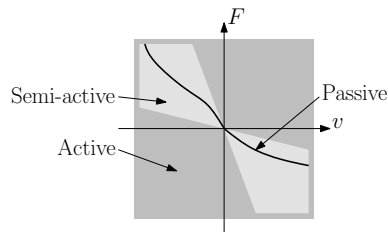


Figure 1.6: Classification of suspension system using the force-velocity diagram.

sipate the damping energy in the form of heat. An example of a regenerative damper is developed by Levant Power Corporation [98]. Their 'GenShock' is a shock absorber where the hydraulic fluid flows through a specialized manifold and a hydraulic motor which drives an electric generator to recuperate the otherwise dissipated energy. Depending on the road conditions and vehicle mass, the recuperated energy ranges from 10 W to 1 kW, resulting in an improved fuel economy of 1 to 6 % [98]. However, these figures are only obtained for heavy duty vehicles and military applications.

1.4.3 Active suspension systems

Although semi-active suspension systems already improve the degree of flexibility and hence performance, they cannot cover the total force-velocity diagram of Fig. 1.6. Active suspension systems are able to supply energy to the system, and hence deliver active forces, even in the direction of the velocity. This allows for both roll and pitch control, leveling and the ability to completely absorb road vibrations. A distinction is generally made between active attitude control, slow active and fast active suspension systems.

Active attitude control

Active attitude control is mainly concerned with eliminating the low frequent body roll during cornering and pitch movement during braking and accelerating. Such a system generally consists of a very soft spring hereby improving comfort, whose stiffness can be increased to eliminate roll and pitch movement, as schematically shown in Fig. 1.3(c). A commercial example is given by the 'Hydractive' system of Citroën which uses spheroidal gas springs at each corner together with an additional sphere for each axle. The height and spring rate can be controlled at each corner, allowing for anti-roll and -pitch control together with leveling. Another commercial example is the BMW Anti Roll Control (ARC) in which hydraulic rotary actuators, operating around 200 bar, are inserted in the front and rear anti-roll bar [140]. Based upon sensor input, the roll is minimized within a response time of 10 ms for lateral accelerations below 0.1 g. Recently, a variable electromagnetic spring (ELMASP), has been developed at the Eindhoven University of Technology in cooperation with SKF (Svenska Kullagerfabriken) [46, 48]. The ELMASP provides an electromagnetic passive spring stiffness of 30 kN/m, a peak force of 6.5 kN at a stroke of 0.175 m. Furthermore, using a novel multi-coil configuration, the force-position response can be shifted, providing leveling or control of the spring rate. However, the volumetric specifications of a general passenger car were not met and a further improvement of the concept is necessary.

Slow active suspension systems

Slow active suspensions systems, as the name suggests, have a low bandwidth which is typically below 5 Hz. The actuator, either hydraulic or electromagnetic, is positioned in series with a spring. Additionally, the actuator itself might have an accumulator spring in parallel for gravity compensation as shown in Fig. 1.3(d). The damper is employed in parallel to the whole system. A commercially available product based on the hydraulic version is given by the Active Body Control (ABC) of Mercedes shown in Fig. 1.7(a). This system requires no anti-roll bar and reduces low-frequency roll and pitch movement. Since it is hydraulic based, it even can provide leveling in a range of 65 mm.

A slow electromagnetic active suspension is developed by ZF and Volkswagen [113]. The electromagnetic actuation consists of an electric motor and a spindle drive as represented in Fig. 1.7(b). Due to the fact that the electric motor can operate in four quadrants and allows for regeneration, the energy consumption is significantly reduced by approximately a factor 4 compared to the hydraulic ABC system of Mercedes [113].

Another example of a slow active suspension system is the low-power variable geometry active suspension system developed for commercial vehicles [49, 50]. The sprung and unsprung masses are connected via a mechanical spring and a wishbone. By means of a PM dc motor, the wishbone is rotated, hereby altering

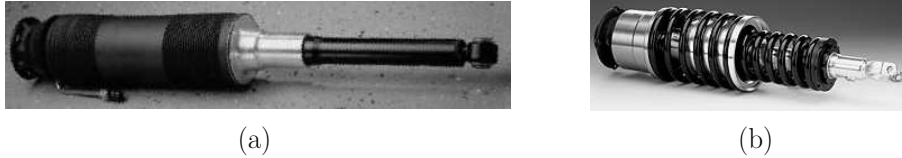


Figure 1.7: Two examples of slow-active suspension systems (see Fig. 1.3(d)), (a) Hydraulic ABC system of Mercedes and (b) electromechanical ABC system of ZF and Volkswagen [113].



Figure 1.8: Bose suspension system [15].

the pretension of the spring. This, in turn, generates a variable active force in series with the spring. Since the direction of rotation is orthogonal to the direction of the suspension, the system consumes a relatively low amount of energy.

Fast active suspension systems

Fast active suspensions are considered to have a high bandwidth, typically beyond 50 Hz. The actuator is directly connected between the sprung and unsprung mass. Often a mechanical spring is placed in parallel for gravity compensation to reduce power consumption, Fig. 1.3(e). Since the actuator directly applies the force between the sprung and unsprung mass, a higher bandwidth can be achieved, given the actuator has a high bandwidth itself. The first fast active suspension system was developed by Colin Chapman for a Lotus Esprit which later was used on a Lotus T92 Formula 1 car in 1983 [161]. The system uses hydraulic actuators in parallel with passive springs which even were removed in a later version. By maintaining a small and constant ground clearance, it resulted in a three seconds faster lap round time. However, it was less competitive than other cars with similar engines due to the additional mass of 12 kg and the required horsepower. Due to the increased cornering speeds and lateral accelerations up to 3 g, the consequence of a system failure would be dramatically. An almost deadly accident at Spa-Francorchamps due to a leak in the hydraulic system resulted in these systems being banned from Formula 1 since 1994.

A fast active electromagnetic suspension system for passenger cars was developed by Bose [15], known for its speaker technology. The system shown in Fig. 1.8 consists of a linear permanent magnet actuator in parallel with a mechanical spring. The bandwidth of this system is beyond the necessity for suspension systems. However, the system is not commercially available and no official test data or scientific papers were published to date besides published videos. Bose claims a power consumption which is less than one third of a traditional air conditioning system [87].

1.4.4 The direct-drive electromagnetic suspension system

Due to the performance and flexibility of a fast active suspension system, it is considered to be the ideal suspension system. Considering hydraulic or electromagnetic suspension systems, some comparisons can be made. The main advantages of a hydraulic system can be listed as

- a very high force density,
- ease of design,
- commercial availability of the various parts,
- reliability and commercial maturity.

The main disadvantages of hydraulic systems are

- the inefficiency due to the required continuously pressurized system,
- relatively high system time constant (due to pressure loss and flexible hoses),
- environmental pollution due to hose leaks and ruptures, where hydraulic fluids are toxic and
- mass and intractable space requirements of the total system including supply system albeit that it mainly contributes to the sprung mass.

On the other hand, the advantages of an electromagnetic system are given by

- an increased efficiency and energy harvesting due to the dual operation of the actuator,
- improved dynamic behavior,
- higher durability,
- accurate force, acceleration, velocity and position control,

with the disadvantages listed as

- increased volume of the suspension unit, since the force density of the active part of hydraulics is higher than for electro-magnetic actuation, however the total system mass and volume could be less,
- initial higher system costs.

The developed suspension system in this thesis is electromagnetic based since it outperforms the hydraulic system in terms of power consumption and efficiency.

Furthermore, direct-drive electromagnetic actuation is chosen since it provides a higher bandwidth compared to a spindle drive [113]. The disadvantage of a low force density is solved by choosing the most suitable actuation topology, electromagnetic modeling and optimization of the force density. The electromagnetic solution is furthermore preferred due to the automotive trend towards full electrical vehicles which even have much higher battery voltage levels, making electromagnetic systems even more efficient and applicable. The fully active suspension system developed comprises of electromagnetic actuation in parallel with a coil spring for gravity compensation. Furthermore, electromagnetic passive damping is integrated within the actuation system to make the total system fail-safe. The schematic representation is shown in Fig. 1.3(f). In case of a power breakdown, a passive suspension system is still apparent. The disadvantage of the initial higher system costs should be reduced in the long term due to mass production and optimization of the fabrication process.

1.5 Thesis outline

The scientific contribution considered in this thesis can be divided into two distinctive parts. The first part considers electromagnetic modeling techniques. A generic electromagnetic modeling technique is developed based on Fourier analysis. This technique can be applied to a broad class of electromagnetic machines and devices offering a high accuracy within a short computation time. The technique is applied for tubular permanent magnet actuators. Furthermore, the modeling of enhanced electromagnetic damping within tubular actuators is described. The second part of the thesis applies the techniques developed in Part I to the design of an electromagnetic active suspension system for automotive applications. This suspension system provides improved comfort and a better handling at the expense of a low power consumption. The outline of the thesis is divided into two parts with the following chapters:

Part I: Electromagnetic modeling techniques

- Chapter 2 presents the generalized harmonic modeling technique for the calculation of the magnetic field distribution in 2D electromagnetic problems. The method and solution as well as its applicability are described. Furthermore, the accuracy and certain implications of the implementation are discussed based on a set of examples in each of the considered coordinate systems which are verified with FEA.
- The application of the harmonic modeling technique to tubular permanent magnet actuators is the subject of Chapter 3. It provides a fast and accurate tool to predict the magnetic field distribution, force output, force ripples, electromotive force and synchronous inductance. Additionally, a thermal equivalent circuit is derived to obtain the temperature distribution.

- The integration and enhancement of fail-safe electromagnetic damping within a tubular permanent magnet actuator is explained in Chapter 4 together with a technique to model the dynamic behavior. Furthermore, the influence on the actuator performance is investigated.

Part II: Design of a direct-drive active suspension system

- Chapter 5 describes the system topology of the direct-drive electromagnetic active suspension system. A set of specifications is derived for a retro-fit in a BMW 530i based upon a quarter car model, road vibration analysis and on-road measurements.
- Chapter 6 applies the modeling techniques of Part I to obtain a final design based upon the specifications of Chapter 5. An automated optimization and design (AOD) algorithm based on a non-linear constrained optimization algorithm is implemented to optimize the various considered topologies and select the optimal configuration for the given application.
- The designed active suspension system of Chapter 6 is manufactured and the performance of the prototype is experimentally verified in Chapter 7. Robust controllers are developed for the improvement of comfort and handling of the vehicle corner. Furthermore, the performance and power consumption of the robust controlled active suspension system is verified with experiments on a full scale quarter car test setup. Finally, on-road measurements with a BMW 530i including the active suspension system are performed to indicate the full-car performance of the developed system.

Part III: Closing

- Chapter 8 concludes with the contributions and achievements of this thesis and provides recommendations for future research and development.

Part I

Electromagnetic modeling
techniques

Chapter 2

Generalized harmonic modeling technique

“Everything in the Universe seems periodic, maybe even its existence...”

For the design of high force density actuation systems, accurate modeling of the electromagnetic phenomena is required. This chapter describes the analytical techniques used for modeling and analysis of the magnetostatic field distribution in 2D electromagnetic problems. The harmonic modeling technique is based on Fourier analysis where the total geometry is divided into separate regions. Within each region, the field solution is obtained by solving the magnetostatic Maxwell equations in terms of the magnetic vector potential. A set of unknown coefficients is solved from a set of boundary conditions determined by the geometry of the problem. The description is generic for a broad class of machines and devices described in the 2D Cartesian, polar and axisymmetric coordinate system.

The contribution of this chapter is published in:

Gysen, B. L. J., Meessen, K. J., Paulides, J. J. H. and Lomonova, E. A. [2010*b*], ‘General formulation of the electromagnetic field distribution in machines and devices using Fourier analysis’, *IEEE Transactions on Magnetics* **46**(1), 39–52.

Gysen, B. L. J., Ilhan, E., Meessen, K. J., Paulides, J. J. H. and Lomonova, E. A. [2010*a*], ‘Modeling of flux switching permanent magnet machines with Fourier analysis’, *IEEE Transactions on Magnetics* **46**(6), 1499–1502.

Gysen, B. L. J., Meessen, K. J., Paulides, J. J. H. and Lomonova, E. A. [2011], ‘3D analytical and numerical modeling of tubular actuators with skewed permanent magnets’, *IEEE Transactions on Magnetics* **47**(9), 2200–2212.

Gysen, B. L. J., Meessen, K. J., Paulides, J. J. H. and Lomonova, E. A. [2009], Computational analysis of fringing fields and forces in the cylindrical coordinate system, *in* ‘Proceedings of the 17th Conference on the Computation of Electromagnetic Fields, COMPUMAG 2009’, Florianopolis, Brasil, pp. 769–770.

2.1 Literature overview

The harmonic modeling technique is a method which considers the direct solution of the Maxwell equations using separation of variables. Depending on the type of boundary value problem, dynamic, quasi-static or static, the Maxwell equations in terms of potentials can be represented by a diffusion, Poisson or Laplace equation.

The method originates from the book of Hague [70] from 1929, which considers the field solution for arbitrary positioned current carrying wires between two parallel or concentric iron surfaces. Consequently, Mishkin [112] applied this method to squirrel cage induction machines in 1953. The toothed machine geometry is approximated by isotropic, homogeneous periodic layers and the stator excitation is modeled by means of a current sheet. The Maxwell equations are solved for each region together with a set of boundary conditions, however only the fundamental harmonic was considered. In 1972, this technique was exploited for linear [4] and tubular induction motors [40]. Williamson extended the theory considering each region to be anisotropic and to incorporate the effect of stator laminations in 1974 [160]. In 1977, Hughes and Miller discussed the use of this method to calculate the magnetic field distribution for iron-cored and air-cored synchronous machines [78]. Melcher [109] described the use of Fourier series to solve 1D diffusion problems.

Permanent magnet machines

Boules, applied the harmonic modeling technique to permanent magnet motors in 1984 by replacing the permanent magnets by an equivalent distribution of ampere-conductors and using Hague's field solution in the Cartesian [16] and later on in the polar coordinate system [17]. The total geometry only consisted of a single periodic region, which height was corrected by an equivalent airgap length to include saturation. The slotting effect of the motor was incorporated using Carter's coefficient.

Gu separated the magnet and airgap region, solved the Maxwell equations directly and obtained the coefficients from the boundary conditions between the regions [55]. However the model was in Cartesian coordinates and the relative permeability of the permanent magnets was not included. Marinescu applied this method for segmented Halbach arrays in the polar coordinate system [104]. Zhu extended this method in 1993 including the relative permeability of the permanent magnets [169]. The armature reaction is obtained by applying a current sheet at the stator bore [166]. Consequently, the effect of slotting was included by means of a relative permeance function in [167]. All these phenomena were combined in [168] to obtain the resultant magnetic field distribution under loaded conditions. In 1996, Trumper [147] applied the theory to a linear motor stage with a single magnetically-levitated moving part. The application to tubular permanent magnet actuators was developed by Wang [157] for various magnetization topologies.

Slotting effect

All previously mentioned literature assumes isotropic regions within the direction of motion. This does not allow for incorporation of the local slotting effect. This effect is only incorporated on a global scale by means of an equivalent airgap or Carter factor. However, this does not allow for calculation of the cogging force which can cause significant vibrations within the machine or actuator. Conformal mapping transforms the slotted geometry to a slotless one and allows for the application of previous mentioned theory. The effect of slotting can be incorporated by means of a relative permeance function as described by Zhu [167]. This function modulates the earlier calculated radial flux density in the airgap and is determined based on conformal mapping of one slot opening. The average decay in flux density determined by this method is the well-known Carter factor for electric machines. Kim [91] extended the method to incorporate the effect on the tangential flux density component and incorporated rotor eccentricity.

Alternatively, one can consider a complex permeance function based on conformal mapping presented by Zarko [164], hereby including the tangential component and calculate the corresponding cogging torque. However, considering permanent magnet machines, some implications exist. The conformal transformation maps the simple magnet geometry to a complicated shape in the slotless domain. Therefore, permanent magnets have to be approximated by current sheets which are again approximated by a finite number of point wires as applied to slotted linear motors by Krop [93]. Therefore, the relative permeability of the permanent magnets should be neglected. The resulting technique becomes time consuming and can be considered more numerical than analytical. Furthermore, the application to the axisymmetric coordinate system for tubular actuators is not possible and should be approximated by an equivalent linear actuator as shown by Gysen [68].

A different method was employed by Ackermann [1] in 1995 in which the slotted geometry is divided into separate regions. The magnetostatic Maxwell equations are solved for each region in the Cartesian and polar coordinate system. The unknown coefficients are again solved by means of the boundary conditions. The difference in previous harmonic modeling techniques is the boundary condition at the stator bore which is now solved by means of mode matching. In contrast to the previous models, where each harmonic was independent of each other, the mode matching causes cross dependency between the various harmonics due to the slotting effect. However, the set of coefficients is solved iteratively which makes it very time consuming. Liu [102] presented this method and the resulting set of equations in matrix notation in 2007 which allowed for the direct solution of the unknown coefficients, however, only one slot was considered. Later in 2009, the theory was exploited for integer-slot machines by Dubas [39].

The generic formulation

Previous work exploits the technique from an application point of view. This results in analytical solutions and expressions which are valid for a particular type

of geometry. Furthermore, several cases or applications are still not considered to date:

- slotting effect in the axisymmetric coordinate system,
- end-effects of an axially magnetized tubular actuator,
- permanent magnets and current sources of arbitrary width within a slot region in any coordinate system,
- combination of different slot regions (slot wedges) in any coordinate system.

Rather than solving these particular cases individually, this thesis presents a generic formulation completing and unifying the prior art into a single framework applicable to a wide class of machines or devices in the 2D Cartesian, polar and axisymmetric coordinate system [61].

2.2 Assumptions

The important geometrical and electromagnetic assumptions of the generic modeling technique can be listed as:

- 2D description of the electromagnetic problem,
- linear, homogeneous and isotropic material properties,
- infinite permeability ($\mu = \infty$) of the soft-magnetic material for non-periodic regions,
- invariant source terms (coils and permanent magnets) in the normal direction within one region.

Electromagnetic devices have a three-dimensional geometry. Since only 2D problems can be considered, the geometry should be invariant with one of the three dimensions, or its dependency should be negligible. This is often a valid assumption since for example, in rotary actuators with a small radius compared to the axial length, the 3D effects due to the finite axial length are often negligible. For tubular actuators, the axisymmetry results inherently in a 2D problem description. A large class of long-stroke actuators and machines exhibit a certain symmetry or periodicity. The use of harmonic analysis allows one to use that periodicity to describe the magnetic field distribution. If the 2D problem has no periodicity, it can be obtained by repeating the problem in the direction where the periodicity should be obtained with the assumption that the electromagnetic influence of the repetition on the 2D problem is negligible.

Table 2.1: Coordinate systems

	Normal	Tangential	Longitudinal
General	p	q	l
Cartesian	y	x	z
Polar	r	θ	z
Axisymmetric	r	z	θ

Three different 2D coordinate systems are considered, Cartesian (x, y) , polar (r, θ) and axisymmetric (r, z) . The direction of periodicity is arbitrary for the Cartesian coordinate system, either the x - or the y -direction can be used, however the x -direction is chosen in this thesis. For the polar and axisymmetric coordinate system, the direction of periodicity is the θ - and z -direction, respectively, since physically no electromagnetic periodicity can be obtained in the r -direction. For generality, the normal direction is referred as the p -direction, the direction of periodicity or the tangential direction is referred as the q -direction and the longitudinal (invariant) direction is referred as the l -direction. A summary of the considered coordinate systems is given in Table 2.1.

The analytical solution only applies to linear problems and the permeability of all materials is assumed to be isotropic and homogenous. The permanent magnets are modeled with a linear B - H magnetization curve with remanence B_{rem} and relative recoil permeability μ_r .

The relative permeability of the soft-magnetic material is assumed to be infinite, hence the magnetic field distribution is not calculated inside the soft-magnetic material but the magnetic field strength normal to the boundary of the soft-magnetic material is set to zero (Neumann boundary condition). However for certain conditions, a finite permeability of the soft-magnetic material can be included. This is described in the following section.

The source regions, magnets or current carrying coils, are invariant in the normal direction. This implies that a source that varies in the normal direction should be described by multiple regions, as shown in [106].

2.3 Division in regions

To solve the total field distribution for the electromagnetic problem, the two-dimensional geometry is divided into several regions. Every region should be orthogonal, hence enclosed by four boundaries where each boundary is in parallel with one of the two variant directions under consideration (normal or tangential). When a boundary is not in parallel with one of the two dimensions, it can be approximated by a finite number of rectangles with varying width [106]. Globally, the total boundary value problem has to be divided into periodic, Fig. 2.1(a), and non-periodic regions, Fig. 2.1(b). For a periodic region, the borders parallel to

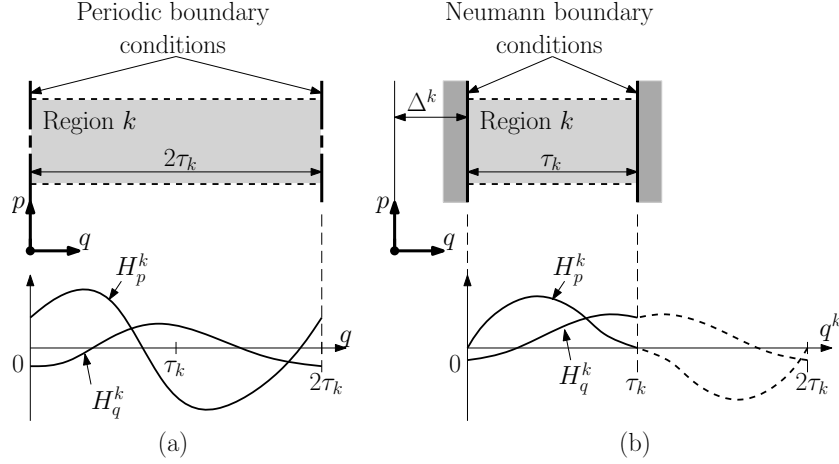


Figure 2.1: Definition of (a) a periodic region and (b) a non-periodic region.

the p -direction should be periodic, see Fig. 2.1(a). For a non-periodic region, Neumann boundary conditions are applied to the borders parallel to the p -direction, see Fig. 2.1(b). Furthermore, each region has to be further divided such that each region is either:

- a source-free region (air, vacuum, iron),
- a magnetized region (permanent magnets),
- a current carrying region (coils, wires),

hence, the division in regions is such that each region has constant permeability and the source term does not vary in the normal direction.

The reason for applying Fourier theory to the solution of the magnetic field distribution is to satisfy the boundary conditions in the tangential direction (constant q). For a region, k , with periodic boundary conditions, Fig. 2.1(a), and width $2\tau_k$, choosing the mean period of $2\tau_k$ for the Fourier series of the magnetic field inherently satisfies the periodic boundary conditions. For a region, k , with soft-magnetic boundaries, Fig. 2.1(b), the tangential magnetic field component at the boundary has to be zero. As a sine function has two zero crossings (at 0 and π), describing the component of the magnetic field tangential to the boundary by means of a Fourier series with mean period $2\tau_k$, where τ_k is the width of the region, inherently satisfies the Neumann boundary condition at the left and right side of the region ($H_p^k = 0$). This division in regions implies that the soft-magnetic material surrounding the region is assumed to have infinite permeability. However, for periodic regions, it is still possible to include a finite permeability. Hence if the soft-magnetic material can be modeled as a periodic region, a finite permeability can be addressed.

To simplify the magnetic field formulation, each region has its own local coordinate system. In this respect, each region is shifted in the tangential direction towards the global coordinate system (p, q) with a given distance Δ^k . Hence, the local coordinate system of region k is denoted as (p, q^k) with

$$q^k = q - \Delta^k, \quad (2.1)$$

where the offset, Δ^k , is indicated in Fig. 2.1(b). This offset is set to zero for all periodic regions. Since all regions have a parameter Δ^k defining the offset in the tangential direction, motion in this direction can easily be implemented. Defining a set of fixed regions and a set of moving regions, an increment of the parameter Δ^k for all regions within the moving set results in a positive displacement.

2.4 Magnetostatic Maxwell equations

For the derivation of the magnetostatic Maxwell equations, the magnetic flux density, \vec{B} , and the electric flux density, \vec{D} , are assumed to be independent of time

$$\frac{\partial \vec{B}}{\partial t} = 0, \quad (2.2)$$

$$\frac{\partial \vec{D}}{\partial t} = 0. \quad (2.3)$$

In such a case, the Maxwell equations can be decoupled into electrostatic and magnetostatic theory. The magnetostatic Maxwell equations can, therefore, be listed as [52]

$$\nabla \times \vec{H} = \vec{J}, \quad (2.4)$$

$$\nabla \cdot \vec{B} = 0. \quad (2.5)$$

The magnetization vector, \vec{M} , of a magnetic material has two components

$$\vec{M} = \vec{M}_0 + \vec{M}_s. \quad (2.6)$$

The first component, denoted as M_0 , results from the permanent magnetization which is present in hard magnetic materials like permanent magnets. This source of permanent magnetization results in a magnetic field, \vec{H} . Due to this magnetic field, a secondary magnetization results since the material has a finite magnetic

susceptibility, χ . This secondary magnetization, \vec{M}_s , is related to the magnetic field as

$$\vec{M}_s = \chi \vec{H}. \quad (2.7)$$

The resulting magnetic flux density is related to the magnetic field and the magnetization via the constitutive relation as

$$\vec{B} = \mu_0(\vec{H} + \vec{M}), \quad (2.8)$$

$$= \mu_0\mu_r\vec{H} + \mu_0\vec{M}_0, \quad (2.9)$$

where $\mu_r = (1 + \chi)$, is the relative permeability of the material and μ_0 is the permeability of air.

To simplify the analysis, the two coupled field equations, eq.(2.4) and (2.5), are rewritten into a single field equation. Since the divergence of the magnetic flux density is zero, this solenoidal field can be written as the rotation of a different vector field, denoted as the magnetic vector potential [52], \vec{A} ,

$$\vec{B} = \nabla \times \vec{A}. \quad (2.10)$$

Substituting the constitutive relation, equation (2.9), into equation (2.4) and substituting equation (2.10) reduces the magnetostatic Maxwell equations into a Poisson equation for every region k , given by

$$\nabla^2 \vec{A} = -\mu_0(\nabla \times \vec{M}_0) - \mu \vec{J}, \quad (2.11)$$

for $\mu = \mu_0\mu_r$. In case only 2D boundary value problems are considered, the magnetization vector \vec{M}_0 only has components in the normal, M_p , and tangential direction, M_q , and the current density vector, \vec{J} , has only a component in the longitudinal direction, J_l . Therefore, the magnetic vector potential has only a component in the longitudinal direction, A_l , which is only dependent on the normal, p , and tangential direction, q . The Poisson equations in the different coordinate systems are therefore, given by

Cartesian:

$$\frac{\partial^2 A_l}{\partial p^2} + \frac{\partial^2 A_l}{\partial q^2} = -\mu_0 \left(\frac{\partial M_p}{\partial q} - \frac{\partial M_q}{\partial p} \right) - \mu J_l, \quad (2.12)$$

Polar:

$$\frac{1}{p} \frac{\partial}{\partial p} p \frac{\partial A_l}{\partial p} + \frac{1}{p^2} \frac{\partial^2 A_l}{\partial q^2} = -\mu_0 \left(\frac{1}{p} \frac{\partial(pM_q)}{\partial p} - \frac{1}{p} \frac{\partial M_p}{\partial q} \right) - \mu J_l, \quad (2.13)$$

Axisymmetric:

$$\frac{1}{p} \frac{\partial}{\partial p} p \frac{\partial A_l}{\partial p} + \frac{\partial^2 A_l}{\partial q^2} - \frac{1}{p^2} A_l = -\mu_0 \left(\frac{\partial M_p}{\partial q} - \frac{\partial M_q}{\partial p} \right) - \mu J_l. \quad (2.14)$$

Note that when a particular region k is considered, the local coordinate system needs to be considered, replacing q by q^k . The magnetic flux density distribution can be obtained from the solution of the magnetic vector potential by means of equation (2.10) and the magnetic field strength, \vec{H} , is obtained from the flux density distribution by means of the constitutive relation (2.9).

2.5 Source term description

In order to create a generalized formulation, the source term description for either periodic or non-periodic regions should be unified. The function which describes the source term for a magnet or coil region can be the normal, M_p^k , or tangential magnetization component, M_q^k , or the longitudinal current density component, J_l^k . For periodic regions, their tangential dependency can be written in terms of a Fourier series as

$$\vec{M}_0^k = M_p^k(q^k) \vec{e}_p + M_q^k(q^k) \vec{e}_q, \quad (2.15)$$

$$M_p^k(q^k) = M_{p0}^k + \sum_{n=1}^{\infty} \left(M_{psn}^k \sin(w_n^k q^k) + M_{pcn}^k \cos(w_n^k q^k) \right), \quad (2.16)$$

$$M_q^k(q^k) = M_{q0}^k + \sum_{n=1}^{\infty} \left(M_{qsn}^k \sin(w_n^k q^k) + M_{qcn}^k \cos(w_n^k q^k) \right), \quad (2.17)$$

$$\vec{J}^k = J_l^k(q^k) \vec{e}_l, \quad (2.18)$$

$$J_l^k(q^k) = J_{l0}^k + \sum_{n=1}^{\infty} \left(J_{lsn}^k \sin(w_n^k q^k) + J_{lcn}^k \cos(w_n^k q^k) \right), \quad (2.19)$$

where the spatial frequencies, w_n^k , for every region k are defined as

$$w_n^k = \frac{n\pi}{\tau_k}. \quad (2.20)$$

For regions k with periodical boundary conditions, the width of the region is defined as $2\tau_k$. Hence, using general Fourier theory, the average, sine and cosine components of the source function, either M_p^k , M_q^k or J_l^k as function of the

tangential direction q^k for region k can be calculated as

$$M_{p0}^k = \frac{1}{2\tau_k} \int_0^{2\tau_k} M_p^k(q^k) dq^k, \quad (2.21)$$

$$M_{psn}^k = \frac{1}{\tau_k} \int_0^{2\tau_k} M_p^k(q^k) \sin(w_n^k q^k) dq^k, \quad (2.22)$$

$$M_{pcn}^k = \frac{1}{\tau_k} \int_0^{2\tau_k} M_p^k(q^k) \cos(w_n^k q^k) dq^k. \quad (2.23)$$

For non-periodic regions, the source term is non-periodic. Hence, quasi-periodicity is introduced assuring the Neumann boundary condition in the tangential direction is satisfied. The total source description is therefore obtained by applying the imaging method [70], where the source is mirrored around its tangential boundaries as indicated in Fig. 2.2. A consequence of this imaging method, is that, for normal magnetized regions, the average and cosine terms are zero ($M_{p0}^k = 0, M_{pcn}^k = 0$) and, for the tangential magnetized regions and longitudinal current density regions, the sine terms are zero ($M_{psn}^k = 0, J_{lcn}^k = 0$). After applying the imaging method, equations (2.21) to (2.23) can be used to calculate the components. Note that this source description is the reason why periodic regions have width $2\tau_k$ and non-periodic regions have width τ_k .

2.6 Semi-analytical solution

Due to the source terms being expressed as a Fourier series, the resulting solution for the magnetic vector potential is also written in terms of harmonic components. The Poisson equation is solved with the use of separation of variables [21]. Hence, the solution of the vector magnetic potential is given by a product of two functions, one dependent on the normal direction, p , and another one-on the tangential direction, q . As mentioned before, the functions for the tangential direction are sine and cosine functions since a Fourier description is used. The function for the normal direction is such that the Poisson equation is satisfied. The general solution of the magnetic vector potential is given by

$$\vec{A}^k = A_l^k(p, q^k) \vec{e}_l, \quad (2.24)$$

$$A_l^k(p, q^k) = \sum_{n=1}^{\infty} \left(A_{lcn}^k(p) \cos(w_n^k q^k) + A_{lcn}^k(p) \sin(w_n^k q^k) \right) + A_{l0}^k(p). \quad (2.25)$$

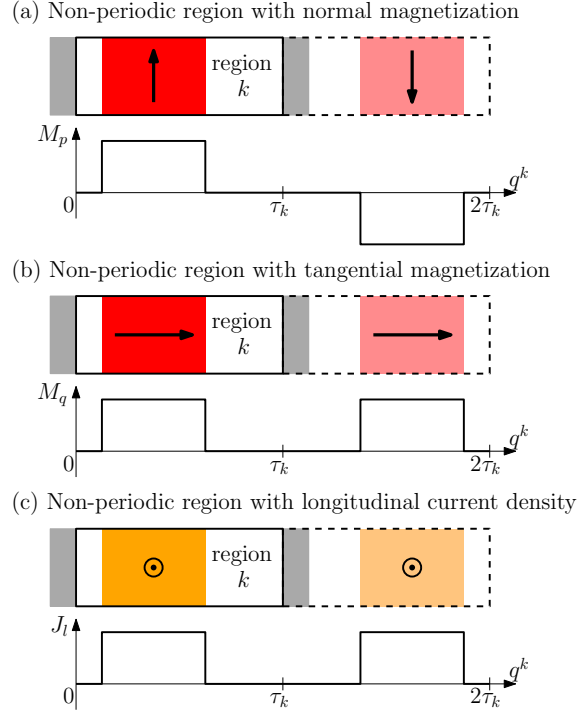


Figure 2.2: Source description for non-periodic regions using the imaging method.

Hence, the general expressions for the magnetic flux density distribution can be written as

$$\vec{B}^k = B_p^k(p, q^k)\vec{e}_p + B_q^k(p, q^k)\vec{e}_q, \quad (2.26)$$

$$B_p^k(p, q^k) = \sum_{n=1}^{\infty} \left(B_{psn}^k(p) \sin(w_n^k q^k) + B_{pcn}^k(p) \cos(w_n^k q^k) \right), \quad (2.27)$$

$$B_q^k(p, q^k) = \sum_{n=1}^{\infty} \left(B_{qsn}^k(p) \sin(w_n^k q^k) + B_{qcn}^k(p) \cos(w_n^k q^k) \right) + B_{q0}^k(p), \quad (2.28)$$

where the functions A_{lcn}^k , A_{lcn}^k , A_{l0}^k , B_{psn}^k , B_{pcn}^k , B_{qsn}^k , B_{qcn}^k , and B_{q0}^k can be obtained by solving the Poisson equations for every coordinate system, and are listed in the following subsections for each of the considered coordinate systems.

2.6.1 Cartesian coordinate system

The functions dependent on the normal direction of the solution for the magnetic vector potential and flux density components in the Cartesian coordinate system are given by

$$A_{lsn}^k(p) = \frac{1}{w_n^k} \left(c_n^k e^{w_n^k p} + d_n^k e^{-w_n^k p} - \mathcal{G}_{pcn}^k \right), \quad (2.29)$$

$$A_{lcn}^k(p) = \frac{1}{w_n^k} \left(a_n^k e^{w_n^k p} + b_n^k e^{-w_n^k p} + \mathcal{G}_{psn}^k \right), \quad (2.30)$$

$$A_{l0}^k(p) = -\mu J_{l0}^k \frac{p^2}{2} + B_0^k p + A_0^k, \quad (2.31)$$

$$B_{psn}^k(p) = a_n^k e^{w_n^k p} + b_n^k e^{-w_n^k p} + \mathcal{G}_{psn}^k, \quad (2.32)$$

$$B_{pcn}^k(p) = -c_n^k e^{w_n^k p} - d_n^k e^{-w_n^k p} + \mathcal{G}_{pcn}^k, \quad (2.33)$$

$$B_{qsn}^k(p) = c_n^k e^{w_n^k p} - d_n^k e^{-w_n^k p}, \quad (2.34)$$

$$B_{qcn}^k(p) = a_n^k e^{w_n^k p} - b_n^k e^{-w_n^k p}, \quad (2.35)$$

$$B_{q0}^k(p) = -\mu J_{l0}^k p + B_0^k, \quad (2.36)$$

where \mathcal{G}_{psn}^k and \mathcal{G}_{pcn}^k are defined as

$$\mathcal{G}_{psn}^k = \mu_0 M_{psn}^k + \frac{\mu J_{lcn}}{w_n^k}, \quad (2.37)$$

$$\mathcal{G}_{pcn}^k = \mu_0 M_{pcn}^k - \frac{\mu J_{lsn}}{w_n^k}. \quad (2.38)$$

2.6.2 Polar coordinate system

The functions dependent on the normal direction of the solution for the magnetic vector potential and flux density components in the polar coordinate system are given by

$$A_{lsn}^k(p) = -\frac{1}{w_n^k} \left(c_n^k p^{w_n^k} + d_n^k p^{-w_n^k} - p \mathcal{G}_{pcn}^k(p) \right), \quad (2.39)$$

$$A_{lcn}^k(p) = -\frac{1}{w_n^k} \left(a_n^k p^{w_n^k} + b_n^k p^{-w_n^k} + p \mathcal{G}_{psn}^k(p) \right), \quad (2.40)$$

$$A_{l0}^k(p) = -\mu J_{l0}^k \frac{p^2}{4} - \mu_0 M_{q0}^k p + A_0^k \ln(p), \quad (2.41)$$

$$B_{psn}^k(p) = a_n^k p^{w_n^k - 1} + b_n^k p^{-w_n^k - 1} + \mathcal{G}_{psn}^k(p), \quad (2.42)$$

$$B_{pcn}^k(p) = -c_n^k p^{w_n^k - 1} - d_n^k p^{-w_n^k - 1} + \mathcal{G}_{pcn}^k(p), \quad (2.43)$$

$$B_{qsn}^k(p) = c_n^k p^{w_n^k - 1} - d_n^k p^{-w_n^k - 1} + \mathcal{G}_{qsn}^k(p), \quad (2.44)$$

$$B_{qcn}^k(p) = a_n^k p^{w_n^k - 1} - b_n^k p^{-w_n^k - 1} + \mathcal{G}_{qcn}^k(p), \quad (2.45)$$

$$B_{q0}^k(p) = \mu J_{l0}^k \frac{p}{2} + \mu_0 M_{q0}^k - \frac{A_0^k}{p}, \quad (2.46)$$

where \mathcal{G}_{psn}^k , \mathcal{G}_{pcn}^k , \mathcal{G}_{qcn}^k and \mathcal{G}_{qsn}^k are defined as

$$\mathcal{G}_{psn}^k(p) = \begin{cases} -\mu_0 \frac{M_{psn}^k - M_{qcn}^k}{2} \ln(p) + \mu \frac{J_{lcn}^k}{3} p, & w_n^k = 1, \\ \mu_0 \frac{4M_{psn}^k - 2M_{qcn}^k}{3} + \mu \frac{J_{lcn}^k}{2} p \ln(p), & w_n^k = 2, \\ \mu_0 w_n^k \frac{w_n^k M_{psn}^k - M_{qcn}^k}{(w_n^k)^2 - 1} - \mu w_n^k \frac{J_{lcn}^k}{(w_n^k)^2 - 4} p, & \text{else,} \end{cases} \quad (2.47)$$

$$\mathcal{G}_{pcn}^k(p) = \begin{cases} -\mu_0 \frac{M_{pcn}^k + M_{qsn}^k}{2} \ln(p) - \mu \frac{J_{lcn}^k}{3} p, & w_n^k = 1, \\ \mu_0 \frac{4M_{pcn}^k + 2M_{qsn}^k}{3} - \mu \frac{J_{lcn}^k}{2} p \ln(p), & w_n^k = 2, \\ \mu_0 w_n^k \frac{w_n^k M_{pcn}^k + M_{qsn}^k}{(w_n^k)^2 - 1} + \mu w_n^k \frac{J_{lcn}^k}{(w_n^k)^2 - 4} p, & \text{else,} \end{cases} \quad (2.48)$$

$$\mathcal{G}_{qsn}^k(p) = \begin{cases} \mu_0 \frac{M_{pcn}^k + M_{qsn}^k}{2} (1 + \ln(p)) - \mu \frac{2J_{lcn}^k}{3} p, & w_n^k = 1, \\ -\mu_0 \frac{2M_{pcn}^k + M_{qsn}^k}{3} - \mu \frac{J_{lcn}^k}{4} p (1 + 2 \ln(p)), & w_n^k = 2, \\ -\mu_0 \frac{w_n^k M_{pcn}^k + M_{qsn}^k}{(w_n^k)^2 - 1} + \mu \frac{2J_{lcn}^k}{(w_n^k)^2 - 4} p, & \text{else,} \end{cases} \quad (2.49)$$

$$\mathcal{G}_{qcn}^k(p) = \begin{cases} -\mu_0 \frac{M_{psn}^k - M_{qcn}^k}{2} (1 + \ln(p)) + \mu \frac{2J_{lcn}^k}{3} p, & w_n^k = 1, \\ \mu_0 \frac{2M_{psn}^k - M_{qcn}^k}{3} + \mu \frac{J_{lcn}^k}{4} p (1 + 2 \ln(p)), & w_n^k = 2, \\ \mu_0 \frac{w_n^k M_{psn}^k - M_{qcn}^k}{(w_n^k)^2 - 1} - \mu \frac{2J_{lcn}^k}{(w_n^k)^2 - 4} p, & \text{else.} \end{cases} \quad (2.50)$$

2.6.3 Axisymmetric coordinate system

The functions dependent on the normal direction of the solution for the magnetic vector potential and flux density components in the axisymmetric coordinate system are given by

$$A_{l'sn}^k(p) = \frac{1}{w_n^k} \left(c_n^k \mathcal{I}_1(w_n^k p) + d_n^k \mathcal{K}_1(w_n^k p) - \mathcal{G}_{pcn}^k(p) \right), \quad (2.51)$$

$$A_{l'cn}^k(p) = \frac{1}{w_n^k} \left(a_n^k \mathcal{I}_1(w_n^k p) + b_n^k \mathcal{K}_1(w_n^k p) + \mathcal{G}_{psn}^k(p) \right), \quad (2.52)$$

$$A_{l'0}^k(p) = -\mu J_{l'0}^k \frac{p^2}{3} + B_0^k \frac{p}{2} + \frac{A_0^k}{p}, \quad (2.53)$$

$$B_{psn}^k(p) = a_n^k \mathcal{I}_1(w_n^k p) + b_n^k \mathcal{K}_1(w_n^k p) + \mathcal{G}_{psn}^k(p), \quad (2.54)$$

$$B_{pcn}^k(p) = -c_n^k \mathcal{I}_1(w_n^k p) - d_n^k \mathcal{K}_1(w_n^k p) + \mathcal{G}_{pcn}^k(p), \quad (2.55)$$

$$B_{qcn}^k(p) = a_n^k \mathcal{I}_0(w_n^k p) - b_n^k \mathcal{K}_0(w_n^k p) + \mathcal{G}_{qcn}^k(p), \quad (2.56)$$

$$B_{qsn}^k(p) = c_n^k \mathcal{I}_0(w_n^k p) - d_n^k \mathcal{K}_0(w_n^k p) + \mathcal{G}_{qsn}^k(p), \quad (2.57)$$

$$B_{q0}^k(p) = -\mu J_{l'0}^k p + B_0^k, \quad (2.58)$$

where \mathcal{G}_{psn}^k , \mathcal{G}_{pcn}^k , \mathcal{G}_{qsn}^k and \mathcal{G}_{qcn}^k are defined as

$$\mathcal{G}_{psn}^k(p) = \left(\mu_0 M_{psn}^k + \mu \frac{J_{l'cn}^k}{w_n^k} \right) \mathcal{F}_{pn}^k(p), \quad (2.59)$$

$$\mathcal{G}_{pcn}^k(p) = \left(\mu_0 M_{pcn}^k - \mu \frac{J_{l'sn}^k}{w_n^k} \right) \mathcal{F}_{pn}^k(p), \quad (2.60)$$

$$\mathcal{G}_{qsn}^k(p) = \left(\mu_0 M_{pcn}^k - \mu \frac{J_{l'sn}^k}{w_n^k} \right) \mathcal{F}_{qn}^k(p), \quad (2.61)$$

$$\mathcal{G}_{qcn}^k(p) = - \left(\mu_0 M_{psn}^k + \mu \frac{J_{l'cn}^k}{w_n^k} \right) \mathcal{F}_{qn}^k(p), \quad (2.62)$$

and \mathcal{F}_{pn}^k and \mathcal{F}_{qn}^k are defined as

$$\mathcal{F}_{pn}^k(p) = \mathcal{K}_1(w_n^k p) \int_{w_n^k p_0}^{w_n^k p} p' \mathcal{I}_1(p') dp' - \mathcal{I}_1(w_n^k p) \int_{w_n^k p_0}^{w_n^k p} p' \mathcal{K}_1(p') dp', \quad (2.63)$$

$$\mathcal{F}_{qn}^k(p) = \mathcal{K}_0(w_n^k p) \int_{w_n^k p_0}^{w_n^k p} p' \mathcal{I}_1(p') dp' + \mathcal{I}_0(w_n^k p) \int_{w_n^k p_0}^{w_n^k p} p' \mathcal{K}_1(p') dp', \quad (2.64)$$

where p_0 is the inner radius of region k .

For non-periodic regions, shown in Fig. 2.1(b), H_p^k should be zero at the tangential boundaries of the region. Consequently, H_p^k and B_p^k only contain sine terms ($B_{pc}^k = 0$). Since the normal and tangential component of the magnetic flux density are linked via the magnetic vector potential, the sine terms of the tangential component are also zero in that case ($B_{qsn}^k = 0$). The set of unknowns a_n^k , b_n^k , c_n^k , d_n^k , and B_0^k or A_0^k for every region are solved considering the boundary conditions in the normal direction which are discussed in the following section.

2.7 Boundary conditions

Due to the proper choice of the solution form for the magnetic flux density distribution, the boundary conditions in the tangential direction are inherently satisfied as discussed in Section 2.3. To solve the unknown coefficients in the set of solutions for the magnetic flux density distribution, the boundary conditions in the normal direction have to be considered. Five types of boundary conditions can be distinguished:

- Neumann boundary conditions,
- Dirichlet boundary conditions,
- continuous boundary conditions,
- combination of Neumann and continuous boundary conditions,
- conservation of magnetic flux,
- Ampère's law.

Each of them are considered in the following subsections.

2.7.1 Neumann boundary condition

A Neumann boundary condition (tangential magnetic field strength must be zero) appears at the normal interface between a periodic or non-periodic region k and a soft-magnetic material at a certain height $p = h_b$, as shown in Fig. 2.3,

$$H_q^k = 0 \Big|_{p=h_b, \forall q}. \quad (2.65)$$

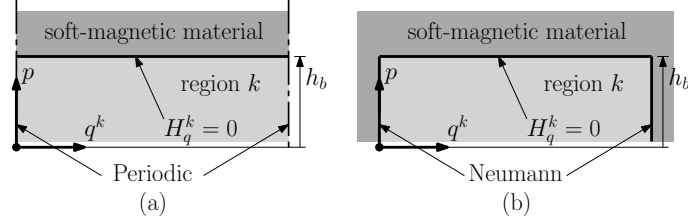


Figure 2.3: Illustration of the Neumann boundary condition at $p = h_b$ for a region k which is (a) periodic and (b) non-periodic.

Using the constitutive relation (2.9), equation (2.65) can be written in terms of the magnetic flux density and magnetization as

$$B_q^k - \mu_0 M_q^k = 0 \Big|_{p=h_b, \forall q}. \quad (2.66)$$

Equation (2.66) implies that the sum of a Fourier series needs to be zero at height $p = h_b$ for all q . This can be obtained if every harmonic term of the Fourier series is zero including the average term, hence both the coefficients for the sine and cosine terms need to be zero as well as the average term. Equation (2.66) can therefore be rewritten in the following set of equations for every harmonic n

$$B_{qsn}^k(h_b) = \mu_0 M_{qsn}^k, \quad (2.67)$$

$$B_{qcn}^k(h_b) = \mu_0 M_{qcn}^k, \quad (2.68)$$

$$B_{q0}^k(h_b) = \mu_0 M_{q0}^k. \quad (2.69)$$

2.7.2 Dirichlet boundary condition

A Dirichlet boundary condition is used to set the magnetic vector potential to zero

$$A_l^k = 0 \Big|_{p=h_b, \forall q}. \quad (2.70)$$

Similar as for the Neumann boundary condition, equation (2.70) implies that a sum of a Fourier series needs to be zero at height $p = h_b$ for all q . Hence again, equation (2.70) can therefore be rewritten in the following set of equations for

every harmonic n and the average term

$$A_{l_{sn}}^k(h_b) = 0, \quad (2.71)$$

$$A_{l_{cn}}^k(h_b) = 0, \quad (2.72)$$

$$A_{l_0}^k(h_b) = 0. \quad (2.73)$$

2.7.3 Continuous boundary condition

For the continuous boundary condition, the normal component of the magnetic flux density, B_p , needs to be continuous as well as the tangential component of the magnetic field strength, H_q , at the boundary between region k and j giving

$$B_p^k = B_p^j \Big|_{p=h_b, \forall q}, \quad (2.74)$$

$$H_q^k = H_q^j \Big|_{p=h_b, \forall q}. \quad (2.75)$$

Using the constitutive relation (2.8), equation (2.75) can be written in terms of the magnetic flux density as

$$\frac{\mu^j}{\mu^k} (B_q^k - \mu_0 M_q^k) = B_q^j - \mu_0 M_q^j \Big|_{p=h_b, \forall q}. \quad (2.76)$$

The two regions (k and j), either both periodic or non-periodic, have the same width and equal offsets ($\Delta^k = \Delta^j$), as shown in Fig. 2.4. This implies that both regions have the same spatial frequencies ($w_n^k = w_n^j$) and the same coordinate systems ($q^k = q^j$). Applying equation (2.74) and (2.76) to the flux density distributions at the boundary height ($p = h_b$) results in equating two Fourier series with equal fundamental frequency. Consequently equation (2.74) and (2.76) should hold for every harmonic, hence, the coefficients for both the sine and the cosine function should be equal as well as the average terms. Equation (2.74) gives the following set of equations for every harmonic n

$$B_{psn}^k(h_b) = B_{psn}^j(h_b), \quad (2.77)$$

$$B_{pcn}^k(h_b) = B_{pcn}^j(h_b). \quad (2.78)$$

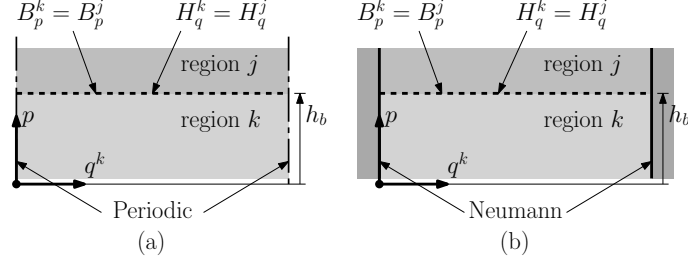


Figure 2.4: Illustration of the continuous boundary condition at $p = h_b$ between a region k and j which are (a) periodic and (b) non-periodic.

The boundary condition for the continuous tangential magnetic field strength, equation (2.76), results in the following set of equations for every harmonic n

$$\frac{\mu^j}{\mu^k} \left(B_{qsn}^k(h_b) - \mu_0 M_{qsn}^k \right) = B_{qsn}^j(h_b) - \mu_0 M_{qsn}^j, \quad (2.79)$$

$$\frac{\mu^j}{\mu^k} \left(B_{qcn}^k(h_b) - \mu_0 M_{qcn}^k \right) = B_{qcn}^j(h_b) - \mu_0 M_{qcn}^j, \quad (2.80)$$

$$\frac{\mu^j}{\mu^k} \left(B_{q0}^k(h_b) - \mu_0 M_{q0}^k \right) = B_{q0}^j(h_b) - \mu_0 M_{q0}^j. \quad (2.81)$$

2.7.4 Combined Neumann and continuous boundary condition

A combination of Neumann and continuous boundary conditions occurs at an interface between regions which have unequal width and/or unequal offsets in the tangential direction. In general, it concerns the boundary condition at height $p = h_b$, between a periodic or non-periodic region k on one side, and one or more non-periodic regions $j_1, j_2, \dots, j_\nu, \dots, j_\nu$, on the other side. A general example for $\mathcal{V} = 2$ is shown in Fig. 2.5(a) when region k is periodic and in Fig. 2.5(b) when region k is non-periodic.

The normal magnetic flux density component B_p^k of every region j_ν should equal the normal magnetic field component of region k at the boundary at $p = h_b$. Furthermore, the tangential magnetic field strength component H_q^k of region k must equal the tangential magnetic field strength component of every region j_ν on the respective boundary, and equal zero elsewhere. Therefore, the boundary

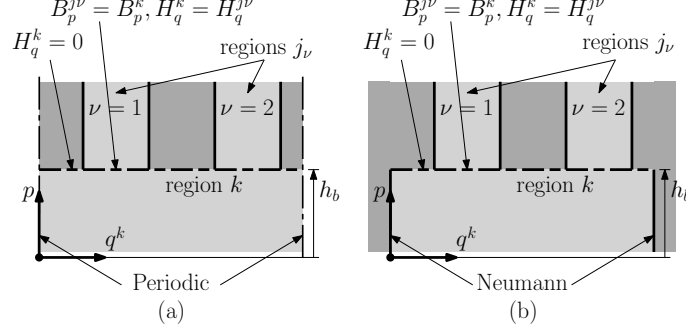


Figure 2.5: Illustration of the combined Neumann and continuous boundary condition at $p = h_b$ between non-periodic regions j_ν and region k which is (a) periodic and (b) non-periodic.

conditions are written in the form

$$B_p^{j_\nu} = B_p^k \Big|_{p=h_b, 0 \leq q^{j_\nu} \leq \tau_{j_\nu}}, \quad \text{for } \nu = 1, \dots, \mathcal{V} \quad (2.82)$$

$$H_q^k = \begin{cases} \sum_{\nu=1}^{\mathcal{V}} H_q^{j_\nu} & \Big|_{p=h_b, 0 \leq q^{j_\nu} \leq \tau_{j_\nu}} \\ 0, & \text{else,} \end{cases} \quad (2.83)$$

Applying the constitutive relation (2.8) to (2.83) gives

$$B_q^k - \mu_0 M_q^k = \begin{cases} \sum_{\nu=1}^{\mathcal{V}} \frac{\mu^k}{\mu^{j_\nu}} (B_q^{j_\nu} - \mu_0 M_q^{j_\nu}) & \Big|_{p=h_b, 0 \leq q^{j_\nu} \leq \tau_{j_\nu}} \\ 0, & \text{else,} \end{cases} \quad (2.84)$$

Boundary condition (2.82) implies that two waveforms which have a different fundamental frequency, should be equal over a certain interval. Boundary condition (2.84) implies that a waveform should be equal to a different waveform with different fundamental frequency and zero elsewhere. Both boundary conditions are solved using the correlation technique which is described in the following subsections.

Normal magnetic flux density

Substituting the general functions for the magnetic flux density distribution in equation (2.82) gives the following \mathcal{V} equations

$$\begin{aligned} & \sum_{m=1}^{\infty} \left(B_{psm}^{j\nu} \sin(w_m^{j\nu} q^{j\nu}) + B_{pcm}^{j\nu} \cos(w_m^{j\nu} q^{j\nu}) \right) \\ &= \sum_{n=1}^{\infty} \left(B_{psn}^k \sin(w_n^k q^k) + B_{pcn}^k \cos(w_n^k q^k) \right) \Bigg|_{p=h_b, 0 \leq q^{j\nu} \leq \tau_{j\nu}} \\ & \qquad \qquad \qquad \text{for } \nu = 1, \dots, \mathcal{V}, \end{aligned} \quad (2.85)$$

However, this equation has to be rewritten into an infinite number of equations in order to solve the infinite number of unknowns. Therefore, the coefficients of region j_ν are written as a function of the coefficients of region k . This can be obtained by correlating equation (2.85) with $\sin(w_m^{j\nu} q^{j\nu})$ and $\cos(w_m^{j\nu} q^{j\nu})$, respectively, over the interval where the boundary condition holds. Since the correlation on the left-hand side is only nonzero for the harmonic m that is considered for the sine or cosine term, respectively, the summation over m disappears giving

$$B_{psm}^{j\nu} = \sum_{n=1}^{\infty} \left(B_{psn}^k(h_b) \varepsilon_s^{k,j\nu}(m, n) + B_{pcn}^k(h_b) \varepsilon_c^{k,j\nu}(m, n) \right), \text{ for } \nu = 1, \dots, \mathcal{V}, \quad (2.86)$$

$$B_{pcm}^{j\nu} = \sum_{n=1}^{\infty} \left(B_{psn}^k(h_b) \eta_s^{k,j\nu}(m, n) + B_{pcn}^k(h_b) \eta_c^{k,j\nu}(m, n) \right), \text{ for } \nu = 1, \dots, \mathcal{V}, \quad (2.87)$$

which is a set of equations for every m and region j_ν . The correlation functions $\varepsilon_s^{k,j\nu}$, $\varepsilon_c^{k,j\nu}$, $\eta_s^{k,j\nu}$ and $\eta_c^{k,j\nu}$ are given by

$$\varepsilon_s^{k,j\nu}(m, n) = \frac{2}{\tau_{j\nu}} \int_0^{\tau_{j\nu}} \sin(w_n^k q^k) \sin(w_m^{j\nu} q^{j\nu}) dq^{j\nu}, \quad (2.88)$$

$$\varepsilon_c^{k,j\nu}(m, n) = \frac{2}{\tau_{j\nu}} \int_0^{\tau_{j\nu}} \cos(w_n^k q^k) \sin(w_m^{j\nu} q^{j\nu}) dq^{j\nu}, \quad (2.89)$$

$$\eta_s^{k,j\nu}(m, n) = \frac{2}{\tau_{j\nu}} \int_0^{\tau_{j\nu}} \sin(w_n^k q^k) \cos(w_m^{j\nu} q^{j\nu}) dq^{j\nu}, \quad (2.90)$$

$$\eta_c^{k,j\nu}(m, n) = \frac{2}{\tau_{j\nu}} \int_0^{\tau_{j\nu}} \cos(w_n^k q^k) \cos(w_m^{j\nu} q^{j\nu}) dq^{j\nu}. \quad (2.91)$$

The solutions of these correlation functions are given in Appendix A.

Tangential magnetic field strength

Substituting the general functions for the magnetic flux density in (2.84) gives the following single equation

$$\begin{aligned}
& \sum_{n=1}^{\infty} \left[\left(B_{qsn}^k - \mu_0 M_{qsn}^k \right) \sin(w_n^k q^k) + \left(B_{qcn}^k - \mu_0 M_{qcn}^k \right) \cos(w_n^k q^k) \right] \\
& + B_{q0}^k - \mu_0 M_{q0}^k \\
& = \begin{cases} \sum_{\nu=1}^{\nu} \frac{\mu^k}{\mu^{j\nu}} \left\{ \sum_{m=1}^{\infty} \left[\left(B_{qsm}^{j\nu} - \mu_0 M_{qsm}^{j\nu} \right) \sin(w_m^{j\nu} q^{j\nu}) \right. \right. \\ \quad \left. \left. + \left(B_{qcm}^{j\nu} - \mu_0 M_{qcm}^{j\nu} \right) \cos(w_m^{j\nu} q^{j\nu}) \right] \right. \\ \quad \left. + B_{q0}^{j\nu} - \mu_0 M_{q0}^{j\nu} \right\} \Big|_{p=h_b, 0 \leq q^{j\nu} \leq \tau_{j\nu}}, \\ 0, & \text{elsewhere.} \end{cases}, \tag{2.92}
\end{aligned}$$

However, this equation has to be rewritten into an infinite number of equations in order to solve the infinite number of unknowns. Therefore, the coefficients of region k are written as a function of the coefficients of region j_ν . This can be obtained by correlating equation (2.92) with $\sin(w_n^k q^k)$ and $\cos(w_n^k q^k)$, respectively, over the interval where the boundary condition holds (width of region k).

The conditional equation (2.92) can be written into an unconditional one by changing the bounds of the right-hand side correlation integrals into the bounds where the boundary condition holds. Since the correlation on the left-hand side is only nonzero for the harmonic n that is considered for the sine or cosine term, respectively, the summation over n disappears giving

$$\begin{aligned}
& B_{qsn}^k - \mu_0 M_{qsn}^k \\
& = \sum_{\nu=1}^{\nu} \frac{\mu^k}{\mu^{j\nu}} \left\{ \sum_{m=1}^{\infty} \left[\left(B_{qsm}^{j\nu} - \mu_0 M_{qsm}^{j\nu} \right) \kappa_s^{k,j\nu}(n, m) \right. \right. \\
& \quad \left. \left. + \left(B_{qcm}^{j\nu} - \mu_0 M_{qcm}^{j\nu} \right) \kappa_c^{k,j\nu}(n, m) \right] + \left(B_{q0}^{j\nu} - \mu_0 M_{q0}^{j\nu} \right) \kappa_0^{k,j\nu}(n) \right\} \Big|_{p=h_b}, \tag{2.93}
\end{aligned}$$

$$\begin{aligned}
& B_{qcn}^k - \mu_0 M_{qcn}^k \\
&= \sum_{\nu=1}^{\nu} \frac{\mu^k}{\mu^{j\nu}} \left\{ \sum_{m=1}^{\infty} \left[\left(B_{qsm}^{j\nu} - \mu_0 M_{qsm}^{j\nu} \right) \zeta_s^{k,j\nu}(n, m) \right. \right. \\
&\quad \left. \left. + \left(B_{qcm}^{j\nu} - \mu_0 M_{qcm}^{j\nu} \right) \zeta_c^{k,j\nu}(n, m) \right] + \left(B_{q0}^{j\nu} - \mu_0 M_{q0}^{j\nu} \right) \zeta_0^{k,j\nu}(n) \right\} \Big|_{p=h_b}, \tag{2.94}
\end{aligned}$$

which is a set of equations for every n . The correlation functions $\kappa_s^{k,j\nu}$, $\kappa_c^{k,j\nu}$, $\kappa_0^{k,j\nu}$, $\zeta_s^{k,j\nu}$, $\zeta_c^{k,j\nu}$ and $\zeta_0^{k,j\nu}$ are given by

$$\kappa_s^{k,j\nu}(n, m) = \frac{s}{\tau_k} \int_{\Delta^{j\nu} - \Delta^k}^{\Delta^{j\nu} - \Delta^k + \tau_{j\nu}} \sin(w_m^{j\nu} q^{j\nu}) \sin(w_n^k q^k) dq^k, \tag{2.95}$$

$$\kappa_c^{k,j\nu}(n, m) = \frac{s}{\tau_k} \int_{\Delta^{j\nu} - \Delta^k}^{\Delta^{j\nu} - \Delta^k + \tau_{j\nu}} \cos(w_m^{j\nu} q^{j\nu}) \sin(w_n^k q^k) dq^k, \tag{2.96}$$

$$\kappa_0^{k,j\nu}(n) = \frac{s}{\tau_k} \int_{\Delta^{j\nu} - \Delta^k}^{\Delta^{j\nu} - \Delta^k + \tau_{j\nu}} \sin(w_n^k q^k) dq^k, \tag{2.97}$$

$$\zeta_s^{k,j\nu}(n, m) = \frac{s}{\tau_k} \int_{\Delta^{j\nu} - \Delta^k}^{\Delta^{j\nu} - \Delta^k + \tau_{j\nu}} \sin(w_m^{j\nu} q^{j\nu}) \cos(w_n^k q^k) dq^k, \tag{2.98}$$

$$\zeta_c^{k,j\nu}(n, m) = \frac{s}{\tau_k} \int_{\Delta^{j\nu} - \Delta^k}^{\Delta^{j\nu} - \Delta^k + \tau_{j\nu}} \cos(w_m^{j\nu} q^{j\nu}) \cos(w_n^k q^k) dq^k, \tag{2.99}$$

$$\zeta_0^{k,j\nu}(n) = \frac{s}{\tau_k} \int_{\Delta^{j\nu} - \Delta^k}^{\Delta^{j\nu} - \Delta^k + \tau_{j\nu}} \cos(w_n^k q^k) dq^k. \tag{2.100}$$

The variable s is equal to 1 when region k is periodic equal to 2 when region k is non-periodic. The solutions of the correlation functions are given in Appendix A.

2.7.5 Conservation of magnetic flux

This boundary condition should be applied in case the source term of a two or more non-periodic regions j_ν inhibit an average term for the magnetization in the tangential direction ($M_{q0}^{j1} \neq 0$) or current density in the longitudinal direction ($J_{i0}^{j1} \neq 0$). In that case, the magnetic flux density in the tangential direction has an extra unknown ($B_0^{j1} \neq 0$ for the Cartesian and axisymmetric coordinate system or $A_0^{j1} \neq 0$ for the polar coordinate system for each of the non-periodic regions).

When these non-periodic regions, j_ν , have a Neumann boundary condition in the normal direction, this extra unknown is solved by the boundary condition given

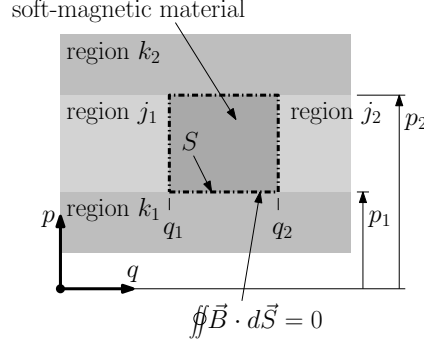


Figure 2.6: Illustration of the boundary condition setting the divergence of the magnetic flux density to zero around an orthogonal soft-magnetic area.

in equation (2.73). In case these regions have a continuous boundary condition in the normal direction, this extra term is solved by equation (2.81). However, when these regions are sandwiched between two periodic or non-periodic regions, k_1 and k_2 , an extra boundary condition is necessary to solve the extra term. In these situations, soft-magnetic orthogonal areas appear in the structure which are surrounded by four different regions (k_1 , k_2 , j_1 and j_2 as shown in Fig. 2.6).

The extra boundary condition is given by setting the divergence of the magnetic field to zero (conservation of magnetic flux) around the surface of the soft-magnetic orthogonal area,

$$\oiint \vec{B} \cdot d\vec{S} = 0. \quad (2.101)$$

Since only 2D problems are considered, this surface integral reduces to a line integral over the boundary of the orthogonal area, hence the boundary condition for every coordinate system is given by

Cartesian:

$$\begin{aligned} \int_{q_1}^{q_2} B_p^{k_2}(p_2, q^{k_2}) dq - \int_{q_1}^{q_2} B_p^{k_1}(p_1, q^{k_1}) dq \\ = \int_{p_1}^{p_2} B_q^{j_1}(p, q_1) dp - \int_{p_1}^{p_2} B_q^{j_2}(p, q_2) dp, \end{aligned} \quad (2.102)$$

Polar:

$$\begin{aligned} \int_{q_1}^{q_2} B_p^{k_2}(p_2, q^{k_2}) p dq - \int_{q_1}^{q_2} B_p^{k_1}(p_1, q^{k_1}) p dq \\ = \int_{p_1}^{p_2} B_q^{j_1}(p, q_1) dp - \int_{p_1}^{p_2} B_q^{j_2}(p, q_2) dp, \end{aligned} \quad (2.103)$$

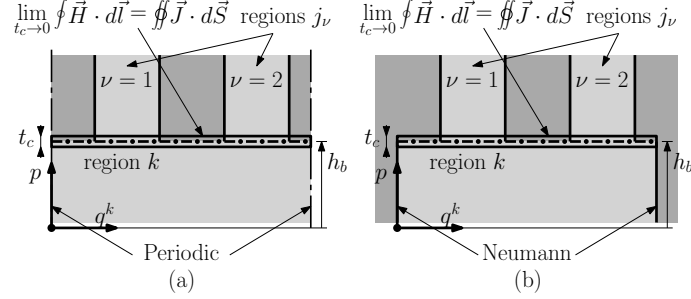


Figure 2.7: Illustration of applying Ampère's law at $p = h_b$ between regions j_ν separated by soft-magnetic material and region k with (a) periodic BCs or (b) Neumann BCs in the tangential direction.

Axisymmetric:

$$\begin{aligned} \int_{q_1}^{q_2} B_p^{k_2}(p_2, q^{k_2}) p dq - \int_{q_1}^{q_2} B_p^{k_1}(p_1, q^{k_1}) p dq \\ = \int_{p_1}^{p_2} B_q^{j_1}(p, q_1) p dp - \int_{p_1}^{p_2} B_q^{j_2}(p, q_2) p dp. \end{aligned} \quad (2.104)$$

For a problem concerning \mathcal{V} orthogonal areas on the same layer, the same number of boundary conditions are obtained. However only $\mathcal{V}-1$ conditions are independent when the total model is periodic. The final independent equation is obtained by applying Ampère's law as explained in the following subsection.

2.7.6 Ampère's law

The final equation for solving the extra terms as explained in the previous section is given by taking the contour integral of the magnetic field strength as shown in Fig. 2.7. The contour integral is given by

$$\lim_{t_c \rightarrow 0} \oint \vec{H} \cdot d\vec{l} = \iint \vec{J} \cdot d\vec{S}. \quad (2.105)$$

For every coordinate system, this equation reduces to

$$\frac{2\tau_k}{\mu^k} \left(B_{q_0}^k(h_b) - \mu_0 M_{q_0}^k \right) = \sum_{\nu=1}^{\mathcal{V}} \frac{\tau_{j\nu}}{\mu^{j\nu}} \left(B_{q_0}^{j\nu}(h_b) - \mu_0 M_{q_0}^{j\nu} \right). \quad (2.106)$$

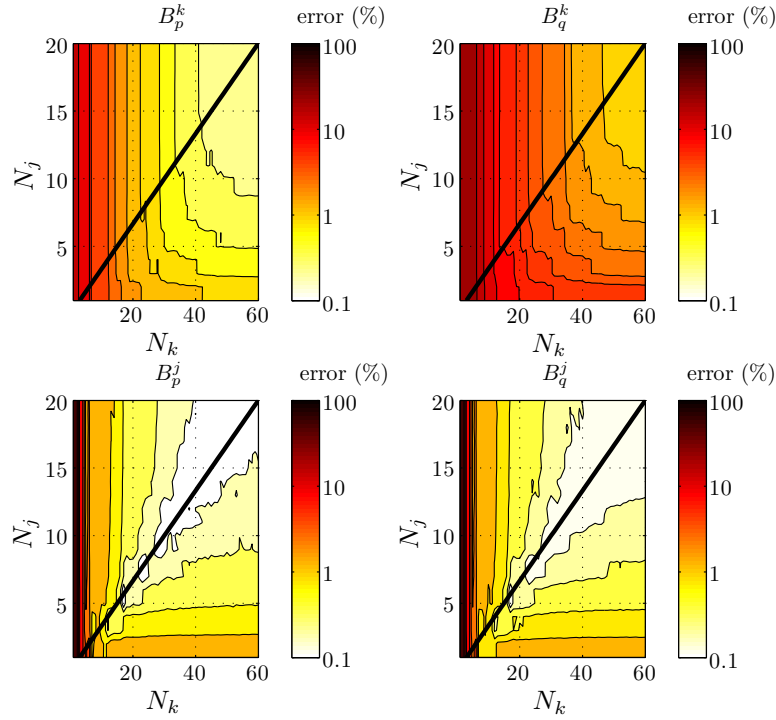


Figure 2.8: Error in logarithmic scale of the normal and tangential flux density in the airgap (B_p^k and B_q^k) and slot opening (B_p^j and B_q^j) related to the included number of airgap (N_k) and slot (N_j) harmonics.

2.8 Numerical implementation

Modeling techniques which use a meshed geometry have a limited accuracy related to the density of the mesh. In contrast, the limited accuracy of the framework based on Fourier theory is related to the truncation of the number of harmonics. Truncation is necessary to limit the computational time. However, a sufficient number of harmonics is necessary to obtain a satisfactory accuracy. For an increased harmonic number, the absolute value of the coefficients a_n^k and c_n^k is decreasing while b_n^k and d_n^k are increasing. Solving the sets of equations for the boundary conditions results in a system of equations which is ill-conditioned, hence, the solution becomes inaccurate. Although correct results might still be obtained, the boundary condition matrix resulting from the set of equations can have a condition number in the order of 10^{200} . To improve the accuracy, the inverse of the boundary condition matrix is obtained using the singular value decomposition.

The numerical accuracy can be improved by applying proper scaling of the coefficients a_n^k , b_n^k , c_n^k and d_n^k for every region. This is possible in the Cartesian and

polar coordinate system since

$$\text{Cartesian:} \quad \frac{e^{w_n^k p}}{e^{w_n^k p_0}} = e^{w_n^k (p-p_0)}, \quad (2.107)$$

$$\text{Polar:} \quad \frac{p^{w_n^k - 1}}{p_0^{w_n^k - 1}} = \left(\frac{p}{p_0}\right)^{w_n^k - 1}, \quad (2.108)$$

$$\text{Axisymmetric:} \quad \text{not applicable}, \quad (2.109)$$

for a given normalization height p_0 . However, to date, this scaling technique cannot be applied for Bessel functions, making problems in the axisymmetric coordinate system difficult, if not impossible, to scale. Limiting the number of harmonics leads to inaccurate field solutions at discontinuous points in the geometry, especially at the corner points of magnets, current regions or soft-magnetic material. The correlation technique which is used to satisfy the boundary conditions between regions with different spatial frequencies has a limited accuracy when only a finite number of harmonics can be considered.

Additionally, the number of harmonics for each region should be chosen carefully, an extensive discussion on the effect of the number of harmonics taken into account is given in [97]. Considering regions with Neumann boundary conditions, the choice of the number of harmonics for these regions should be related to the number of harmonics included in the adjacent regions.

In order to visualize this effect on the accuracy, the field solution due to a single slot opening above a quasi-Halbach magnet array is calculated with the analytical model in the axisymmetric coordinate system. The maximum relative error of the field solution in the center of the airgap and inside the slot opening between the analytical and FEA model is shown in Fig. 2.8 as a function of included airgap and magnet harmonics, N_k , and included slot harmonics, N_j . A trend for the best accuracy is obtained when the number of slot harmonics is given by [60]

$$N_j = \left\lceil \frac{\tau_j}{\tau_k} N_k \right\rceil, \quad (2.110)$$

which is indicated by the solid line in Fig. 2.8.

2.9 Finite element verification

To verify the accuracy and limitations of the proposed generic method, three benchmark examples are considered in each of the considered coordinate systems. Each of the examples addresses certain issues and considerations which have to be

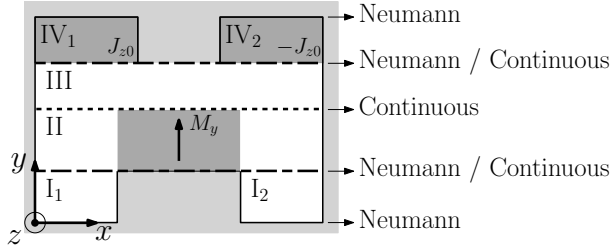


Figure 2.9: Division in regions and boundary conditions for the first example in the Cartesian coordinate system.

taken into account when the method is applied. The first example considers a non-periodic problem in the Cartesian coordinate system to indicate the issues related to the mode matching technique and permanent magnet modeling. The second example models a flux switching permanent magnet (FSPM) machine with 12 poles and 10 rotor slots [58, 165] in the polar coordinate system and investigates the assumption of infinite permeability of the soft-magnetic materials. The third example considers the modeling of end-effects of an axially magnetized slotless tubular permanent magnet actuator (TPMA) in the axisymmetric coordinate system. This example illustrates how a non-periodic problem can be transformed into a quasi-periodic problem.

2.9.1 Cartesian coordinate system

A 2D model of a magnet fixture with an electromagnet is considered, shown in Fig. 2.9. This fixture could be used to investigate the demagnetization properties of a certain permanent magnet material within a soft-magnetic structure. The application is however, irrelevant since the idea is to prove that the proposed semi-analytical model is capable of calculating the magnetic field distribution within a non-periodic structure enclosed by soft-magnetic material.

End-effects in the z -direction are neglected, the magnet is magnetized in the y -direction, M_y , and the electromagnet is modeled by two regions having a positive and negative current density, J_{z0} and $-J_{z0}$, which is uniformly distributed. The structure is divided into non-periodic regions which all have Neumann boundary conditions in the tangential direction, x . Regions I_1 and I_2 are air regions, region II is the PM region, region III is the airgap between the electromagnet and permanent magnet and regions IV_1 and IV_2 are the coil regions of the electromagnet. The division in regions and the appropriate boundary conditions for this problem are indicated in Fig. 2.9.

The calculated flux density distribution with the semi-analytical model is shown in Fig. 2.10 where 150 harmonics are included in region III and the number of harmonics for the other regions are determined using equation (2.110). The finite element verification is shown in Fig. 2.11 with a very good agreement however

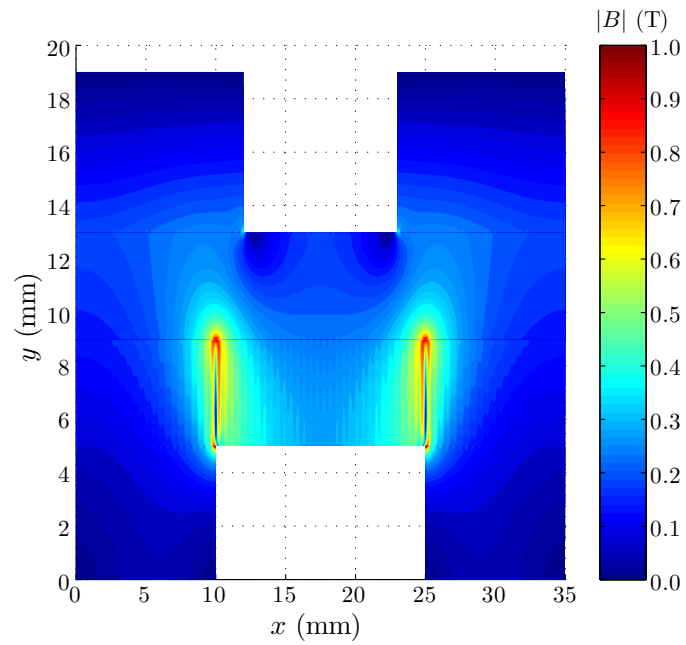


Figure 2.10: Flux density distribution of the magnet fixture shown in Fig. 2.10 in the Cartesian coordinate system calculated with the semi-analytical model.

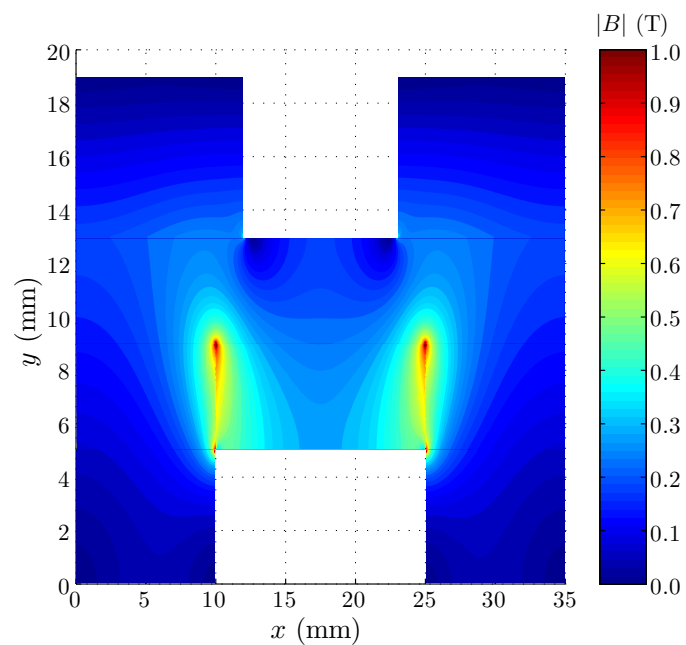


Figure 2.11: Flux density distribution of the magnet fixture shown in Fig. 2.10 in the Cartesian coordinate system calculated with FEA.

several small differences can be observed. First the field solution within the magnet contains a high harmonic content compared to the FEA result, especially close to the borders of the magnet. This is a consequence of the truncated Fourier description of the square wave magnetization function which leads to the so called Gibbs phenomenon [75]. This leads to an overshoot in the description of M_0 , and hence an overshoot in the predicted flux density at those points. Second, the continuity of the flux between regions III and IV at $y = 9$ mm for $25 \leq x \leq 35$ mm and $0 \leq x \leq 10$ mm is not exact. This is due to the fact that for region II a relative permeability of $\mu^{\text{II}} = 1.05$ is assumed which is true within the magnet, however on the left and right side it introduces an error. In order to reduce the overall error, the relative permeability should be selected as $\mu^{\text{II}} = 1 + \alpha_p(\mu_r - 1)$ where α_p is the ratio of permanent magnet material in the region, and $\mu_r = 1.05$ is the relative permeability of the permanent magnet.

2.9.2 Polar coordinate system

The second example considers a 12/10 FSPM shown in Fig. 2.12 for verification of the semi-analytical model in the polar coordinate system [58, 165, 170]. This machine inhibits half periodicity, hence only half of the machine needs to be modeled using the proposed method. Again end-effects in the axial direction are neglected, and the cross section of the machine can be divided into different regions as shown in Fig. 2.13. The airgap (region II) and outer air (region V) are considered as periodic regions. The rotor slot openings (regions I_ν , for $\nu = 1 \dots 5$) have Neumann boundary conditions. The same holds for the coil regions (regions IV_ν , for $\nu = 1 \dots 6$) and the permanent magnet regions (regions III_ν , for $\nu = 1 \dots 6$). Since the borders of the regions should be in parallel with the radial or angular direction, a modification of the geometry is necessary. The modification is such that the electrical loading and magnetic loading are kept equal [58]. The applied boundary conditions are indicated in Fig. 2.13.

The field solution including armature reaction in the center of the airgap is calculated with the analytical model for 110 harmonics in the airgap and compared with non-linear FEA in Fig. 2.14, where a good agreement is obtained in terms of the shape. Around the locations where the rotor and stator teeth align, an error in the amplitude of the radial flux density is observed due to saturation of the soft-magnetic material which is neglected in the analytical model. Therefore, the magnetic flux density within the soft-magnetic material should be estimated to predict when saturation occurs and adapt the field solution or the design if necessary. This is discussed in more detail in Chapter 3.

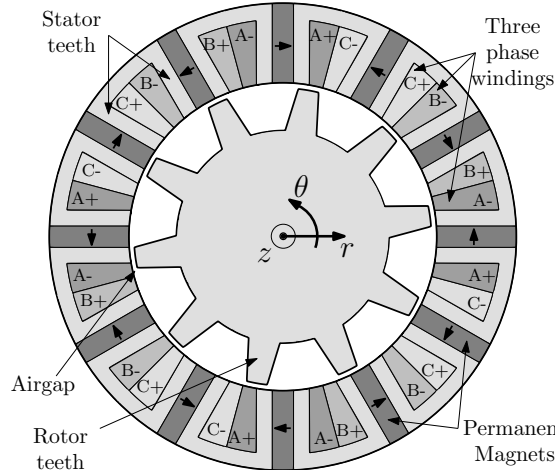


Figure 2.12: Parallel flux switching permanent magnet machine with 12 stator poles and 10 rotor teeth.

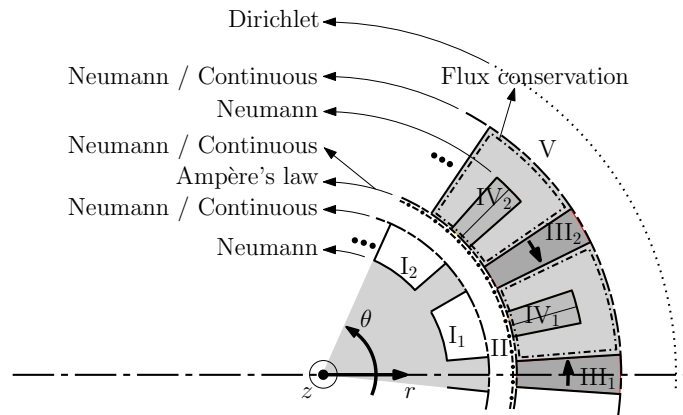


Figure 2.13: Division in regions and boundary conditions of a 12/10 pole FSPM machine in the polar coordinate system.

2.9.3 Axisymmetric coordinate system

The third example considers the calculation of the flux density distribution due to the end-effects in a slotless axially magnetized tubular permanent magnet actuator. A quasi-periodic model is constructed as shown in Fig. 2.15. A periodical boundary condition is applied at a random axial position around the center of the actuator. Assuring a sufficient distance between the left and right end of the stator back-iron, the end-effect can be modeled as a very large slot opening. This idea was applied to slotless TPMA with radial and quasi-Halbach magnetization in [155, 156]. The division in regions considers three periodic regions, the non-magnetic shaft (region I), the airgap (region III) and the outer air (region V). Re-

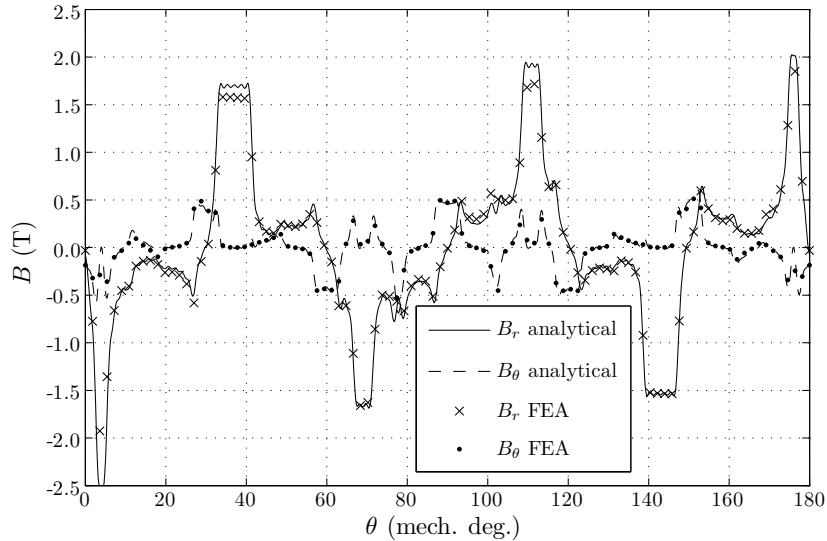


Figure 2.14: Flux density in the center of the airgap of a 12/10 FSPM machine verified with non-linear FEA.

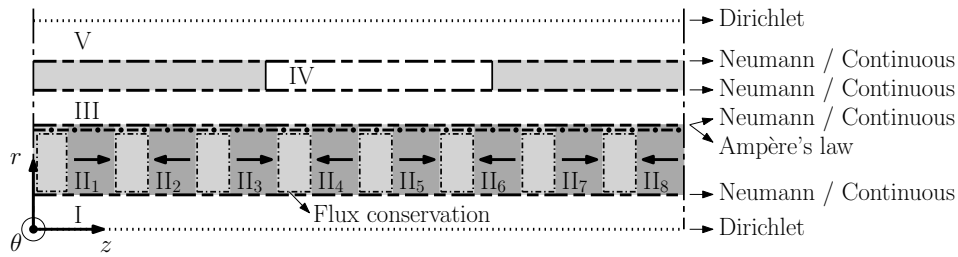


Figure 2.15: Division in regions and boundary conditions for an axial magnetized slotless TPMA in the axisymmetric coordinate system.

regions with Neumann boundary conditions in the tangential direction include the permanent magnets (regions II_ν , for $\nu = 1 \dots 8$) and the end region (region IV). The applied boundary conditions are listed in Fig. 2.15.

The calculated flux density distribution with the semi-analytical model is shown in Fig. 2.16 and verified with FEA in Fig. 2.17. An excellent agreement is obtained, even in the magnet regions. The field solution inside the magnet is better due to the reason that this magnetization description only requires the average component (see Fig. 2.2) and the Gibbs phenomenon is not apparent. Furthermore, the demagnetization at the corner points of the magnets is correctly predicted.

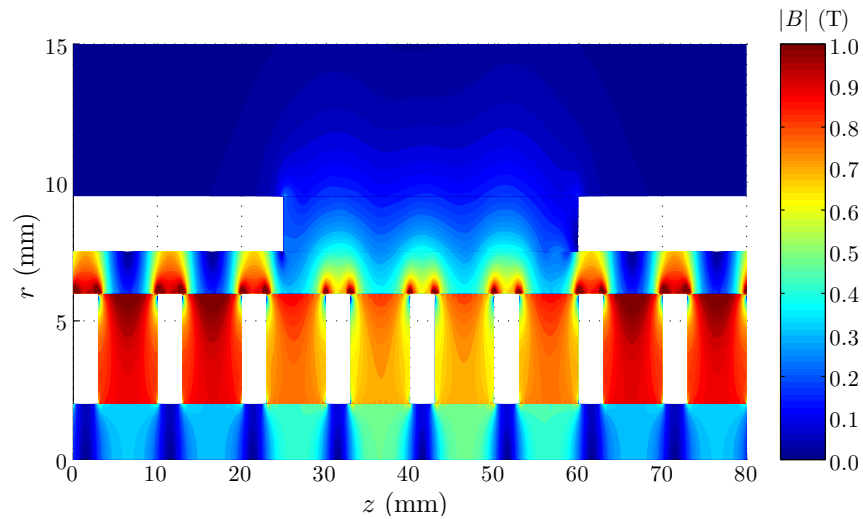


Figure 2.16: Flux density distribution for an axial magnetized slotless TPMA in the axisymmetric coordinate system calculated with the semi-analytical model.

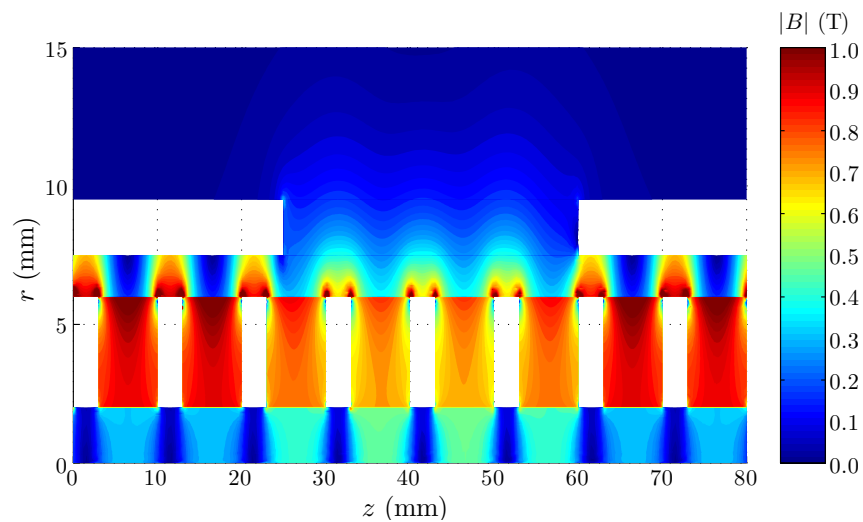


Figure 2.17: Flux density distribution for an axial magnetized slotless TPMA in the axisymmetric coordinate system calculated with FEA.

2.10 Summary and conclusions

A general formulation of the magnetostatic field distribution is given based on harmonic modeling. This formulation applies to 2D problems in the Cartesian, polar or axisymmetric coordinate system. It unifies prior art and completes the unsolved problems like slotted geometries in the axisymmetric coordinate system and sources (PMs and coils) within a slot region.

The 2D problem is divided into orthogonal regions with periodical or Neumann boundary conditions in the tangential direction (non-periodic regions). The width of the regions are defined such that a general field solution can be written for both regions. Furthermore, imaging of the sources in non-periodic regions is applied such that the source term description is general for both periodic and non-periodic regions.

For each region, the field solution is obtained by solving the magnetostatic Maxwell equations in terms of the magnetic vector potential. The total solution is obtained by solving the set of coefficients resulting from the various boundary conditions between each region. All the types of boundary conditions necessary to solve any boundary value problem are treated. Numerical implementation is discussed together with the accuracy of the truncation of harmonics in each region [60]. The semi-analytical framework is verified with FEA for three benchmark problems in each of the considered coordinate systems where a very good agreement is obtained. Furthermore, the limitations are identified and discussed.

This generic formulation is published in [61] and allows for automated model creation in which the build up of the boundary condition matrix is automatically generated. This enables the fast and automated creation of complicated models with a large number of regions as, for example, in a parallel flux switching permanent magnet machine published in [58] or multi-airgap permanent magnet machines [118].

Chapter 3

Modeling of tubular permanent magnet actuators

“Humans are the center of their own axisymmetric coordinate system. Being the origin of their actions, while everything revolves around them.”

This chapter applies the generic harmonic electromagnetic modeling technique to tubular permanent magnet actuators (TPMA). These types of actuators are considered to be the best candidate for the application of an active suspension in Part II of this thesis. First the various topologies and configurations for TPMAs are described, followed by the method in which the modeling technique is applied to TPMAs. Apart from the field solution in the low-permeability regions, the flux density in the soft-magnetic regions is estimated to predict saturation. The field calculations are verified with finite element analysis for three benchmark geometries. Subsequently, the induced electromotive force, inductance and force profile, derived from the field solutions, are calculated. Additionally, a thermal model is constructed to predict the worst case coil and magnet temperatures. These models are used for design and optimization of the active suspension system in Chapter 6.

The contribution of this chapter is published in:

Gysen, B. L. J., Meessen, K. J., Paulides, J. J. H. and Lomonova, E. A. [2008a], ‘Semi-analytical calculation of the armature reaction in slotted tubular permanent magnet actuators’, *IEEE Transactions on Magnetics* **44**(11), 3213–3216.

Gysen, B. L. J., Paulides, J. J. H., Lomonova, E. A. and Vandenput, A. J. A. [2008a], ‘Analytical and numerical techniques for solving Laplace and Poisson equations in a tubular permanent magnet actuator: Part I. Semi-analytical framework’, *IEEE Transactions on Magnetics* **44**(7), 1751–1760.

Meessen, K. J., Gysen, B. L. J., Paulides, J. J. H. and Lomonova, E. A. [2008a], ‘Halbach permanent magnet shape selection for slotless tubular actuators’, *IEEE Transactions on Magnetics* **44**(11), 4305–4308.

Janssen, J. L. G., Paulides, J. J. H., Gysen, B. L. J., Meessen, K. J., Encica, L. and Lomonova, E. A. [2009], Separation of the cogging force components in a tubular permanent magnet acutator using fem, *in* ‘Proceedings of the 2009 FLUX Users Conference’, Autrans, France, pp. 1–7.

3.1 Topologies and configurations

A long stroke TPMA, see Fig. 3.1(a) and (b), has a permanent magnet array which moves with respect to a coil configuration, referred as stator. Due to the tubular configuration, from a constructive point of view, it is beneficial to fix the outer moving tube to the fixed world, and move the inner one, which is generally longer than the outer one in order to obtain a certain stroke. If however, the inner tube is fixed at its ends, bending of the tubes occurs when a long translator and horizontal installation is considered. In general, to avoid cable slabs and for ease of winding interconnections, the permanent magnet array resembles the moving inner tube, referred as translator, and the static outer tube consists of the stator, see Fig. 3.1(a). However, if a vertical installation is considered, bending of the shaft is not apparent and one can consider both the permanent magnets on the inner or outer tube, further referred to as internal or external magnet topology (IMT and EMT), shown in Fig. 3.1(a) and (b), respectively. The stator can be either slotless [59] or slotted [67] where the former gives a lower force ripple and the latter a higher performance.

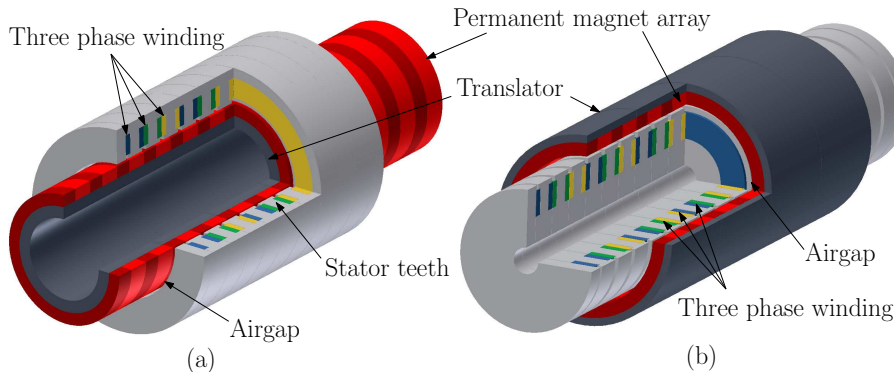


Figure 3.1: Slotted tubular permanent magnet actuators (TPMAs): (a) internal magnet topology (IMT) and (b) external magnet topology (EMT).

3.1.1 Translator configurations

The permanent magnet array on the translator has to be magnetized such that the magnetic field travels across the airgap, hence has to be dominantly radial. In tubular permanent magnet actuators, it is common to use surface mounted magnets. Embedded magnets, in V-form as for example in rotary machines, can provide a higher performance [99], however, are difficult and complex to manufacture for tubular actuators. There are several configurations of surface mounted magnet arrays. The first configuration consists of alternating radial magnets, see Fig. 3.2(a). A high permeable return path is necessary to increase the flux density in the airgap, hence, a soft-magnetic back-iron is required. One could consider

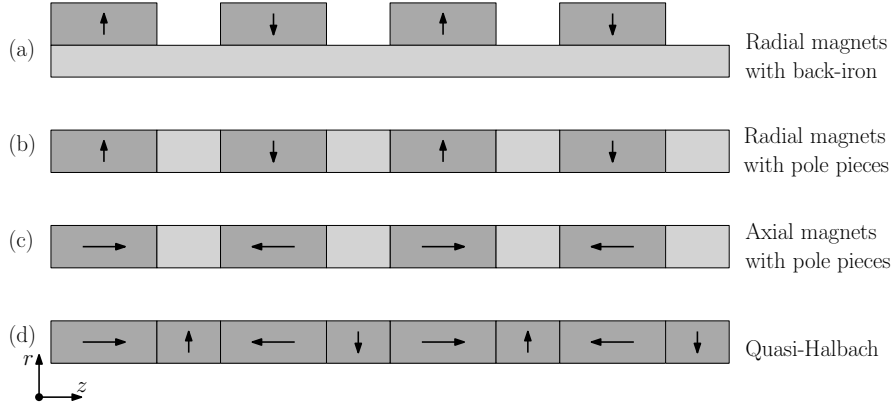


Figure 3.2: Translator configurations.

only positive or negative radial magnets, hence, the return path is established by either a soft-magnetic back-iron, or by soft-magnetic pole pieces between the magnets, see Fig. 3.2(b). It should be mentioned that from a manufacturing point of view, radial magnets are more expensive since magnetizing radially is rather difficult, and in most cases it is approximated by means of a finite number of parallel magnets [108].

Changing the radial magnets into axial magnets, as shown in Fig. 3.2(c), results in a lower reluctance path and hence a higher magnetic field in the airgap. This configuration does not require a soft-magnetic back-iron, as it would short-circuit the magnetic field, preventing it from crossing the airgap. When an IMT is considered, the magnetic field is inherently forced outwards, since no magnetic field can flow toward the center axis due to axisymmetry. However, this effect is only apparent for small radii. If axial magnetization is used for EMT, a significant amount of leakage flux appears on the outside of the magnet array, resulting in poor performance. However, a strong advantage of this configuration is the ease of magnetization and manufacturing.

When the pole pieces of the axial magnetization topology are replaced by radial magnets, a quasi-Halbach configuration is obtained, see Fig. 3.2(d). This configuration has the possibility to focus the magnetic field on either the inner or outer side of the array, hence makes it applicable in both IMT and EMT. No soft-magnetic material is necessary resulting in lower cogging forces. However, since radial magnets are used, it is an expensive solution, in terms of magnetization and manufacturing. Alternatively, one can use trapezoidal magnets, however it has been shown that the influence on the performance is very limited [106]. The three configurations considered in this thesis are radial magnets with back-iron, Fig. 3.2(a) (referred as radial magnetization from hereon), axial magnets with pole pieces, Fig. 3.2(c) (referred as axial magnetization from hereon) and quasi-Halbach magnetization, Fig. 3.2(d).

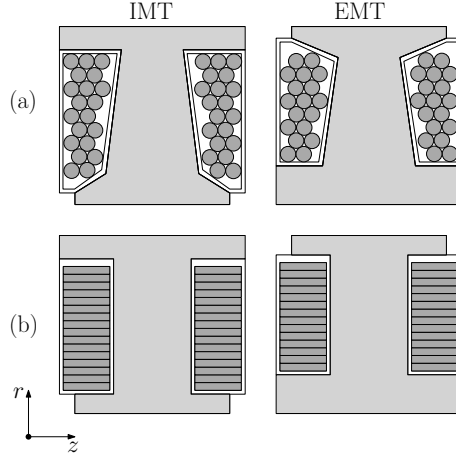


Figure 3.3: Slot geometries for IMT and EMT with (a) conventional slots and (b) rectangular slots.

3.1.2 Stator tooth geometry

The stator can be of slotless or slotted type. The slotless configuration has no cogging force component due to the absence of the ferromagnetic teeth, hence a lower force ripple is obtained, despite of a lower force density due to the increased effective airgap. A low cogging force component is necessary for high precision servo applications, however, the reduction of the force ripple of a slotted actuator can be achieved using accurate modeling of the fringing fields and optimization of the magnet sizes and tooth tip widths.

The stator of a slotted TPMA consists of an array of teeth with embedded coils. Each tooth has a coil on its left and right side as shown in Fig 3.3. The magnetic field inside the tooth is dominantly radial and since the cross section increases linear with the radius, the tooth width is allowed to decrease with the radius, hereby increasing the slot area and effective coil area. This is shown for the IMT and EMT in Fig 3.3(a). However, the non-rectangular slot shape results in a filling factor, k_f , which is highly dependent on the number of windings and wire diameter. In Fig. 3.3(b) a rectangular slot is shown which allows the use of profile wire which results in a higher filling factor which is less dependent on the number of windings and wire thickness. Furthermore, the coil manufacturing is simplified in terms of manufacturing and isolation. The use of profile wire significantly improves the thermal behavior since a higher filling factor increases the thermal conductivity of the total coil.

3.1.3 Slot, pole and winding configurations

The winding distribution is configured such that, given a feasible number of poles and slots, the flux linkage per phase is maximized. For rotary permanent magnet machines, numerous configurations are applied which can be classified as: concentrated, distributed, multi-layer, modular, etc. [73, 74, 121]. Their classification relates generally to how the windings are interconnected or the way the end windings are configured. However, since, in a tubular actuator, no end windings exist, the comparison in performance is different and other configurations are even possible. In a rotary or linear actuator, each turn of a coil consists of a forward and a backward wire since a return path for the current should be established. In tubular actuators however, each turn ends at its origin and the return path is inherently established. This increases the design freedom for different winding configurations.

The active length of a tubular PM actuator is made of an integer number of active periodic sections, N_{pa} and an additional number of sections N_{px} for either the stator or translator to obtain the necessary stroke. Denote the number of poles per periodic section as P which is always a multiple of two and the number of slots per periodic section as S which is a multiple of three since three phase machines are considered. Furthermore, a feasible combination should satisfy the following relation: $\text{gcd}(P/2, S/3) = 1$ (gcd =greatest common divisor), otherwise the length of the periodic section can be reduced (e.g. when $P = 4$ and $S = 6$). Additionally, the winding configuration should be such that the induced emf waveforms are balanced. In Fig. 3.4 the most common winding configurations up to nine slots, $S = 9$, per periodic section are given [153, 154].

- (a) A combinations of two poles and three slots with a concentrated winding is shown in Fig. 3.4(a) (a fractional slot to pole number of 1.5), resulting in a trapezoidal emf waveform for large pitch magnets. This concentrated winding is characterized by the positive and negative coil of each phase surrounding one tooth. In rotary machines, this topology has the advantage of a short end winding, increasing efficiency, however for tubular actuators, this advantage is not applicable.
- (b) The winding configuration shown in Fig. 3.4(b) is similar as configuration (a), however four poles are now considered (slot to pole number of 0.75), resulting in a more sinusoidal emf waveform and a lower cogging force in case of ac excitation. Furthermore, the magnetic loading per slot is lower than for configuration (a) which might be beneficial since saturation might occur for a lower radius to length ratio of the actuator if configuration (a) is considered. Additionally, the height of the translator back-iron can be reduced compared to configuration (a) in case radial magnetization is considered. However, the frequency is doubled at a given velocity, hence the iron losses might be more significant.

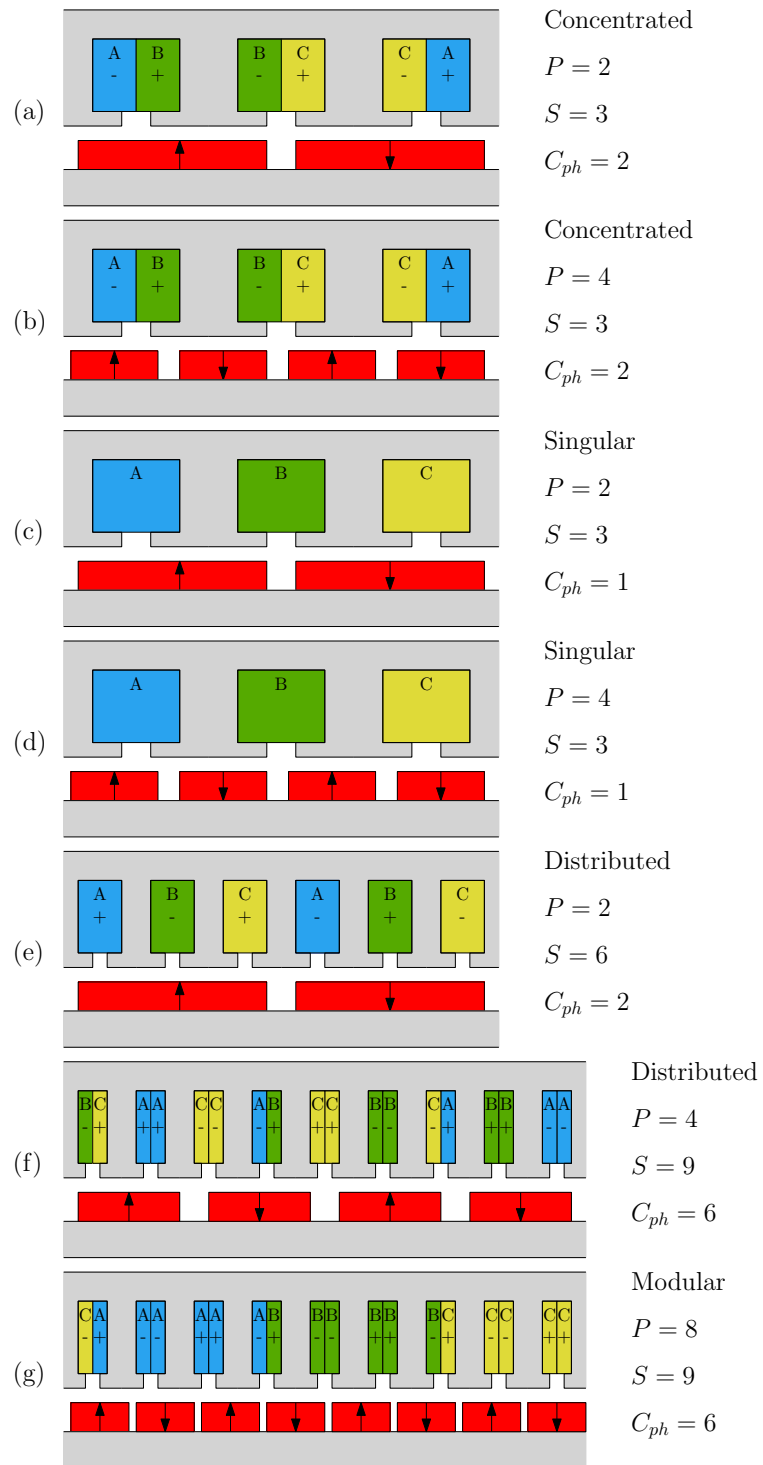


Figure 3.4: Considered slot, pole and winding configurations for the TPMA.

- (c) As mentioned earlier, due to the nonnecessity of a return coil, the concentrated winding configuration (a) can be transformed into a singular winding configuration as shown in Fig. 3.4(c). It achieves the same performance with a $\sqrt{3}$ higher current, but lower total copper loss (75%) since the winding resistance is reduced by a factor four. Furthermore this configuration is easier to manufacture and has a higher total filling factor than (a) due to absence of the isolation between two coils within one slot.
- (d) The singular winding configuration of Fig. 3.4(d) achieves the same performance as the concentrated winding configuration (b) however, again with a lower copper loss (75%) and higher filling factor for the same reasons as mentioned in (c).
- (e) The integral slot distributed winding configuration shown in Fig. 3.4(e) considers six slots per two poles (slot-pole number of 3). This is a full pitch winding, resulting in a maximum winding factor and a sinusoidal emf waveform. However, due to the integer slot-pole number, a large cogging force is obtained.
- (f) A fractional number of slots per pole is given by the distributed winding configuration of Fig. 3.4(f), with nine slots per four poles or a slot per pole number of 2.25. This configuration has a high winding factor together with a relatively low cogging force and force ripple.
- (g) For the winding configuration with nine slots per eight poles, as shown in Fig. 3.4(g), the coils of each phase are grouped together in modules with a high winding factor. This modular winding configuration has therefore advantages from a construction point of view. Furthermore, the fractional number of slots per pole of 1.125 results in a very low cogging force.

Each of these winding configurations are considered in the modeling and optimization since each of them has advantages and disadvantages. It depends on the performance and volumetric specifications which one is the most preferable.

3.2 Application of the generic modeling technique

3.2.1 Assumptions and simplifications

In Chapter 2, the generic formulation for the magnetic field distribution for 2D geometries was presented. This technique is now applied to the TPMA topologies presented in previous sections. Due to the axisymmetric structure, the 2D axisymmetric coordinate system (r, z) is selected. The first geometrical assumption is neglecting the finite length of the stator and translator. This simplification leads to the fact that the actuator can be modeled as a finite number of sections

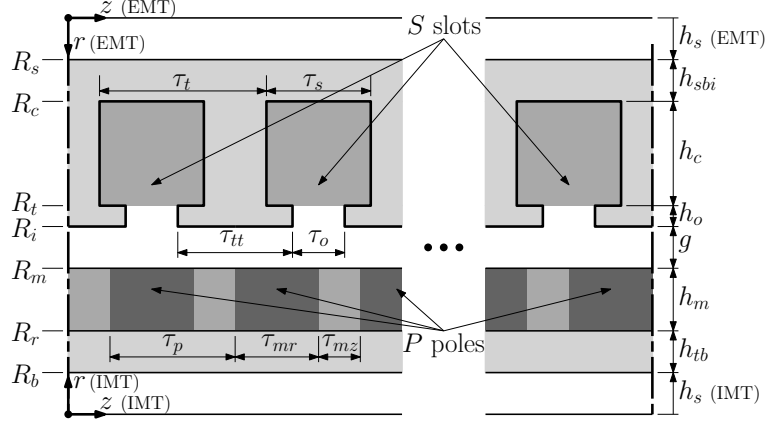


Figure 3.5: Geometrical parameters and variables of the TPMA for the IMT and EMT listed in Table 3.1.

Table 3.1: List of geometric parameters and variables shown in Fig. 3.5.

Name	Description	Name	Description
N_{pa}	Number of active periods	τ_{mz}	Axial pole width
N_{px}	Number of inactive periods	τ_t	Tooth pitch
P	Number of poles per period	τ_s	Slot width
S	Number of slots per period	τ_{tt}	Tooth tip width
h_{sbi}	Stator back iron height	τ_o	Slot opening width
h_{tb}	Translator height	R_b (IMT)	Shaft radius
h_c	Coil height	R_b (EMT)	Translator outer radius
h_m	Magnet height	R_r	Translator radius
g	Airgap length	R_m	Magnet radius
h_t	Tooth tip height	R_i	Stator bore radius
h_s (IMT)	Translator shaft height	R_t	Tooth tip radius
h_s (EMT)	Stator shaft height	R_c	Coil radius
τ_p	Pole pitch	R_s (IMT)	Stator outer radius
τ_{mr}	Radial pole width	R_s (EMT)	Shaft radius

which have periodic boundary conditions in the axial direction. Such a section consists of P poles and S slots as shown in Fig. 3.5 with the various parameters listed in Table 3.1. Although the finite length of the stator and/or translator can lead to a large force ripple, it can be minimized by altering the additional length [155, 156]. This additional length does not significantly influence the main actuator performance and can therefore be disregarded during the actuator design. When the design of the periodic sections is established, the end-effects, if apparent can be minimized afterwards.

Although the generic modeling technique allows for modeling of a semi-closed slot geometry, it is further simplified. The slot width is set equal to the width of the slot tip opening, Fig. 3.6. This assumption holds when saturation in the

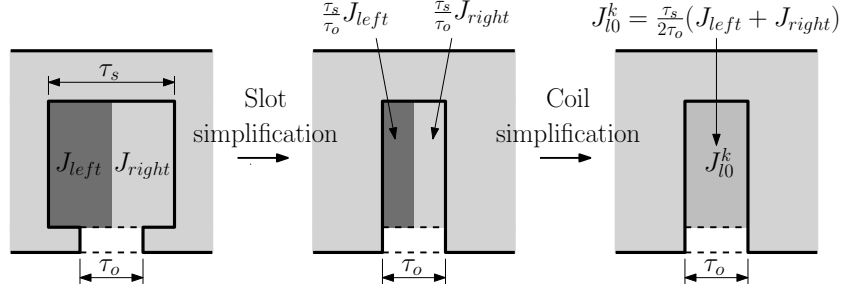


Figure 3.6: Simplification of the slot and coil geometry.

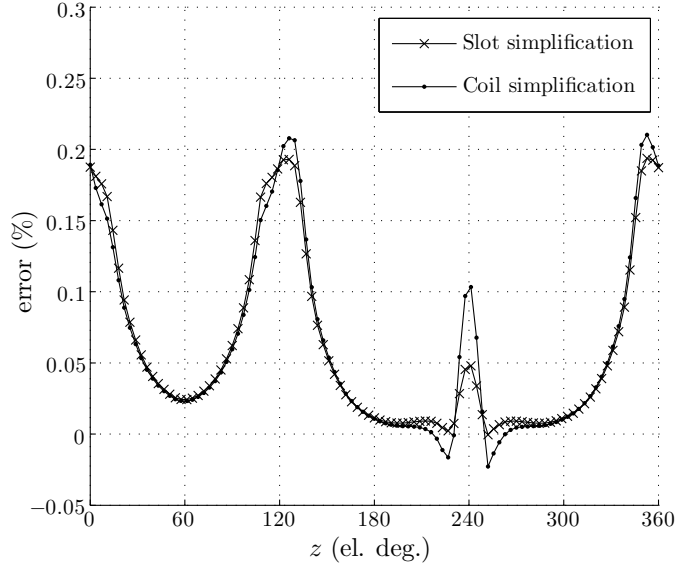


Figure 3.7: Error in the field solution due to the slot and coil simplification.

tooth is low and hence the slot leakage is small. In that case, the influence on the magnetic field in the airgap is insignificant. This simplification drastically decreases the complexity of the analytical model, hence the model becomes faster and stability is more guaranteed. Since this decreases the effective coil area, the current density is corrected by a factor τ_s/τ_o .

Another simplification is made by regarding the left and right coil as a single coil with the average current density of the left and right coil as shown in Fig. 3.6. This introduces a very small local error of the magnetic field distribution inside the coil, however globally the effect can be neglected due to the high permeability of the ferromagnetic material of the stator. In Fig 3.7, the error of the magnetic flux density in the airgap is shown due to the slot simplification and due to the coil simplification. The maximum error is 0.21 % which is considered negligible.

3.2.2 Division in regions for tubular actuators

The geometry has to be divided into periodic regions and/or non-periodic regions with Neumann boundary conditions in the tangential direction. In Fig. 3.8(a), (b) and (c), the total division in regions is shown for radial, quasi-Halbach and axial magnetization, respectively. For each topology, the periodic region I is the airgap. Region II contains the permanent magnets, which is a periodic region for the radial and quasi-Halbach topology but has to be modeled by separate, non-periodic regions, II_ν for $\nu = 1 \dots P$, for the axial magnetization topology since the axial magnets are separated by soft-magnetic pole-pieces, see Fig. 3.8(c). The periodical region III is the non-magnetic translator which only has to be considered for the quasi-Halbach and axial magnetization topology since the translator is soft-magnetic for the radial magnetized topology. The slot openings are modeled by non-periodic regions, IV_ν for $\nu = 1 \dots S$, and the coils by non-periodic regions, V_ν for $\nu = 1 \dots S$.

The relative displacement between the stator and translator is defined as Δ_z which can be expressed in electrical radians as $\theta_e = \frac{\pi \Delta_z}{\tau_p}$ or electrical degrees $\theta_e = \frac{180 \Delta_z}{\tau_p}$. This relative displacement is indicated in Fig. 3.8 and corresponds to zero when phase A has maximum flux linkage, referred as the direct or d-axis from hereon. The minimum flux linkage for phase A is obtained at 90 electrical degrees, referred as the quadrature or q-axis from hereon. The width of one periodic section is $P\tau_p$ and the spatial frequencies of the periodic regions are given by $w_n^k = \frac{n2\pi}{P\tau_p}$. For the regions II_ν for $\nu = 1 \dots P$, for the axial magnetization topology, the spatial frequencies are given by $w_n^k = \frac{n\pi}{\tau_{mz}}$. The stator consists of regions $\text{IV}_{1\dots S}$ (slot openings) and $\text{V}_{1\dots S}$ (coils) which have each their offset in axial direction, Δ^k . Motion in the axial direction by Δ_z results in an increment of the parameter Δ^k for all these regions. The spatial frequencies of the slot and slot opening regions are given by $w_n^k = \frac{n\pi}{\tau_o}$.

3.2.3 Assignment of the boundary conditions

In Fig. 3.8 the boundary conditions for each magnetization topology are shown. The assignment of boundary conditions is similar for IMT and EMT topologies. The only difference is that the Dirichlet boundary for region III (for quasi-Halbach and axial magnetization) is defined at $r = 0$ and $r = \infty$ for IMT and EMT, respectively. For each topology, a Neumann boundary condition is applied for each slot at the coil radius, $r = R_c$. Furthermore, a continuous boundary condition is applied between the coil and slot opening regions at $r = R_t$. A combined continuous and Neumann boundary condition between every slot opening and the airgap is applied ($r = R_i$). The radial and quasi-Halbach magnetization topology have a continuous boundary condition between the airgap and the magnet array ($r = R_m$). The radial magnetization has a Neumann condition at the radius between the magnet array and translator ($r = R_r$). Since the quasi-Halbach

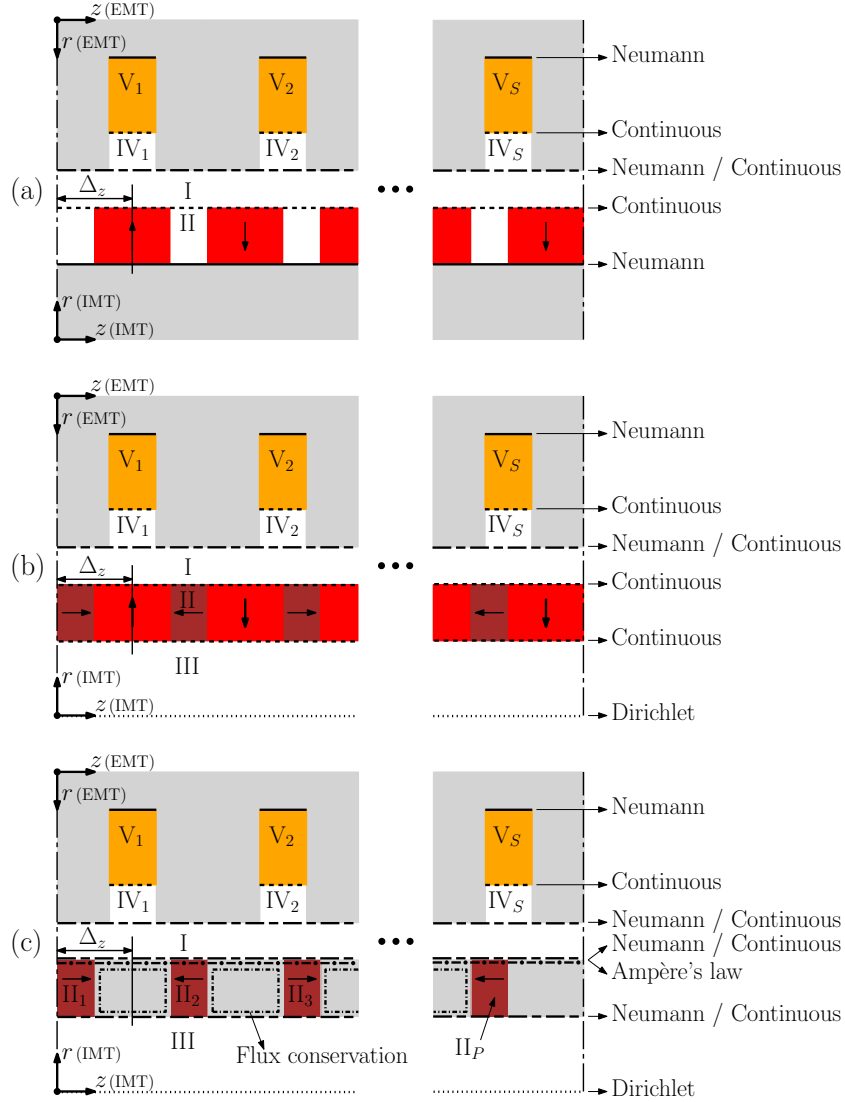


Figure 3.8: Division in regions and boundary conditions for (a) radial, (b) quasi-Halbach and (c) axial magnetization.

magnet array has no back-iron, a continuous boundary condition is necessary between the magnet array and the non-magnetic translator region ($r = R_r$). The axial magnetization topology has a combined continuous and Neumann boundary condition between the magnet regions and the airgap ($r = R_m$) as well as the non-magnetic translator ($r = R_r$). In order to solve the average components of the magnetic field inside the magnet regions for axial magnetization, additional boundary conditions have to be applied as was explained in Section 2.7. Around every pole-piece, the divergence of the magnetic flux density is set to zero. How-

ever, these P equations are not independent and this boundary conditions can only be applied for $P - 1$ pole-pieces. The last equation is obtained by applying Ampère's law between the airgap and every magnet region ($r = R_m$). These boundary conditions result in a set of algebraic equations which is solved using matrix inversion with the singular value decomposition since the matrix is ill conditioned. The resulting matrices are described in Appendix B.1, B.2 and B.3 for radial, quasi-Halbach and axial magnetization, respectively.

3.2.4 Finite element verification

The proposed analytical model is verified with non-linear FEA. Three benchmark topologies are considered and the various sizes are given in Table 3.2. The topologies are chosen such that most of the possible configurations are covered. The magnetic field is calculated with the previous described method and the radial and axial component of the flux density in the center of the airgap, $R_{ag} = \frac{R_m + R_i}{2}$, over one periodic section is compared with FEA in Figs. 3.9 to 3.11 for benchmark topologies 1 to 3, respectively. Armature reaction is included and it can be observed that excellent agreement is obtained and all the harmonic content resulting from the slotted stator is correctly modeled.

It should be noted that although the analytical model verifies well with non-linear FEA, the topologies are chosen such that no extreme saturation in the soft-magnetic regions is obtained. This is the major drawback of the analytical model and therefore, the magnetic flux density inside the soft-magnetic material has to be predicted in order to make sure that the analytical prediction are correct and valid. The implemented method to calculate these flux densities is discussed in the following section.

3.3 Flux density inside the soft-magnetic regions

Although the aforementioned obtained magnetic field solution is very accurate, it assumes the permeability of the soft-magnetic material to be infinite. When one uses this particular modeling technique in an optimization algorithm for the design of an electromagnetic actuator, the flux density inside the soft-magnetic material should be known in order to estimate if saturation occurs and the assumption and therefore the solution is still valid. With this information, one can limit these flux density levels during optimization given the saturation magnetic flux density of the ferromagnetic material. This can be obtained by using the field solution surrounding the ferromagnetic material.

Table 3.2: Parameters of the benchmark topologies.

	Topology 1	Topology 2	Topology 3
IMT/EMT	IMT	EMT	IMT
Magnetization	Radial	Axial	Halbach
Winding	Concentrated	Distributed	Modular
P	2	2	8
S	3	6	9
C_{ph}	2	2	6
h_{sbi}	5 mm	12 mm	6 mm
h_{tb}	10 mm	n.a.	n.a.
h_c	10 mm	8 mm	11 mm
h_m	5 mm	6 mm	4 mm
g	1 mm	1.2 mm	1 mm
h_t	3 mm	2.5 mm	2.7 mm
h_s	5 mm	6 mm	5 mm
τ_p	30 mm	40 mm	35 mm
α_p	0.9	0.4	0.6
τ_s	10 mm	5 mm	10 mm
τ_o	2.5 mm	2 mm	2.5 mm
B_{rem}	1.34 T	1.34 T	1.34 T
μ_r	1.06	1.06	1.06
J_{phRMS}	5 A/mm ²	4 A/mm ²	6 A/mm ²
N_I	50	70	120

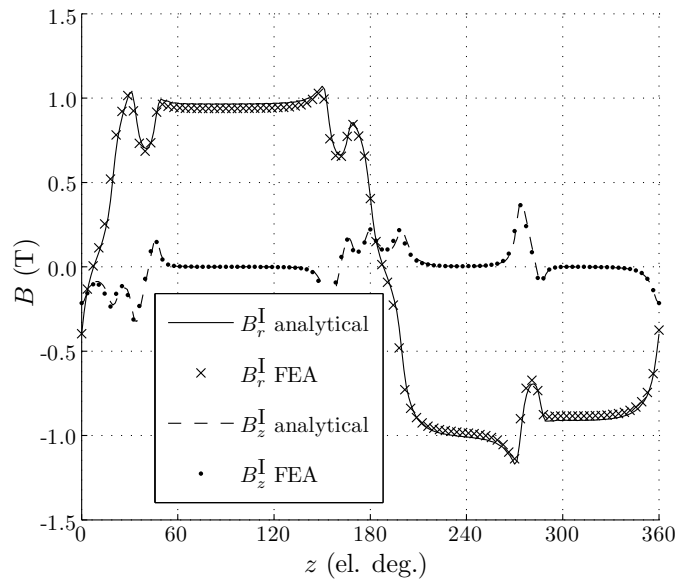


Figure 3.9: Flux density in the center of the airgap for benchmark topology 1 listed in Table 3.2.

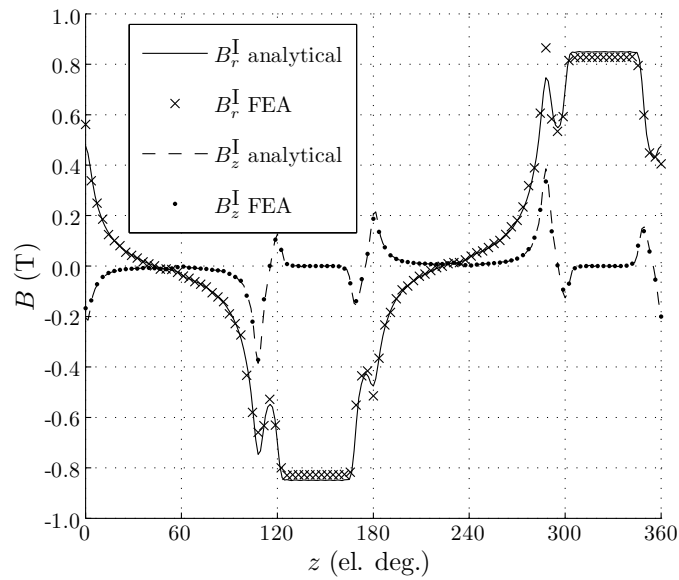


Figure 3.10: Flux density in the center of the airgap for benchmark topology 2 listed in Table 3.2.

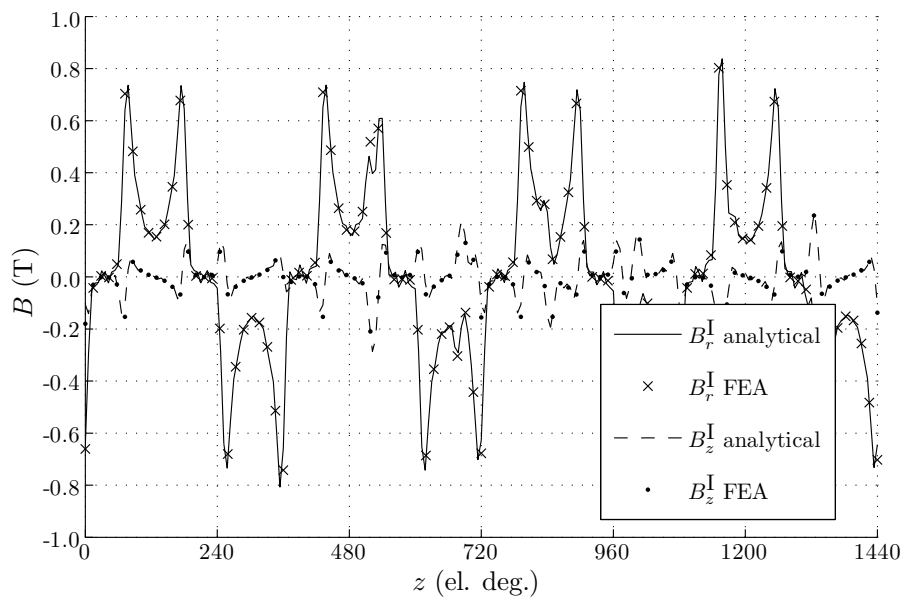


Figure 3.11: Flux density in the center of the airgap for benchmark topology 3 listed in Table 3.2.

3.3.1 Stator teeth and stator back-iron

In case slot leakage can be neglected, the amount of flux entering the tooth can be estimated by integrating the radial component of the flux density at the tooth tip, surface S_{tt} , see Fig. 3.12. Hence, one can obtain the flux entering tooth i at a particular position Δ_z by

$$\phi_{t_i}(\Delta_z) = 2\pi R_i \int_{\Delta_z - \frac{\tau_t}{2} + i\tau_t}^{\Delta_z + \frac{\tau_t}{2} + i\tau_t} B_r^I(R_i, z) dz. \quad (3.1)$$

This integral is evaluated giving the following expression in terms of the relative displacement θ_e as

$$\begin{aligned} \phi_{t_i}(\theta_e) = 2\tau_p P R_i \sum_{n=1}^{\infty} \frac{1}{n} \left[B_{rsn}^I(R_i, \theta_e) \sin\left(\frac{n2\pi}{S}\right) \cos\left(2n\left(\frac{\theta_e}{P} + \frac{i\pi}{S}\right)\right) \right. \\ \left. + B_{rcn}^I(R_i, \theta_e) \cos\left(\frac{n2\pi}{S}\right) \sin\left(2n\left(\frac{\theta_e}{P} + \frac{i\pi}{S}\right)\right) \right]. \quad (3.2) \end{aligned}$$

The maximum flux density in the stator tooth is situated at its inner radius, which is R_t for the IMT topology and R_c for the EMT topology. Therefore, the flux density in the stator tooth is obtained as

$$B_{t_i}(\theta_e) = \begin{cases} \frac{\phi_{t_i}(\theta_e)}{2\pi R_t w_t}, & \text{for the IMT topology,} \\ \frac{\phi_{t_i}(\theta_e)}{2\pi R_c w_t}, & \text{for the EMT topology.} \end{cases} \quad (3.3)$$

From the estimated magnetic flux density in the every tooth, the average flux density in the stator back-iron can be obtained by solving the network of inter-connecting fluxes shown in Fig 3.12. A general expression for the flux through the back-iron with number j is given for a variable number of slots S as

$$\phi_{s_j}(\theta_e) = -\frac{1}{S} \sum_{i=0}^{S-2} (S-i-1) \phi_{t_b}(\theta_e), \text{ for } b = (i+j+1) \bmod S. \quad (3.4)$$

The flux density in back-iron j is then obtained as

$$B_{s_j}(\theta_e) = \frac{\phi_{s_j}(\theta_e)}{\pi(R_s^2 - R_i^2)}. \quad (3.5)$$

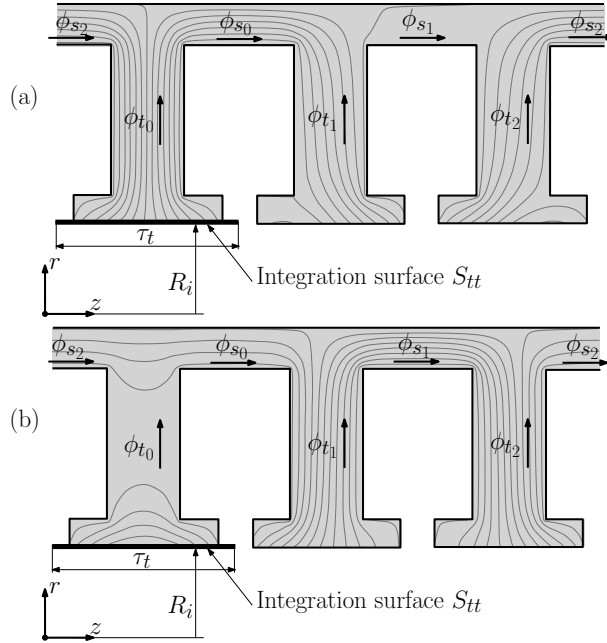


Figure 3.12: Flux line distribution inside the stator for the IMT with a concentrated winding configuration with two poles per three slots and radial magnetization at (a) the d-axis and (b) the q-axis.

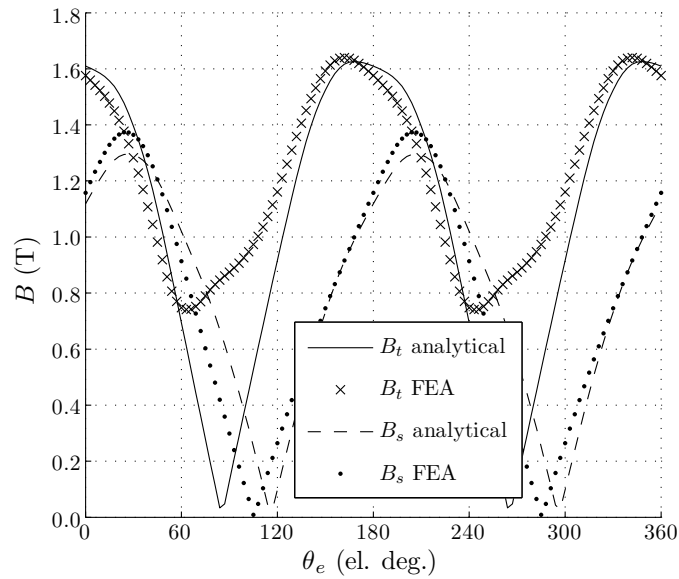


Figure 3.13: Estimated flux density in the teeth and stator back-iron verified with FEA for benchmark topology 1 listed in Table 3.2.

In Fig. 3.13 the analytical solution is compared with the FE calculation. It can be observed that very good agreement is obtained. Only at the position of 90 electrical degrees there is a discrepancy since no net radial flux is existing in the first tooth, however some axial flux is still apparent as observed in Fig. 3.12(b). This results in a net flux density inside the tooth but since this level is always lower than at 0 electrical degrees, the maximum average magnetic flux density is still correctly estimated. Furthermore, since this net axial flux does not pass the stator back-iron, it does not affect the magnetic flux density estimation in the stator back-iron as observed in Fig. 3.13.

3.3.2 Translator back-iron

The radial magnetized topologies have a soft-magnetic translator back-iron. Hence, the estimation of the magnetic flux density can be obtained from the amount of flux entering the translator at $r = R_r$ over the surface S_{tbi} as indicated in Fig. 3.14,

$$\phi_{tbi}(\Delta_z) = \pi R_r \int_{\tau_{mz}/2}^{\tau_{mz}/2 + \tau_p} B_r^{\text{II}}(R_r, z) dz. \quad (3.6)$$

Evaluating this expression gives

$$\begin{aligned} \phi_{tbi}(\theta_e) = \tau_p P R_r \sum_{n=1}^{\infty} \frac{1}{n} \sin\left(\frac{n2\pi}{P}\right) & \left[B_{rsn}^{\text{II}}(R_r, \theta_e) \sin\left(\frac{n2\pi}{P}(2 - \alpha_p)\right) \right. \\ & \left. + B_{rcn}^{\text{II}}(R_r, \theta_e) \cos\left(\frac{n2\pi}{P}(2 - \alpha_p)\right) \right]. \quad (3.7) \end{aligned}$$

with $\alpha_p = \tau_{mr}/\tau_p$ the radial magnet width to pole pitch ratio. The average flux density in the translator is therefore obtained as

$$B_{tbi}(\theta_e) = \frac{\phi_{tbi}(\theta_e)}{\pi(R_r^2 - R_b^2)}. \quad (3.8)$$

In Fig. 3.15 the estimated flux density is compared with FEA which is within 2 % accuracy. For both methods, the slight variation with the relative stator position is visible.

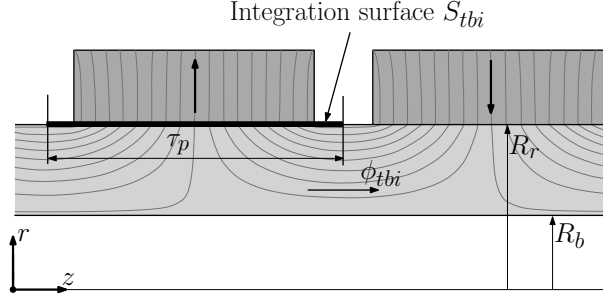


Figure 3.14: Flux line distribution inside the translator of the IMT with a concentrated winding configuration with two poles per three slots and radial magnetization.

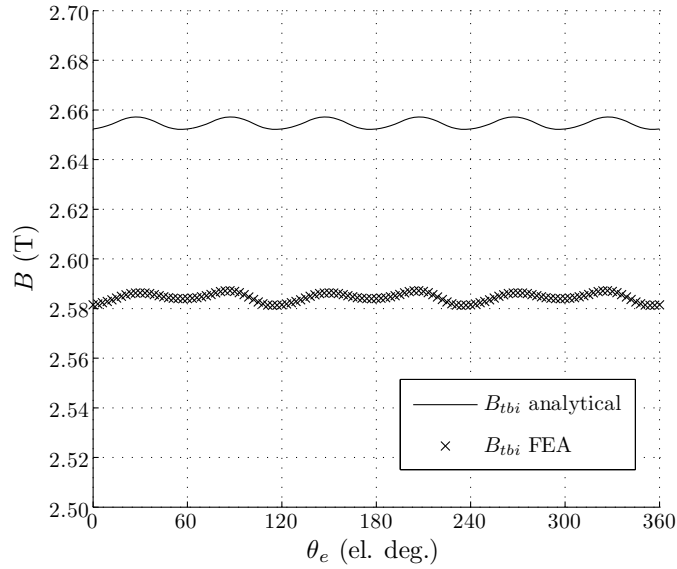


Figure 3.15: Estimated flux density in the translator back-iron verified with FEA for benchmark topology 1 listed in Table 3.2.

3.3.3 Pole pieces

The permanent magnet array for axial magnetization consists of axially magnetized magnets separated by soft-magnetic pole-pieces. In Fig. 3.16 the flux line distribution within this array is shown. In order to estimate the average flux density inside the pole-pieces, the field solution in the airgap can be used. The flux entering the pole piece can be calculated by integrating the radial component of the flux density over the surface S_{pole} as indicated in Fig. 3.16

$$B_{pp}(\Delta z) = \frac{1}{\tau_{mr}} \int_{\tau_{mz}}^{\tau_p} B_r^I(R_m, z) dz. \quad (3.9)$$

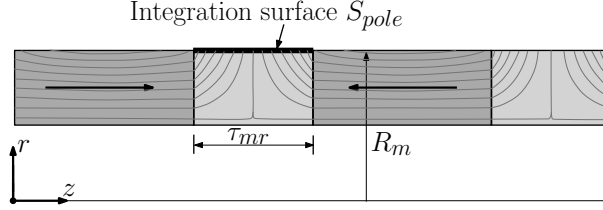


Figure 3.16: Flux line distribution inside the translator of the IMT with a concentrated winding configuration with two poles per three slots and axial magnetization.

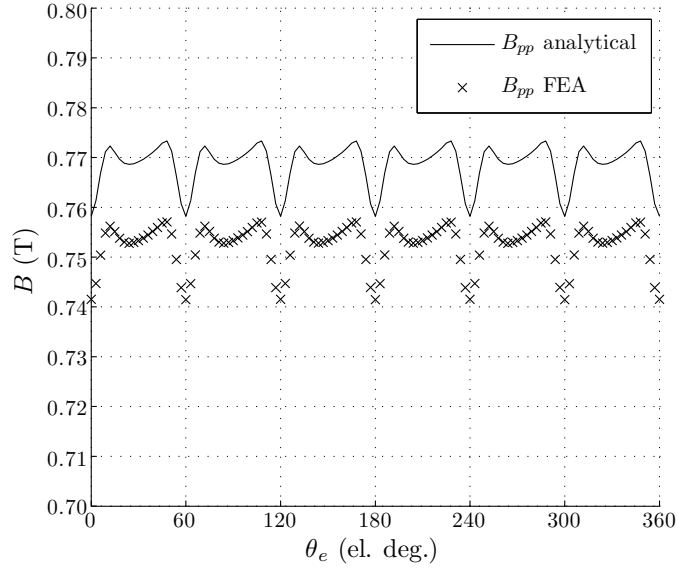


Figure 3.17: Estimated flux density in the pole piece verified with FEA for benchmark topology 2 listed in Table 3.2.

An evaluation of the expression is given by

$$B_{pp}(\Delta_z) = \frac{P}{\alpha_p \pi} \sum_{n=1}^{\infty} \frac{1}{n} \sin\left(\frac{n2\pi\alpha_p}{P}\right) \left[B_{rsn}^I(R_m, \theta_e) \sin\left(\frac{n2\pi}{P}(2 - \alpha_p)\right) + B_{rcn}^I(R_m, \theta_e) \cos\left(\frac{n2\pi}{P}(2 - \alpha_p)\right) \right]. \quad (3.10)$$

The FEA verification in Fig. 3.17 shows a good agreement within 4 % and the variation as function of stator displacement is also apparent.

3.4 Electromotive force

The induced electromotive force of each phase of the three phase winding configuration is obtained from the calculated fluxes inside the stator teeth. The electromotive force results from the moving magnet array at a certain velocity v . Therefore, no armature reaction is considered for the magnetic field calculation. Additionally, the eddy current effect is neglected, hence the calculation is only valid for relatively low velocities. From the field calculation, all the fluxes in each tooth, $\phi_{t_i}(\theta_e)$ (for $i = 1..S$) are estimated as explained in Section 3.3. For the concentrated, distributed and modular winding configurations, each phase winding consists of a set of positive and corresponding negative coils. Each positive and negative coil set enclose a set of teeth and therefore, the total flux linked by that coil set can be obtained from the summation of the corresponding fluxes in each of the teeth. In Fig. 3.18(a) the flux network in the stator of the modular winding configuration is shown, in order to calculate the total flux linkage of phase winding A with N_t turns for N_{pa} active periodic sections is given by

$$\Lambda_{pm}(\theta_e) = N_{pa}N_t \left(\phi_{t_1}(\theta_e) - \phi_{t_2}(\theta_e) + \phi_{t_3}(\theta_e) \right). \quad (3.11)$$

When a singular winding configuration is considered, no negative coils exist and hence no teeth are enclosed, see Fig. 3.18(b). Therefore, the amount of flux linked by each coil is the amount of flux passing the stator back-iron behind the coil. The total flux linkage of a singular winding configuration for phase A with N_t turns for N_p periodic sections is given by

$$\Lambda_{pm}(\theta_e) = N_{pa}N_t \phi_{s_3}(\theta_e). \quad (3.12)$$

The induced emf waveform of each phase e_{ph} at a constant velocity $v = \frac{\tau_p}{\pi} \frac{d\theta_e}{dt}$ is given by

$$e_{ph}(\theta_e) = -\frac{d\Lambda_{pm}(\theta_e)}{dt} = -\frac{d\theta_e}{dt} \frac{d\Lambda_{pm}(\theta_e)}{d\theta_e} = -v \frac{\pi}{\tau_p} \frac{d\Lambda_{pm}(\theta_e)}{d\theta_e}. \quad (3.13)$$

Note that the derivative of the calculated flux linkage has to be taken numerically since the semi-analytical model does not allow for a derivative towards the relative displacement of the stator, θ_e . The emf waveforms per turn per periodic section for each topology are calculated at a velocity of $v = 1$ m/s and verified with non-linear FEA. Note that the eddy current effect is not included in the semi-analytical and the FEA method. The result is shown in Fig. 3.19 where again a good agreement is obtained in terms of amplitude and shape. The harmonic content due to the slotted stator and the winding configuration is predicted correctly for each benchmark topology.

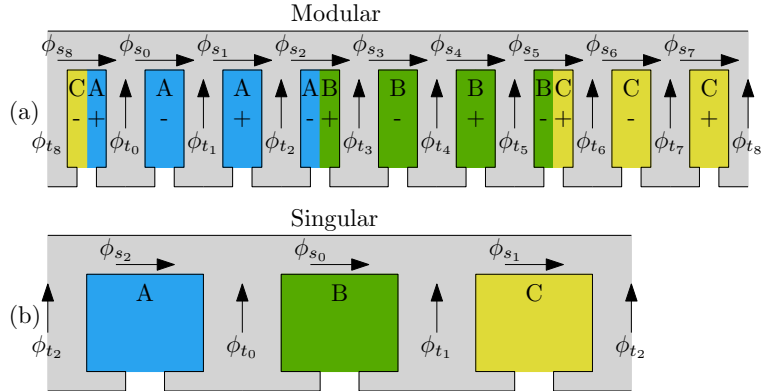


Figure 3.18: Flux network for (a) the modular winding configuration and (b) the singular winding configuration.

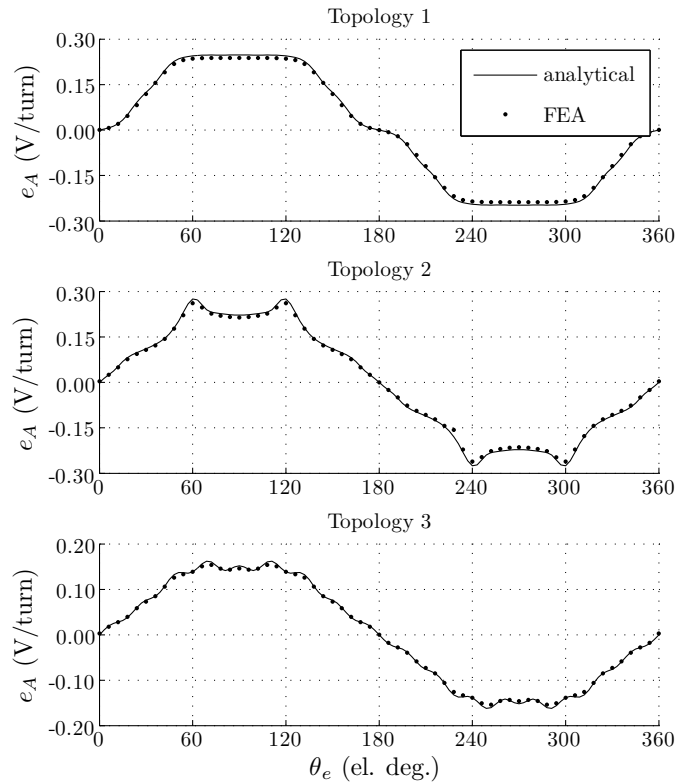


Figure 3.19: The electromotive force per turn of phase A verified with non-linear FEA at a velocity of 1 m/s for each of the benchmark topologies listed in Table 3.2.

3.5 Synchronous inductance

The synchronous inductance of each phase is defined as the amount of flux linked by that phase per ampere phase current. Hence for the analytical calculation of the inductance, only the armature reaction field should be considered and therefore, the remanence of the permanent magnets is set to zero, $B_{rem} = 0$. The relative permeability of the permanent magnets, μ_r , is however still included. One could obtain the flux linked by each coil in the same way as for the emf calculation where the flux through each tooth is used for an estimation of the flux linkage. However, this is assuming the flux crosses the airgap and is predominantly radial directed. However, when considering only the armature reaction field, the slot leakage is dominant, and the majority of the flux travels through the tooth tips instead of the airgap as shown in Fig. 3.20(a). Hence, using the same method as for the emf calculation would lead to a wrong estimation of the flux linkage. The integration path for obtaining the total linked flux should include the flux linked in the slot openings and the coil regions as well, as denoted in Fig. 3.20(a).

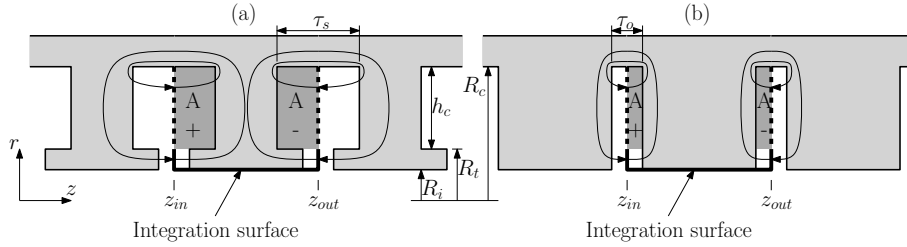


Figure 3.20: (a) Idealized flux line distribution for the armature reaction and (b) with slot simplification.

Furthermore, the flux linked through the dashed line surface is only partly linked by the coil with a fraction $(R_c - r)/h_c$. Additionally, due to the slot simplification as shown in Fig. 3.20(b), the flux crosses a shorter coil width and therefore, the flux density of the coil region has to be corrected by τ_o/τ_s . The total flux linkage of two coils (inward and outward) situated at the slots, which are located at z_{in} and z_{out} , can be calculated as

$$\begin{aligned}
 \Lambda_{ph,i}(\theta_e) = & 2\pi N_{pa} N_t \left[R_i \int_{z_{in}}^{z_{out}} B_r^I(R_i, z) dz \right. \\
 & + \int_{R_i}^{R_t} B_z^{IV, sin}(r, z_{in}) r dr + \int_{R_i}^{R_t} B_z^{IV, s_{out}}(r, z_{out}) r dr \\
 & \left. + \int_{R_t}^{R_c} B_z^{V, sin}(r, z_{in}) f_c(r) r dr + \int_{R_t}^{R_c} B_z^{V, s_{out}}(r, z_{out}) f_c(r) r dr \right], \quad (3.14)
 \end{aligned}$$

with the correction function, f_c , written as

$$f_c(r) = \frac{\tau_o}{\tau_s} \frac{R_c - r}{h_c}. \quad (3.15)$$

Note that these slots do not necessarily have to be adjacent. This is solely the flux linked by one pair of coils. In order to obtain the total flux linkage, Λ_{ph} , the flux linked by all pairs of coils have to be superimposed. Integration in the axial direction can be performed analytically, however the integrations in the radial direction are performed numerically since these Bessel integrals do not have a direct analytical solution. The linearized synchronous inductance can be obtained as

$$L_s(\theta_e) = \frac{\Lambda_{ph}(\theta_e)}{I_{ph}}. \quad (3.16)$$

This synchronous inductance per periodic section for one turn per coil ($N_t = 1$) is calculated as a function of the relative displacement, θ_e , and verified with non-linear FEA. The semi-analytical solution is shown in Fig. 3.21 for benchmark topology 2 (since only this topology has a dependency on θ_e), and verified with non-linear FEA with very good agreement. The d-axis inductance, L_d , and q-inductance, L_q , can be obtained at $\theta_e = 0$ and $\theta_e = 90$ electrical degrees, respectively.

3.6 Force profile

The total axial force between the stator and translator of a linear permanent magnet actuator consists of four components listed as

- Electromagnetic component, F_{em} : resulting from the interaction of the current in the stator winding and its flux linkage due to the permanent magnets on the translator. By means of proper current commutation, an average axial force is obtained. Additionally, the higher harmonics of the flux linkage waveform and current commutation cause a force ripple. Furthermore, due to the finite length of stator or translator, an unbalanced flux linkage results in an additional ripple in the force output. This component only exists under excitation and is linear dependent on the stator current.
- Reluctance component, F_{rel} : resulting from the interaction of the current excitation in the stator winding and the position dependent permeability of the translator. Like the electromagnetic component, this component can have an average force under correct commutation and only exists under excitation but is quadratically dependent on the stator current.

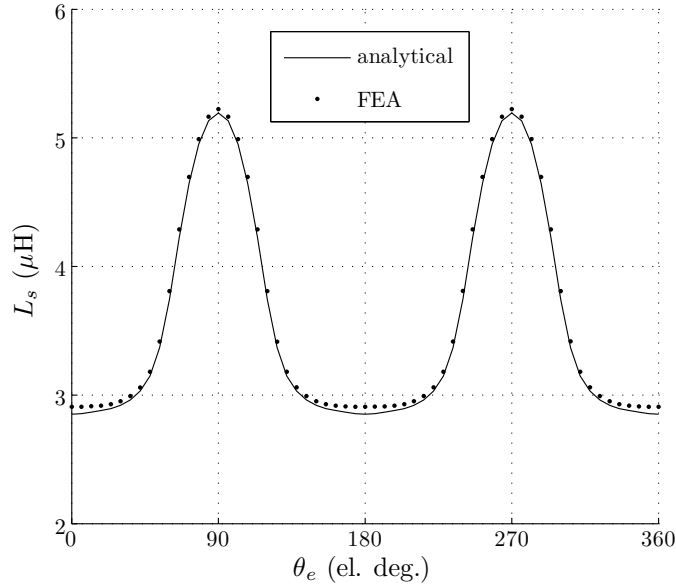


Figure 3.21: Synchronous inductance per turn as a function of relative displacement verified with FEA for benchmark topology 2 listed in Table 3.2.

- Cogging component, F_{cog} : resulting from the interaction of the magnetic field of the permanent magnets and the position dependent permeability of the stator (slotting effect). This component is independent on the presence of current excitation.
- End-effect component, F_{end} : resulting from the interaction of the magnetic field of the permanent magnets and the finite length of the stator or translator. In case of the EMT, this effect results from the finite length of the translator in combination with the slotted stator.

The following subsections describe the method of calculation for the various components.

3.6.1 Calculation methods

Several methods for force calculation exist where the three most common in the literature are the Lorentz force, the virtual work method and the Maxwell Stress Tensor [52]. The Lorentz force describes the force between a current carrying wire and an external field,

$$\vec{F}(\theta_e) = \int_V \vec{J}(\theta_e) \times \vec{B}(\theta_e) dV, \quad (3.17)$$

hence this method is not capable of calculating cogging forces due to the interaction of ferromagnetic materials and permanent magnets. To overcome this problem, the imaging method and current model for permanent magnets is used to find an equivalent current source and consequently apply the Lorentz force method. In a slotted actuator, the magnetic field is concentrated in the ferromagnetic material, not at the location of the coils, hence the Lorentz force cannot be applied directly.

The virtual work method calculates the force from an energy point of view. The total change in magnetic coenergy, W'_m , of the system due to an infinite small movement results in the force

$$F_z(\theta_e) = \frac{dW'_m}{d\Delta_z} = \frac{d}{d\Delta_z} \int_V \int_0^H \left(\vec{B}(\theta_e) \cdot d\vec{H}(\theta_e) \right) dV. \quad (3.18)$$

Since this method is generically valid, it is often used in finite element methods where the magnetic field, and energy are known for the whole system under consideration. Two field calculations are necessary in order to obtain the force. Since in the generic modeling technique, only the magnetic field in the non-ferro regions is known, this method is not suitable. The semi-analytical model is also not differentiable to the relative displacement, Δ_z , which would make the force calculation numerical.

The Maxwell Stress method calculates the force from a magnetic field point of view. More specifically, the force is determined from the magnetic stress tensor between the two objects on which the force is calculated.

$$\vec{F}(\theta_e) = \frac{1}{\mu} \oint_S \mathbb{T}(\theta_e) \cdot d\vec{S}, \quad (3.19)$$

with the tensor, $\mathbb{T}(\theta_e)$, in cylindrical coordinates given by

$$\mathbb{T}(\theta_e) = \begin{bmatrix} \frac{B_r^2 - B_\theta^2 - B_z^2}{2} & B_r B_\theta & B_r B_z \\ B_\theta B_r & \frac{-B_r^2 + B_\theta^2 - B_z^2}{2} & B_\theta B_z \\ B_z B_r & B_z B_\theta & \frac{-B_r^2 - B_\theta^2 + B_z^2}{2} \end{bmatrix}. \quad (3.20)$$

Hence, only the field solution between the objects should be known, more specifically, on a surface S separating the objects on which the force should be obtained. In the case of an actuator, this surface can be positioned in the center of the air-gap. Only on this surface, the field solution should be obtained correctly, hence this method is more suitable in combination with the developed generic modeling technique. Since the Maxwell stress method is an integral method, the force calculation is sensitive to discretization, and therefore rarely used in finite element analysis. However, for the semi-analytical model, the force can be evaluated analytically. For this reason, this method is applied in this thesis.

The surface S should enclose the object on which the force is calculated. More specifically, this surface should enclose the translator or stator, considering the IMT or EMT, respectively. Since the model is periodic, a cylindrical surface S_{ag} in the airgap, region I, covers the object completely. The airgap surface with normal vector \vec{n} is given by

$$\vec{n} = \vec{e}_r. \quad (3.21)$$

Evaluating equation (3.19), the axial force can be calculated as

$$F_z(\theta_e) = \frac{2\pi}{\mu} \int_0^{P\tau_p} B_r^I(\theta_e) B_z^I(\theta_e) r dz \Big|_{r=R_{ag}}, \quad (3.22)$$

since the angular flux density component is zero ($B_\theta = 0$). The radial strain force is zero under the assumption of axisymmetry. The integral suggests the force is dependent on the radius R_{ag} where the integral is evaluated. However, after evaluation using the derived field solution inside the airgap the expression for the axial force becomes independent of R_{ag} ,

$$F_z(\theta_e) = \frac{N_{pa} P \tau_p^2}{\mu_0} \sum_{n=1}^{\infty} \frac{b_n^I(\theta_e) c_n^I(\theta_e) - a_n^I(\theta_e) d_n^I(\theta_e)}{n}, \quad (3.23)$$

$$= F_{em} + F_{rel} + F_{cog}. \quad (3.24)$$

Note, that this method is extremely fast, independent on discretization but does depend on the truncation of harmonics N_I included in the model. Since the total periodic field solution is considered, this resulting force contains the electromagnetic, reluctance and cogging component. End-effects are not taken into account since only a single periodic section is considered. The separation of the various components is discussed in the following section.

3.6.2 Force calculation and separation of components

Each force component exhibits a certain force ripple and only the electromagnetic and reluctance force component can contribute to an average axial force independent of the relative position. As mentioned earlier, the proposed analytical model neglects the finite length of stator and translator. Therefore, using the Maxwell stress tensor method on the derived analytical field solution results in a force expression excluding the end-effects. However, the electromagnetic force, reluctance force as well as the cogging force are calculated at once. The cogging force component can be obtained separately by setting the current density of the stator windings to zero.

In order to obtain long stroke constant axial force, the correct current density should be applied in each coil region. Using sinusoidal commutation, the current for each phase, i_{ph} can be written as

$$i_{ph,A}(\Delta_z) = I_{\text{RMS}}\sqrt{2} \cos\left(\frac{\pi\Delta_z}{\tau_p} + \varphi_c\right), \quad (3.25)$$

$$i_{ph,B}(\Delta_z) = I_{\text{RMS}}\sqrt{2} \cos\left(\frac{\pi\Delta_z}{\tau_p} + \varphi_c + \frac{2\pi}{3}\right), \quad (3.26)$$

$$i_{ph,C}(\Delta_z) = I_{\text{RMS}}\sqrt{2} \cos\left(\frac{\pi\Delta_z}{\tau_p} + \varphi_c + \frac{4\pi}{3}\right), \quad (3.27)$$

where φ_c is the commutation angle in radians. The current densities in each coil region with N_t turns are then obtained as

$$J_{sl}(\Delta_z) = \frac{N_t i_{ph}(\Delta_z)}{S_c}, \quad (3.28)$$

where S_c is the coil surface area given by

$$S_c = \begin{cases} \frac{h_c \tau_s}{2} & \text{for configuration (a), (b), (f) and (g),} \\ h_c \tau_s & \text{for configuration (c), (d) and (e).} \end{cases} \quad (3.29)$$

The RMS current densities are given in Table 3.2 for each topology. Describing the phase currents as phasors in the dq0 reference frame results in the direct I_d and quadrature I_q current given by

$$I_d = I_{\text{RMS}} \cos(\varphi_c), \quad (3.30)$$

$$I_q = I_{\text{RMS}} \sin(\varphi_c). \quad (3.31)$$

Apart from equation (3.23), the average force can be approximately expressed in terms of the direct and quadrature current as

$$\langle F_z \rangle \cong \frac{3\pi}{\tau_p} \left(I_{\text{RMS}} \Lambda_{pm,\text{RMS}} \sin(\varphi_c) - \frac{I_{\text{RMS}}^2}{2} (L_q - L_d) \sin(2\varphi_c) \right), \quad (3.32)$$

$$\cong \frac{3\pi}{\tau_p} \left(I_q \Lambda_{pm,\text{RMS}} - (L_q - L_d) I_q I_d \right), \quad (3.33)$$

$$\cong \langle F_{em} \rangle + \langle F_{rel} \rangle, \quad (3.34)$$

which allows for separation of the electromagnetic and reluctance force. Since the definition of $\Delta_z = 0$ is given such that the maximum flux linkage is obtained

from the permanent magnet array, defined by the d-axis, the electromagnetic force, F_{em} , is maximum for $\varphi_c = 90$ electrical degrees. This point is optimal if the permeance of the translator is considered independent on Δ_z , referred as non-salient when the direct and quadrature inductance components are equal, $L_q = L_d$, which is the case for the quasi-Halbach magnetization topology. The radial magnetization topology has a slight variance in permeability, and therefore, has a reluctance force component, although extremely low and negligible. The axial magnetization topology has a more significant reluctance component due to the soft-magnetic pole pieces.

Using equation (3.23), the force waveforms as a function of the relative position, Δ_z , are calculated for each benchmark topology. The commutation angle is set to 90 degrees (maximum electromagnetic force). The force profile is periodic with 60 electrical degrees and hence only this part has to be calculated. The force profiles for each of the topologies are shown in Fig. 3.23 together with the non-linear FEA verification. In general, the force, calculated with the analytical model has a higher mean value than the FEA. This occurs due to the fact that the analytical model neglects the mmf drop in the soft-magnetic regions, and therefore, the magnetic field solution and the resulting force are slightly higher. When no saturation occurs, the maximum error is in the order of 3.32%, 3.94% and 0.65% for benchmark topologies 1, 2 and 3, respectively, as observed in Fig. 3.23. The force ripple is predicted perfectly in both amplitude and shape, even for the modular winding configuration where nine slot openings are considered in the model.

In order to investigate the significance of the reluctance component of benchmark topology 2, the average force using the Maxwell stress method, $\langle F_z \rangle$, the electromagnetic force, F_{em} , and reluctance component F_{rel} , are calculated while varying the commutation angle, ϕ_c . The dependency can be observed in Fig. 3.22. Using the Maxwell stress method, a lower reluctance force is predicted than using the approximate equation (3.32). This can be observed in the difference in the maximum point of F_z and $F_{em} + F_{rel}$. The approximate equation (3.32) gives a less accurate result since it only includes the first harmonic of the flux linkage and neglects the influence of the higher harmonics. Furthermore, the change in direct and quadrature inductance component is assumed to be sinusoidal which in reality is not the case, as was observed in Fig. 3.21. In any case, the reluctance component is negligible compared to the electromagnetic component for this topology.

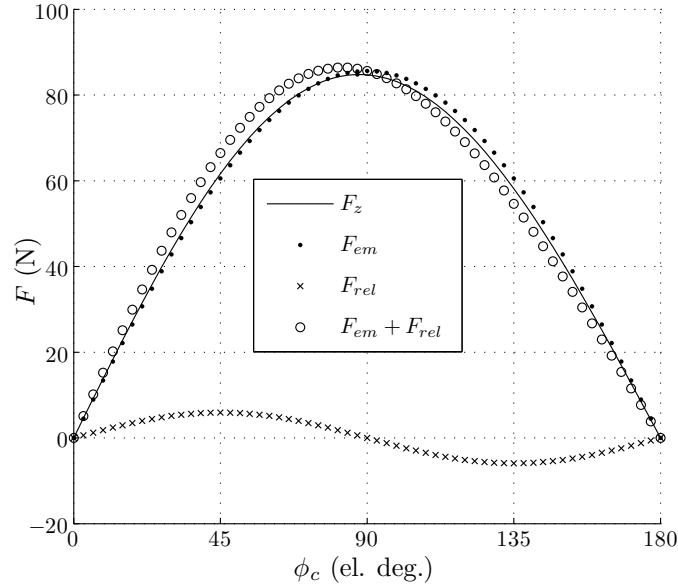


Figure 3.22: Axial force at $\theta_e = 0$ dependent on the commutation angle ϕ_c for benchmark topology 2 listed in Table 3.2.

3.6.3 End-effects

The force ripple due to the end-effects can be dominant and has to be taken into account. However, during the design of the TPMA, this effect can be disregarded since techniques exist to minimize this component without altering the actuator design. Each end of the stator causes a force ripple due to interaction with the permanent magnet array. By altering the additional length of the stator, one can control the relative phase shift of these waveforms with respect to each other and therefore, minimize the total force ripple. Only if each waveform is a perfect sinusoid with equal amplitude, the total ripple can be canceled out completely, however in practice, each waveform contains higher harmonics, and a small ripple is still present.

When the stator is shorter than the translator, each magnetization topology exhibits a similar level of end-effects. However since a quasi-Halbach magnetization has a more sinusoidal field distribution, the waveform is more sinusoidal and hence, the best minimization by means of changing the additional length of the stator is possible [156]. Although the cogging force is hereby minimized, it should be taken into account that by altering the length, the synchronous inductances for each phase are still balanced. Otherwise additional force ripples are obtained under loaded conditions.

In case the translator is shorter than the stator, the quantification of the end-effects is determined by the change in permeability of the translator at the ends.

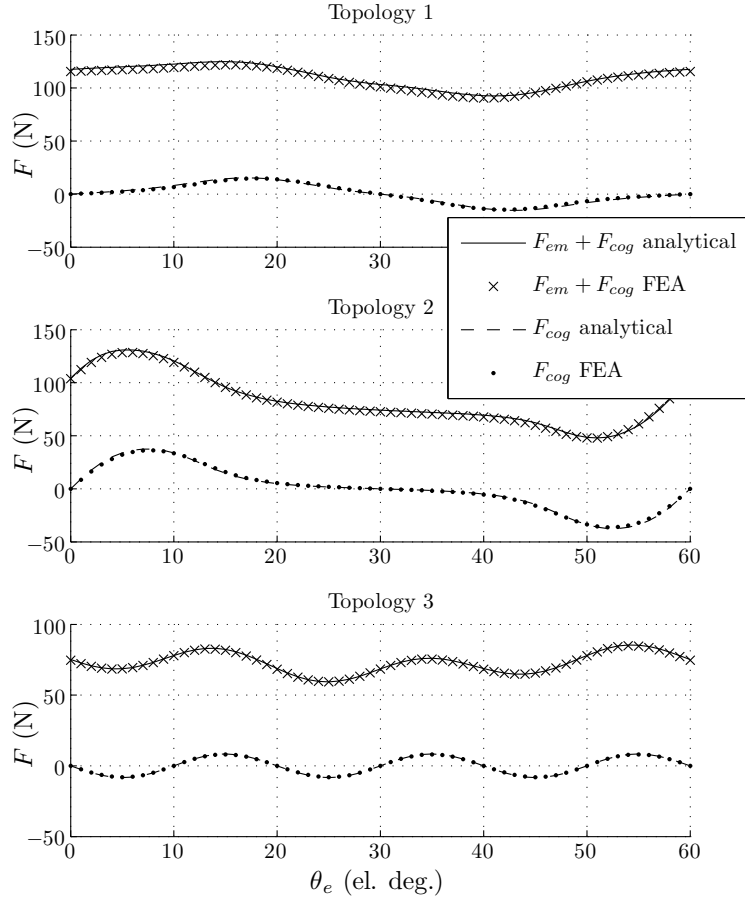


Figure 3.23: Axial electromagnetic force profile and cogging profile verified with FEA for each of the benchmark topologies listed in Table 3.2.

Therefore, this effect is large for the axial magnetized topology due to the soft-magnetic pole pieces. It is furthermore significant for radial magnetization due to the soft-magnetic back-iron, however smaller than for axial magnetization since the radial distance of the back-iron to the stator is larger. The quasi-Halbach magnetization has a relatively low end-effect component since no soft-magnetic material exists within the translator. A very small ripple is still apparent due to the relative permeability of the magnet array. Again one should take into account that altering the additional length of the translator results in an unbalanced magnetic loading in the three phase windings and unbalanced emf waveforms.

Modeling of the end-effect phenomenon is obtained by considering a quasi-periodic model, as presented in Section 2.9.3 for the slotless IMT with axial magnetization. Since each different topology and magnetization requires a different model to be constructed, it is not considered here. The end-effects can be minimized after the

design of a single periodic section and is therefore only considered for the optimal design later on in Chapter 6.

3.7 Copper losses

Given the RMS current density in each coil region, denoted as J_{slRMS} , the respective copper losses can be obtained. Given the number of coils per phase per period, C_{ph} , the total phase resistance is calculated as

$$R_{ph} = \begin{cases} \frac{\rho_{cu}(\Delta T_c) N_{pa} C_{ph} N_t^2 \pi (R_t + R_c)}{k_f S_c}, & \text{for IMT,} \\ \frac{\rho_{cu}(\Delta T_c) (N_{pa} + N_{px}) C_{ph} N_t^2 \pi (R_t + R_c)}{k_f S_c}, & \text{for EMT.} \end{cases} \quad (3.35)$$

with the coil surface area, S_c , given by

$$S_c = \begin{cases} \frac{\tau_s h_c}{2}, & \text{for winding configuration of Fig. 3.4(a), (b), (f) and (g),} \\ \tau_s h_c, & \text{for winding configuration of Fig. 3.4(c), (d) and (e).} \end{cases} \quad (3.36)$$

Note that for EMT topologies, the extra number of periodic sections, N_{px} , has to be taken into account. The resistivity of copper, ρ_{cu} , is considered to be dependent on the coil temperature increase ΔT_c . The total power dissipation, P_{cu} is then calculated as

$$P_{cu} = 3I_{RMS}^2 R_{ph}, \quad (3.37)$$

$$= \begin{cases} \frac{\rho_{cu}(\Delta T_c) J_{slRMS}^2 S_c N_{pa} C_{ph} \pi (R_t + R_c)}{k_f}, & \text{for IMT,} \\ \frac{\rho_{cu}(\Delta T_c) J_{slRMS}^2 S_c (N_{pa} + N_{px}) C_{ph} \pi (R_t + R_c)}{k_f}, & \text{for EMT.} \end{cases} \quad (3.38)$$

Because the coil temperature increment is dependent on the dissipated power P_{cu} , the calculation of the losses is performed iteratively together with a thermal model which is presented in the following section.

3.8 Thermal model

A thermal equivalent circuit is developed for both internal magnet topologies, as well as external magnet topologies. End-effects are again neglected, which reduces the model to only half of the tooth together with half of the slot opening. Every model has two different heat sources, the average copper losses of half the slot opening, $P_{cu/2}$ and the iron losses per half slot $P_{fe/2}$. The calculation of the iron losses is discussed in Chapter 4.

For periodic axisymmetric structures, the main heat flux is always directed radially outwards. This results in a negative temperature gradient in the radial direction. Furthermore, beyond the smallest inner radius where heat generation occurs, the temperature is constant at smaller radii. For the IMT topology, all the heat generation is in the stator (neglecting magnet losses). Therefore, the temperature in the translator back-iron, PM array and airgap is homogenous.

As a result, the model only has to include the temperature variation in the stator. The thermal equivalent circuit for the internal magnet topologies is shown in Fig. 3.24(a). In case of EMT, the heat flux has to travel through the translator and therefore has to be included as shown in Fig. 3.24(b). The various thermal resistances, copper loss per coil and iron losses per half a tooth can be calculated as

$$\mathcal{R}_{c1} = \frac{|\ln(R_{cc}/R_t)|}{2\pi k_c \tau_w}, \quad \mathcal{R}_{fe1} = \frac{|\ln(R_{cc}/R_t)|}{\pi k_{fe}(\tau_t - \tau_s)}, \quad (3.39)$$

$$\mathcal{R}_{c2} = \frac{\tau_w}{2\pi k_c |R_c^2 - R_t^2|}, \quad \mathcal{R}_{fe2} = \frac{\tau_t - \tau_s}{4\pi k_{fe} |R_c^2 - R_t^2|}, \quad (3.40)$$

$$\mathcal{R}_{c3} = \frac{|\ln(R_c/R_{cc})|}{2\pi k_c \tau_w}, \quad \mathcal{R}_{fe3} = \frac{|\ln(R_c/R_{cc})|}{\pi k_{fe}(\tau_t - \tau_s)}, \quad (3.41)$$

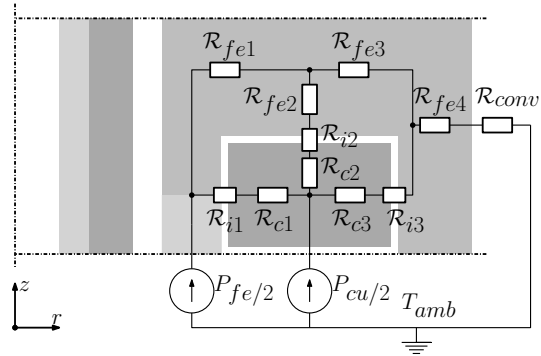
$$\mathcal{R}_{i1} = \frac{|\ln((R_t + w_{ins})/R_t)|}{2\pi k_{ins} \tau_w}, \quad \mathcal{R}_{fe4} = \frac{|\ln(R_s/R_c)|}{\pi k_{fe} \tau_t}, \quad (3.42)$$

$$\mathcal{R}_{i2} = \frac{w_{ins}}{\pi k_{ins} |R_c^2 - R_t^2|}, \quad \mathcal{R}_{conv} = \frac{1}{h\pi R_{out} \tau_t}, \quad (3.43)$$

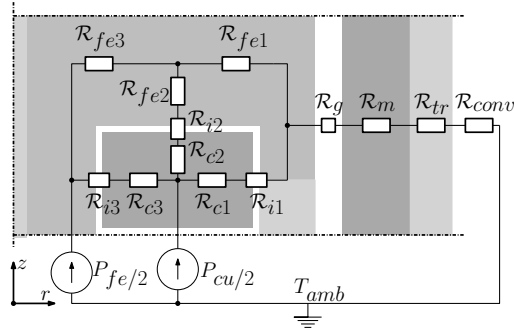
$$\mathcal{R}_{i3} = \frac{|\ln(R_c/(R_c - w_{ins}))|}{2\pi k_{ins} \tau_w}, \quad \mathcal{R}_g = \frac{\ln(R_m/R_i)}{\pi k_g \tau_t}, \quad (3.44)$$

$$\mathcal{R}_m = \frac{\ln(R_r/R_m)}{\pi k_m \tau_t}, \quad \mathcal{R}_{tr} = \frac{\ln(R_b/R_r)}{\pi k_{tr} \tau_t}, \quad (3.45)$$

where $R_{cc} = (R_t + R_c)/2$ is the center coil radius and R_{out} is the outer radius which is R_s for IMT and R_b for EMT. For both IMT and EMT, these circuits can be simplified to the one shown in Fig. 3.25 where the parameters for IMT and EMT are listed in Table 3.3. This circuit has four unknown temperatures, hence



(a)



(b)

Figure 3.24: Thermal equivalent circuit for (a) IMT and (b) EMT.

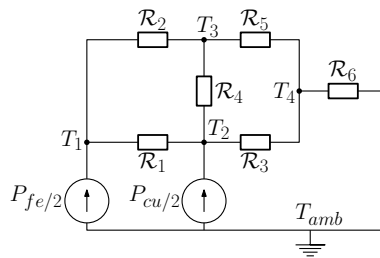


Figure 3.25: Simplified thermal equivalent circuit for both IMT and EMT.

Table 3.3: Parameters of the TEC model for IMT and EMT

Parameter	IMT	EMT
$P_{cu/2}$	$\frac{P_{cu}}{2N_{pa}S}$	$\frac{P_{cu}}{2(N_{pa} + N_{px})S}$
$P_{fe/2}$	$\frac{P_{fe}}{2N_{pa}S}$	$\frac{P_{fe}}{2(N_{pa} + N_{px})S}$
\mathcal{R}_1	$\mathcal{R}_{i1} + \mathcal{R}_{c1}$	$\mathcal{R}_{i3} + \mathcal{R}_{c3}$
\mathcal{R}_2	\mathcal{R}_{fe1}	\mathcal{R}_{fe3}
\mathcal{R}_3	$\mathcal{R}_{i3} + \mathcal{R}_{c3}$	$\mathcal{R}_{i1} + \mathcal{R}_{c1}$
\mathcal{R}_4	$\mathcal{R}_{i2} + \mathcal{R}_{c2} + \mathcal{R}_{fe2}$	$\mathcal{R}_{i2} + \mathcal{R}_{c2} + \mathcal{R}_{fe2}$
\mathcal{R}_5	\mathcal{R}_{fe3}	\mathcal{R}_{fe1}
\mathcal{R}_6	$\mathcal{R}_{fe4} + \mathcal{R}_{conv}$	$\mathcal{R}_g + \mathcal{R}_m + \mathcal{R}_{tr} + \mathcal{R}_{conv}$

the four node equations can be written as

$$P_{fe/2} + \frac{T_3 - T_1}{\mathcal{R}_2} + \frac{T_2 - T_1}{\mathcal{R}_1} = 0, \quad (3.46)$$

$$P_{cu/2} + \frac{T_3 - T_2}{\mathcal{R}_4} + \frac{T_1 - T_2}{\mathcal{R}_1} + \frac{T_4 - T_2}{\mathcal{R}_3} = 0, \quad (3.47)$$

$$\frac{T_1 - T_3}{\mathcal{R}_2} + \frac{T_2 - T_3}{\mathcal{R}_4} + \frac{T_4 - T_3}{\mathcal{R}_5} = 0, \quad (3.48)$$

$$\frac{T_3 - T_4}{\mathcal{R}_5} + \frac{T_2 - T_4}{\mathcal{R}_3} + \frac{T_{amb} - T_4}{\mathcal{R}_6} = 0. \quad (3.49)$$

Finally, the resulting coil and magnet temperature can be obtained from the nodal temperatures as

$$T_c = T_2, \quad (3.50)$$

$$T_m = \begin{cases} T_1, & \text{for IMT,} \\ (T_2 - T_{amb}) \left(1 - \frac{\mathcal{R}_g}{\mathcal{R}_6}\right) + T_{amb}, & \text{for EMT.} \end{cases} \quad (3.51)$$

The TEC model is iteratively solved. Each iteration updates the conductivity of the copper according to the coil temperature after which the copper losses are recalculated and the TEC model updates the coil temperature. The iteration loop ends when conversion of the coil temperature is reached. This model is verified with periodic FEA using the parameters shown in Table 3.4, performing the same assumptions as the analytical model. The FEA however, does not update the copper losses as a function of the coil temperature, hence the final copper losses calculated by the analytical TEC model are used in the finite element modeling.

Table 3.4: Parameters of the thermal model.

Symbol	Value	Unit
k_m	12	W/mK
k_{fe}	30	W/mK
k_{tr} Rad.	30	W/mK
k_{tr} Halb./Axi.	235	W/mK
k_g	0.1	W/mK
k_{ins}	0.1	W/mK
k_{cu}	401	W/mK
k_c	$k_f k_{ins} / (k_f k_{ins} + (1 - k_f) k_{cu})$	W/mK
T_{amb}	40	°C
h	30	W/m ² K
$P_{fe/2}$	1	W

Table 3.5: Calculated copper loss per coil, coil and magnet temperatures for each benchmark topology.

Topology	$P_{cu/2}$	T_c (°C) (analytical/FEA)	T_m (°C) (analytical/FEA)
1	4.07	133 / 124	110 / 109
2	1.19	118 / 113	87 / 86
3	2.91	107 / 97	83 / 82

3.9 Summary and conclusions

The generic semi-analytical modeling technique based on harmonic modeling of Chapter 2 is applied to slotted TPMA. With this technique, the slot openings and slots of the stator are included and the associated fringing fields can be modeled accurately. Prior art considered the effect of slotting in TPMA only by means of a Carter coefficient or current sheet modeling which does not provide the required accuracy of the force ripples.

Various translator configurations, radial, quasi-Halbach or axial magnetization are considered. Both internal magnet topologies (IMT) as well as external magnet topologies (EMT) with any winding configuration can be modeled. Although the semi-analytical model allows for modeling of slot wedges, the slot width is considered equal to the slot opening for simplification and stability improvement of the semi-analytical model. Furthermore, a combined current density is considered in each slot.

Since the semi-analytical model does not incorporate the soft-magnetic regions (stator teeth, back-iron, translator and pole pieces), the flux density within these regions is estimated in order to predict saturation of the soft-magnetic material. The field solution surrounding the soft-magnetic material is integrated to estimate the average flux density inside the soft-magnetic material.

The induced emf waveforms are calculated from the estimated flux density in the teeth, hereby neglecting slot leakage. The calculated emf waveforms include the harmonic effect due to the slotted stator. For the calculation of the synchronous inductance, the slot leakage has to be included due to its significance. The inductance calculation includes the dependency of relative position for axial magnetization to predict the direct and quadrature inductance components. The force profile including the electromagnetic, reluctance and cogging component is accurately predicted using the Maxwell stress tensor method in both shape and amplitude. This method gives a relatively simple expression for the force within a very short computational time. Finally, the copper losses are calculated together with a thermal equivalent circuit in order to determine the worst-case coil and magnet temperature.

This total framework provides a tool for the design and analysis of TPMA within a short computational time. This allows automated design and optimization for various topologies and configurations. The analysis is verified with FEA with a good accuracy for three benchmark topologies covering the broad spectra of possible configurations.

Chapter 4

Integrated electromagnetic passive damping

“Eddy current damping, utilizing dissipated energy.”

This chapter considers the integration and enhancement of the eddy current damping phenomenon in tubular permanent magnet actuators. In general, this effect is minimized for high speed and servo applications since the damping force is undesired and leads to high losses. However, for the application considered in this thesis, this damping force is desired for a fail-safe functioning which is more extensively discussed in Chapter 5. Since this application is a more low-speed application, these eddy current losses are not dominant, but a given damping ratio is desired. The TPMA already exhibits a certain damping due to the use of soft-magnetic material within the stator, however this is generally insufficient and this chapter describes a method for enhancement and tuning of the damping ratio without significantly influencing the actuator performance, volume and mass.

The contribution of this chapter is published in:

Gysen, B. L. J., Paulides, J. J. H., Lomonova, E. A., Encica, L. and van Leeuwen, B. G. [2009], ‘Electromagnetic actuator with integrated passive damper’, WIPO Patent Application WO/2010/136049.

Gysen, B. L. J., Paulides, J. J. H. and Lomonova, E. A. [2011*a*], ‘Direct-drive electromagnetic active suspension system with integrated eddy current damping for automotive applications’, *Mechatronics* (submitted).

Gysen, B. L. J., Paulides, J. J. H. and Lomonova, E. A. [2011*b*], Direct-drive electromagnetic active suspension system with integrated eddy current damping for automotive applications, *in* ‘The 8th International Symposium on Linear Drives for Industry Applications, LDIA 2011’, Eindhoven, The Netherlands, pp. 1–4.

Gysen, B. L. J., Paulides, J. J. H. and Lomonova, E. A. [2011*b*], Dynamic analysis and optimization of tubular eddy current dampers, *in* ‘IEEE International Magnetics Conference, Intermag 2011’, Taipei, Taiwan, pp. 1–2.

4.1 Electromagnetic damping

Electromagnetic passive damping within the TPMA is obtained from phenomena like induction or eddy currents and hysteresis. A variation of the magnetic field distribution due to the moving translator leads to losses within the stator, hereby dissipating a portion of the kinetic energy and providing a certain amount of damping. Each phenomenon has a different dependency on the frequency and amplitude of the magnetic field. Separation of losses is generally applied since each term can be physically explained and determined, although they are not completely independent of each other [12]. The total amount of iron losses is generally written as the sum of hysteresis, classical (eddy current) and excess losses

$$P_{fe} = P_h + P_e + P_x. \quad (4.1)$$

The following sections describe these phenomenon and the type of damping that can be achieved.

4.1.1 Hysteresis

Ferromagnetic hysteresis exists in all magnetic materials. Those materials consist of magnetic domains having a certain magnetization in a particular direction. Due to an externally applied magnetic field H_a , these domains tend to align with this external field. When the applied magnetic field increases, more domains align until all of them are in parallel and magnetic saturation is obtained, see Fig. 4.1. Reducing the applied field to zero does not result in the original arrangement of the domains and a net alignment or magnetization is still present, M_0 . Reversing the applied field up to the coercivity, H_c , decreases this net alignment to zero. This process can be continued until the so called hysteresis loop of the magnetic material is obtained. Reversing the magnetic domain walls requires a certain amount of energy which is quantified by the area of the particular hysteresis loop, Fig. 4.1.

Considering the TPMA, the applied field within the soft-magnetic stator changes as a result of the moving magnet array. In case the amplitude of these movements is larger than 360 electrical degrees, the magnetic field within the stator covers the whole hysteresis loop or major loop. For smaller amplitudes, one should consider the minor hysteresis loops as indicated in Fig. 4.1. In any case, a certain amount of energy is necessary to alter the magnetic flux within the stator and this amount of energy is converted from the available kinetic energy which moves the magnet array. When the magnet array moves at a constant velocity v , the magnetic field fluctuates with fundamental frequency $f = \frac{v}{2\tau_p}$. The associated losses are then

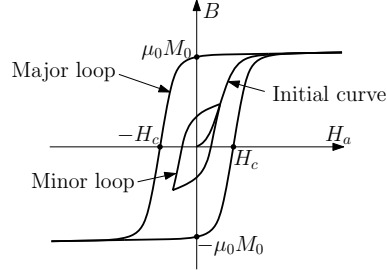


Figure 4.1: Typical hysteresis curve of ferromagnetic material with initial curve, major and minor loop [12].

given by [12]

$$P_h = f \int_V \oint_{\text{loop}} H_a dB dV, \quad (4.2)$$

$$\cong C_0 M f, \quad (4.3)$$

where V is the volume and M the mass of the soft-magnetic material. Note that the considered loop is dependent on the location within the volume V . The approximated formula with constant C_0 , in J/kg, is generally provided in the data sheet of the material for various values of the amplitude of the magnetic field, under the assumption that the magnetic field is homogenous within the material. These losses are equal to the extracted kinetic power which can be written as

$$P_h = F_h v, \quad (4.4)$$

hence, the hysteresis effect can be regarded as a macroscopic static force written as

$$F_h = \frac{1}{2\tau_p} \int_V \oint_{\text{loop}} H_a dB dV, \quad (4.5)$$

$$\cong \frac{C_0 M}{2\tau_p}. \quad (4.6)$$

Although this force is velocity independent, it is always in the opposite direction of the velocity and functions as a damping force.

4.1.2 Eddy currents

Eddy currents are induced by a relative change of the magnetic field linked by a conductive material. Considering the TPMA, this change in magnetic field results from movement of the permanent magnet array with respect to the stator. This change in magnetic field induces an electrical field in the stator according to Faraday's law given by

$$\nabla \times \vec{E} = -\frac{\partial \vec{B}}{\partial t}, \quad (4.7)$$

which for the axisymmetric coordinate system can be written as

$$\frac{1}{r} \frac{\partial r E_\theta}{\partial r} - \frac{\partial E_\theta}{\partial z} = -\left(\frac{\partial B_r}{\partial t} + \frac{\partial B_z}{\partial t} \right), \quad (4.8)$$

hence, the induced electrical field only has a component in the angular direction. This electrical field in turn causes a current density to flow in the conductive materials in the stator, so called 'eddy currents' or 'Foucault currents',

$$J_e = \sigma E_\theta. \quad (4.9)$$

These eddy currents in turn generate a magnetic field which is opposing the field that caused the eddy currents, hence these currents generate a force opposing the relative movement. This induced electrical field is linear dependent on the speed as well as the induced eddy currents. The force produced by the eddy currents is linear dependent on the speed and in the opposite direction, hence a damping force is generated. The eddy current density together with the finite conductivity of the material gives rise to Joule losses, hence the kinetic energy is converted into heat. These losses can be written as

$$P_e = \int_V \frac{J_e^2}{\sigma} dV, \quad (4.10)$$

$$\cong C_1 M f^2. \quad (4.11)$$

In this case, the constant C_1 in the approximated formula depends on the square of the magnetic field and is dependent on lamination thickness. Again, the amount of energy is equal to the amount of converted kinetic energy, hence the damping force due to these induced eddy currents can be written as

$$F_d = \frac{1}{v} \int_V \frac{J_e^2}{\sigma} dV, \quad (4.12)$$

$$\cong \frac{C_1 M}{4\tau_p^2} v. \quad (4.13)$$

At relatively low velocities, the eddy currents are linear dependent on the velocity, hence the damping force is linear dependent on the velocity. However, if the speed increases beyond a certain critical point, the field produced by the eddy currents in turn becomes more dominant. This effect reduces the impregnation of the fields within the material and causes the eddy currents to flow on the skin, hence the name skin effect. This increases the impedance of the material and reduces the amount of damping at higher velocities. Therefore, from an electromagnetic point of view, the damping force F_d is generally regressive.

4.1.3 Excess loss

Excess loss results from the existence of domain walls. A domain wall jump causes local induced eddy currents which lead to the previously described hysteresis loss. However, a domain wall jump increases the probability of a jump of another domain wall in its vicinity [12]. Hysteresis loss does not take this effect into account and considers domain walls to be independent. However in reality correlation occurs resulting in an additional loss term which empirically has the dependency

$$P_x \propto (B_{max}f)^{3/2}, \quad (4.14)$$

$$\cong C_2 M f^{3/2}, \quad (4.15)$$

resulting in a damping force approximated by

$$F_x \cong \frac{C_2 M}{2\tau_p} \sqrt{v}. \quad (4.16)$$

4.1.4 Solid steel versus laminations

The importance of the previously described damping phenomena is the independence on power electronics or software, hence this effect is inherently apparent, providing a fail-safe property to the system. However, hysteresis, eddy currents and excess loss give quantitatively different damping forces and different dependencies on the velocity. Depending on the application and the desired damping characteristic, these three phenomena can be combined to achieve the proper behavior. However, it should be noted that none of these phenomena provides a progressive damping characteristic in terms of the velocity. Generally, a linear damping characteristic is desired and in that case, the hysteresis loss as well as the excess loss have to be minimized with respect to the classical loss or eddy currents. Additionally, the eddy current damping is only linear up to a certain velocity as was described in 4.1.2.

In order to increase the amount of eddy current loss with respect to the hysteresis and excess loss, one can consider the use of solid steel instead of laminations. Ad-

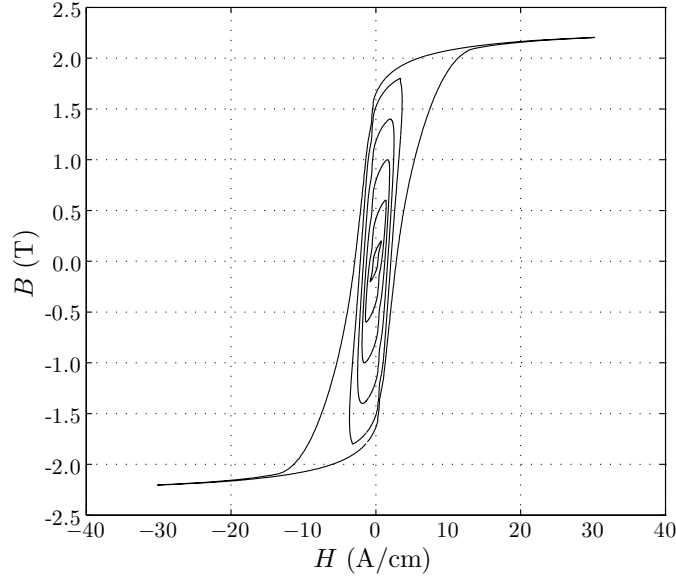


Figure 4.2: Measured hysteresis curve of solid cobalt iron (VACOFLUX50) including major and minor loops at $f = 1$ Hz.

ditionally, using steel with a higher magnetic saturation flux density furthermore increases the obtained eddy current damping. The magnetic material properties of a ring core of cobalt iron (VACOFLUX50 with optimal magnetic properties from Vacuumschmelze [148]) with a cross section of 10 mm by 10 mm and an inner radius of 15 mm are measured. The measurement is performed with an electrical steel tester MPG 200D of Brockhaus Measurements [18] with an accuracy of 0.1 %. The measured hysteresis curve at 0.1 Hz of cobalt iron is shown in Fig. 4.2 where a saturation flux density of 2.2 T is observed.

To indicate the effect of using solid steel rather than laminations, the iron losses are measured on the same setup and compared with measurements on 0.35 mm laminations provided by the manufacturer [148]. The total measured iron losses together with the fitted hysteresis, classical and excess losses for a maximum flux density of $B_{max} = 1$ T and $B_{max} = 2$ T are shown in Fig.4.3(a) and (b), respectively. It can be observed that the classical loss component is significantly larger than the hysteresis and excess loss component, especially for $B_{max} = 2$ T. The loss coefficients C_0 , C_1 and C_2 fitted on the measurement for solid steel together with the loss coefficients for laminated steel (0.35 mm) provided in the data sheet are shown in Table 4.1. It is observed that the classical loss and excess loss for a $B_{max} = 2$ T are increased by a factor 350 and 150, respectively. Similar conclusions were drawn in [119]. In case a close to linear damping characteristic is desired, the eddy current effect should be maximized, hence the use of solid steel is preferred. Additionally, this has an advantage in terms of cost and manufacturing complexity since for tubular actuators the laminations should be radially directed.

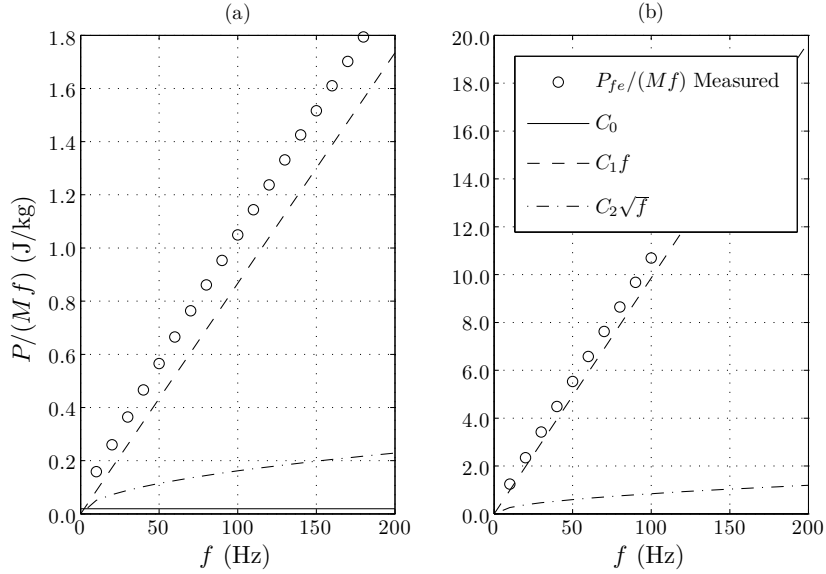


Figure 4.3: Measured iron losses on a solid cobalt iron sample at together with the fitted hysteresis, classical and excess loss component for (a) $B_{max} = 1$ T and (b) $B_{max} = 2$ T.

Table 4.1: Loss coefficients for laminated and solid cobalt iron.

	B_{max}	C_0	C_1	C_2
Laminated (0.35 mm)	1 T	$17.1e^{-3}$	$5.05e^{-5}$	$9.38e^{-5}$
Solid (ring core)	1 T	$19.1e^{-3}$	$8.7e^{-3}$	$16.2e^{-3}$
Laminated (0.35 mm)	2 T	$35.1e^{-3}$	$2.76e^{-4}$	$5.72e^{-4}$
Solid (ring core)	2 T	$147e^{-3}$	$98.6e^{-3}$	$84.3e^{-3}$

4.2 Enhancing damping using conductive materials

Considering the fact that passive damping is desirable, solid steel can be used as mentioned in the previous section. The amount of damping force generated by means of iron losses might not be sufficient to obtain a specified fail-safe damper characteristic. Furthermore, it is desirable to be able to enhance and tune the damping force without significantly altering the actuator design. This could be achieved by adding conductive material in the structure. In order to obtain an efficient damping effect from these conductive materials, they should be positioned in order to link a fast changing B-field of sufficient magnitude. Furthermore, they

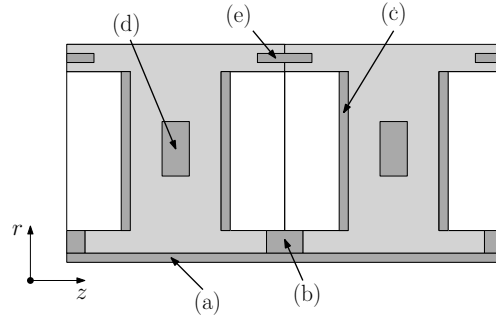


Figure 4.4: Methods of enhancing the eddy current damping.

should be positioned on the stator side, since the translator is the primary source of the changing B-field. Several ways of obtaining additional damping might be considered, see Fig. 4.4,

- (a) a conductive layer on the stator bore,
- (b) conductive rings positioned within the slot tip openings,
- (c) conductive discs or layers positioned within the slot opening, next to the coils,
- (d) conductive rings positioned inside the stator teeth,
- (e) conductive rings positioned inside the stator back-iron.

To quantify the effect of these options on the obtained damping force, a finite element analysis for each of the options is performed at a velocity of 1 m/s for benchmark topology 1. The soft-magnetic material is chosen to be cobalt-iron (CoFe) which provides a better performance due to the improved saturation magnetization of around 2.2 T. Additionally its conductivity is 12 % higher than that of traditional steel (steel 1010), offering more damping. First, the damping due to the soft-magnetic material is calculated. Consequently, each of the options shown in Fig. 4.4 are applied such that the cross section area of the conductive material is kept equal for each of the options. Copper is chosen in this case for the conductive material and the steady state damping per meter length as a function of the relative displacement is shown in Fig. 4.5.

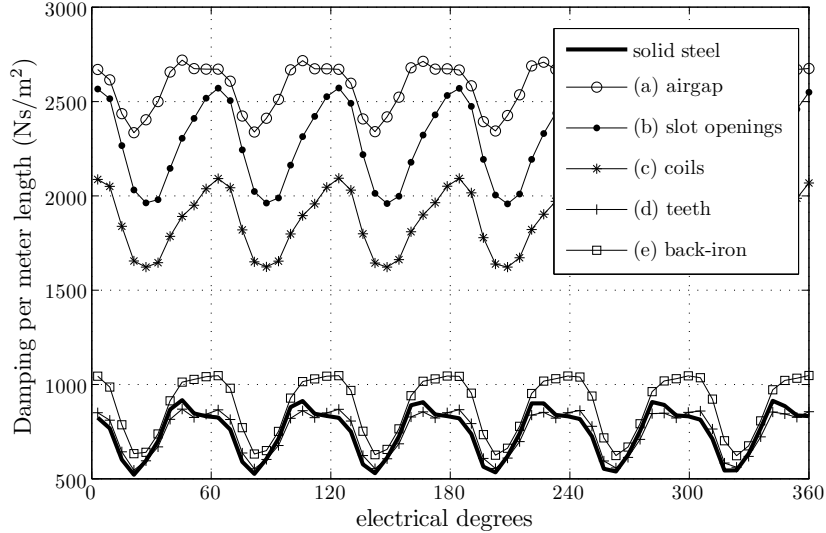


Figure 4.5: Damping force per meter length for each of the enhancement configurations for benchmark topology 1.

4.2.1 Conductive layer on the stator bore

Option (a) is the most effective method, increasing the total average damping by a factor 3.4. It can be manufactured by coating the stator with a conductive layer, hence can be favorable from a manufacturing point of view. However, it results in a larger airgap length g (0.375 mm was used in the simulation), which significantly reduces the performance of the TPMA. A certain minimum airgap length is necessary for a mechanical (sliding) bearing and therefore, only in the case this conductive material can perform as a sliding bearing or be integrated within the bearing, it would not significantly decrease the performance of the TPMA.

4.2.2 Conductive rings in the slot openings

The second most effective method is option (b), inserting conductive rings within the slot openings. As for option (a), the permanent magnet flux is completely linked by these rings, increasing the amount of damping by a factor 3 for this case, however a higher ripple is observed. This is due to the geometric distribution of the rings compared to a continuous layer in the case of option (a). It should be noted that for this calculation no optimization in terms of shape is performed and the ripple might be reduced. Since the rings are inserted in the slot opening, they occupy an unused space and therefore, have less influence on the actuators performance compared to option (a).

4.2.3 Conductive discs in the slots

A third effective method is option (c), inserting conductive discs within the slots increasing the damping by a factor 2.5. They have a similar flux linkage as the coils themselves, which however is less than the rings in the slot opening or the coating in the airgap. It is easy to manufacture these discs and even a coating could be considered as for option (a). However, this option results in a less effective coil area and again decreases the performance of the TPMA.

4.2.4 Conductive rings within the stator teeth

This option is the least effective method, in this case it even does not provide any additional damping. Although the rings are situated within the highest flux density point, no flux is linked by these rings. The radial flux does not pass through the ring and the axial flux closes within the ring itself leading to an almost zero net flux linkage. The slight increase in damping is counteracted by the fact that the effective tooth area is decreased which lowers the magnetic flux in the airgap. Furthermore, this option is not favorable from a manufacturing point of view since the stator teeth have to be produced in two halves instead of a single tooth.

4.2.5 Conductive rings within the stator back-iron

Inserting rings in the stator back iron is only slightly better than option (d). Again very little flux is linked, only the part of flux passing over the ring inside the stator back-iron. Although the disadvantage in manufacturing of option (d) is not apparent, it causes a major decrease in the cross section area of the back-iron, leading to saturation and decreased performance of the TPMA.

Considering the aforementioned options and their related advantages and disadvantages, option (b) is chosen to be the most favorable regarding the ability to increase the amount of damping without decreasing the amount of space available for the TPMA, thereby influencing the obtained performance, [66].

4.3 Prediction of the enhanced damping constant

4.3.1 Dynamic modeling techniques

To predict the damping characteristic of the integrated conductors, an electromagnetic model is necessary. Although the advantage of an analytical model over

FEA is already stated in previous chapters, for the calculation of the damping characteristic, the advantage is even greater. To obtain the full damping characteristic, a transient simulation at each velocity has to be performed. Furthermore each transient eddy current simulation needs a finite amount of time steps to converge to the correct steady state value. This significantly increases the total computation time and makes the use of an analytical model of greater importance.

The dynamic solution of eddy current problems has been discussed in the literature for simple geometric problems where the most fundamental approach is the direct solution of the Maxwell equations which leads to the diffusion equation in terms of the magnetic vector potential in case the displacement current is neglected,

$$\nabla^2 \vec{A} - \mu\sigma \frac{d\vec{A}}{dt} = 0. \quad (4.17)$$

The solution can be obtained using separation of variables and Fourier analysis. This method is extensively described in [142] for various simple geometries in different coordinate systems. For example for rotating couplers with single- or double-sided permanent magnet frames [22]. Furthermore, this method is used to calculate the damping effect due to a conductive vacuum chamber wall in the airgap of a moving-magnet linear actuator [82]. A tubular eddy current damper consisting of a quasi-Halbach array and a conductive tube has been modeled using this method in [65].

Complex geometries require more assumptions and therefore, in most cases, the skin effect or reaction field due to the eddy currents is neglected which holds for thin conductors at low velocities or frequencies. The flux density due to the field source (PM or electromagnet) is described in an analytical manner. The induced voltage within the conductor is derived which results in the eddy current distribution. The damping force is then calculated using the Lorentz force method using the analytical source field description and the eddy currents [41, 137]. This method is also used for the design of an electromagnetic shock absorber using a permanent magnet array and a conductive tube. The quasi-Halbach configuration proved to give the best performance which was experimentally verified with a scaled down prototype [43].

To include the effect of the reaction field due to the eddy currents for more complex geometries, a different approach is possible. The force velocity characteristic of an eddy current damper is the inverse of the characteristic of an induction machine and can be characterized by an electrical pole, ω_p , defined by the resistance, R_r , and inductance, L_r , of the eddy current carrying conductors

$$\omega_p = \frac{R_r}{L_r}. \quad (4.18)$$

The dynamic damping characteristic can be determined with the initial damping, d_0 , and electrical pole which both can be determined using magnetostatic

modeling techniques

$$d_r(\omega) = \frac{d_0}{1 + j\frac{\omega}{\omega_p}}. \quad (4.19)$$

This method is for example applied for torsional dampers and couplers in [146], however the electrical pole was not determined in an analytical manner. In [5], this method was applied using Fourier analysis for a torsional damper.

To model the eddy current damping due to the proposed damper rings in a TPMA, the direct solution of the diffusion equation is preferred since it offers the best accuracy. However for a slotted actuator, the damping due to the moving magnet array cannot be calculated by solving the diffusion equation in the conductive regions directly. To explain this problem, consider the actuator moving with constant velocity v , resulting in a relative displacement $\Delta_z = vt$. The diffusion equation (4.17) can be rewritten into

$$\nabla^2 \vec{A} - \mu\sigma v \frac{d\vec{A}}{d\Delta_z} = 0, \quad (4.20)$$

which involves the derivative of the magnetic vector potential towards relative displacement. Using separation of variables and Fourier analysis, the solution to the diffusion equation using separation of variables for the axisymmetric coordinate system is given by [65]

$$\vec{A} = \sum_{n=1}^{\infty} g_r(r, n) g_z(z, n) g_t(t, n) \vec{e}_\theta, \quad (4.21)$$

with

$$g_r(r, n) = a_n \mathcal{I}_1\left(r\sqrt{w_n^2 + jvw_n\sigma\mu_0}\right) + b_n \mathcal{K}_1\left(r\sqrt{w_n^2 + jvw_n\sigma\mu_0}\right), \quad (4.22)$$

$$g_z(z, n) = e^{jw_n z}, \quad (4.23)$$

$$g_t(t, n) = e^{jw_n vt}, \quad (4.24)$$

for j the complex number and with a_n and b_n constants determined by the boundary conditions. However, given the boundary value problem discussed in Chapter 2, where the permanent magnet array has a relative position with respect to the slots Δ_z , the list of boundary conditions and the resulting solution of the coefficients, a_n and b_n , is dependent on Δ_z . Therefore, considering a given velocity, these coefficients are dependent on time as well and the solution given in equation (4.21) cannot be applied. The generalized modeling technique can therefore only be used in case the position of the sources does not change with respect to the non-periodic regions, [115], or in problems where only periodic regions are considered, [22, 65, 82].

Therefore, the modeling approach based on determination of the electrical pole is considered in this thesis. This method enables the reuse of the magnetostatic

model presented in Chapters 2 and 3. The conductive rings are considered as a complex impedance, Z_r , given by

$$Z_r = R_r + j\omega L_r, \quad (4.25)$$

with R_r the dc resistance and L_r the synchronous inductance (including self and mutual inductance of adjacent rings). The self-inductance accounts for the reaction field caused by the eddy currents which leads to the current flowing at the skin of the conductor (skin effect) and the mutual inductance represents the effect of neighboring conductors, referred as the proximity effect. The frequency is determined by the velocity and pole pitch of the permanent magnet array and therefore, given by

$$\omega = \frac{v\pi}{\tau_p}. \quad (4.26)$$

Since the rings are considered as a complex impedance, the eddy current density at a particular point in time is considered constant over the whole area of the ring. Hence, the skin and proximity effect are included in the form of a reduced overall eddy current rather than a change in the current density distribution. This assumption is valid when the width of the ring is relatively small with respect to the pole pitch, $\tau_o \ll \tau_p$, which is generally the case. By means of calculating the flux linkage in each ring as a function of the displacement, Δ_z , the induced voltage can be obtained. This flux linkage can be obtained from the field solution proposed in Chapter 2. Given the induced voltage and complex impedance, the eddy currents can be calculated. From the solution of the eddy currents in each ring, the total dissipated power, resulting damping force and damping ratio as a function of the velocity are obtained. This method is discussed in [146] for torsional eddy current dampers and couplers, however this thesis extends the analysis for slotted tubular actuators. Furthermore, the analysis is not restricted to a sinusoidal flux linkage, multi-phase conductors (more than two) are considered as well as a semi-analytical expression for the inductance of the damping rings.

4.3.2 Induced flux linkage in the conductive rings

This section describes the method to calculate the induced eddy currents in each ring positioned in the slot opening. The model presented in Chapters 2 and 3 is used for the analysis. This model is a magnetostatic model, however, under certain conditions, this model can be used to predict the induced eddy currents. Within one periodic section of the TPMA, the number of rings is equal to the number of slots S . The ring does not necessarily have to occupy the full space of the slot opening. Hence, the ring has its own dimension as shown in Fig. 4.6 assuming that the ring is positioned centrally in the slot opening with respect to the z -direction. Due to the variation in the magnetic field distribution when the permanent magnet array is moving at a velocity v , an electric field is induced

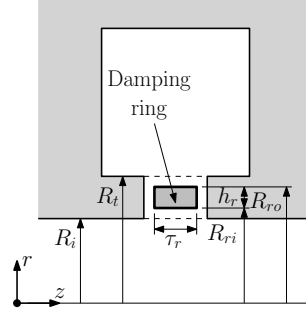


Figure 4.6: Sizes of the damping rings in the slot openings of the TPMA.

in the stator, equation (4.7). Introducing the magnetic vector potential again as $\vec{B} = \nabla \times \vec{A}$ and substituting gives

$$\nabla \times \left(\vec{E} - \frac{\partial \vec{A}}{\partial t} \right) = 0, \quad (4.27)$$

$$\Downarrow$$

$$\vec{E} = -\frac{\partial \vec{A}}{\partial t} - \nabla \varphi, \quad (4.28)$$

where the term $-\nabla \varphi$ represents the accumulation in charge, which is assumed zero in this situation. The term $-\frac{\partial \vec{A}}{\partial t}$ represents the magnetic field due to the moving magnet array. Since the magnetic vector potential has only a component in the angular direction $\vec{A} = A_\theta \vec{e}_\theta$, the electric field is only directed in the angular direction, $\vec{E} = E_\theta \vec{e}_\theta$. The expression of the magnetic vector potential in the slot opening, region $IV\nu$ for $\nu = 1 \dots S$, as derived in the generic semi-analytical method is used (equations. (2.25), (2.51), (2.52) and (2.53)). No sine terms are apparent since the region is bounded by soft-magnetic material in the tangential direction ($A_{\theta sn}^{IV\nu} = 0$). Furthermore, the function $\mathcal{G}_{psn}^{IV\nu}$ is zero since no permanent magnets or external current sources are apparent in the slot opening. For the same reason, the constants $B_0^{IV\nu}$ and $J_{i0}^{IV\nu}$ are zero, simplifying the expression of the magnetic vector potential to

$$A_\theta^{IV\nu}(r, z, \Delta z) = \sum_{n=1}^{\infty} \frac{1}{w_n^{IV\nu}} \left(a_n^{IV\nu} \mathcal{I}_1(w_n^{IV\nu} r) + b_n^{IV\nu} \mathcal{K}_1(w_n^{IV\nu} r) \right) \cos(w_n^{IV\nu} z_{IV\nu}) + \frac{A_0^{IV\nu}}{r}. \quad (4.29)$$

The coefficients $a_n^{IV\nu}$, $b_n^{IV\nu}$ are determined considering the solution of the boundary condition matrix, as presented in Appendix B.1, B.2 and B.3, for radial, quasi-Halbach and axial magnetization, respectively. The constants $A_0^{IV\nu}$ results from the continuity of the magnetic vector potential between the airgap and slot

opening regions and its calculation is described in Appendix B.4. Note that the calculation of these coefficients and constants has to be performed at each relative displacement, Δ_z . The flux linkage in ring ν due to the permanent magnet array can now be obtained as

$$\Lambda_{r\nu,pm}(\Delta_z) = \frac{2\pi}{\tau_r(R_{ro} - R_{ri})} \int_{R_{ri}}^{R_{ro}} \int_{(\tau_o - \tau_r)/2}^{(\tau_o + \tau_r)/2} A_{\theta}^{IV\nu}(r, z, \Delta_z) r dr dz_{IV\nu}, \quad (4.30)$$

which simplifies to

$$\Lambda_{r\nu,pm}(\Delta_z) = 2\pi A_0^{IV\nu}(\Delta_z), \quad (4.31)$$

if the rings are situated in the center of the slot opening. Considering the actuator moving at a velocity $v = \Delta_z/t$ and using Fourier analysis and Euler's formula, the induced flux linkage can be written as a sum of complex exponentials given by

$$\Lambda_{r\nu,pm}(t) = \Re \left\{ \sum_{n=1}^N \Lambda_{r\nu,pm} e^{j \frac{n\pi v}{\tau_p} t} \right\}, \quad (4.32)$$

with $\frac{\pi v}{\tau_p}$ the fundamental angular frequency and the complex amplitude $\Lambda_{\nu n,pm}(n)$ given by

$$\Lambda_{r\nu,pm}(n) = \frac{v}{\tau_p} \int_0^{\frac{2\tau_p}{v}} \Lambda_{r\nu,pm}(\Delta_z) e^{-j \frac{n\pi v}{\tau_p} t} dt. \quad (4.33)$$

Only positive n have to be included since $\Lambda_{r\nu,pm}(t)$ is a real function. The flux linkage in the first ring is calculated for each benchmark topology as a function of the relative displacement and shown in Fig. 4.7 together with the FEA. It can be observed that a very good agreement is obtained for each topology, the only discrepancy is due to saturation of the soft-magnetic material.

4.3.3 Impedance of the conductive rings

The complex impedance of the damper rings within one periodic section is defined by the dc resistance and the synchronous inductance. The dc resistance can be calculated in a straightforward manner,

$$R_{\nu} = \frac{\pi(R_{ro} + R_{ri})}{\sigma_r \tau_r |R_{ro} - R_{ri}|}, \quad (4.34)$$

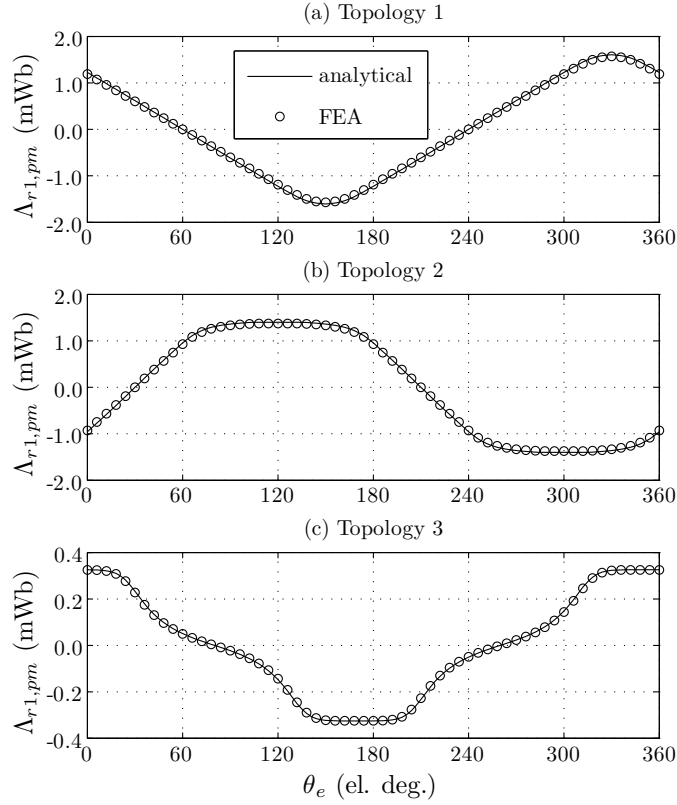


Figure 4.7: Flux linkage in damping ring 1 (region IV_1 , see Fig. 3.8) due to the permanent magnets as a function of the relative position verified with FEA for each of the benchmark topologies listed in Table 3.2.

with σ_r the conductivity of the material used for the damper rings.

In order to derive the synchronous inductance of the damper rings, the distribution of the eddy currents within the different rings has to be considered. When modeling a 2D periodic section of a rotational or linear damper each eddy current should have their return path within the periodic section, hence the sum of the total eddy currents is always zero. However, for a tubular damper, the return path of each eddy current is inherently set due to the axisymmetry. Therefore, within one periodic section it is possible that the sum of all eddy currents in each damper ring is not equal to zero.

However, considering the generic modeling method together with the assumption of modeling only a single periodic section, the sum of currents within one periodic section should always equal zero. Otherwise, a net flux exists in the tangential direction, which in reality closes via the ends of the actuator, but in the case of a periodic model, the return path of the flux is undefined. Therefore, the sum of

eddy currents is assumed to be zero for calculation of the synchronous inductance of the rings. The waveform of the eddy current in each ring ring is identical with a phase shift of $\frac{180P}{S}$ degrees. Therefore, the current distribution among the rings $\nu = 1 \dots S$ for calculation of this single inductance is defined as

$$i_{r\nu} = i_r \cos\left(\frac{(\nu - 1)P\pi}{S}\right) \text{ for } \nu = 1 \dots S. \quad (4.35)$$

for a certain amplitude i_r . The current density in the rings, region IV_ν , is therefore given by

$$J_{l0}^{IV\nu} = \frac{i_{r\nu}}{\tau_o h_r}. \quad (4.36)$$

For the calculation of the ring inductance, the generic semi-analytical model presented in Chapter 2 and 3 is used. However, the permanent magnets are considered to have zero remanence ($B_{rem} = 0$) and the armature reaction is zero ($J_{l0}^{V\nu} = 0$). The only sources within the model are the current densities within the slot openings, regions IV_ν . The same boundary conditions are applied and the field distribution is solved. The expression of the magnetic vector potential within regions IV_ν is given by equations (2.25), (2.51), (2.52) and (2.53). Again, no sine terms are apparent since the region is bounded by soft-magnetic material in the tangential direction ($A_{l_{sn}}^{IV\nu} = 0$). Since the applied current density is constant over the whole slot opening, the source description only has a dc component, hence the function $\mathcal{G}_{psn}^{IV\nu}$ is zero. The constants $B_0^{IV\nu}$ should however be included since there is a dc current density in the slot opening. The expression of the magnetic vector potential is now

$$\begin{aligned} A_\theta^{IV\nu}(r, z, \Delta_z) &= \sum_{n=1}^{\infty} \frac{1}{w_n^{IV\nu}} \left(a_n^{IV\nu} \mathcal{I}_1(w_n^{IV\nu} r) + b_n^{IV\nu} \mathcal{K}_1(w_n^{IV\nu} r) \right) \cos(w_n^{IV\nu} z_{IV\nu}) \\ &- \mu J_{l0}^{IV\nu} \frac{r^2}{3} + B_0^{IV\nu} \frac{r}{2} + \frac{A_0^{IV\nu}}{r}. \end{aligned} \quad (4.37)$$

The coefficients $a_n^{IV\nu}$, $b_n^{IV\nu}$ and constants $B_0^{IV\nu}$ are again solved considering the solution of the set of boundary conditions as described in Appendix B.1, B.2 and B.3, for radial, quasi-Halbach and axial magnetization, respectively. Again, the constants $A_0^{IV\nu}$ are solved by applying the continuity of the magnetic vector potential between the airgap and slot openings, see Appendix B.4. The flux linkage in each ring due to its own current is obtained using equation (4.30) which in this case simplifies to

$$\begin{aligned} \Lambda_{r\nu,i}(i_\nu, \Delta_z) &= 2\pi \left(A_0^{IV\nu}(\Delta_z) + \frac{B_0^{IV\nu}(\Delta_z)}{3} (R_{ri}^2 + R_{ri}R_{ro} + R_{ro}^2) \right. \\ &\quad \left. - \frac{\mu_0 J_{l0}^{IV\nu}}{6} (R_{ri} + R_{ro})(R_{ri}^2 + R_{ro}^2) \right). \end{aligned} \quad (4.38)$$

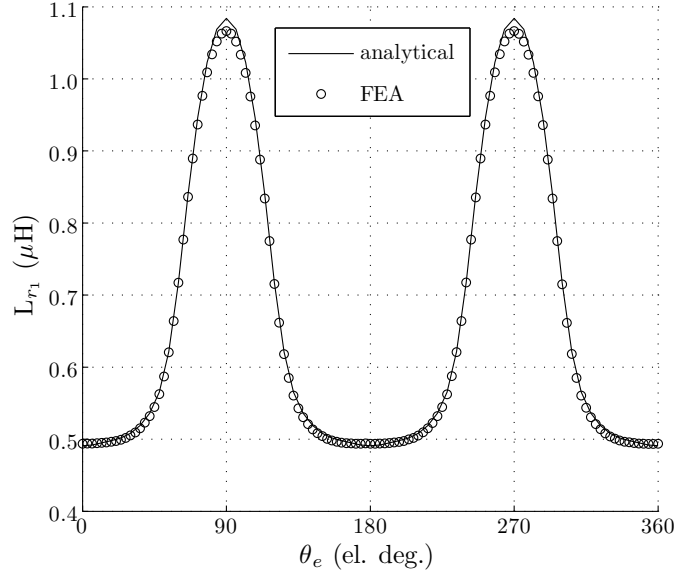


Figure 4.8: Inductance of damping ring 1 (region IV_1 , see Fig. 3.8) as a function of the relative position verified with FEA for topology 2 listed in Table 3.2.

From the expression of the flux linkage, the synchronous ring inductance can be obtained using

$$L_{r\nu}(\Delta_z) = \frac{\Lambda_{r\nu,i}(\Delta_z)}{i_{r\nu}}, \quad (4.39)$$

which results in the same inductance for every ring ν . For radial and quasi-Halbach magnetization, this inductance is independent of the relative displacement. However, considering axial magnetization, this inductance varies with Δ_z due to the soft-magnetic pole-pieces as shown in Fig. 4.8 verified with FEA with a very good agreement. The maximum inductance is obtained when the pole pieces are aligned with the ring, which is at 90 electrical degrees for this topology. Since the induced flux linkage due to the permanent magnets is maximum at the d-axis and the resulting eddy currents at the q-axis, the chosen inductance for the rings is the q-inductance component. Since the inductance is assumed independent of Δ_z and equal for every ring, the notation L_r is used from hereon.

4.3.4 Eddy currents in the conductive rings

Using the derived flux linkage in the rings and the ring impedance, the differential equation governing the eddy currents in each ring, $i_{e\nu}(t)$, can be written as (considering generating regime)

$$\frac{d\Lambda_{r\nu}(i_{e\nu}, t)}{dt} + R_r i_{e\nu}(t) = 0. \quad (4.40)$$

The total flux linkage in the rings is the sum of the flux linkage due to the permanent magnets and due to the induced eddy currents hence

$$\frac{d\Lambda_{r\nu,pm}(t)}{dt} + \frac{d\Lambda_{r\nu,i}(i_{e\nu}, \Delta_z)}{dt} + R_r i_{e\nu}(t) = 0, \quad (4.41)$$

$$\Downarrow$$

$$L_r(\Delta_z) \frac{di_{e\nu}}{dt} + i_{e\nu}(t)v \frac{dL_r}{d\Delta_z} + R_r i_{e\nu}(t) = -\frac{d\Lambda_{r\nu,pm}(t)}{dt}. \quad (4.42)$$

In order to simplify the analysis, the assumption is made that $\frac{dL_r}{d\Delta_z} = 0$ as was described in previous section which is valid for radial and quasi-Halbach magnetization however it introduces an error for axial magnetization topologies. The resulting differential equation is given by

$$L_r \frac{di_{e\nu}(t)}{dt} + R_r i_{e\nu}(t) = -\frac{d\Lambda_{r\nu}(t)}{dt}. \quad (4.43)$$

Since the flux linkage is written as a sum of complex exponentials, equation (4.32), the solution of the differential equation takes a similar form

$$i_{e\nu}(t) = \Re \left\{ \sum_{n=1}^N i_{e\nu n} e^{j \frac{n\pi v}{\tau_p} t} \right\}, \quad (4.44)$$

for complex amplitude $i_{e\nu n}$. Solving the differential equation gives for the complex amplitude of the eddy currents

$$i_{e\nu n} = -\frac{j \frac{n\pi v}{\tau_p} \Lambda_{r\nu n}}{R_r - j \frac{n\pi v}{\tau_p} L_r}, \quad (4.45)$$

which can be rewritten into

$$i_{e\nu n} = -\frac{j n \pi \Lambda_{r\nu n}}{\tau_p R_r} \frac{v}{1 - j \frac{v}{v_{cn}}}, \quad (4.46)$$

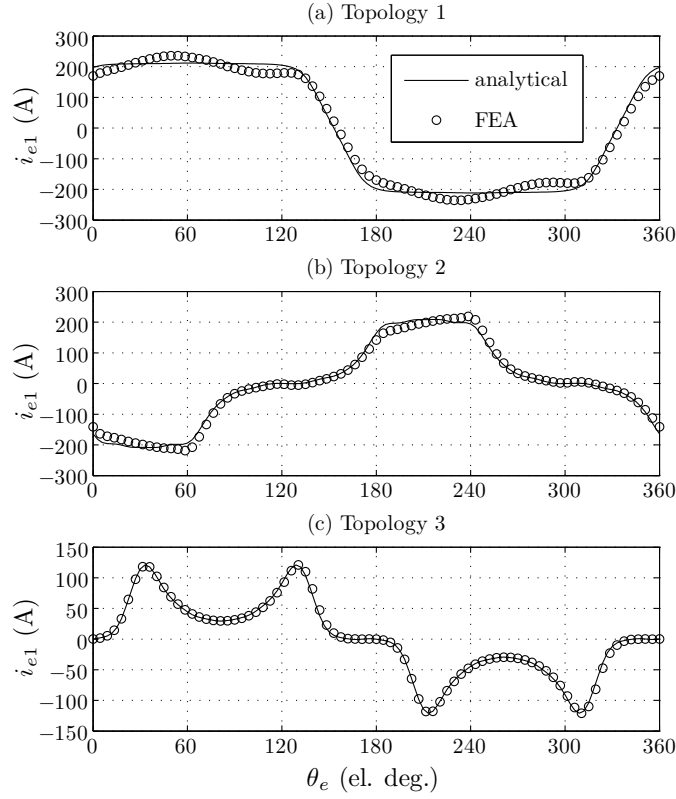


Figure 4.9: Eddy current in damping ring 1 (region IV_1 , see Fig. 3.8) as a function of the relative position at $v = 1$ m/s verified with FEA for each of the benchmark topologies listed in Table 3.2.

with the critical velocity of every harmonic given by

$$v_{cn} = \frac{\tau_p R_r}{n\pi L_r}. \quad (4.47)$$

The induced eddy currents are calculated for benchmark topology 1 at a velocity of $v = 1$ m/s using aluminum rings and verified with FEA as shown in Fig. 4.9(a). An additional oscillation can clearly be seen in the eddy currents of the FEA solution for benchmark topology 1 which is not apparent in the analytical solution. This is due to the assumption of that the sum of currents is equal to zero in the calculation of the synchronous inductance of the rings. The error in Fig. 4.9(b) of benchmark topology 2 has besides the previous mentioned assumption also the dependency of the inductance on relative displacement which is not included in the derivation of the eddy currents. This assumption is only valid when the sum of currents is zero. For benchmark topology 3, the sum of the currents is closer to zero, hence the determination of the eddy currents is much better as observed in Fig. 4.9(c).

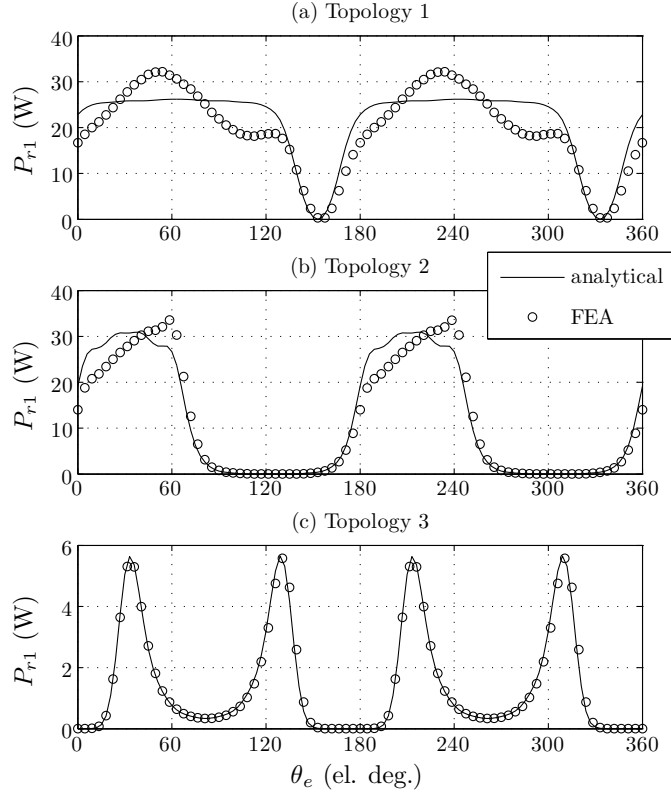


Figure 4.10: Power in damping ring 1 (region IV_1 , see Fig. 3.8) as a function of the relative position at $v = 1$ m/s verified with FEA for each of the benchmark topologies listed in Table 3.2.

4.3.5 Dissipated power, damping force and constant

Damping means dissipating energy, in this case the mechanical energy from the vibrations is converted into heat. The dissipated power in each of the rings, $P_{rv}(t)$, can be deduced from the eddy currents

$$P_{rv}(t) = i_{ev}(t)^2 R_r = \omega^2 R_r \sum_{n=1}^N n^2 \operatorname{Re} \left\{ \frac{j \Lambda_{rvn}}{R_r - j n \omega L_r} e^{jn\omega t} \right\}^2, \quad (4.48)$$

which is verified with FEA in Fig. 4.10 where the discrepancies have the same cause as in the derivation of the eddy currents. However, this error is now of greater influence due to the quadratical dependency on the eddy current. The average power in each ring, $\langle P_r \rangle$, which is equal for every ring within the active length of the actuator, is obtained by integrating the power over one electrical

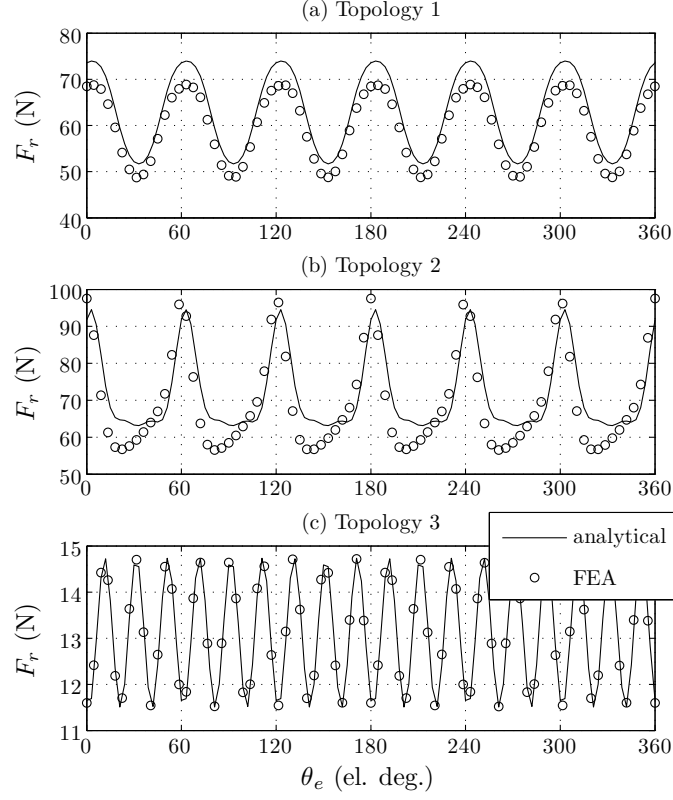


Figure 4.11: Damping force as a function of the relative position at $v = 1$ m/s verified with FEA for each of the benchmark topologies listed in Table 3.2.

period hence

$$\langle P_r \rangle = \frac{\omega}{2\pi} \int_0^{2\pi} P_{r\nu}(t) dt = \frac{\omega^2 R_r}{2} \sum_{n=1}^N \frac{n^2 |\Lambda_{rn}|^2}{R_r^2 + n^2 \omega^2 L_r^2}, \quad (4.49)$$

where $\Lambda_{r\nu n}$ is replaced by Λ_{rn} since the absolute value of the flux linkage for each harmonic is equal for each ring. All the mechanical energy is dissipated in the rings and the damping force can be related to the dissipated power as

$$F_r(t) = \frac{N_{pa}}{v} \sum_{\nu=1}^S P_{r\nu}(t), \quad (4.50)$$

$$= \frac{N_{pa} \omega^2 R_r}{v} \sum_{\nu=1}^S \sum_{n=1}^N n^2 \operatorname{Re} \left\{ \frac{j \Lambda_{r\nu n}}{R_r - j n \omega L_r} e^{jn\omega t} \right\}^2, \quad (4.51)$$

which is shown in Fig. 4.11 and verified with FEA. It can be observed that although a large error appears in the prediction of the dissipated power, the prediction of the force is still accurate. This is due to the fact that the error, in the power of each ring separately, is canceled out due to the relative displacement of the rings. The average damping force as a function of velocity or the damping characteristic due to the conductive rings is given by

$$\langle F_r \rangle = \frac{\omega}{2\pi} \int_0^{\frac{2\pi}{\omega}} P_{rv}(t) dt = \frac{\omega^2 R_r}{2} \sum_{n=1}^N \frac{n^2 |\Lambda_{rn}|^2}{R_r^2 + n^2 \omega^2 L_r^2}, \quad (4.52)$$

which is shown in Fig 4.12(a)-(c) for each of the benchmark topologies together with the FEA verification up to a velocity of $v = 30$ m/s. A good agreement is obtained for topologies 1 and 3, however for topology 2, which is the axial magnetized topology, the electrical pole considered with the analytical model is higher than the FEA prediction. This is due to the assumption of a constant synchronous inductance, L_r , since, for axial magnetization, it is dependent on the relative position. However, for relatively low velocities, a very good agreement is obtained. Furthermore, it should be noted that for the benchmark topology 3 using quasi-Halbach magnetization, a more linear damping can be obtained because the electrical pole is larger due to a lower ring inductance compared to the topologies using radial or axial magnetization. This conclusion can be drawn regardless of the chosen geometrical sizes. The average damping as a function of velocity is obtained from the average total power and can be written as

$$\langle d_r \rangle(v) = \frac{N_{pa} S}{v^2} \langle P_{rv} \rangle = \frac{N_{pa} S \pi^2 R_r}{2} \sum_{n=1}^N \frac{n^2 |\Lambda_{rn}|^2}{\tau_p^2 R_r^2 + n^2 \pi^2 v^2 L_r^2}. \quad (4.53)$$

For small velocities, only resistive damping is apparent and hence the initial damping is described as

$$\langle d_{r0} \rangle = \frac{N_{pa} S \pi^2}{2 \tau_p^2 R_r} \sum_{n=1}^N n^2 |\Lambda_{rn}|^2. \quad (4.54)$$

4.4 Influence on the actuator performance

Although the integration of eddy current damping by means of inserting conductive rings in the slot tips has the least influence on the initial design of the actuator, an influence on the performance is inevitable. This section identifies and quantifies this influence. As a result of the moving permanent magnet array,

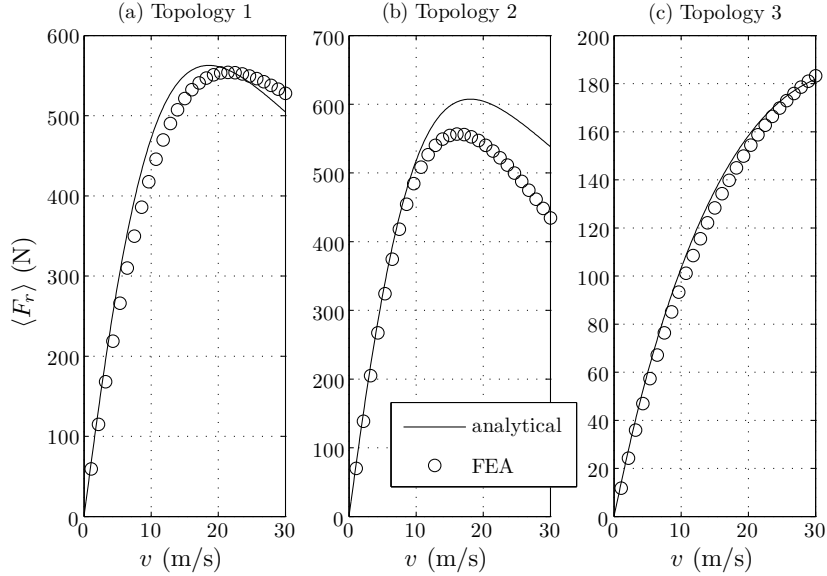


Figure 4.12: Average damping force due to the conductive rings as a function of the velocity for each benchmark topology verified with FEA.

eddy currents are induced in the conductive rings and the ferromagnetic stator. These eddy currents are directed such that they counteract their cause and hence cause an overall reduction and delay or phase shift in the produced magnetic field of the permanent magnet array. This has an effect on the induced electromotive force (emf) of the stator windings as well. Since the eddy currents reduce the field of the permanent magnet array, the induced emf waveform is lower. Hence, depending on the velocity, the emf constant is lower compared to the emf constant at zero velocity. Furthermore, because the eddy currents prevent the build up of magnetic field, the emf has a phase shift which is again dependent on the velocity.

These effects are quantified for each benchmark topology using FEA. In order to be able to quantify the effect due to the conductive rings and ferromagnetic stator separately, three situations for each benchmark topology are considered. First, only the rings are conductive. Second, only the soft-magnetic material is conductive and third, both the rings and soft-magnetic material are considered conductive. The simulations are performed at various speeds from 0 to 2 m/s. In Fig. 4.13(a)-(c), these emf waveforms normalized on the velocity are shown for each benchmark topology for the situation that eddy currents are induced in both the conductive rings and the soft-magnetic material. The phase shift as well as a slight amplitude variation can be observed, however this effect is quantitatively different for each topology.

From the calculated emf waveform, the amplitude of the fundamental harmonic and its phase shift are derived which are related to the emf waveform without any eddy current effect. Figures 4.14(a), (c) and (e) show the reduction in the

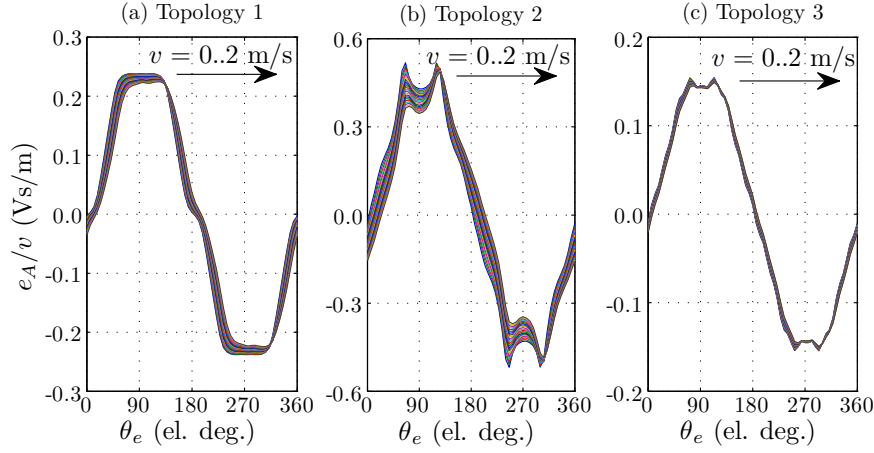


Figure 4.13: The emf waveforms at various velocities normalized to the velocity including the eddy current effect in the rings and soft-magnetic material.

fundamental emf harmonic with respect to the fundamental emf harmonic without any eddy current effect for each of the benchmark topologies. The resulting phase shift for each of the benchmark topologies is shown in Figs. 4.14(b), (d) and (f). Three situations are considered, the case when only eddy currents in the rings are induced (circles), the case only eddy currents in the soft-magnetic material are induced (crosses) and the case eddy currents are induced in both the rings and the soft-magnetic material (squares).

The reduction in the fundamental emf harmonic per velocity in percentage is a measure for the reduction in actuator force. Regarding the effect due to the rings, a relatively small reduction in the fundamental emf harmonic is observed, the reduction due to the soft-magnetic material is far more significant for each topology. Benchmark topology 3 has a far less overall reduction (2.5 %) than benchmark topology 2 (12 %), however, the amount of damping force is also lower as observed in Fig. 4.12. Regarding the phase shift, the rings and soft-magnetic material have almost a similar effect, where for relatively low velocities, this phase shift is approximately linear with the velocity. The phase shift indicates that the supplied commutated currents need to have the same phase shift in order to obtain the maximum output force. If no phase shift correction is applied, the reduction in actuator force is even lower. Hence the commutated current of phase A as described in equation (3.25) is now written as

$$i_{ph,A}(\Delta_z, v) = I_{\text{RMS}}\sqrt{2} \cos\left(\frac{\pi\Delta_z}{\tau_p} + \varphi_c + K_{ph,v}v\right), \quad (4.55)$$

where $K_{ph,v}$ is the phase deviation per speed in radians second per meter, which can be approximated using the simulation shown in Figs. 4.14(b), (d) and (f).

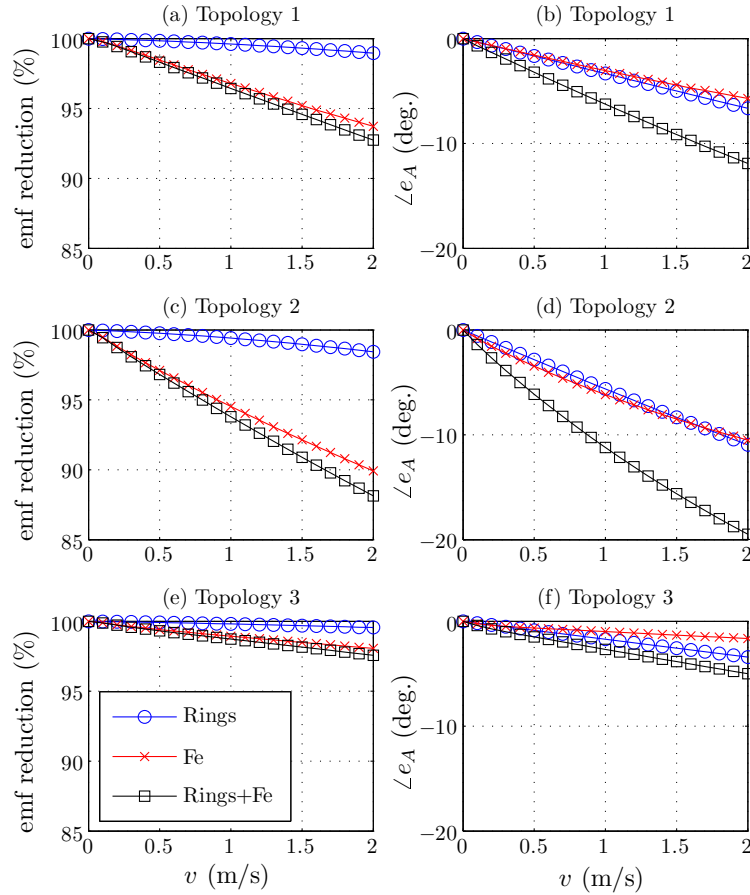


Figure 4.14: Reduction in fundamental emf waveform and phase shift as a result of the eddy currents in either damping rings (Rings) or soft-magnetic material (Fe) or both (Rings+Fe).

Phase B and C are again shifted by 120 and -120 degrees, respectively. Since the reduction in fundamental harmonic is significantly lower for the case eddy currents in the rings are considered, it is beneficial to obtain as much as damping from the eddy current rings. It might even better to consider laminations in the stator teeth and enhance the eddy current effect due to the rings by proper design. However, this complicates construction and leads to increased costs.

4.5 Summary and conclusions

This chapter considered the integration of electromagnetic damping within a tubular permanent magnet actuator. This passive form of damping provides a fail-safe functioning for the active suspension system considered in Part II of the thesis. Each of the three loss phenomena, hysteresis, eddy currents and excess losses provide damping. Based upon measurements, the use of solid soft-magnetic material improves the amount of eddy current losses and excess losses by a factor 350 and 150, respectively.

To obtain a more linear damping characteristic, alternative methods of enhancing the eddy current damping are investigated. The inclusion of conductive rings within the slot openings is considered to be the most appropriate since it improves the passive damping by a factor two to three. Additionally, because the rings occupy an unused space within the TPMA, the additional damping is obtained without concession of the original design. This invention has been patented in [66].

A modeling technique to calculate the dynamic damping characteristic due to these rings is proposed which applies the framework of Chapter 2 to calculate the electrical pole of the conductive rings. The flux linkage within the rings together with the ring impedance determine the dynamic damping characteristic. The method includes the dependency on position, velocity and material properties and has been published in [64]. The best accuracy of the damping characteristic is obtained for radial and quasi-Halbach magnetization (within 10 %), however, at higher velocities, the solution for axial magnetization becomes inaccurate due to the position dependency of the ring inductance.

The effect on actuator performance is investigated using FEA, where it is concluded that the influence of the eddy currents in the rings is insignificant compared to the effect of the eddy currents in the soft-magnetic material. Hence, the eddy current damping resulting from the rings should be maximized with respect to the damping due to the iron losses to obtain a close to linear damping characteristic.

The second Part of the thesis applies the developed modeling framework of Part I to the design of an electromagnetic active suspension system. This framework allows for automated multi-physical design and optimization of a broad spectra of topologies and configurations within a short computational time.

Part II

Design of a direct-drive active suspension system

Chapter 5

System topology and specifications

“The shortest travel between two points is a straight line. Navigation approximates it horizontally, while the ideal suspension system should provide it vertically.”

This chapter describes the system topology of the direct-drive electromagnetic active suspension system. The benchmark vehicle, for which the active suspension system should be designed, is presented. The characteristics of the passive suspension of the benchmark vehicle are measured and used as a reference for the fail-safe behavior of the developed active suspension system. Consequently, the topology of the direct-drive active suspension system is explained. The chosen actuator technology as well as the integration of the fail-safe electromagnetic passive damping and considered power electronics are presented. A two degrees of freedom quarter car model is introduced together with stochastic road descriptions based on on-road measurements. The set of specifications depends on the required objectives and type of vehicle. Therefore, objectives on a corner level and a resulting set of specifications are derived based upon the quarter car model and on-road measurements. Finally, the sensor set for each vehicle corner is selected together with the total system integration.

The contribution of this chapter is published in:

Gysen, B. L. J., Paulides, J. J. H., Janssen, J. L. G. and Lomonova, E. A. [2010], 'Active electromagnetic suspension system for improved vehicle dynamics', *IEEE Transactions on Vehicular Technology* **59**(3), 1156–1163.

Gysen, B. L. J., Sande, T. P. J. v. d., Paulides, J. J. H. and Lomonova, E. A. [2011], 'Efficiency of a regenerative direct-drive electromagnetic active suspension', *IEEE Transactions on Vehicular Technology* **60**(4), 1384–1393.

5.1 The benchmark vehicle

To present the proof of concept of a direct-drive electromagnetic active suspension system, a prototype is implemented in a benchmark vehicle. This presents the viability of the solution, its effectiveness, since not only the theory, modeling, optimization and design are dealt with, but also the practical implementation giving a clear indication of the overall complexity. Ideally, one would design the complete suspension system all over, however, to be able to present a prototype on short notice, the choice for a retrofit design is inevitable.



Figure 5.1: The benchmark vehicle: a BMW 530i.

The benchmark and test vehicle for the developed electromagnetic active suspension system is the BMW 5-series shown in Fig. 5.1. This German built executive saloon car is well known for its quality in terms of reliability, sportiness and agility. More specifically, a BMW 530i with a three liter inline six cylinder engine is considered which, due to its aluminum engine, has a near to perfect 50.9/49.1 front to rear mass distribution. Furthermore, the complexity of the front suspension system is reduced since it is rear-wheel driven. Some key parameters of the vehicle are listed in Table 5.1.

5.2 The passive suspension system of the benchmark vehicle

The benchmark vehicle has the front MacPherson suspension as explained in Section 1.4.1, shown in Fig. 5.2. This system uses two suspension arms that are connected to the bottom part of the hub and provide lateral and longitudinal fixation of the wheel. The top of the hub is attached to a coilover which consists of a coil spring and a hydraulic damper in parallel, see Fig. 5.3(a) and (b) for the front and rear suspension, respectively. Furthermore, a rebound spring is fitted inside the damper, increasing the spring stiffness for larger rebound.

Table 5.1: Technical data of the BMW 530i.

Parameter	Symbol	Value	Unit
Unloaded vehicle mass	$M_{s,u}$	1546	kg
Maximum vehicle mass	$M_{s,m}$	2065	kg
Unsprung mass front per corner	$M_{u,f}$	48.3	kg
Unsprung mass rear per corner	$M_{u,r}$	44.9	kg
Initial spring stiffness front	k_p	29	kN/m
Average damping front	d_p	1600	Ns/m
Tire vertical stiffness min-max	k_t	310-370	kN/m
Weight distribution front-rear	γ	50.9-49.1	%
Maximum compression (bump)	S_b	60	mm
Maximum extension (rebound)	S_r	80	mm
Track width	T_w	1.56	m

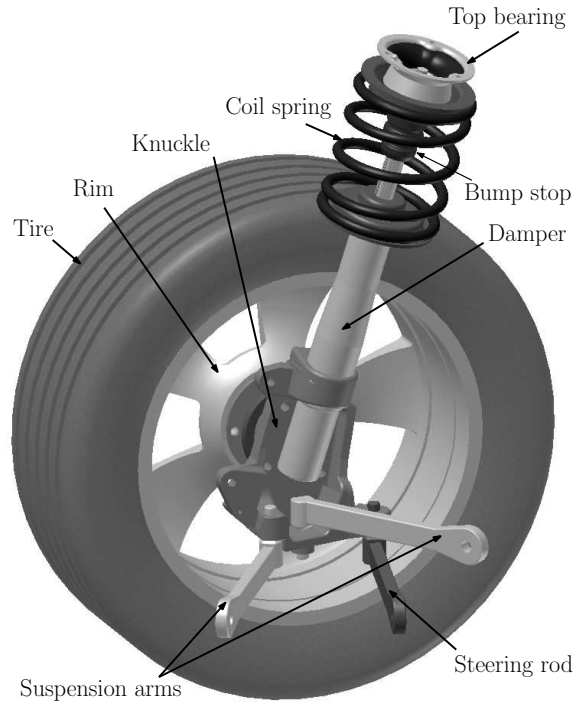


Figure 5.2: MacPherson suspension.

The passive spring and damping characteristic of the front coilover, measured by Janssen [83], are shown in Fig. 5.4(a) and (b), respectively. The effect of the rebound spring is clearly visible from the change in gradient at 25 mm rebound stroke in Fig. 5.4(a). Furthermore, the effect of the bump stop becomes dominant after 25 mm compression stroke. Within the range of ± 25 mm, the spring characteristic is linear with a stiffness of 29 kN/m. The damping characteristic shown in Fig. 5.4(b) is clearly asymmetrical in the bump and rebound region.

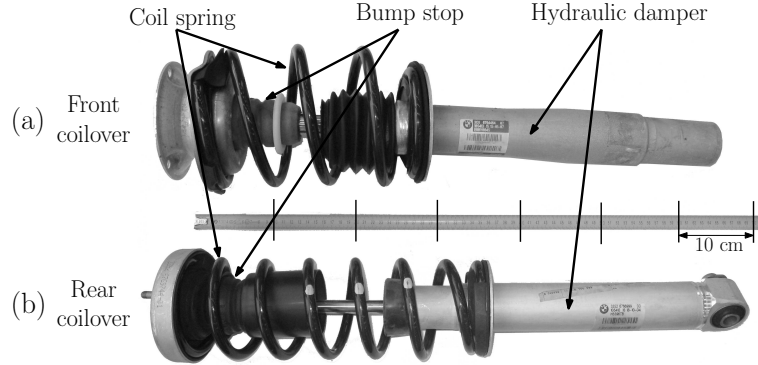


Figure 5.3: (a) Front and (b) rear coilovers of the passive BMW suspension system.

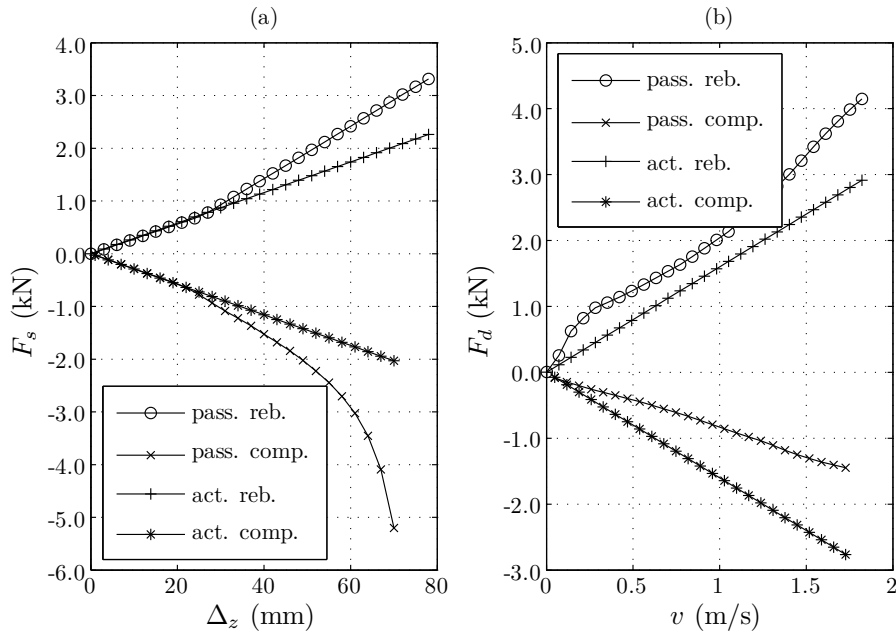


Figure 5.4: Compression and rebound (a) spring and (b) damping characteristic of the front coilover of the passive BMW suspension together with the specified active characteristic.

In compression, as little damping as possible is desired, such that the vehicle is capable of absorbing bumps. Kinematic limitations, however, require a certain amount of damping to limit suspension travel. Generally, more rebound damping is applied to prevent 'abruptness' in the suspension [9].

Tires are generally considered to have non-linear vertical and cornering stiffness. The vertical stiffness is measured for the Dunlop SP Sport 225/50R17 94W tires

of the benchmark vehicle on a flat plank tire tester [13]. These measurements showed that, under nominal operating conditions, the tire stiffness varies between 310-370 kN/m. The parameters of the passive suspension system are summarized in Table 5.1.

5.3 The active suspension system

The developed system is a fast direct-drive electromagnetic active suspension system including fail-safe damping as explained in Section 1.4.4. The topology consists, like the MacPherson strut, of a coil spring to provide levitation of the sprung mass. A direct-drive electromagnetic actuator is placed in parallel converting electrical energy to kinetic energy and provides vertical forces without the need for a gearbox. This process is reversible, hence the kinetic energy can be converted into electrical energy, hereby increasing the total efficiency of the system. Furthermore, passive electromagnetic damping is integrated to make the total system fail-safe. In case a power breakdown occurs, the active suspension behaves as a passive suspension system. The specifications and choices of each of the components are described in the following subsections.

5.3.1 Spring characteristic

The chosen spring stiffness together with the damping characteristic determines the passive behavior of the suspension system. A low or soft spring stiffness is more comfortable whereas a higher stiffness results in a better handling. However, given a certain vehicle mass, a soft spring requires a longer free length and generally more turns. The chosen spring characteristic determines the necessary force the electromagnetic actuator has to provide for a given stroke. Therefore, in the case leveling is required, a softer spring is preferable. However, when leveling is not required, the choice in spring characteristic does not influence the required mechanical energy from the actuator since the spring is not a dissipative element. However, when a low spring stiffness is chosen, the cornering forces for the actuator increase, requiring significant higher copper losses and the total system requires more power consumption. Regarding the fail-safe behavior of the system, the stiffness is chosen to be equal to the stiffness of the current passive suspension system. The only difference is that the stiffness is linear over the full stroke since this simplifies the control of the total active suspension system. Hence the spring stiffness is chosen to be $k_a = 29$ kN/m over the full stroke of the suspension system as shown in Fig. 5.4(a).

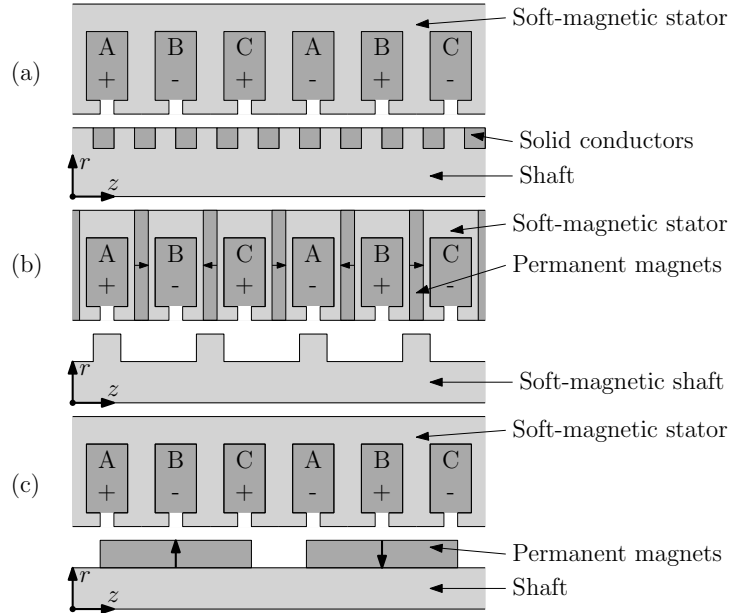


Figure 5.5: Schematic representation of a (a) tubular induction actuator, (b) tubular parallel flux switching actuator and (c) tubular permanent magnet actuator.

5.3.2 Direct-drive actuation

The active force, F_{act} , supplied to each suspension corner, is obtained by means of electromagnetic energy. In order to achieve a high bandwidth, a direct-drive solution is preferred. Considering the volumetric efficient solution of the coilover topology, a tubular actuator together with the coil spring offers an elegant alternative for the electromagnetic actuation. In general, it consists of two distinctive tubes, an outer and an inner one, which move with respect to each other in the axial (z) direction. Due to its cylindrical structure, this technology is more efficient due to the absence of end windings. Furthermore, it has an ideally zero net attraction force between stator and translator, reducing the friction in the bearings.

One of the tubes is considered to be the stator with a multi-phase winding topology and dependent on the type of translator and working principle, several different technologies can be considered:

- tubular induction actuator (TIA), Fig. 5.5(a),
- tubular parallel flux switching actuator (TPFSA), Fig. 5.5(b),
- tubular permanent magnet actuator (TPMA), Fig. 5.5(c).

The TIA suffers from a lower force density compared to the permanent magnet excited topologies, and it is therefore not considered suitable for an active suspension system. In [159], a comparative study is performed between the latter two topologies where it is concluded that the TPMA has the best performance. First of all, the force density of the TPMA is 16 % higher than the TPFSA for equal thermal loading. Additionally, the force ripple of the TPFSA is 1.6 times higher than the TPMA. Finally, the peak force achieved with the TPMA is much higher than the TPFSA since saturation of the soft-magnetic materials has a larger influence on the TPFSA. Since the objective is to obtain a high force density actuator, the TPMA is chosen as technology for the electromagnetic actuation of the active suspension. Specifications of this actuator are given in terms of stroke, maximum speed, continuous force and peak force which are derived later on in this chapter.

5.3.3 Damping characteristic

The development of electromagnetic systems is very progressive and ever more X-by-wire systems appear in passenger cars [19]. However, the introduction of electromagnetic systems in the automotive industry is always hampered due the absence of a fail-safe mode. Hydraulic systems are generally considered to be more fail-safe due to the mechanical and hydraulic link between for example the brake-pedal and brake-pads. Since the suspension system is, next to the brakes, required to be the most fail-safe system of a car, an electromagnetic suspension system should prove to be 100 % fail-safe.

A rather easy way to achieve this is to include a parallel hydraulic damper [45], however, this solution requires additional space and mass and vanishes the advantage of having no toxic fluids. Hence, the solution is preferably obtained from an electromagnetic point of view and integrated into the aforementioned TPMA. The actuator should exhibit the passive damping, d_a , and form a passive suspension system together with the coil spring, k_a , in case of the absence of the active force, F_{act} .

This phenomenon is already applied in several applications such as brakes, couplers and dampers for rotary as well as linear and tubular topologies [5, 41–44, 65, 136, 137, 146]. These systems are interesting for the automotive sector due to the low maintenance, reliability and contactless operation. Although the application for automotive braking systems is not applied yet due to the high system volume and the absence of a braking force up to zero velocity, therefore additional aids have to be applied to stop the vehicle completely [136]. The introduction of passive eddy current dampers in the automotive sector is hampered due to the low damping ratio per volume and costs of rare earth materials. Furthermore, tuning of the damping characteristic is very difficult and impractical. Additionally, the passive damping characteristic is always symmetric in terms of direction. However, in combination with an active element such as the TPMA, the previous two disadvantages vanish due to the ability of altering the characteristic.

The damping characteristic defines the behavior of a damper and is generally referred to as the force versus velocity characteristic. The ratio of force over velocity is the damping ratio which can be position, velocity, direction and even temperature dependent. The most common type of passive damper in the automotive industry is the telescopic hydraulic damper where the damping force is based on the controlled restriction of a fluid (generally oil) or gas (nitrogen) through valves [32]. Various variations on this principle are available but they all work on the same principle. In general, more than one valve is used to obtain a tunable damping characteristic as well as a different damping ratio for compression and rebound. Although comfort is a subjective measure, it is generally considered that a lower damping ratio for compression results in a better comfort since, during bump, the suspension is easier compressed and hence the bump is better 'absorbed'. Obtaining the ideal damping characteristic is more art than science [9], and iterative valve tuning is generally performed to obtain a satisfying performance. In contrast, this thesis proposes the use of an integrated passive electromagnetic damper which is based on the eddy current phenomenon as described in Chapter 4. The total passive damping in the active suspension system, d_a , consists of damping due to the ferromagnetic material, d_{fe} and the conductive rings, d_r . For relatively low velocities and when no saturation occurs one can write

$$d_a = d_{fe} + d_r. \quad (5.1)$$

One key difference is that the damping characteristic of the eddy current damping should be as such to obtain a fail-safe functioning rather than the ideal performance since this is obtained in combination with the active force of the actuator within a certain control strategy. The following sections discuss some aspects of the desired damping characteristic for the common hydraulic damper versus the proposed electromagnetic damper.

Position dependency

A position dependent damping can be desirable to obtain a progressive damping ratio. This provides a 'bump stop' without the bounce effect that rubber bump stops have. In a hydraulic damper, this is obtained by placing the bump valve at the side of the piston. The opening of the orifice is than position dependent since the piston passes the opening during compression. Alternatively, dual piston dampers are applied where the second valve acts after a certain stroke.

Considering the methods of enhancing the eddy current damping, this can be achieved by increasing the cross section of the damper rings towards the ends of the actuator or, in the case of a conductive tube in the airgap, by varying the tube thickness as shown in Fig. 5.6. Furthermore, due to the discrete distribution of the rings and permanent magnets, the induced flux linkage contains higher harmonics and the damping characteristic has a certain ripple as a function of

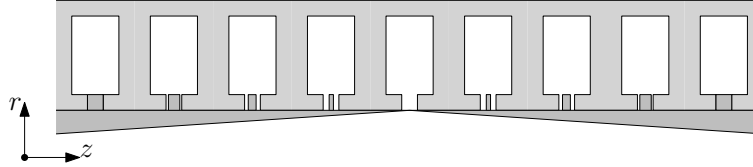


Figure 5.6: Possible configurations of electromagnetic damping with a progressive damping ratio as function of position.

the position. As for the cogging force due to the slotted stator, this ripple reduces for a fractional number of slots per pole. Furthermore, this ripple is lower in the case of a conductive cylinder in the airgap since a more continuous distribution is obtained, however due to the fringing fields at the slot tips, a ripple as function of position still exists. In any case, this ripple has to be minimized since it contributes to resonances and discomfort. It can be compensated by means of control, however, at the expense of a higher energy consumption.

Velocity and direction dependency

The velocity dependency, or the damping characteristic of a general hydraulic damper is depicted schematically in Fig. 5.7(a). Because the characteristic of a single valve is quadratic (the pressure drop across a valve depends quadratically on the flow), a set of two valves (A and B) is necessary for both compression and rebound to achieve a desirable damping characteristic with a hydraulic damper. At low velocities, only valve A is active, and at higher velocities, valve B is opened gradually, leading to the resulting damping characteristic shown in Fig 5.7(a) [32]. Note that the shown force levels are typical values. The benchmark vehicle considered in this thesis has a much higher damping characteristic as observed in Fig. 5.4(b).

Furthermore, a hydraulic damper is designed to have an asymmetric damping characteristic for rebound and compression which is generally a ratio of 2:1 [32]. In order to absorb a bump optimally, one would exclude any compression damping, however this might result in very high suspension travels with the risk of continuously hitting the bump stop. Furthermore, an extremely low compression damping might result in excessive wheel hop, roll and pitch movement [9].

Considering the velocity dependency of electromagnetic damping as derived in Chapter 4, three different regions can be considered as shown in Fig. 5.7(b). At the first region (the low speed region), the magnetic field caused by the eddy currents is significantly lower than the magnetic field due to the permanent magnets. Since this reaction field is low, the eddy currents and the resulting damping force are linearly dependent on the induced flux due to the permanent magnets. This induced flux is again linearly dependent on the velocity. Hence in this region a constant damping is obtained, referred as resistive damping. At higher velocities, around the critical velocity v_c , the induced flux of the reaction field has the same

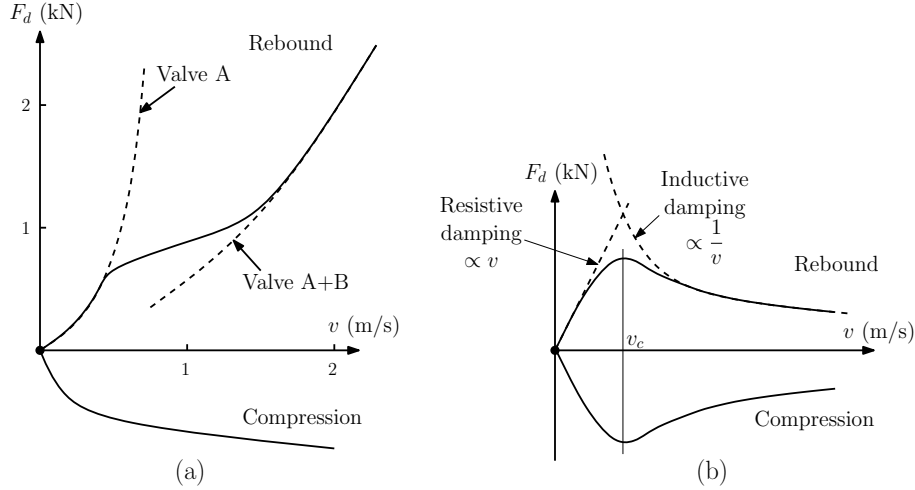


Figure 5.7: (a) Quantitative schematic characteristic of a hydraulic damper and (b) qualitative schematic characteristic of an electromagnetic damper.

order of magnitude as the induced flux due to the moving permanent magnets. This is the region where the maximum damping force is exerted. At even higher velocities, the induced flux of the reaction field is dominant and the phase shift of the eddy currents with respect to the induced flux increases, resulting in a decreasing inductive damping force proportional to $F_d \propto \frac{1}{v}$. Hence, electromagnetic damping is never progressive as in a hydraulic damper. However, since an active suspension system is considered, to facilitate modeling and control, a linear damping is desired and the design of the rings should be such that the critical velocity v_c , is far beyond the maximum operating velocity, around 2 m/s. If similar behavior is required as the passive BMW suspension system, the initial damping should be $d_a = 1600$ Ns/m, as shown in Fig. 5.4(b).

Eddy current damping, as presented in Chapter 4, is directional independent and therefore, the choice of $d_a = 1600$ Ns/m is a trade-off since the rebound damping is decreased and compression damping is increased. The direction dependency is the most difficult, if not impossible, to implement by means of eddy currents. Eddy currents are induced due to a change of magnetic field in a conductor with a certain impedance. Hence, in order to implement direction dependency, the change in magnetic field should differ in inverse direction. Alternatively, the impedance could be directional dependent which is difficult to achieve with passive elements only. Even when the eddy currents are made directional dependent, e.g. by integrating diodes, it does not result in a direction dependency in damping. It only reduces the total damping since the damping force is only generated 50 % of the time. It is still a question if direction dependency is desired in combination with an active element, since again, it complicates modeling and control. However, this could be scope of further research.

Temperature dependency

The damping characteristic of a hydraulic damper is strongly temperature dependent due to the change in fluid properties. The most influential parameters are the density and viscosity resulting in a decreased damping ratio at elevated temperatures. In [3], a decrease of 16.6 % in damping force after five minutes of operation is measured at an initial temperature of 20 °C. However, the final temperature or steady state conditions were not given. In [100], a thermomechanically coupled model for shock absorbers was derived, indicating a decrease of 14.4 % in damping ratio for a temperature change from -20 °C to 100 °C where the steady state temperature was reached after two hours of operation.

As a comparison, the temperature dependency of the enhanced eddy current damping due to the conductive rings, d_r , is investigated. Considering the analytical expression derived for the average initial damping ratio, $\langle d_{r0} \rangle$, in Chapter 4 equation (4.54), the temperature dependency for this electromagnetic damper can be investigated. It originates from the temperature dependency of the remanence of the permanent magnets and the conductivity of the damper rings. The flux linkage due to the permanent magnets linked by the damper rings, Λ_{rn} , is linear dependent on the remanence of the permanent magnets. The temperature dependency of this remanence is generally considered to be linear dependent on the temperature and can be written as

$$B_{rem}(T_m) = B_{rem,20}(1 - \alpha_m T_m), \quad (5.2)$$

where T_m is the temperature of the magnets in degrees Celsius (°C), $B_{rem,20}$ the remanence at $T_m = 20^\circ\text{C}$ and α_m the decrease per degree given by the material properties (e.g. $9.5e^{-4}/^\circ\text{C}$ for neodymium-iron-boron (NdFeB)). Furthermore, the resistance of the damper rings increases with temperature since the conductivity as a function of temperature is given by

$$\sigma_r(T_r) = \sigma_{r,20}(1 - \alpha_r T_r), \quad (5.3)$$

where T_r is the temperature of the damper rings in degrees Celsius (°C), $\sigma_{r,20}$ the conductivity at $T_r = 20^\circ\text{C}$ and α_r the decrease per degree which is $3.9e^{-4}/^\circ\text{C}$ for copper and $4.0e^{-4}/^\circ\text{C}$ for aluminum and hence, is considered equal. Using the expression for the average initial damping and the temperature dependency of the materials, the following expression is found

$$\langle d_{r0} \rangle(T_m, T_r) = \langle d_{r0} \rangle \Big|_{T=20} (1 - \alpha_m T_m)^2 (1 - \alpha_r T_r), \quad (5.4)$$

with $\langle d_{r0} \rangle \Big|_{T=20}$ the initial damping at room temperature. This indicates that the effect on temperature is dominated by the permanent magnet material due to

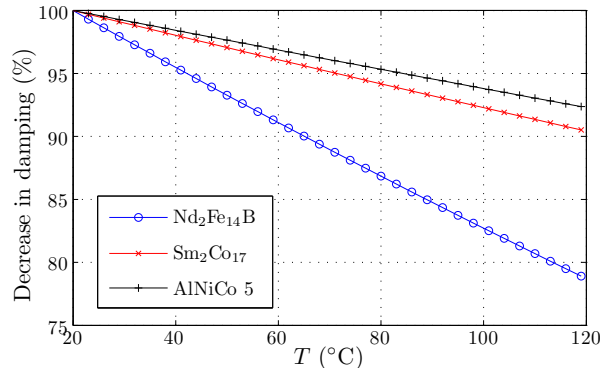


Figure 5.8: Decrease in damping as a function of temperature for various types of magnet alloys together with copper or aluminum rings.

the squared dependency on temperature. Neglecting the difference in temperature between the permanent magnets and damper rings, the percentual difference with respect to the damping at room temperature is plotted in Fig. 5.8. It can be observed that the difference is quite significant, in the order of 20 % between room temperature and maximum operating temperatures. Samarium cobalt and AlNiCo alloys have a lower negative temperature coefficient and hence a less dependency on the temperature for the passive damping, around 10 %. The temperature dependency of electromagnetic shock absorbers can, therefore, be considered in the same order of magnitude as for hydraulic shock absorbers.

5.4 Power electronics

The three phase TPMA is driven by means of a three phase PWM inverter as shown in Fig. 5.9. The dc bus of the amplifier could be connected to the battery of the vehicle. However, considering general ICE vehicles, this voltage is around 12 Vdc which is relatively low to drive a high performance permanent magnet actuator due to the high induced electromotive force (emf) at higher speeds. Even more, high currents have to be drawn resulting into thick cables which would complicate installation and could even increase the sprung mass. Therefore, it is beneficial to have a higher dc bus voltage which is already the case for current commercial hybrid and full electrical vehicles. The design of the actuator is therefore based on a 340 Vdc bus, in which case a commercially available inverter can be used.

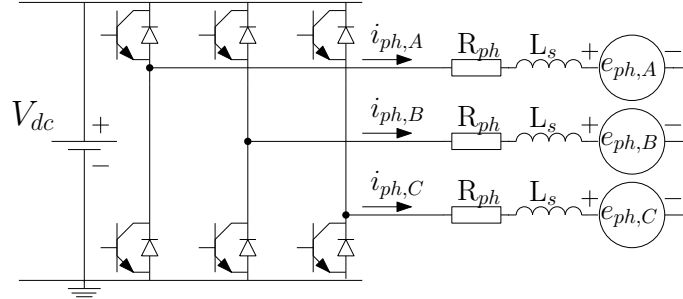


Figure 5.9: Schematic representation of the three phase PWM inverter together with the equivalent circuit of the three phase TPMA.

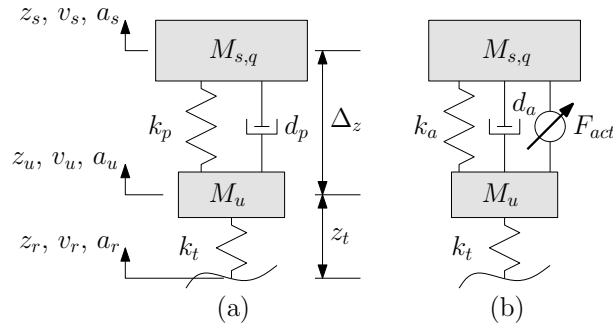


Figure 5.10: Quarter car model of (a) the passive and (b) active suspension system.

5.5 Two degrees of freedom quarter car model

Models to assess the vertical dynamics of a vehicle range from a simple one degree of freedom (DoF) model [77] up to a non-linear large number of DoF model [94]. The two-DoF quarter car model is however the most commonly used due to its simplicity while still providing an accurate description of the vertical dynamics. This thesis is restricted to the performance on a corner level and therefore, this model is considered for the derivation of the specifications and controller design [90, 96]. However, to obtain the full benefit of the active suspension, controller design should be based on a full-car model including vertical as well as horizontal dynamics.

A quarter car model represents one corner of the vehicle for which only the vertical dynamics are considered. Figure 5.10 shows a graphical representation of the quarter car model for (a) the passive BMW suspension and (b) the active suspension system. Here, $M_{s,q}$ is the quarter sprung mass of the vehicle and M_u is the unsprung mass of one corner, which usually consists of the mass of the rim, tire, brake and unsprung part of the suspension. The stiffness and damping of the passive and active suspension are denoted by k_p , k_a , d_p and d_a , respectively.

The vertical tire stiffness is denoted as k_t . Since a rolling tire has an insignificant amount of damping, it is disregarded in the quarter car model. The degrees of freedom are the displacement of the sprung (z_s) and unsprung mass (z_u). The inputs of the model are the road displacement, z_r , and the actuator force, F_{act} . The suspension travel and tire compression are denoted with Δ_z and z_t , respectively. The equations of motion for the active suspension are given by

$$M_{s,q}a_s = -k_a(z_s - z_u) - d_a(v_s - v_u) + F_{act}, \quad (5.5)$$

$$M_u a_u = k_a(z_s - z_u) + d_a(v_s - v_u) - k_t(z_u - z_r) - F_{act}. \quad (5.6)$$

Similar equations hold for the passive suspension by setting $F_{act} = 0$ and replacing k_a with k_p and d_a with d_p . Considering the linear parameters given in Table 5.1 and the quarter sprung mass given by $M_{s,q} = M_{s,u}/4$, the quarter car model can be analyzed in the frequency domain by considering the various transfer functions between the outputs and inputs. The amplitude characteristics of the transfer functions are shown in Fig 5.11. The response of the body acceleration (a measure for comfort) to the road input is shown in Fig. 5.11(a) where two resonances are clearly visible, the body or sprung resonance, f_s , and the wheel hop or unsprung resonance, f_u , which approximately are given by

$$f_s \cong \frac{1}{2\pi} \sqrt{\frac{k_a}{M_{s,q}}}, \quad (5.7)$$

$$f_u \cong \frac{1}{2\pi} \sqrt{\frac{k_t}{M_u}}. \quad (5.8)$$

The frequencies below the sprung resonance and above the unsprung resonance are filtered by the passive suspension system. Hence, within the region of the sprung and unsprung resonance, the active suspension should minimize the transfer of road vibrations. Figure 5.11(b) shows the response on the body acceleration due to the actuator where at the unsprung resonance, the actuator cannot influence the body acceleration by any means. Another invariant point is observed in the suspension travel at the rattle frequency defined as

$$f_r \cong \frac{1}{2\pi} \sqrt{\frac{k_t}{M_{s,q} + M_u}}. \quad (5.9)$$

Hence, at that particular frequency, the actuator cannot prevent excessive travel motions and, given a certain road profile, a sufficient suspension travel should be provided.

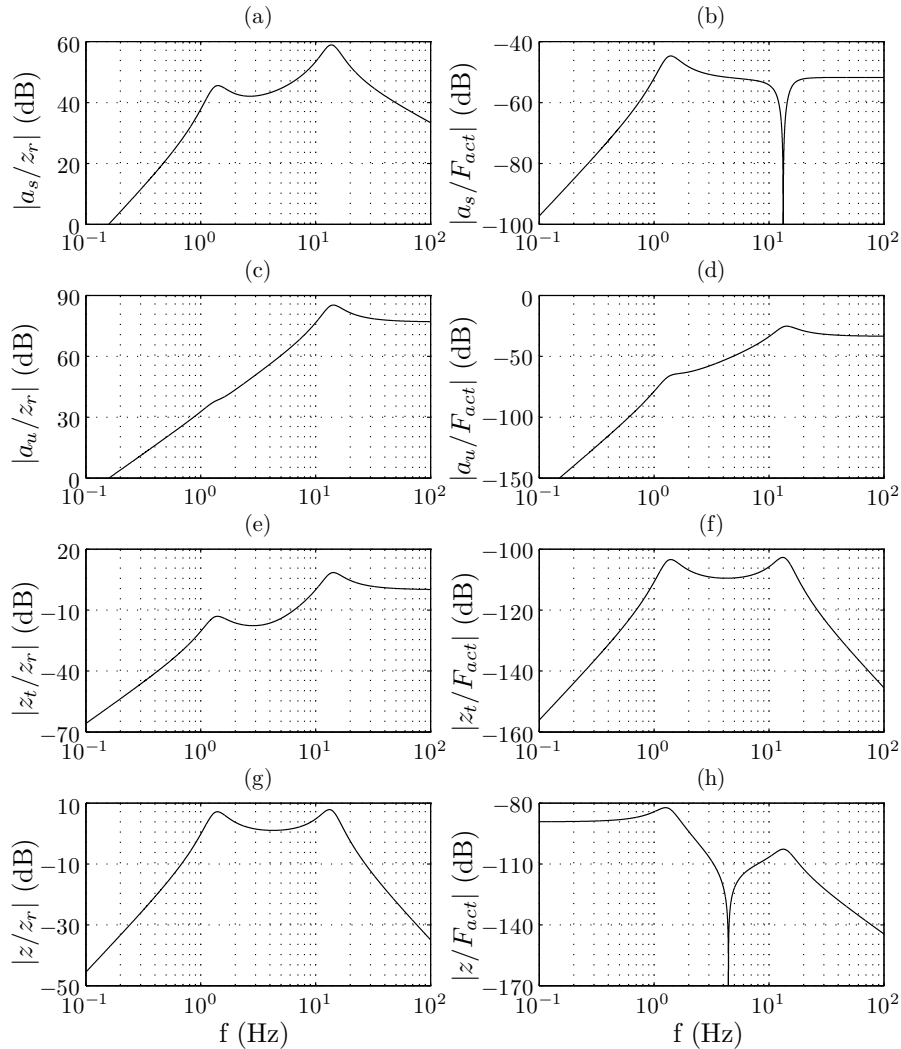


Figure 5.11: Bode diagrams of the transfer functions between relevant outputs and inputs of the quarter car model.

5.6 Road vibrations

A vehicle is subjected to a spectrum of disturbances while driving. Typically, two types of disturbances can be identified: stochastic and deterministic disturbances. Stochastic disturbances describe normal driving conditions, where the road is considered homogeneous and isotropic. This means that when large transients, bumps and potholes are removed, the distribution of the road profile is nearly Gaussian [20].

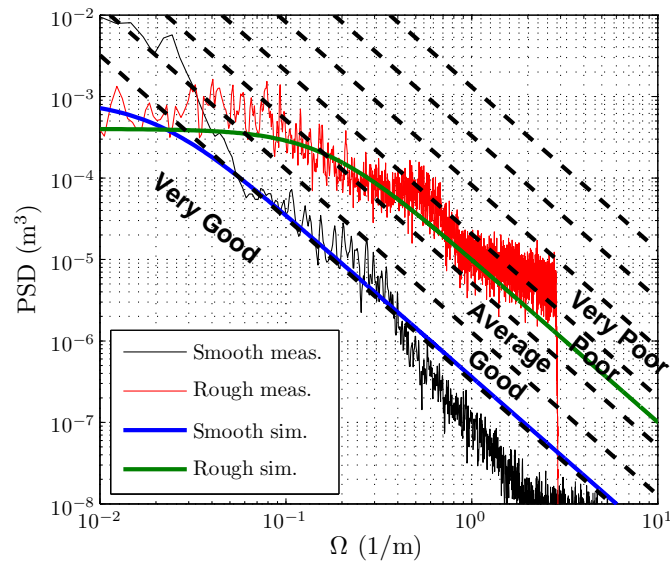


Figure 5.12: PSD spectrum of the measured and simulated road profiles together with the ISO 8608 classifications.

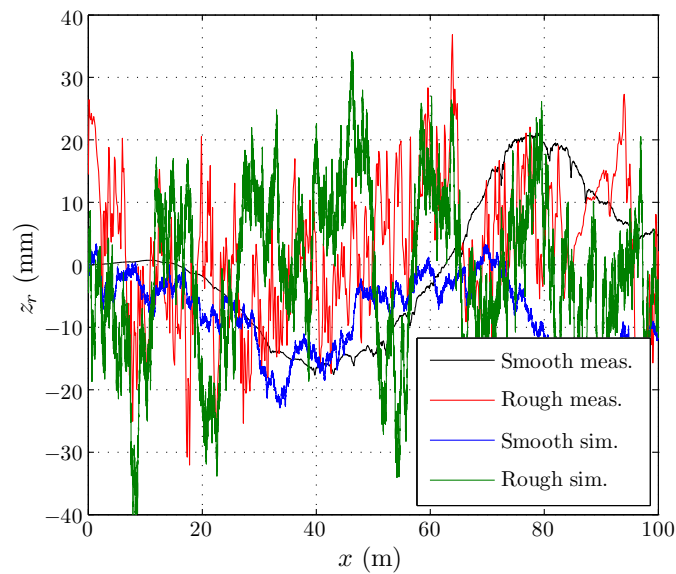


Figure 5.13: Measured and simulated road profiles of a typical smooth and rough road.

In the literature, it is common to describe a certain road by means of its power spectral density (PSD). These PSDs are usually obtained from profile measurements on a large set of various road profiles. This gives the opportunity to fit a relatively simple function which closely matches the trend of the measurements

Table 5.2: Road profile parameters.

Parameter	Smooth road	Rough road
C_r	0.03	0.02
β	0.02	0.16

and can be used into the mathematical models and simulations. An overview of various fits is given in [6]. The simplest one is the straight line approximation which also is standardized in the ISO 8608 [80] and given by

$$P_r(\Omega) = C_r \Omega^{-\beta}, \quad (5.10)$$

where $\Omega = f/v_x$ is the spatial frequency in m^{-1} , v_x is the forward velocity, C_r the general roughness and β the wavelength distribution. The various ISO 8608 classifications are shown by the dashed lines in Fig. 5.12. This straight line fit is favorable since the complete road is described by only two parameters. However, this has some implications at longer wavelengths since the PSD goes to infinity which complicates simulations and profile generation on, for example, an experimental setup where only a limited stroke is available [34]. Therefore, the road description is considered to be white noise filtered by a first order low pass filter, H_r ,

$$H_r(\Omega) = \frac{C_r}{j\frac{\Omega}{\beta} + 1}, \quad (5.11)$$

giving the following PSD spectrum

$$P_r(\Omega) = |H_r|^2 = \frac{C_r^2}{\frac{\Omega^2}{\beta^2} + 1}. \quad (5.12)$$

Measurements have been performed on a smooth road and a relatively rough road (Belgian pavement) [129], where the PSDs of these measurements are shown in Fig. 5.12. The PSD spectrum, equation (5.12), has been fitted to these measurements giving the parameters in Table 5.2. Figure 5.13 shows the measured and simulated profiles as a function of the longitudinal position x where a close trend is achieved. The measured smooth road has a second corner frequency at $\Omega = 0.4/\text{m}$. Since this corner frequency is not included for the simulated smooth road, the simulation has a higher frequency content, see Fig. 5.12. The incorporation of this second corner frequency is not attractive regarding the small increase in accuracy versus the increase in complexity [49].

Since a random road does not contain potholes and bumps, a deterministic disturbance of a 30 mm high speed bump is considered with a 45° degree angle relative to the road surface. The three aforementioned road profiles are considered as the benchmark road inputs for the remainder of the thesis.

5.7 Objectives and specifications

Specifications of the suspension system are strongly dependent on the type of vehicle and the objectives which should be achieved. Therefore, using the given road profiles, quarter car model and on-road measurements, benchmark performance specifications are derived.

5.7.1 Suspension stroke and velocity

The available stroke of the suspension systems defines the amplitude of disturbances which can be absorbed. The larger the suspension stroke, the more comfortable the ride can be made. For passenger cars, the full stroke is generally around 160 mm [33]. Measurements on the passive suspension of the benchmark vehicle indicated a total stroke of 140 mm, $S_b = 60$ mm in bump or compression and $S_r = 80$ mm in rebound. To make a fair comparison between the currently installed passive suspension system and the developed active suspension system, the specified stroke is kept equal to the passive suspension system.

Motions of the suspension system have four main causes [33]. The first and most obvious one are the road vibrations which have a wide spectrum and are dependent on the vehicles forward velocity. The dominant suspension response is around the heave frequency which is typically in the order of 1-1.5 Hz. Ride amplitudes of maximum 20 mm are considered normal driving conditions which results in a maximum suspension velocity of 0.19 m/s for a body heave of 1.5 Hz. Measurements on the TU/e campus, which can be considered as a fairly rough ride, resulted in an average suspension velocity of 0.0385 m/s, a maximum bound velocity of 1.28 m/s and maximum rebound velocity of 2.25 m/s.

The second cause are pitch motions which result in associated suspension velocities of 0.2 m/s for normal braking. Roll motions are the third cause which generally have a slightly higher suspension velocity than pitch motions, around 0.3 m/s. The final cause is wheel drop, when driving off a kerb. This condition indicates the peak velocity a suspension system might experience, generally referred as the drop test. A kerb of 100 mm can result in a peak velocity of 1.4 m/s. Considering all aforementioned situations and their probability of occurrence, a peak velocity of $\max(v) = 2$ m/s and an RMS velocity of $v_{\text{RMS}} = 0.1$ m/s are assumed for the active suspension system.

5.7.2 Comfort and human sensitivity

Motion sickness

Motion sickness, especially when reading, is a common by-product of exposure to optical depictions of inertial motion [134]. This phenomenon, called visually induced motion sickness, has been reported in a variety of virtual environments, such as fixed-base flight and automobile simulators [51, 123, 163]. Further Gahlinger [53] discussed that motion sickness occurs most commonly with acceleration in a direction perpendicular to the longitudinal axis of the body, which is why head movements away from the direction of motion are so provocative. He further mentioned that vertical oscillatory motion (appropriately called heave) at a frequency of 0.2 Hz is most likely to cause motion sickness, although that the incidence of motion sickness falls quite rapidly at higher frequencies. This results in the design criteria for active systems that frequencies (lower than 1 Hz) need to be eliminated. This is underlined by surveys documenting that motion sickness occurs in 58 % among the children [11].

Head toss

Head toss happens when a car makes a sudden roll motion, e.g. occurring when one tire drives through a deep hole. This is not due to optical depictions but since the receptor mechanisms of the three orthogonally oriented canals in each inner ear are activated by angular acceleration of the head [53]. This especially occurs when a suspension with coupled left and right wheels is used as is the case with passive anti-roll bars.

At frequencies below 1-2 Hz the head moved with the body, but in the frequency range of 2-8 Hz the amplitude of head acceleration is augmented. This indicates that oscillations about a center of rotation low in the body may induce large angular movements in this frequency range because of the linear component of acceleration delivered at the cervical vertebrae. At higher frequencies, the acceleration at the head was attenuated with an associated increase in phase lag, probably due to the absorption of input acceleration by the upper torso [95].

In order to quantify the acceptable accelerations levels, the ISO 2631-1 standard is often used as a reference set of RMS accelerations which produce equal fatigue-decreased-proficiency [105]. Figure 5.14 shows the frequency dependent weighting function. As can be seen, humans are most sensitive to vibrations in the 4-10 Hz range, with fast decreasing sensitivity beyond this range. At lower frequencies humans are also less sensitive. Hence, the ideal suspension system should minimize the frequency response of the sprung mass accelerations to the road disturbances in the band between 0.2 Hz and 10 Hz while maintaining a stiff ride during cornering.

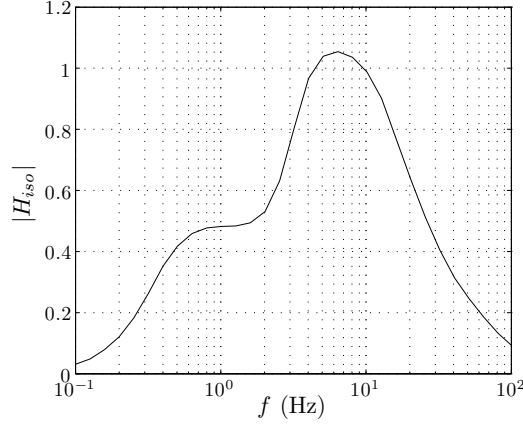


Figure 5.14: ISO 2631-1 weighting filter of human sensitivity to vertical body accelerations.

The objective for comfort can be written as

$$\min a_{sw} = \min a_s |H_{iso}|. \quad (5.13)$$

Assuming an ideal controller which provides the specified force F_{spec} with the correct amplitude and phase angle at each frequency, the weighted acceleration can be reduced to zero if

$$\left| \frac{a_s}{z_r} \right| |H_{iso}| |H_r| - F_{spec} \left| \frac{a_s}{F_{act}} \right| = 0, \quad (5.14)$$

from which the specified force can be calculated as

$$F_{spec} = |H_{iso}| |H_r| \left| \frac{a_s}{z_r} \right| / \left| \frac{a_s}{F_{act}} \right|. \quad (5.15)$$

The absolute value of this specified force is shown as a function of the frequency for the smooth and rough road in Fig. 5.15. It can be observed that an infinite force is necessary at the wheel hop frequency since this frequency cannot be suppressed with an active suspension system of this form as explained in Section 5.5. For the remaining frequency band of interest, the specified force is below 500 N for both the smooth and rough road. It should be noted that the specified force should be increased since, in practice, an ideal controller, sensors and actuator are not realistic and hence, a higher force is necessary to compensate for this.

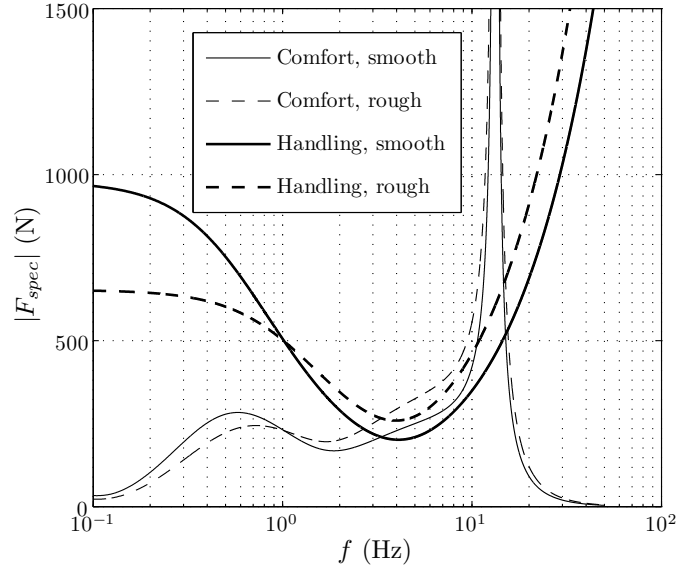


Figure 5.15: Absolute value of the force specification considering an ideal comfort or handling setting for both smooth and rough road profiles.

5.7.3 Handling

Handling defines the cornering behavior of the vehicle. Stability, on the other hand, is the unwillingness of a vehicle to alter its existing path. The three external working forces on the vehicle are the road vibrations, the aerodynamic and the gravitational force. Each of them influence the handling and stability of the vehicle. In terms of handling, the tire and its contact with the road are of most importance while aerodynamics is of secondary influence [32].

Handling generally concerns lateral and longitudinal behavior and hence, the quarter car model has not the ability to fully model the handling performance with and without active suspension. However, there is a relationship between the dynamic vertical tire compression, z_t , and the corner force a tire develops. Generally, when the tire compression changes, it needs a certain traveling distance to develop its side force or cornering force. Hence, in order to guarantee a sufficient side force during high speed cornering, the dynamic tire compression should be minimized [116].

In a similar manner as was derived for the comfort objective, the specified force for minimizing the dynamic tire load due to the road vibrations in the case of an ideal controller can be obtained as

$$F_{spec} = |H_r| \left| \frac{z_t}{z_r} \right| / \left| \frac{z_t}{F_{act}} \right|. \quad (5.16)$$

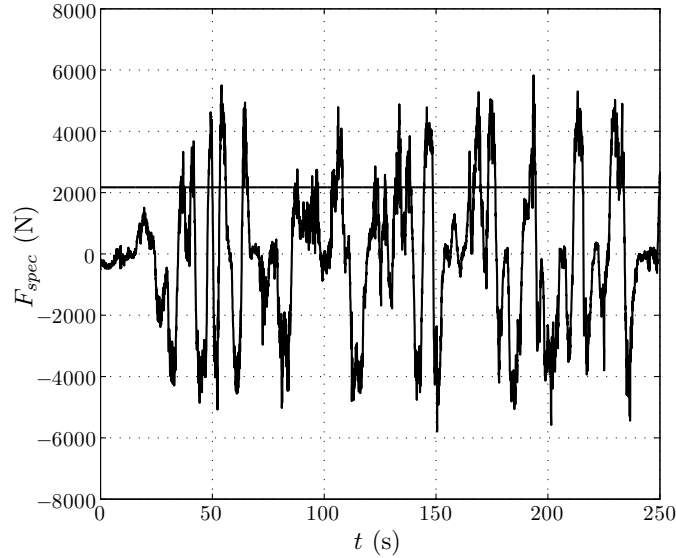


Figure 5.16: Specified front suspension forces, calculated from data measured during a test drive on the Nürburgring in Germany.

This specified force is shown in Fig. 5.15, where a force of around 1 kN and 650 N is required for the smooth and rough road, respectively. The reason for the higher requirement on the smooth road is due to the increased low frequency content in the road profile as observed in Fig. 5.12. The high force requirement above 30 Hz is irrelevant since a tire needs a certain traveling distance to build up the side force. Hence, high frequent variations in the vertical load do not translate to high frequency side force variations.

Aside from road vibrations, steering, accelerating and braking inputs cause lateral and longitudinal forces and acceleration on the vehicle body. This causes a load transfer from one side to another. To guarantee proper handling and stability, the total force needs to be distributed evenly on all tires. In order to identify the necessary suspension forces, the lateral acceleration is measured during a test drive with a similar vehicle on the Nürburgring in Germany. The front suspension forces were derived in [83] and shown in Fig. 5.16. It can be observed that the RMS force specification for the front suspension is 2.17 kN. However, it should be taken into account that a driving cycle on the Nürburgring does not represent normal driving conditions and hence, an additional arbitrary duty cycle of 50 % is taken into account. Regarding all previously discussed situations, the front suspension system should be capable of delivering a nominal force larger than 1 kN.

5.8 Sensors

Each coilover is equipped with a set of sensors to control the actuator. Generally, the more sensor inputs, the better the controllability and performance of the suspension system are, however, it increases cost and complexity. The most valuable measured quantity would be the road height in front of each corner, which could be obtained by mounting laser sensors or ultrasonic sensors in front of the wheels. The general problem with these systems is that they can sense the distance of the road to the car accurately, but cannot distinguish the material or mass density of the road or object. Since this dominantly determines the behavior, the active suspension system can therefore even cause instability while expecting a speed bump, but driving onto a cardboard box instead. Road preview is necessary when having a low-bandwidth actuation system since any reduction in time delay in the sensing system improves the overall performance [120].

The most common measurement set in active suspension systems is the sprung acceleration, a_s , the unsprung acceleration, a_u and the suspension travel, z , [145, 152]. The sprung acceleration is a measure of comfort and directly one of the objectives to minimize. The unsprung acceleration determines the wheel hop vibrations which gives information about the handling and stability. The suspension travel provides information for the ride height control and is necessary for correct commutation of the TPMA. Furthermore, as shown in Chapter 4, the suspension velocity is necessary for correct commutation due to the introduction of the eddy current damping. However, it can be determined from the measured suspension travel and sprung and unsprung acceleration.

Depending on the control strategy, different sets of sensors are possible and, by means of observers, a reduction of the set is possible [145, 152]. To correctly prove the performance of the proposed electromagnetic active suspension system and to verify different control strategies, all three sensors (sprung and unsprung acceleration and suspension travel) are considered for each corner. This sensor set allows for control of a single corner improving both comfort and handling. However, on the full vehicle level, additional sensors such as forward velocity, lateral acceleration, steering angle, pitch, roll and yaw rate should be incorporated as well as estimation of the side slip angle to ensure total control and stability of the full vehicle.

Research and development have been performed at the SKF automotive development center on load sensing bearings [8]. The available measured wheel forces and torques can be used for vehicle state information and global chassis control [54]. These sensors already proved their advantage in ABS systems since force measurements give a better prediction of the tire-to-road characteristics [30]. The use of these type of sensors in combination with the proposed active suspension has similar advantages, however, it is recommended for future research.

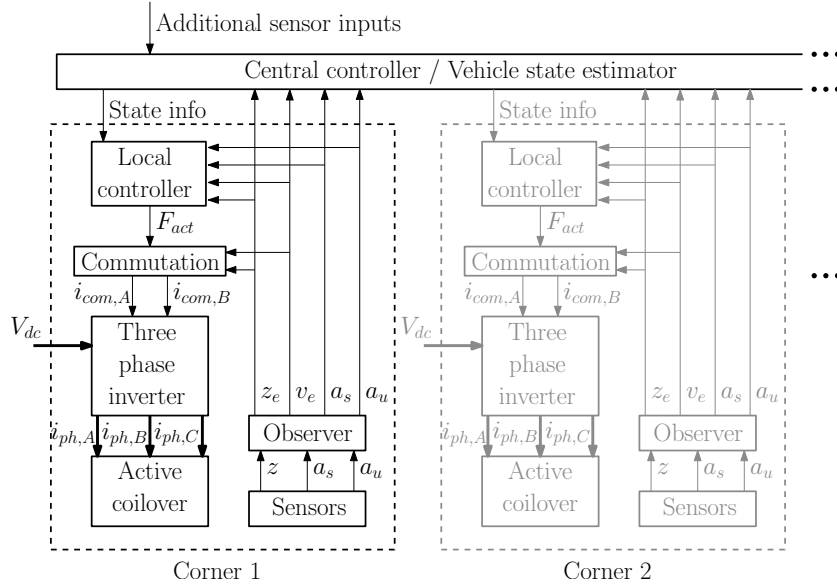


Figure 5.17: Block scheme of the total active suspension system.

5.9 System integration

The total active suspension system consists of four active coilovers, each having their own three phase PWM inverter which is fed by a common dc bus. These amplifiers contain current controllers for each of the phases ($i_{ph,A}$, $i_{ph,B}$ and $i_{ph,C}$). The commutation algorithm transfers the force command, F_{act} , together with the information of the suspension travel and velocity into a two phase current command ($i_{com,A}$ and $i_{com,B}$), the third phase is determined since the sum of currents equals zero. The local controller and the commutation algorithm are fed by sensor information which first runs through an observer for correct estimation of the measured inputs. This sensor information is also sent to a central controller on the vehicle level which determines the total state of the vehicle based on additional sensor inputs. Each local controller can change its settings according to the state information of the central controller. The total block scheme is shown in Fig. 5.17. The scope of this thesis is focused on one corner and only a local controller is developed including different settings from comfort to handling.

5.10 Summary and conclusions

The novel system topology of the developed active suspension system is presented in this chapter. The system is considered to be a retrofit for a benchmark vehicle, a BMW 530i, to prove its viability for passenger cars. The passive MacPherson front suspension of the benchmark vehicle is analyzed which is considered as a reference in terms of performance and fail-safe behavior of the active suspension system. This passive suspension is replaced by a retrofit fast direct-drive electromagnetic active suspension system. It consists of a mechanical spring for gravity compensation in parallel with a direct-drive electromagnetic actuator. Additionally, passive damping is integrated by means of eddy currents, creating a fail-safe system. This innovative integration using conductive rings in the tooth tip openings is patented in [66].

The spring characteristic for the active suspension is chosen equal to the spring characteristic of the passive suspension, $k_a = 29$ kN/m, without the progressive spring rate. As such, a similar behavior and stroke is obtained as for the passive suspension system. The type of actuator is a long stroke slotted tubular permanent magnet actuator since it is the most promising technology in terms of force density which is a key parameter for an active suspension. The integrated electromagnetic damping characteristic is described and compared with hydraulic passive damping characteristics in terms of their position, velocity, direction and temperature dependency. Since electromagnetic damping is generally symmetric in compression and rebound compared to asymmetric hydraulic dampers, a compromise is made and the damping ratio is specified to be 1600 Ns/m. The TPMA is considered to be driven by a three phase PWM inverter. The dc bus of the amplifier is not restricted to a supply voltage of 12 V, anticipating on the fact that hybrid and electrical vehicles already have a high voltage supply.

Since the benchmark vehicle has a nearly ideal front to rear mass ratio, a two DoF quarter car model is considered suitable for the description of the vertical suspension characteristics. This model showed that two invariant points are existing, the actuator cannot influence the body acceleration at the wheel hop frequency and the suspension travel at the rattle frequency. Road profiles are mathematically described using white noise with a first order low pass filter. The parameters of this filter are based upon road profile measurements.

Specifications for the TPMA are not given since they are based on suspension topology, objectives and the benchmark vehicle. Objectives of the suspension system are minimization of the weighted sprung acceleration (improving comfort) and minimization of the dynamic tire load (improving handling). The weighting for the sprung acceleration is determined by the ISO 2631-1 criterion for human exposure to body vibrations. With the use of this model and the road descriptions, specifications in terms of rated force ($\langle F_{act} \rangle = 1$ kN), peak force ($\max(F_{act}) > 2$ kN), stroke ($S_b = 60$ mm and $S_r = 80$ mm) and velocity ($\langle v \rangle = 0.1$ m/s and $\max(v) = 2$ m/s) are derived for the TPMA.

Furthermore, measurements performed on the Nürburgring provided force specifications for the rated force and peak force for anti-roll and pitch control. The choice in sensor set is body acceleration, wheel acceleration and suspension travel. Finally, the total system integration requiring a local controller for each corner together with a central controller is presented. However, the thesis is restricted to the control and performance on a corner level.

Chapter 6

Automated optimization and design

“A design is a product of choices, decisions and compromises inspired by experience and is therefore, never truly ‘optimal’.”

The automated optimization and design of the electromagnetic active suspension system is treated in this chapter. First, a proper optimization algorithm is selected. Consequently, the integration of the TPMA within the geometry of the suspension system is presented together with the resulting geometric specifications and limitations. The selected materials and their properties are described briefly. Using the developed analytical and semi-analytical tools in Part I of the thesis and the selected optimization algorithm, the force density of the TPMA is optimized for each of the considered topologies. A set of topologies achieving the required force density are selected and optimized for minimal copper losses. Afterwards, the sizes of the conductive rings are calculated to obtain the required passive damping ratio. Consequently, minimization of the end-effects is discussed for the optimal topology. The number of turns per coil is determined to match the specification of the inverter. Finally, the total design of the suspension strut is presented together with the choice of position sensor.

The contribution of this chapter is published in:

Gysen, B. L. J., Janssen, J. L. G., Paulides, J. J. H. and Lomonova, E. A. [2009], ‘Design aspects of an active electromagnetic suspension system for automotive applications’, *IEEE Transactions on Industry Applications* **45**(5), 1589–1597.

Gysen, B. L. J., Sande, T. P. J. v. d., Paulides, J. J. H. and Lomonova, E. A. [2011], ‘Efficiency of a regenerative direct-drive electromagnetic active suspension’, *IEEE Transactions on Vehicular Technology* **60**(4), 1384–1393.

Gysen, B. L. J., Paulides, J. J. H., Encica, L. and Lomonova, E. A. [2009], Slotted tubular permanent magnet actuator for active suspension systems, *in* ‘The 7th International Symposium on Linear Drives for Industry Applications, LDIA 2009’, Incheon, South Korea, pp. 292–295.

6.1 The optimization algorithm

The design of permanent magnet motors or actuators has been discussed in many textbooks [73, 74, 121]. A standardized method does not exist since the application together with the given constraints determines the strategy. The design of an active suspension is not an exception in this case. The desired performance requires a high force density actuator for a relatively low speed application. The dominant copper losses should be minimal. One aspect which distinguishes from many other applications is the desired integrated passive damping. Furthermore, the force ripple due to cogging, end-effects, damping and armature reaction should be minimal.

In Part I of the thesis, accurate modeling tools are developed for the prediction of the various physical parameters of the tubular actuator with integrated passive damping within a very small computational time. These models are applicable to a wide range of topologies. Furthermore, the models allow for parameter variation without adaptation or tuning of the model. It introduces the possibility to use automated optimization algorithms to obtain a design, satisfying the given specifications. This algorithm can be implemented in the same software environment as the semi-analytical model. This excludes the need for data transfer or parameter extraction and adaptation between different software packages which would increase the total computation time. Furthermore, time consuming finite element analysis is extracted from the design process, and it only functions as a verification tool of the optimal solution or intermediate steps.

Various optimization algorithms can be combined with the semi-analytical modeling technique. One can consider gradient methods, in which the search direction is determined by the local gradient of the objective function at the current search point, e.g. linear or non-linear programming. Another class are evolutionary algorithms or heuristical methods, where the successive search points are determined by natural selection using a fitness function. Additional search points are created using crossover or mutation. These types of algorithms tend to converge more to the global optimum whereas gradient methods have the disadvantage to converge to local optima. Although heuristical methods are more suitable to minimize a complex fitness landscape, the implementation requires more parameters for crossover, selection, mutation, reproduction, etc. such that a gradient method becomes more attractive from an implementation point of view. The chosen optimization algorithm for the design of the active suspension system is, therefore, the non-linear programming algorithm [150] implemented as a standard tool in Matlab. In general, the optimization problem is formulated as [10, 150]

$$\text{minimize} \quad f(\mathbf{x}), \quad (6.1)$$

$$\text{subject to} \quad g_i(\mathbf{x}) \leq 0, \text{ for } i = 1, \dots, m, \quad (6.2)$$

$$h_j(\mathbf{x}) = 0, \text{ for } j = 1, \dots, n, \quad (6.3)$$

$$\mathbf{x} \in \mathbf{X}, \quad (6.4)$$

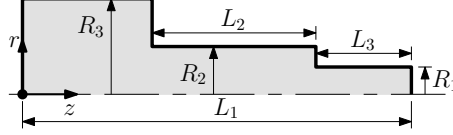


Figure 6.1: Schematic representation of the available space envelope for the active suspension system as listed in Table 6.1

Table 6.1: Volumetric requirements of the active suspension system (Fig. 6.1).

Description	Symbol	Limitations
Radius of the knuckle clamp	R_1	31 mm
Radius limited by the tire width	R_2	39 mm
Radius limited by the engine compartment	R_3	100 mm
Equilibrium length of the suspension strut	L_1	493.5 mm
Length from the knuckle to the tire radius	L_2	205.7 mm
Available length in the knuckle clamp	L_3	156.3 mm

where $f(\mathbf{x})$ is the objective function to be minimized subject to the m inequality constraints given by $g_i(\mathbf{x})$ and the n equality constraints given by $h_j(\mathbf{x})$. The variable vector is denoted as \mathbf{x} within the variable space \mathbf{X} .

6.2 Coilover integration and mechanical design

The developed active suspension is a retrofit for the BMW 530i, and therefore, the volumetric requirements are given. The available space envelope for the active suspension system is shown in Fig. 6.1, where the various limitations are listed in Table 6.1. For the integration of a tubular permanent magnet actuator in the coilover topology, one can consider the spring surrounding the TPMA [63] or integrated within the TPMA [158]. When the spring is integrated, the TPMA can have a larger outer diameter, and therefore, a higher performance although at the expense of a higher volume and mass. However, it complicates side-force cancelation in a MacPherson strut using a special coil spring geometry [101]. In the case of the benchmark vehicle, the outer diameter is limited by the location of the wheel, radius R_2 in Fig. 6.1, and integrating the spring only leads to a larger available outer diameter above the tire, radius R_3 in Fig. 6.1. Due to the aforementioned reasons, the coil spring is considered to surround the TPMA.

Four configurations are possible as shown in Fig. 6.2 together with the necessary stroke specifications for bound, S_b , and rebound, S_r . In Fig. 6.2(a) and (b) the outer tube of the TPMA is connected to the sprung mass for the IMT and EMT topology, respectively. These configurations result in a topology with two airgaps, increasing the total friction force and are less preferable from a construction point of view. Additionally, for varying strokes, these topologies have a varying active length which complicates control and results in imbalanced induced emf wave-

forms. Even more, the end-effects at both sides are different which makes them difficult to minimize, as explained in Section 3.6.3.

The options shown in Fig. 6.2(c) and (d) have the outer tube connected to the unsprung mass for the IMT and the EMT topology, respectively. These configurations result in a single airgap topology, reducing friction, simplifying linear guiding and alignment, and are therefore, very favorable. The active length is independent on the position, and the end-effects are equal on both sides. Regarding the aforementioned reasons, options (c) and (d) are considered more suitable.

Given the desired bound stroke of $S_b = 60$ mm and rebound stroke of $S_r = 80$ mm, the available active length for these topologies is given by

$$L_{act} = L_1 - L_3 - S_b = 277.2 \text{ mm.} \quad (6.5)$$

Furthermore, the maximum total stroke is limited by

$$S_b + S_r < L_2, \quad (6.6)$$

which is achievable for the given specifications.

A sliding bearing, selected for linear guidance (it occupies less space than a linear roll bearing), has a lower maintenance and in principal is lubricant free. A poly-tetra-fluor-ethene (PTFE) is chosen due to the low friction coefficient of the material. This bearing requires a minimal thickness, which defines the airgap length g , and is fixed to 1 mm.

Mechanical finite element calculations showed that, given a side force specification of 7 kN, which is equivalent to cornering at 8.5 m/s^2 , the minimal thickness of the housing should be at a minimum of $d_h = 3$ mm. Since the geometric specification only limits the outer radius of the actuator at the angle where the wheel is located, the thickness of the housing is increased at the angle tangential to the wheel to improve the mechanical strength. Therefore, the outer housing has a larger radius with flattened sides, see Fig. 6.3. Together with the given volumetric specifications in Table 6.1, a limit on the outer radius of the inner tube, R_{in} , and outer tube, R_{out} , can be set

$$R_{in} = R_1 - d_h - g, \quad (6.7)$$

$$R_{out} = R_2. \quad (6.8)$$

Note that the thickness of the housing, d_h , does not put a constraint on the outer radius, R_{out} , since the stator back iron for IMT and translator back iron for EMT can function as the housing itself. However, this thickness puts a constraint on the minimal height of the stator back iron ($h_{sbi} \geq d_h$) for IMT or on the height

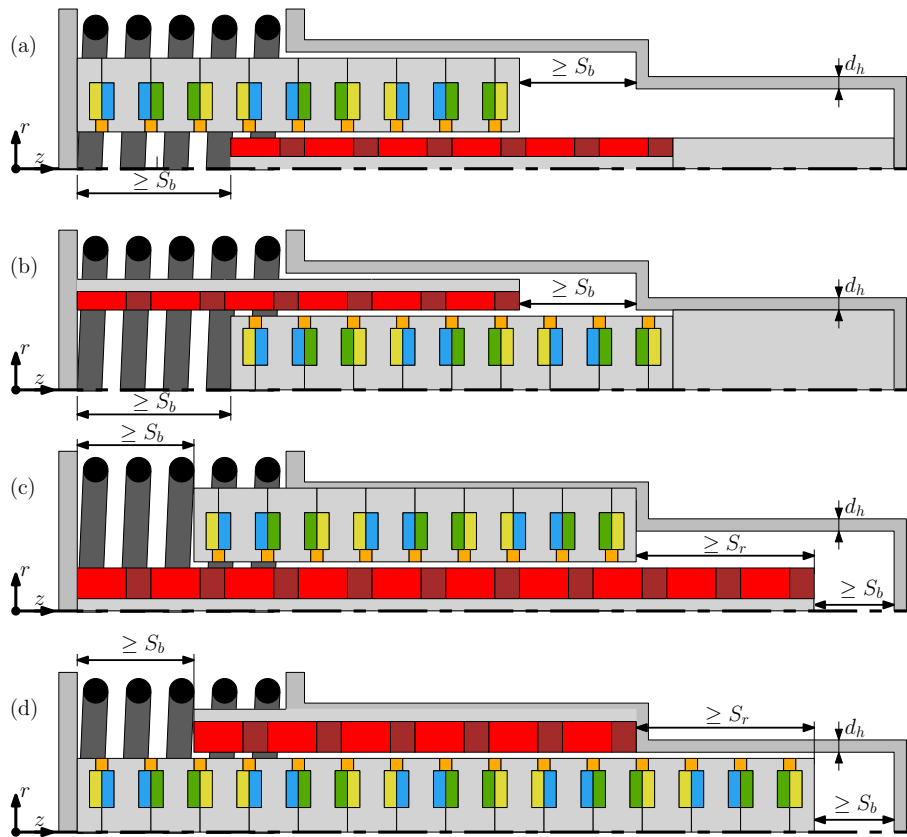


Figure 6.2: Integration of the TPMA and the mechanical spring into a coilover suspension strut.

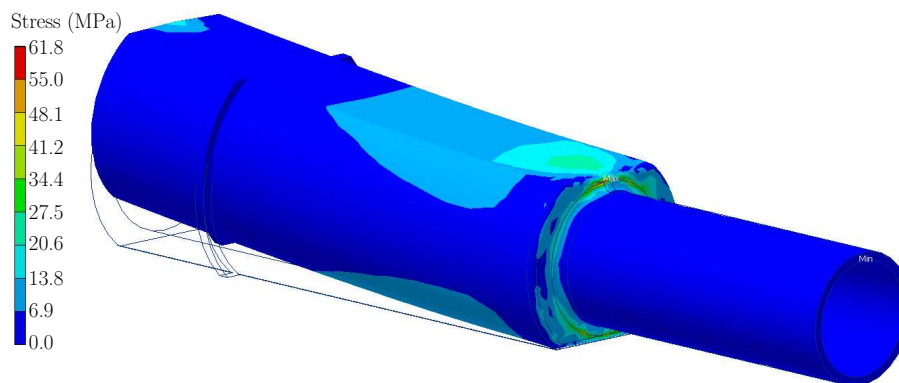


Figure 6.3: Mechanical stress distribution of the housing the active suspension system due to a 7 kN side force on the tire.

Table 6.2: Properties of the PM material VACODYM 633 HR.

Parameter	Symbol	Value	Unit
Remanence at 20°C	$B_{rem,20}$	1.35	T
Recoil permeability	μ_r	1.06	-
Temperature coefficient	α_m	$9.5e^{-4}$	1/°C
Conductivity	σ_m	$9.091e^5$	S/m

of the translator back iron for EMT ($h_{tb} \geq d_h$). To guarantee a sufficient stiffness of the inner tube, the height of the translator tube for IMT, h_{tb} , and the minimal height of the stator back iron for EMT, h_{sbi} , should be larger than 5 mm.

6.3 Material selection

A high force density actuator is required and the choice of materials significantly determines the performance of the active suspension system. Concerning the permanent magnets, this hard magnetic material should have a high remanent flux density, resulting in a higher magnetic loading. This lowers the amount of electrical loading to obtain a given output force, and hence, a lower power consumption. The chosen PM material is neodymium-iron-boron (NdFeB) which typically has the highest remanent flux density of around 1.35 T at room temperature. More specifically, VACODYM 633 HR from Vacuumschmelze GmbH & Co. KG [148] is selected which has the properties as summarized in Table 6.2.

A high magnetic loading requires the soft-magnetic material to have a high saturation flux density, B_{sat} . Especially for a TPMA with EMT, which has a smaller stator radius, it results in very high flux densities at the center axis. To obtain the required force density within the small volume, it is essential to have a high value of B_{sat} . Typical cast steel, silicon steel or nickel-iron alloys have a saturation magnetization which is typically in the order of maximum 1.5-1.7 T. However a cobalt-iron alloy has a significantly higher saturation flux density in the order of 2.3 T allowing for a higher performance. The specific alloy considered is VACOFLUX50 from Vacuumschmelze GmbH & Co. KG [148] where the measured BH-curve is shown in Fig. 4.2. The cobalt-iron alloy is however still more expensive than conventional steel. Therefore, both types of steel are considered during the optimization and design. The virgin curve of the BH-characteristic of both steel 1010 and cobalt iron are shown in Fig. 6.4.

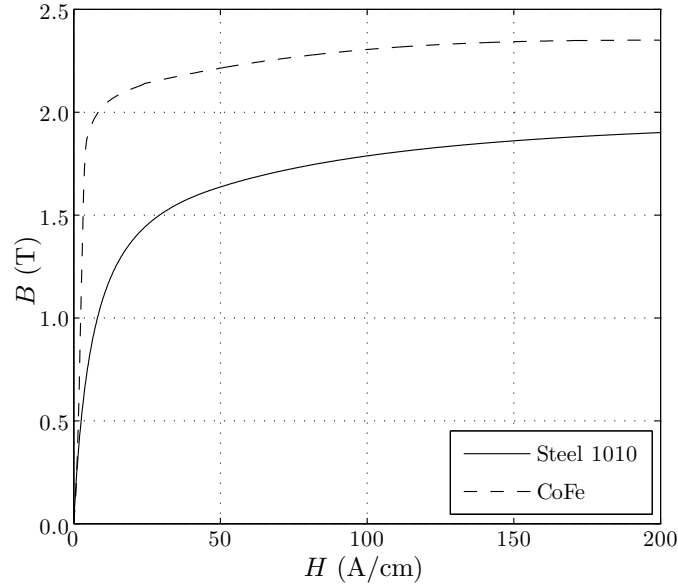


Figure 6.4: Virgin curve of the BH-characteristic of steel 1010 and cobalt iron.

6.4 Thermal constraints

The permanent magnets and coils are the most sensitive components to an increase in temperature. To assure a proper lifetime, the maximum temperature of these components has to be limited. A model should, therefore, be constructed which relates their temperature to the amount of average electrical loading at the rated force output. The model should incorporate heat produced by the electrical loading which are the copper losses as calculated in the previous section as well as the eddy current losses in the soft-magnetic stator and the conductive rings. Since the operating temperature of the actuator is around 100 °C, heat transport via radiation is neglected, and only conduction and convection are included. For an automotive suspension system, several factors influence the environment temperature and the convection coefficient at the suspension system:

- variation in environment temperature (-20 °C to 40 °C),
- heat generated from the engine compartment,
- heat generated from the brake disc,
- air flow due to the rotating wheel and brake disc,
- air flow due to the vertical movement of the wheel,
- air flow from the air inlets at the front bumper.

Furthermore, depending on the type of suspension system used, the conduction via the wheel hub, suspension arms and additional clamps significantly influence the thermal behavior of this system. In order to ensure that the suspension system works properly in any condition, the worst case parameters are considered in the thermal model. An environment temperature of $T_{amb} = 40$ °C is assumed. Considering the amount of air flow, a reasonable convection coefficient of $h = 30$ W/m²K is applied. Furthermore, a periodic model is investigated, hence only radial heat flux is assumed. Although axial heat flux exists due to the finite length of the actuator, a periodic model reduces the complexity and provides the worst-case temperature estimation.

The developed thermal models of Chapter 3 consider two heat sources, the copper losses per coil, P_{coil} , and the iron losses P_{fe} . Due to the high thermal conductivity of the conductive rings and the soft-magnetic material, the steady state temperature is considered to be homogenous, and the location of the heat source within the stator is assumed to be insignificant. Therefore, the additional losses due to the eddy currents in the conductive rings are embedded in the contribution of iron losses. The sliding bearing in the airgap has a thermal conductivity of $k_g = 0.1$ W/mK and the coil insulation is made of Nomex with a thermal conductivity $k_{ins} = 0.1$ W/mK.

The accurate determination of the eddy current losses in the soft-magnetic material requires transient finite element analysis. However, the design of an active suspension with a certain required damping defines the amount of necessary total losses in the soft-magnetic material and the rings. Since the design of the rings is such that a required damping is obtained, the amount of losses are predetermined and considered constant during the optimization routine, given by

$$P_{fe} = d_a v_{\text{RMS}}^2 = 16 \text{ W.} \quad (6.9)$$

6.5 Design criteria and strategy

Several criteria have to be met for the final design. First of all, it should fit within the apparent available space envelope of the test car which is in this case the BMW 530i. Furthermore, the total additional unsprung mass of the system should not increase the existing unsprung mass by 30 % since this would significantly deteriorate the performance in the passive and active case. However, considering the limited available space envelope and relatively high unsprung mass of the benchmark vehicle, this specification is inherently satisfied.

An average force of 1 kN should be achieved with minimal power consumption giving the constraints on maximum magnet temperature ($T_{m,max} = 110$ °C) and coil temperature ($T_{c,max} = 140$ °C). Furthermore, a total stroke of 140 mm is necessary. A fail-safe passive damping should be integrated while an initial

damping around 1600 Ns/m with a close to linear characteristic, where the critical velocity is far beyond the maximum operating velocity, $v_c \gg 2$ m/s in order to meet the specifications.

Essentially, the optimal design is obtained by minimizing the power loss constraint to the specifications mentioned before. However, at this point, it is not clear whether or not the specified force can be achieved within the given space envelope. Hence, if the constraints cannot be met, the optimization fails to converge. Therefore, it is more convenient to optimize the force density first and discard the configurations which do not achieve the specified force density. The design strategy considers five distinctive steps:

- First, the optimization of the force density of a single periodic section is considered which provides an overview of the force density for each topology. These designs are obtained by a non-linear optimization problem for IMT and EMT topologies, radial, quasi-Halbach and axial magnetization and the various slot/pole and winding configurations shown in Fig. 3.4.
- Second, given the stroke and space requirements, an optimal number of periodic sections is obtained. Consequently, for the topologies achieving the force specification in the first step, the copper losses are minimized.
- Third, for each of the optimal designs in the second step, the eddy current damping in the soft-magnetic material, d_{fe} , is calculated using FEA. Afterwards, the sizes and material of the conductive rings are determined in order to obtain the total required fail-safe damping, $d_a = d_{fe} + d_r$.
- Fourth, the force ripple due to the end-effects of the final design are minimized.
- Finally, regarding the chosen dc bus voltage and form of excitation, the number of turns per coil is determined.

6.6 Force optimization

6.6.1 Problem formulation

During the force optimization, the average force per volume of one periodic section of a given topology is optimized. This gives an overview which configurations are capable of providing the average force of 1 kN within the available volume and additional constraints. The necessary force density given the available active length and maximum outer radius is 755 kN/m³. The optimization problem has the following variable vector, \mathbf{x} ,

$$\mathbf{x} = \left[\tau_p \quad \alpha_p \quad \tau_s \quad \tau_o \quad h_{tb} \quad h_m \quad h_o \quad h_c \quad h_{sbi} \quad J_{sl_{RMS}} \right]. \quad (6.10)$$

The objective of the non-linear constrained optimization problem is given by the maximization of the force density, hence

$$f(\mathbf{x}) = -f_d(\mathbf{x}) = -\frac{\langle F_z(\mathbf{x}, \theta_e) \rangle}{P\tau_p\pi R_{out}^2}, \quad (6.11)$$

the minus sign is required to write the objective function (maximization of the force density) as a minimization problem. The inequality constraints are listed as

$$g_1(\mathbf{x}) = \tau_o - \tau_s \leq 0, \quad (6.12)$$

$$g_2(\mathbf{x}) = \begin{cases} h_s + h_{tb} + h_m - R_{in} \leq 0, & \text{for IMT,} \\ h_s + h_{sbi} + h_c + h_o - R_{in} \leq 0, & \text{for EMT,} \end{cases} \quad (6.13)$$

$$g_3(\mathbf{x}) = h_s + h_{tb} + h_m + g + h_o + h_c + h_{sbi} - R_{out} \leq 0, \quad (6.14)$$

$$g_4(\mathbf{x}) = \frac{\max(F_z(\mathbf{x}, \theta_e)) - \min(F_z(\mathbf{x}, \theta_e))}{\langle F_z(\mathbf{x}, \theta_e) \rangle} - F_{\sim} \leq 0, \quad (6.15)$$

$$g_5(\mathbf{x}) = T_m(\mathbf{x}) - T_{m,max} \leq 0, \quad (6.16)$$

$$g_6(\mathbf{x}) = T_c(\mathbf{x}) - T_{c,max} \leq 0, \quad (6.17)$$

$$g_7(\mathbf{x}) = \max(B_{t_1}(\mathbf{x}, \theta_e)) - B_{max} \leq 0, \quad (6.18)$$

$$g_8(\mathbf{x}) = \max(B_{s_1}(\mathbf{x}, \theta_e)) - B_{max} \leq 0, \quad (6.19)$$

$$g_9(\mathbf{x}) = \max(B_{tbi}(\mathbf{x}, \theta_e)) - B_{max} \leq 0, \text{ for radial magnetization,} \quad (6.20)$$

$$g_{10}(\mathbf{x}) = \max(B_{pp_1}(\mathbf{x}, \theta_e)) - B_{max} \leq 0, \text{ for axial magnetization,} \quad (6.21)$$

for θ_e ranging from zero to 360 electrical degrees and the force ripple constraint given by $F_{\sim} = 10\%$. The first constraint enforces the slot opening to be smaller than the slot width (see Fig. 3.5). The second and third constraint limit the inner and outer radius, respectively (see Fig. 3.5). The fourth constraint penalizes the percentage of force ripple and the fifth and sixth constraint limit the magnet and coil temperature, respectively. Finally, constraints number seven until ten limit the average flux density within the soft-magnetic regions over a relative movement of 360 electrical degrees, since, depending on the amount of armature reaction, the maximum flux density in each tooth or back-iron has its maximum at a different relative position.

A single model evaluation considers three different steps as outlined in Fig. 6.5. The inputs of the model are the variable vector \mathbf{x} and the parameter vector \mathbf{p} containing information about the topology (IMT or EMT), magnetization (radial, quasi-Halbach or axial) and winding configuration (a)-(g) and the total iron losses, P_{fe} . The thermal model determines the coil and magnet temperatures, copper losses and remanence of the permanent magnets at the resulting operating temperature. In case the objective function should be determined, the electromagnetic model calculates the output force. In case the inequality constraints should be determined, the average force, the force ripple and the various flux densities in the soft-magnetic regions (teeth, stator back-iron, translator back-iron and/or pole piece) are calculated. Due to the given periodicity, the force

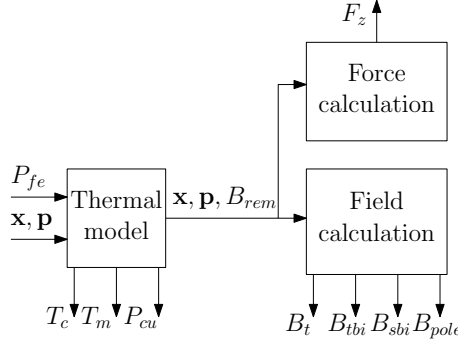


Figure 6.5: Block diagram of one model evaluation.

calculation is performed over a relative displacement of $\theta_e = 60$ electrical degrees within 24 steps, and the field calculations are performed over a relative displacement of $\theta_e = 360$ electrical degrees within 60 steps.

6.6.2 Implementation aspects

One important aspect of the semi-analytical model in combination with an optimization technique is the determination of the number of included harmonics. This number of harmonics for the slot openings, slots and permanent magnet regions (for axial magnetization) are linked to the number of harmonics for the periodic regions, as defined in equation (2.110). However, the selection of the number of harmonics included in the periodic regions determines the overall accuracy. When insufficient harmonics are taken into account, the force calculation is incorrect. If too many harmonics are considered, numerical inaccuracies occur, and the result is unreliable.

During optimization, the variables can attain extreme values and the result should still be accurate in order to converge towards a more optimal solution. To assess this problem, a reasonable sufficient number of harmonics is selected at the initial stage, typically from 25 to 50, where the higher number relates to a higher number of poles (P) per period. The semi-analytical model verifies the solution in several ways. First, the calculated force profile should exhibit periodicity over 60 electrical degrees. The force level cannot exceed a certain estimated limit. Furthermore, the number of oscillations around the average value within 60 electrical degrees is equal to $S/3$. In case the force profile does not inhibit all of the previous properties, the calculation is repeated for a lower number of harmonics. The recursion is repeated until a viable solution is obtained. In this way, a high accuracy is guaranteed during the whole optimization process.

Scaling of the variables is performed to improve numerical accuracy and convergence. In Fig. 6.6, the convergence history is shown for one of the optimized topologies (singular winding topology of Fig. 3.4(d), EMT, quasi-Halbach magne-

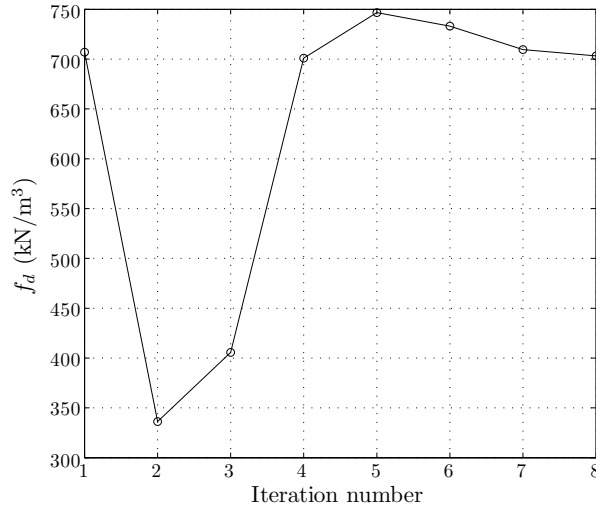


Figure 6.6: Convergence history of the force density during the non-linear constrained optimization.

tization). Convergence is reached after eight iterations within a total calculation time of 204 seconds. Each iteration contains 11 model evaluations. One at the current search point, and one at a finite difference within each of the 10 variables. Each model evaluation considers the calculation of the objective function which is the force calculation and the non-linear constraints (the force calculation plus the flux density estimations). Hence a total number of 9504 inversions of the boundary condition matrix are performed with an average calculation time of 21.5 ms. The convergence time for winding configurations with a higher slot number is longer, however, still within 25 iterations.

6.6.3 Comparison of the optimized force densities

First, the optimized force density of each of the topologies using steel 1010 as the soft-magnetic material are discussed. The results, together with the non-linear finite element verification, are shown in Fig. 6.7. Overall, the IMT outperforms the EMT. The EMT requires very high flux densities due to the small radius of the stator and saturation occurs, hereby limiting the obtained force density. Furthermore, it should be noted that the distributed winding configuration, Fig. 3.4(e), does not meet the required specification of the force ripple and has the lowest force density. This configuration is known for its high force ripple [74]. The highest force densities are obtained using four poles and three slots where a singular winding configuration, Fig. 3.4(d), is better than a concentrated winding configuration, Fig. 3.4(b), due to the lower copper losses for an equal electrical loading. For the latter winding configuration, axial magnetization provides the highest force density, however the required force density is not obtained with FEA.

Second, considering cobalt-iron as soft-magnetic material, the force density is again optimized, and the results are shown in Fig. 6.8 for each topology verified with FEA. Comparing with the results of using steel 1010, the performance of the IMT did not improve significantly. However, the EMT gained significantly in force density, especially for the concentrated and singular winding configurations with four poles and three slots, Fig. 3.4(b) and (d), due to the higher obtained flux densities in the stator back-iron. For the distributed winding configuration with two poles per six slots, Fig. 3.4(e), the force ripple constraint was again the limiting factor. The distributed winding configuration with four poles per nine slots, Fig. 3.4(f), and the modular winding configuration with eight poles per nine slots, Fig. 3.4(g), have a very low force ripple but only the axial IMT topology of the latter configuration is capable of providing the nominal force of 1 kN as observed in Fig. 6.8. However, the solution is close to saturation level and the finite element verification does not achieve the force density specification.

With respect to the magnetization topologies, axial magnetization, Fig. 3.2(c), offers the highest force level for IMT since the soft-magnetic pole pieces lead to a lower reluctance of the main flux path. However, for EMT, the quasi-Halbach and axial magnetization, Fig. 3.2(c) and (d), achieve similar performance as observed in Figs. 6.7 and 6.8. The gain in using axial magnetization for EMT is lost due to leakage flux on the outside of the translator. Normally, the performance of a quasi-Halbach magnetization is generally considered better than radial magnetization. Quasi-Halbach magnetization does not require any back iron, however, considering the mechanical stiffness of the translator, it is still necessary to incorporate a support tube. Consequently, the advantage of quasi-Halbach or axial magnetization over radial magnetization is reduced.

The selected viable topologies are the EMT with quasi-Halbach magnetization for a concentrated winding configuration with four poles per three slots, Fig. 3.4(b), the IMT with axial magnetization for a singular winding configuration with four poles per three slots, Fig. 3.4(d), and the EMT with radial, quasi-Halbach and axial magnetization for a singular winding configuration with four poles per three slots, Fig. 3.4(d). These topologies are selected for minimization of the copper losses in the following section.

6.7 Loss minimization

6.7.1 Number of periodic sections

For calculation of the total copper losses, the number of active periods, N_{pa} , and the extra number of periods achieving the necessary stroke, N_{px} , have to be selected. These extra periods also contribute to the total amount of copper losses for the EMT. Consider the total available length for the actuator to be L_t . Depending on the chosen total number of periods, $N_{pa} + N_{px}$, the length per

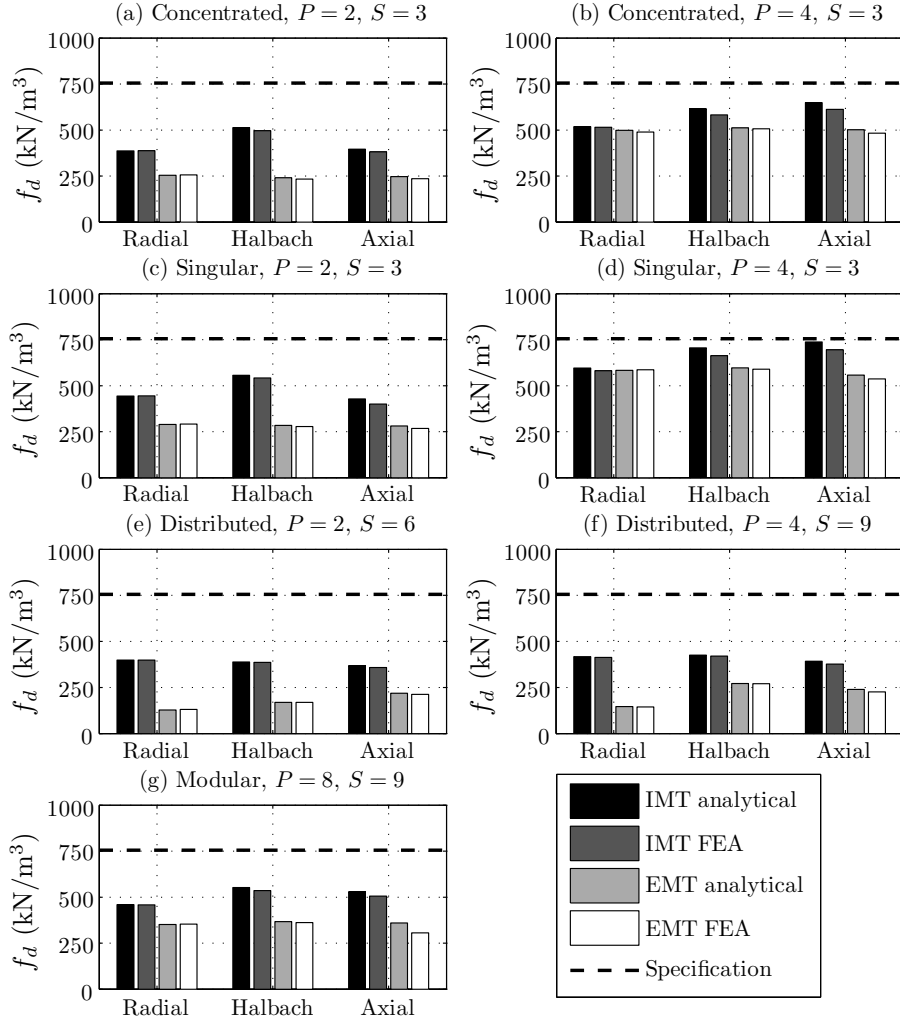


Figure 6.7: Optimized force density of the various slot/pole and winding configuration of Fig. 3.4 using steel 1010 as a soft-magnetic material.

period, L_{per} , is given by

$$L_{per} = \begin{cases} \frac{L_t}{N_{pa} + N_{px}}, & \text{for IMT,} \\ \frac{L_t - L_x}{N_{pa} + N_{px}}, & \text{for EMT,} \end{cases} \quad (6.22)$$

where $L_x = 20$ mm is the extra length needed for the stator for winding connections and the star point connection. Given the length of each period, the number

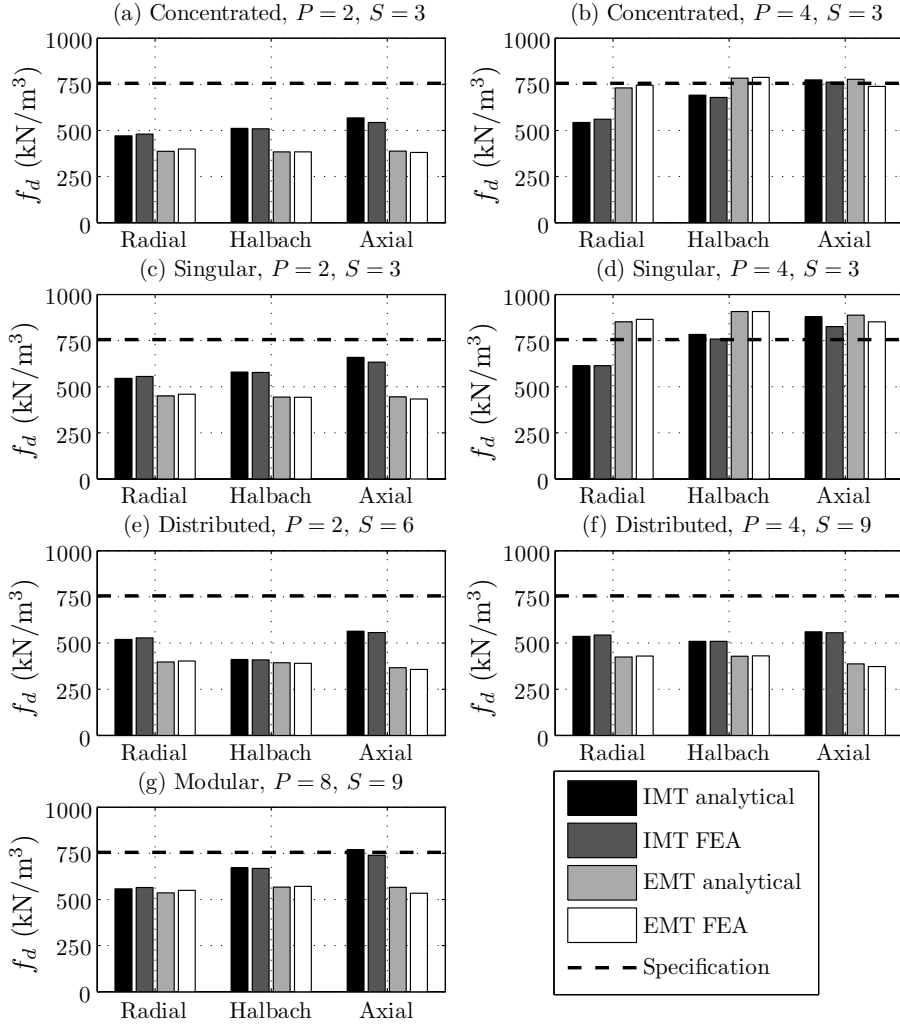


Figure 6.8: Optimized force density of the various slot/pole and winding configuration of Fig. 3.4 using cobalt iron as a soft-magnetic material.

of active periods within the available length can be calculated as

$$N_{pa} = \begin{cases} \left\lfloor \frac{L_t - S_b - S_r - L_x}{L_{per}} \right\rfloor, & \text{for IMT,} \\ \left\lfloor \frac{L_t - S_b - S_r}{L_{per}} \right\rfloor, & \text{for EMT,} \end{cases} \quad (6.23)$$

where L_x is subtracted from the available active length for IMT for stator winding connections and star point connection. The obtained total active length is then given by $L_{act} = N_{pa}L_{per}$. This active length is shown in Fig. 6.9 as a function of

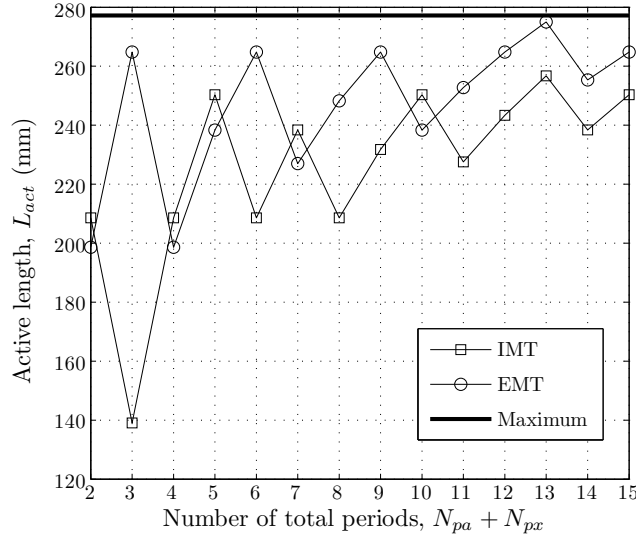


Figure 6.9: Obtained stroke as a function of the number of periods for IMT and EMT topologies.

the number of total periods. It can be observed that a total number of 13 periods allows for the optimal use of the available active length, and hence has the highest performance. This corresponds with 9 active and 4 extra periods. Furthermore, a higher number of periodic sections decreases the pole pitch and increases the frequency of the magnetic field at a given velocity. This enhances the amount of passive damping that can be achieved.

6.7.2 Problem formulation

With the given number of periods, the copper losses are minimized for the topologies achieving the specified force density in Section 6.6. The loss minimization problem has the same variable vector \mathbf{x} as for the force optimization problem. The objective of the non-linear constrained optimization problem is given by the minimization of the copper losses, hence

$$f(\mathbf{x}) = P_{cu}(\mathbf{x}). \quad (6.24)$$

The inequality constraints for the loss minimization are identical to the inequality constraints for the force optimization with an additional constraint on the average force, which should be minimal $F_{min} = 1$ kN and an additional constraint on the

Table 6.3: Minimized copper losses for the five feasible topologies.

Topology	Magnetization	Winding	P	S	P_{cu} (W)
EMT	quasi-Halbach	Concentrated	4	3	201
IMT	axial	Singular	4	3	131
EMT	radial	Singular	4	3	188
EMT	quasi-Halbach	Singular	4	3	138
EMT	axial	Singular	4	3	158

length of the periodic section are introduced

$$g_{11}(\mathbf{x}) = F_{min} - \langle F_z(\mathbf{x}, \theta_e) \rangle \leq 0, \quad (6.25)$$

$$g_{12}(\mathbf{x}) = \tau_p - \frac{L_{per}}{P} \leq 0, \quad (6.26)$$

for θ_e varying from zero to 360 electrical degrees.

6.7.3 Comparison of the optimized copper losses

Scaling of the variables and recursion in the semi-analytical model are applied as during the force optimization. The optimized copper losses for each topology are listed in Table 6.3. All topologies with winding configuration (d) have lower copper losses than the EMT with quasi-Halbach magnetization and winding configuration (b). Although the copper losses per periodic section for the IMT are higher than the EMT, the necessity of additional stator sections for the EMT makes this topology more power demanding than the IMT. The lowest level of copper losses is obtained with IMT using axial magnetization although the EMT with quasi-Halbach magnetization follows closely.

The corresponding force profiles calculated with the analytical model are verified with FEA and shown in Fig. 6.10(a)-(e). A very good agreement is obtained for the radial, Fig. 6.10(d), and quasi-Halbach magnetization, Fig. 6.10(a) and (d), and a slightly higher mean force level is predicted for axial magnetization than verified with FEA, Figs. 6.10(b) and (e). Saturation has a more significant effect on the axial magnetized topologies due to the use of soft-magnetic pole pieces. The ripple, however, is correctly predicted and only slightly higher than the specified 10 %. The choice of the final topology depends on the integration of passive damping which is discussed in the following section.

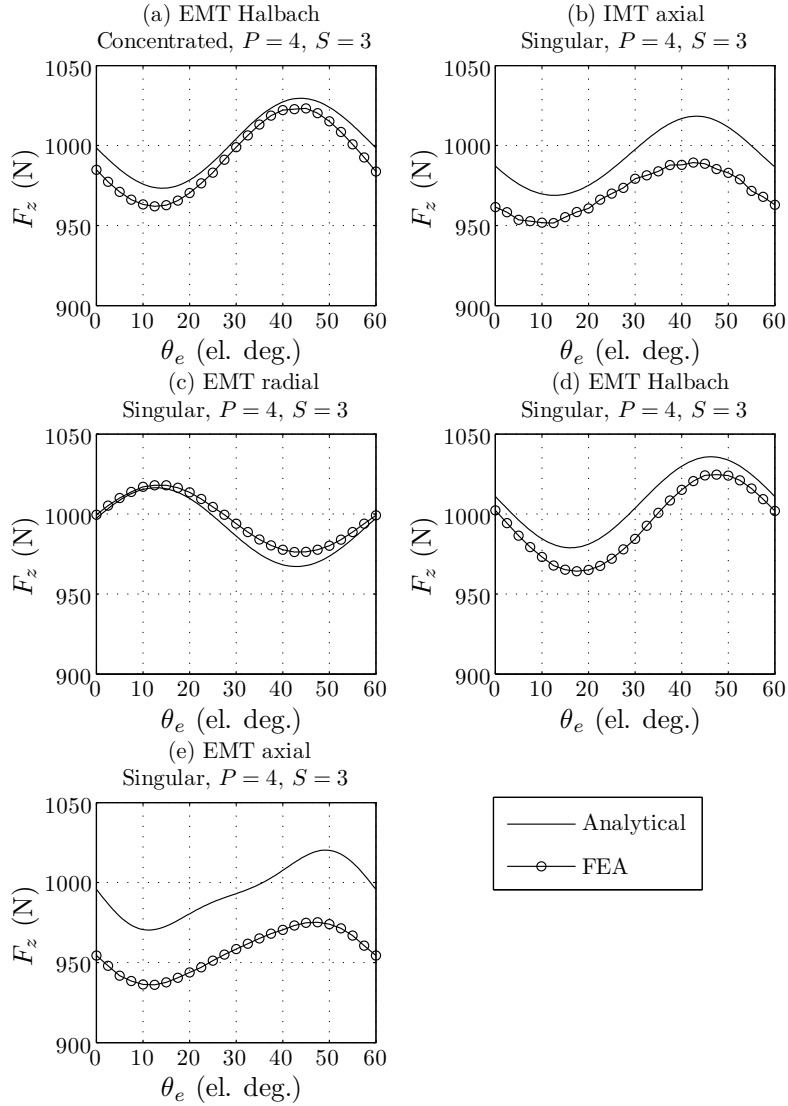


Figure 6.10: Force profiles of the optimized configurations of Table 6.3 for minimum copper losses verified with FEA.

6.8 Electromagnetic damping

This section considers the design of the integrated passive damping. First, the amount of integrated passive damping on the power consumption of the active suspension system is discussed. Consequently, the sizes and material selection for the conductive rings for the desired damping ratio are determined.

6.8.1 Fail-safe damping versus power consumption

Although the inclusion of passive damping incorporates a fail-safe function, it decreases the overall efficiency or energy consumption of the system. Since this passive damping is always apparent, the amount of dissipated kinetic energy cannot be recuperated by the system. Hence, the amount of necessary fail-safe damping should be kept to a near minimum. In this thesis, the definition of fail-safe and the corresponding amount of passive damping is not considered, but the dependency of the amount of passive damping on the energy consumption is given instead. Simulations are performed using the two DoF quarter car model, together with given road profiles and the active suspension system, where the amount of included damping, d_a , is considered as a parameter.

The total system is considered linear and linear quadratic Gaussian (LQG) control is applied for the objectives of improving comfort (reducing a_s) or improving handling (reducing z_t) constrained to a limited suspension travel (equal to the passive BMW suspension system) and actuator force ($\langle F_{act} \rangle = 1$ kN). A more detailed treatment on the controller design can be found in [69]. The total power delivered to the actuator, P_s , is assumed to consist of copper losses, P_{cu} , and mechanical output power, P_{me} . Induced eddy current and iron losses are contributed to the term d_a . The average power over a simulation time of one minute is determined for varying passive damping, d_a , on a smooth and rough road, respectively, for both objectives.

The results for the comfort objective are shown in Fig. 6.11(a) and (c) for a smooth and rough road, respectively. It can be observed that the actuator works in generation mode ($P_{me} < 0$) when d_a is smaller than 287 Ns/m and in motor mode beyond. For a comfort setting, the total damping is required to be relatively low and therefore the actuator forces are relatively low for a low passive damping, resulting in very low copper losses. For extreme low values of d_a , the system becomes regenerative, although the obtained power level is low (in the order of 10 to 20 W per corner). When the passive damping increases, the actuator needs to lower this passive damping, hence should work in motor mode and changes the system from delivering energy to consuming energy. The power levels for the tire load objective are shown in Fig. 6.11(b) and (d) for a smooth and rough road, respectively. The actuator works in generator mode up to 1845 Ns/m, since a tire load setting requires a very stiff suspension system (high damping). Furthermore, the copper losses are more significant since higher actuator forces are necessary. Therefore, the system never becomes regenerative for the handling setting. Although for the handling setting, the actuator works as a generator, all the energy is dissipated since extreme force levels are required to obtain the required handling.

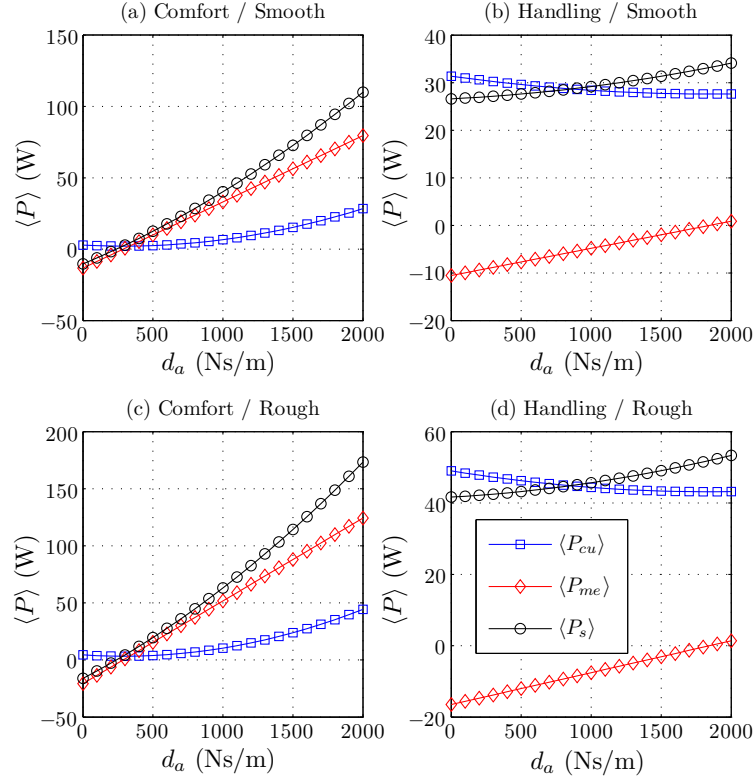


Figure 6.11: Average power consumption of the active suspension system as a function of the included fail-safe damping for improvement in comfort or handling on a smooth or rough road.

6.8.2 Design of the conductive rings

For the five optimal designs calculated in Section 6.7, the damping due to the soft-magnetic stator teeth is calculated with non-linear FEA at rated velocity and shown in Fig. 6.12 as a function of the relative position. It can be observed that the IMT axial magnetized topology gives the least amount of damping since the stator teeth have a higher circumference and smaller cross section, resulting in a higher resistance and damping force.

Consequently, the size of the conductive rings can be adjusted to obtain the total desired damping ratio of 1600 Ns/m. The required additional initial (low speed) average damping ratio due to the rings is given by

$$\langle d_{r0} \rangle = \langle d_{a0} \rangle - \langle d_{fe0} \rangle. \quad (6.27)$$

From a manufacturing point of view, the best method to vary the damping ratio is by considering the inner or outer radius of the rings equal to stator bore.

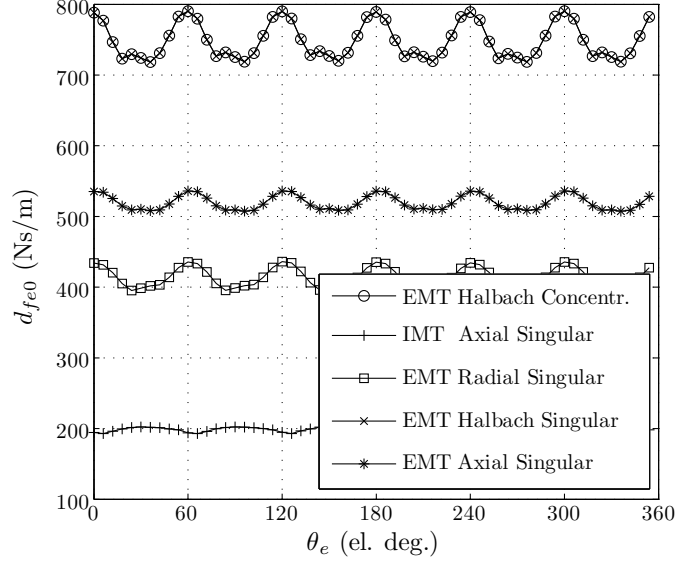


Figure 6.12: Damping ratio due to the soft-magnetic teeth as a function of relative displacement at a velocity of $v = 0.1$ m/s for the optimized configurations of Table 6.3.

Furthermore, considering the width of the rings equal to the width of the slot openings does not require additional filling material inside the slot opening. The only variational parameter is the height of the ring which is defined as

$$h_r = \frac{2R_i}{\left(\frac{N_{pa} S \pi \sigma_r \tau_o \sum_{n=1}^N n^2 |\Lambda_{rn}|^2}{2\tau_p^2 (\langle d_{a0} \rangle - \langle d_{fe0} \rangle)} \mp 1 \right)} \text{ for IMT or EMT.} \quad (6.28)$$

If the calculated height exceeds the available slot tip height ($h_r > h_t$), copper is used instead of aluminum. This is the case for all topologies, except for quasi-Halbach magnetization. For the IMT topology with axial magnetization, the damping due to the soft-magnetic material is relatively low. Even when using copper as conductive material, where the rings cover the full slot opening, a sufficient damping cannot be achieved.

The chosen design from hereon is the EMT quasi Halbach magnetization using a singular winding configuration, Fig. 3.4(d), since it has the lowest copper losses while achieving sufficient damping. Furthermore, the damping is more linear for this topology due to the lower inductance of the conductive rings.

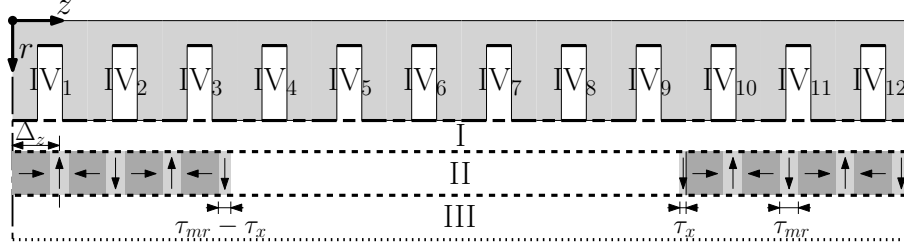


Figure 6.13: Division in regions for the semi-analytical calculation of the end-effects for the EMT with quasi-Halbach magnetization.

6.9 End-effects

For the EMT topology using quasi-Halbach magnetization, the finite length of the translator together with the slotted stator causes a force ripple referred as end-effects, F_{end} . For EMT topologies, the slot openings cause both the slotting effect and the end-effect. Therefore, these force ripples are not separable as for example done for IMT topologies [85]. Hence, an analytical model based upon harmonic modeling is constructed to calculate the force ripple resulting from the end-effect and the slotting effect. Minimization of the force ripple due to the end-effects for the quasi-Halbach EMT topology can be obtained by altering the width of the permanent magnets at the end of the translator. However, this results in an unbalanced magnetic loading and unbalanced emf waveforms. This causes additional undesired electromagnetic force ripples. Alternatively, the total translator length can be fixed but the final radial magnet can be divided among the left and right end of the translator. In order to calculate the resulting force ripple, the harmonic modeling technique can be used. The division in regions is shown in Fig. 6.13 where region II consists of two periodic sections of the permanent magnet array separated by a gap with a width of two periodic sections. The radial magnet at the end of the translator has width $\tau_{mr} - \tau_x$ for the right side and τ_x for the left side. The same set of boundary conditions is applied as shown in Fig. 3.8(b). Region V is not considered since the armature reaction is excluded.

The force profile as a function of the relative displacement, Δ_z , is calculated for τ_x ranging from zero to τ_{mr} . The peak force ripple, F_p , is shown in Fig. 6.14 as a function of τ_x/τ_{mr} . The minimum peak force ripple is obtained when the left and right side of the translator end with half a radial magnet. However, the relative decrement is only around 10 %. Since the width of the radial magnet for the optimal topology is only 2.4 mm, half a radial magnet is difficult and expensive to manufacture and the magnetization direction is not guaranteed. Because the benefit is small compared to the cost, the final radial magnet is not distributed among the left and right side, hence, $\tau_x = 0$.

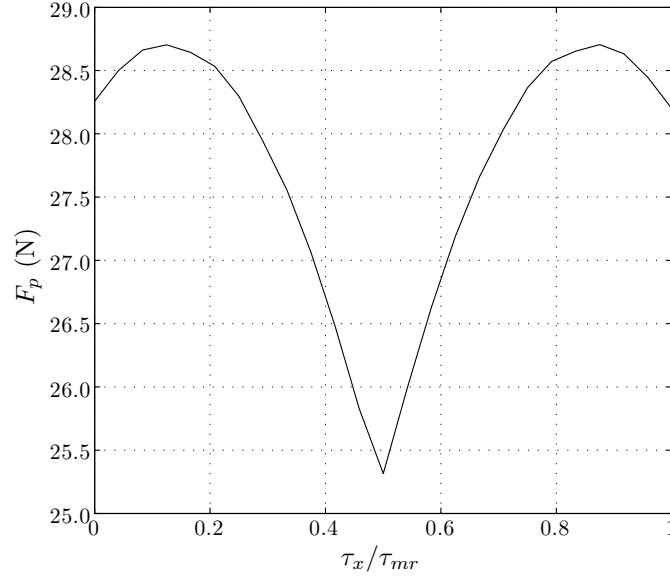


Figure 6.14: Peak force ripple as a function of the distribution of the final radial magnet on the left and right side of the translator.

6.10 Number of turns

The number of turns per coil have to be chosen such that, given maximum operating conditions, the total winding voltage does not exceed the specified dc bus voltage. Considering a dc bus voltage of $V_{dc} = 340$ V and a wye connected sinusoidal three phase actuator, the line voltage is given by $V_{ll} = \sqrt{3}V_{ph}$ where the phase voltage is the vectorial sum of the voltage drop over the phase resistance, the synchronous inductance and the induced emf voltage. The absolute value of the line voltage is then given by

$$|V_{ll}| = \sqrt{3((i_{ph}R_{ph} + e_{ph})^2 + (\omega L_{ph}i_{ph})^2)} < V_{dc}. \quad (6.29)$$

Given that $\omega = \frac{\pi v}{\tau_p}$, the maximum velocity is $v = 2$ m/s and the current corresponding to the peak force, the line voltage is 8.79 V per turn, giving a maximum of 38 turns.

In case a 12 V dc bus is considered, only a single turn per coil would be feasible. From a manufacturing point of view this is very hard to achieve. Therefore, during the optimization routine, one should limit the peak emf which would lower the magnetic loading and increase the electrical loading. This would decrease the obtained performance since the electrical loading is already limited by thermal constraints and hence has not much room for improvement. Therefore, considering efficiency and performance, a high dc bus voltage is preferred.

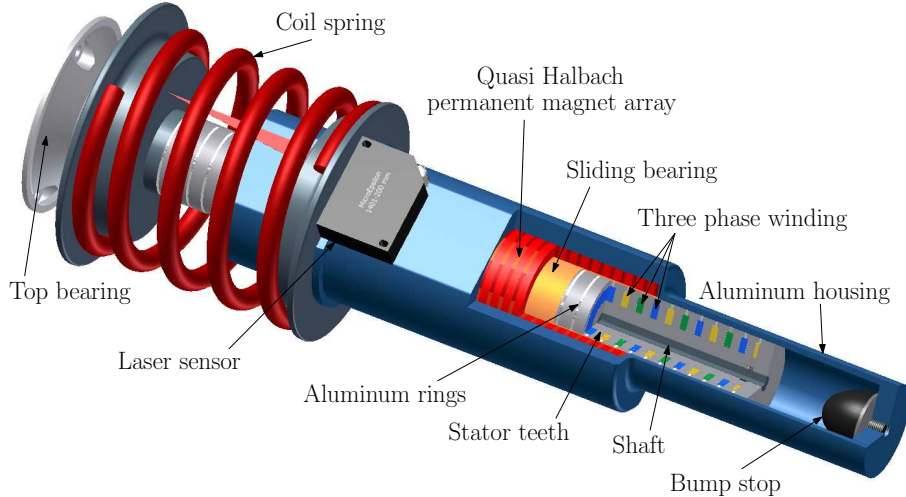


Figure 6.15: Final design of the active electromagnetic suspension system.

6.11 Final design

This section concludes the various design choices and results obtained in the previous sections of this chapter. The required force density could not be obtained using conventional steel and therefore, cobalt-iron alloy is considered as a soft-magnetic material. This significantly enhances the obtained force density of the EMT topologies which allows for a higher magnetic loading. For the available space envelope given in the benchmark vehicle, the singular winding topology with four poles per three slots gives the highest force density. The best efficiency, or lowest copper losses is obtained using the IMT with axial magnetization however the EMT with quasi-Halbach magnetization has an almost similar efficiency. The IMT with axial magnetization has significantly more end-effects due to the finite length of the stator and the use of pole pieces. On the other hand, the EMT with quasi-Halbach has a low end-effect force since the translator contains no soft-magnetic material.

Considering the integrated electromagnetic damping, the EMT with quasi-Halbach magnetization is favorable over the IMT with axial magnetization due to two reasons. First, the EMT exhibits a higher damping since the ferromagnetic stator teeth have a larger cross section and lower circumference, providing a lower resistance to induced eddy currents. Second, the inductance of the conductive rings of the EMT with quasi-Halbach magnetization is lower and position independent compared to the IMT with axial magnetization, resulting in a more linear damping characteristic in terms of position and speed dependency. Even more, the IMT topology is not capable of providing the necessary damping. The EMT with quasi-Halbach magnetization reached the necessary damping using aluminum rings covering the total slot opening. The list of final parameters and

Table 6.4: List of parameters of the final design.

Parameter	Value	Parameter	Value
Winding	Singular	τ_p	7.70 mm
N_{pa}	9	τ_{mr}	2.40 mm
N_{px}	4	τ_{mz}	5.30 mm
P	4	τ_s	5.10 mm
S	3	τ_{tt}	8.60 mm
h_{sbi}	8.27 mm	τ_o	1.67 mm
h_{tb}	3.00 mm	N_t	38
h_c	10.50 mm	$J_{sl_{RMS}}$	5.15 A/mm ²
h_m	8.00 mm	I_{RMS}	5.67 A
g	1.00 mm	$V_{il,max}$	334 V
h_t	3.23 mm	R_{ph}	1.42 Ω
h_s	5.00 mm	L_s	1.1 mH

sizes are listed in Table 6.4, and the total design of the suspension strut is shown in Fig. 6.15.

Regarding the position sensing, several options can be considered. An incremental encoder could be implemented where the ruler is integrated in the stator at the stator bore. However, the encoder head has to be integrated either at the top of the translator, within the coil spring or at the bottom. Both options require a reduction of the active length. Additionally, only the relative position is obtained, resulting in the necessity of homing at start-up to determine the absolute position with the help of a reference mark. Furthermore, the use of an encoder requires rotational alignment of the stator and translator with respect to each other. This would result in additional friction forces since compression of the coil spring results in rotational moments.

Alternatively, Hall sensors could be integrated at the center of the stator, at the stator bore. However, this requires additional cabling within the stator shaft. Additionally, the position accuracy is low and since the velocity has to be determined for correct commutation, this option results in poor performance. Therefore, the option of a laser sensor is chosen. It allows for easy installation, gives a sufficient position and velocity accuracy and provides an absolute position, hence, no homing is necessary. The disadvantage of a laser sensor is the fixed measurement delay, which results in inaccuracies at higher operating velocities. Therefore, a Kalman filter is used together with information of the acceleration sensors to determine the correct position.

Finally, the original top bearing of the passive BMW suspension system is connected at the top of the active suspension system as observed in Fig. 6.15. A bump stop is inserted in the bottom of the aluminum housing to reduce hard impact shocks exceeding the limited stroke.

6.12 Summary and conclusions

In this chapter, an automated optimization and design procedure is presented for the electromagnetic active suspension system including fail-safe damping. The non-linear programming algorithm is selected since it is appropriate for the considered optimization problem due to the ease of implementation. The optimization algorithm together with the analytical and semi-analytical tools of Part I are implemented in the same software environment, Matlab, improving the overall calculation time.

The geometrical integration of the TPMA within the coilover is discussed leading to a set of geometrical specifications for the TPMA. Furthermore, mechanical finite element calculations are performed to select the required thickness of the housing to exhibit sufficient mechanical strength to side load impacts. The permanent magnet material is selected to be NdFeB due to the high remanent flux density. For the soft-magnetic material, both conventional steel (steel 1010) and cobalt iron are considered during the optimization process.

The force density of each topology is optimized given the constraints of volume, force ripple, magnetic flux density and temperature. To obtain the required force density, cobalt iron should be used since it enhances the capability of the magnetic flux density in the stator for EMT which has a higher magnetic loading. The best performance is obtained with the singular winding topology with three slots per four poles. Consequently, the copper losses are minimized for the topologies achieving the required force density. The highest force per copper loss is obtained for the axial magnetized IMT. However, the force per copper loss of the quasi-Halbach EMT is only slightly lower.

Next, the sizes of the damping conductors are calculated to obtain the required damping ratio. The axial magnetized IMT offers a relatively low damping due to the low cross section and large radius of the stator teeth. Even with the additional damping conductors, the damping ratio is not sufficient. Therefore, the quasi-Halbach EMT is selected together with aluminum conductors. This topology offers a more linear damping characteristic with less ripple due to the absence of soft-magnetic pole pieces.

Furthermore, minimization of the end-effects is considered by means of dividing the final radial magnet over both ends of the translator since it does not alter the balanced magnetic loading. However, this method did not result in a significant minimization of the end effect ripple and is therefore disregarded. The number of windings are calculated for maximum operating conditions to match the inverter specifications. A laser sensor is chosen as position sensor due to the ease of integration, accuracy and non-necessity of homing since an absolute position measurement is obtained.

Chapter 7

Control and experimental verification

“The success of a technology results not always from its performance but from the guarantee not to fail.”

The experimental verification of the direct-drive electromagnetic active suspension system is presented in this chapter. First, the realization of the prototype is considered together with measurements of the magnetic flux density due to the permanent magnet array and the armature reaction of the stator. Second, the electromotive force, damping characteristic and force output of the suspension strut are measured. Third, after verification of the suspension strut, the quarter car test setup is presented. This setup mimics the vertical dynamics of one corner of the vehicle. Fourth, robust controllers are developed for both comfort and handling settings taking into account parameter variation of the vehicle corner. Consequently, the performance of these controllers and the active suspension system are verified on the quarter car test setup. Finally, two prototypes are installed in the front suspension of the benchmark vehicle and initial performance tests are undertaken.

The contribution of this chapter is published in:

Gysen, B. L. J., Paulides, J. J. H. and Lomonova, E. A. [2011a], Direct-drive electromagnetic active suspension system with integrated eddy current damping for automotive applications, *in* ‘The 8th International Symposium on Linear Drives for Industry Applications, LDIA 2011’, Eindhoven, The Netherlands, pp. 1–4.

Gysen, B. L. J., Paulides, J. J. H. and Lomonova, E. A. [2011a], ‘Direct-drive electromagnetic active suspension system with integrated eddy current damping for automotive applications’, *Mechatronics* (submitted).

Gysen, B. L. J., Sande, T. P. J. v. d., Paulides, J. J. H. and Lomonova, E. A. [2011], ‘Efficiency of a regenerative direct-drive electromagnetic active suspension’, *IEEE Transactions on Vehicular Technology* **60**(4), 1384–1393.

Sande, T. P. J. v. d., Gysen, B. L. J., Besselink, I. J. M., Paulides, J. J. H., Lomonova, E. A. and Nijmeijer, H. [2011], Robust control of a direct-drive electromagnetic active suspension system, *in* ‘The 8th International Symposium on Linear Drives for Industry Applications, LDIA 2011’, Eindhoven, The Netherlands, pp. 1–4.

Sande, T. P. J. v. d., Gysen, B. L. J., Besselink, I. J. M., Paulides, J. J. H., Lomonova, E. A. and Nijmeijer, H. [2011], ‘Robust control of a direct-drive electromagnetic active suspension system’, *Mechatronics* (submitted).

7.1 Realization of the prototype

The realized prototype is the final design obtained in Chapter 6 with the only difference that a concentrated winding is considered instead of a singular one. Singular winding configurations were not yet considered at the time the prototype was developed. Since these winding configurations are magnetically identical, the sizes are equal. Additionally, the resulting damping characteristic is equivalent. The only difference is a lower number of turns ($N_t = 22$) since the induced emf is higher. Furthermore, the continuous force per copper loss is lower as is shown in Table 6.3. However, this prototype is still a feasible solution, especially for validation of the semi-analytical modeling and design method.

7.1.1 Permanent magnet array

The quasi-Halbach permanent magnet array consists of alternating axially and radially magnetized magnets. However, the radially magnetized magnets are difficult to magnetize and a radial ring magnet is therefore approximated by a finite number of parallel magnetized magnets, as shown in Fig. 7.1(a). The number of parallel magnets is chosen to be twelve to assure approximate radial magnetization. In [108], the influence on the segmentation is investigated, and it is shown that eight segments only introduce an error of 1 %, hence a lower number of segments might be chosen, hereby reducing costs. The permanent magnet array is glued on a PTFE sliding bearing, as shown in Fig. 7.1(b).

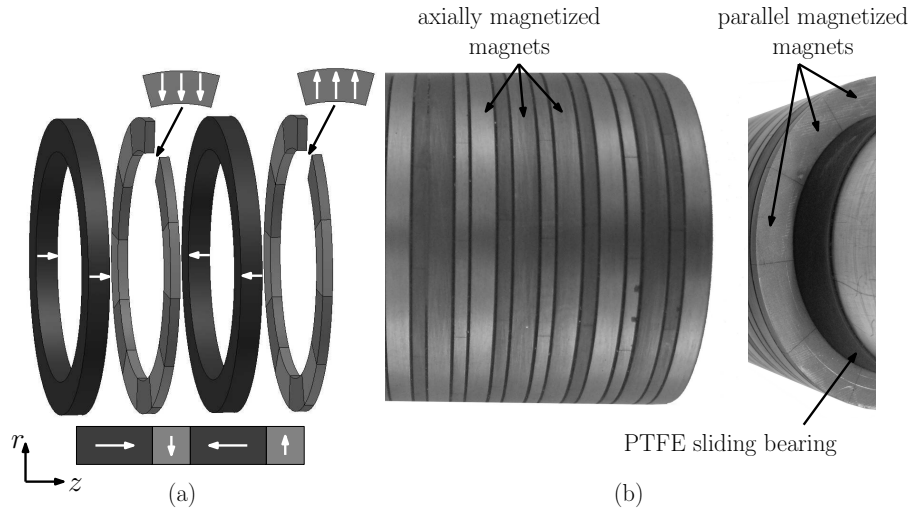


Figure 7.1: (a) Exploded view of one pole pair (four magnet rings) and (b) picture of the permanent magnet array.

The radial and axial component of the magnetic flux density, $B_{pm,r}$ and $B_{pm,z}$, of the stand-alone permanent magnet array are measured, at a 2 mm distance from

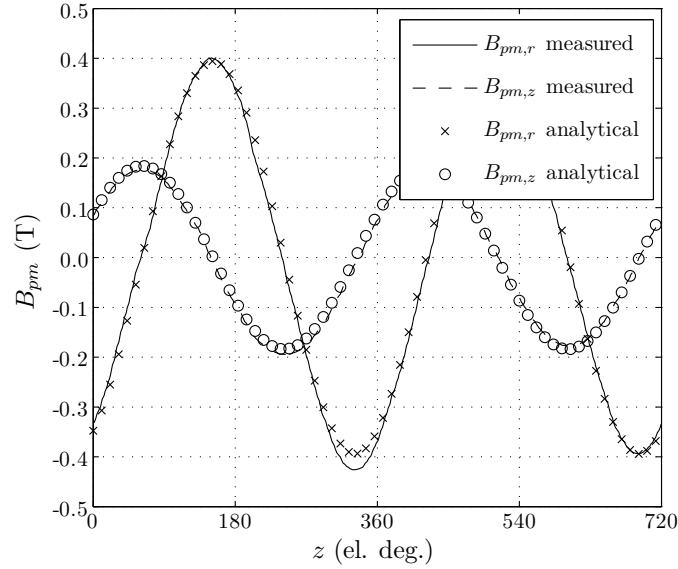


Figure 7.2: Magnetic flux density due to the permanent magnet array, at a radius 2 mm below the inner radius of the magnet array, measured on a test setup and calculated with the semi-analytical model.

the inner radius of the magnet array, with a flux-probe and verified with the semi-analytical framework of Chapter 2. The results are shown in Fig. 7.2, where a very good agreement is obtained. The segmentation of the radial magnets results in a slight variation of the amplitude in both flux density components since the angular positions of the transition of the segments are randomly orientated to distribute this effect. From these measurements it can be concluded that the properties of the permanent magnets as well as the resulting magnetic flux density distribution are well predicted. Additionally, the influence of radial magnet segmentation is negligible.

7.1.2 Stator assembly

The stator consists of an array of segments where each segment consists of one tooth, two coils, two lead wires and one aluminum ring. The exploded view of one segment is shown in Fig. 7.3(a). Each coil has a filling factor of $k_f = 0.79$ due to the use of profile wire with single sided insulation. The two coils are positioned on the left and right side of the tooth and are enclosed by Nomex insulation paper of 0.35 mm thickness. The coils are interconnected by a lead wire inserted in a hole through the tooth tip. Another lead wire is connected at the inner radius of the coil which connects the consecutive segment of the particular phase. Each segment is rotated by 120 degrees with respect to each other to guide the lead wires as shown in Fig. 7.3(b). A star connection is made in the final end-tooth

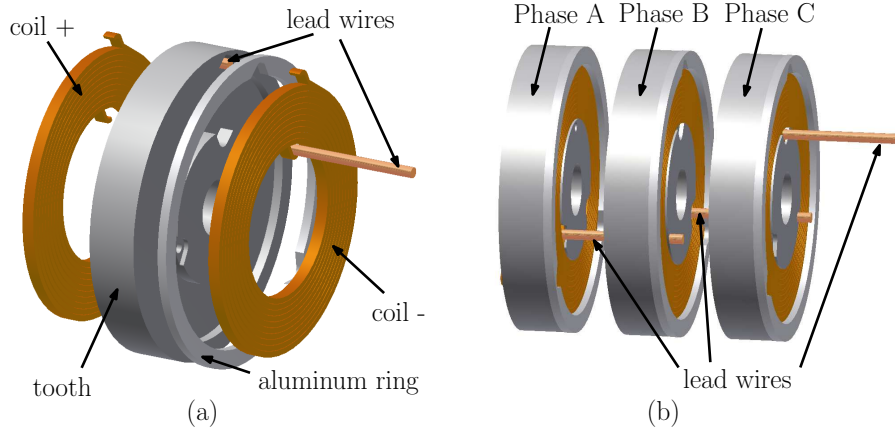


Figure 7.3: Exploded view of (a) one segment (b) three segments.

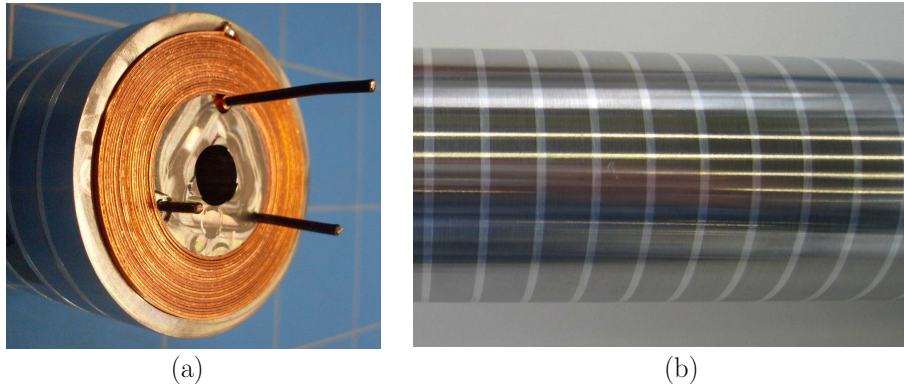


Figure 7.4: Image of (a) the interior of the stator and (b) the finished surface.

at the bottom of the stator, access is provided to perform measurements. A view of the interior of the stator assembly is presented in Fig. 7.4(a) with the finished stator surface shown in Fig. 7.4(b), where the aluminum rings can be observed.

The radial and axial component of the armature reaction field, $B_{arm,r}$ and $B_{arm,z}$, are measured with a flux probe at 2 mm distance from the stator bore as a function of the axial displacement. The stator windings are excited with a dc current of $i_{ph,A} = 4$ A for phase A and $i_{ph,B} = i_{ph,C} = -2$ A for phases B and C. The measured radial and axial flux density component of the armature reaction field are shown in Fig. 7.5 and compared with the semi-analytical model where a very good agreement is obtained. It can be concluded that the semi-analytical model considering armature reaction is correct and that the adaptations of the teeth for guidance of the lead wires have no significant effect on the resulting magnetostatic field distribution.

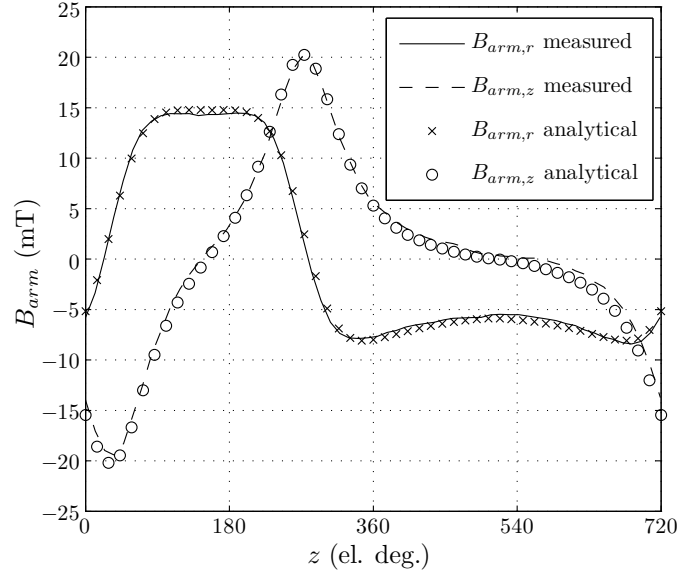


Figure 7.5: Magnetic flux density due to the armature reaction, at a radius 2 mm above the stator bore, measured on a test setup and calculated with the semi-analytical model.

7.1.3 Strut assembly

The stator assembly is connected to a spring disc for positioning of a coil spring. A top bearing is attached on top to form the total sprung part of the suspension system as shown in Fig. 7.6(a). A thermocouple is inserted in the center axis to monitor the temperature. The permanent magnet array is inserted and glued into an aluminum housing which forms the translator and unsprung part of the strut as shown in Fig. 7.6(b). Another spring disc is attached for supporting the coil spring to the unsprung part of the suspension. Furthermore, a bump stop is inserted for the absorption of extreme impacts. The stator is inserted into the sliding bearing and a coil spring is positioned between the two spring discs to form the total assembly of the active suspension system as shown in Fig. 7.6(c).

The mass of the total unsprung part is 6.47 kg which is around 14 % of the total unsprung mass. The mass of the sprung part is 8.06 kg and the coil spring, connecting the sprung and unsprung part weighs 2.9 kg. In total, the suspension strut has a mass of 17.43 kg compared to the passive suspension which has a mass of around 5 kg. The mass of the developed suspension system is therefore, within the predetermined specifications. Although, this system contributes to a total increase of the vehicle mass, other suspension components like anti-roll bars could be excluded, hereby reducing the total added mass. Mechanical optimization of the aluminum housing of the translator could minimize the mass even further.

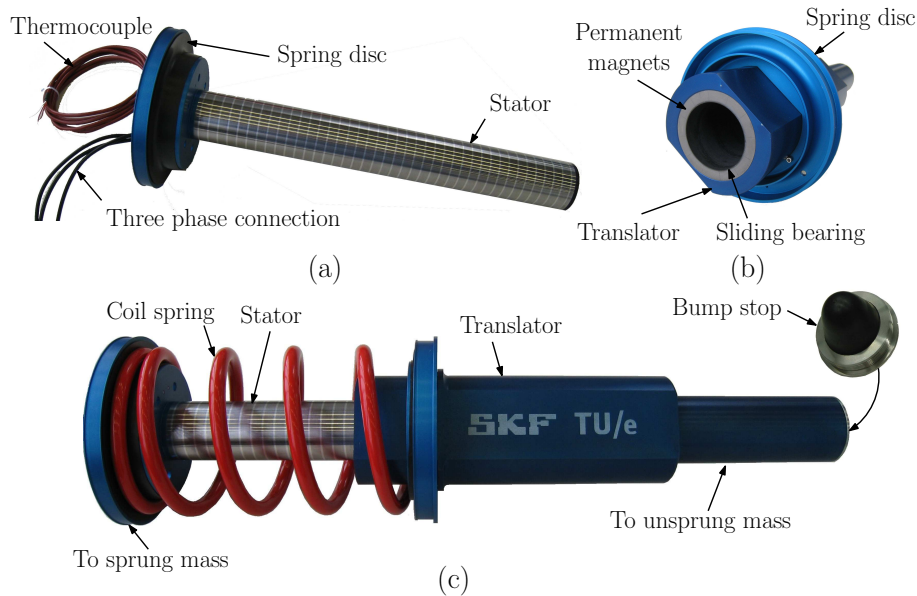


Figure 7.6: (a) Sprung part, (b) unsprung part and (c) complete assembly of the active electromagnetic suspension system.

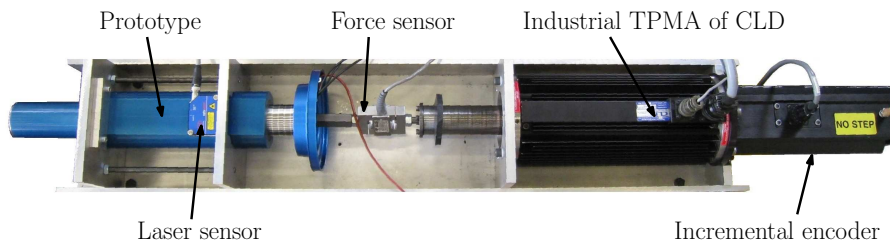


Figure 7.7: Test bench with the prototype and the industrial TPMA.

7.2 Experimental verification of the active suspension strut

The determination of the passive and active characteristics of the prototype is performed on the test bench shown in Fig. 7.7. This test bench couples the prototype to an industrial tubular actuator via a force sensor. The mechanical spring is excluded in this setup. The industrial TPMA is from California Linear Drives (CLD) [27], type 40206D and used as a prime drive. The displacement of the industrial tubular actuator is measured with an incremental encoder with a resolution of $1 \mu\text{m}$. The displacement of the prototype is measured with a laser sensor of Micro-Epsilon [111], type optoNCDT 1402, with an accuracy between $13 \mu\text{m}$ and $100 \mu\text{m}$. The force sensor is a load cell, model 616 of TedeA [141] with a capacity of 500 kg and an error of 0.03 % of the rated load.

7.2.1 The electromotive force

The phase emf is measured while the actuator is moved by the CLD actuator at constant velocity. First, a measurement at a very low velocity is performed, $v = 0.05$ m/s, to obtain the emf waveforms without significant influence of the eddy current effect. The waveforms are shown in Fig. 7.8 together with the semi-analytical and FEA verification. The difference between the semi-analytical and FEA model occurs due to the eddy current effect and non-linearity of the soft-magnetic material. Changes in the design during the manufacturing stage were made, producing the tooth width slightly smaller, increasing the saturation of the actuator. This causes a lower emf waveform than predicted by the semi-analytical model. The difference between the FEA and the measurements are due to manufacturing tolerances, necessary holes for lead wires, connections and unavoidable airgaps between the stator segments. A measurement at a velocity of $v = 1$ m/s shows a similar agreement with the FEA model, the eddy current effect is obviously more significant which is not included in the semi-analytical model. The emf constant and the phase shift dependent on the velocity are shown in Fig. 7.10 together with a first order fit. Due to the eddy current effect the emf constant and phase shift drops linearly depending on the velocity as was shown in Section 4.4. The first order fit for the emf constant and phase shift are given by

$$K_e = K_{e0}(1 - K_{e,v}v), \quad (7.1)$$

$$\phi_e = -K_{ph,v}v, \quad (7.2)$$

where the initial emf constant is $K_{e0} = 80$ Vs/m, and the emf velocity dependency constant is $K_{e,v} = 0.13$ s/m. The phase shift of the emf waveform per velocity is $K_{ph,v} = 23.8$ deg s/m. These first order fits are used for the commutation of the stator currents to obtain maximum force output, equation (4.55).

7.2.2 The cogging and end-effect force

For the verification of the cogging and end-effect force, the actuator is moved at a very low speed $v = 5$ mm/s to eliminate the eddy current effect while the force profile is measured. The result is shown in Fig. 7.11 for 720 electrical degrees which corresponds to the displacement over one periodic section. It can be observed that the fundamental waveform has a periodicity of 240 electrical degrees which indicates that this ripple predominantly results from the end-effects. Since the end of the magnet array moves along the slotted stator, the ripple repeats over each slot pitch, which is $\frac{P180}{5} = 240$ electrical degrees. The slotting effect has a periodicity of 60 electrical degrees and has a significant less amplitude than the end-effect. The peak ripple is around the specified 10 % of the mean force which is 100 N peak to peak. A good agreement is obtained with the semi-analytical method and FEA.

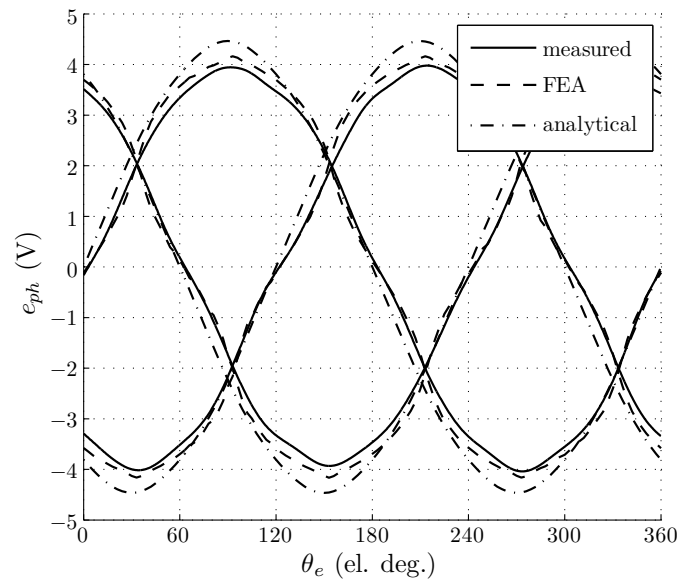


Figure 7.8: Electromotive force at a velocity of $v = 0.05$ m/s, measured and calculated with FEA and the semi-analytical model.

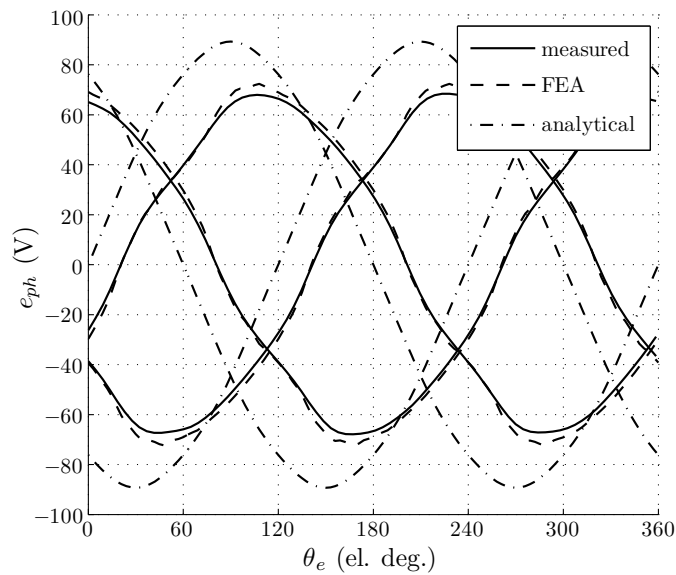


Figure 7.9: Electromotive force at a velocity of $v = 1$ m/s, measured and calculated with FEA and the semi-analytical model.

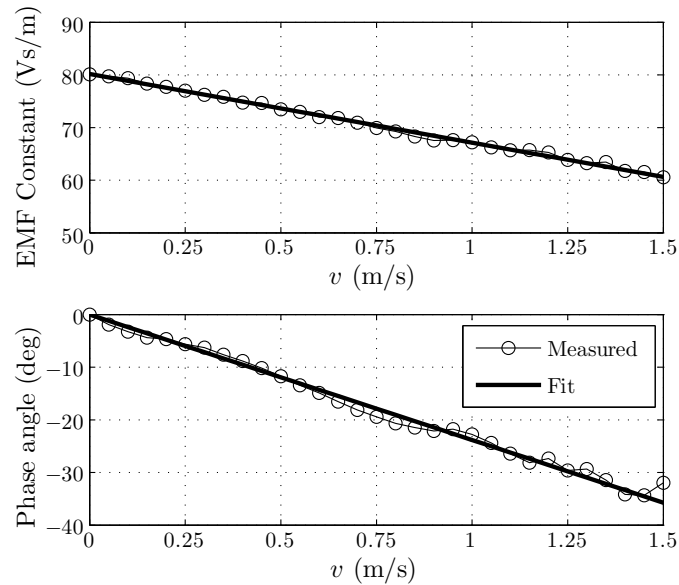


Figure 7.10: Measured emf constant and phase angle as a function of the velocity together with a first order fit.

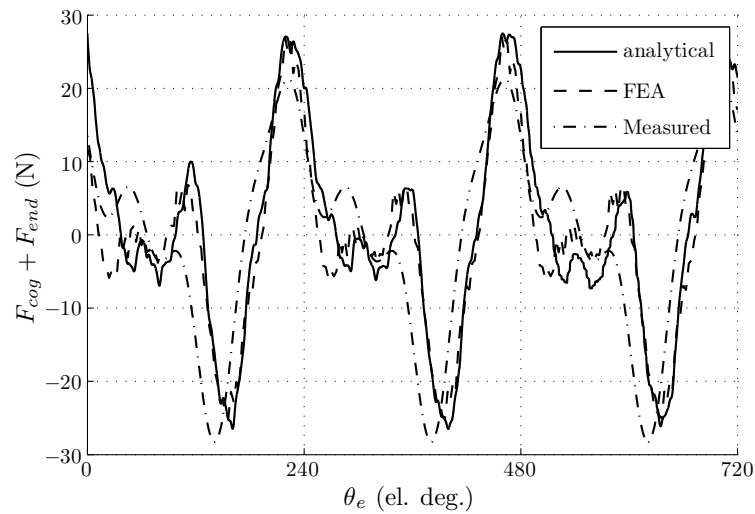


Figure 7.11: Cogging force and end-effects as a function of the relative displacement, measured and calculated with FEA and the semi-analytical model.

7.2.3 The damping force

The damping force is measured using a standard VDA (Verband Der Automobilindustrie) test. The test prescribes sinusoidal motions with an amplitude of 50 mm

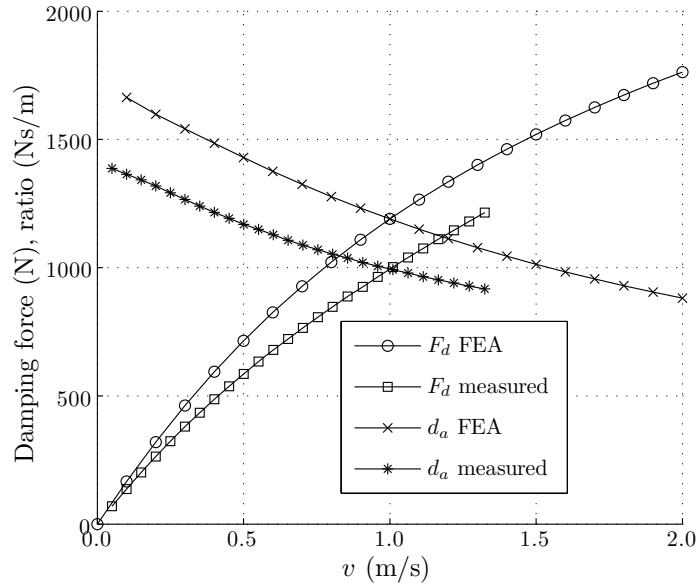


Figure 7.12: Damping force and ratio, measured and predicted using FEA.

with varying frequencies up to a peak velocity of 1.05 m/s (3.33 Hz). However, higher velocities, up to 1.35 m/s are included. Higher velocities could not be obtained due to the limited performance of the industrial TPMA. Five periods were considered for each frequency and the resulting force response is measured using a force sensor. The results are shown in Fig. 7.12 together with the FEA.

It can be observed that the measured response is 11 % lower than the FEA. In Fig. 7.3(a), the tooth assembly is shown, where a slit is made in the aluminum rings for the lead wire. This slit increases the resistance of the ring by 6 %. Additionally, slits and holes are made in the tooth for the lead wires and the coil connections. These holes pass the tooth at the coil radius ($r = R_c$), where normally, the maximum induced eddy currents are obtained. Therefore, these holes have a significant influence on the reduction of the eddy current damping. Although the damping is lower than predicted, a fail-safe behavior is still obtained. In order to improve the damping, alternative possibilities for interconnection of the coils and lead wires have to be considered.

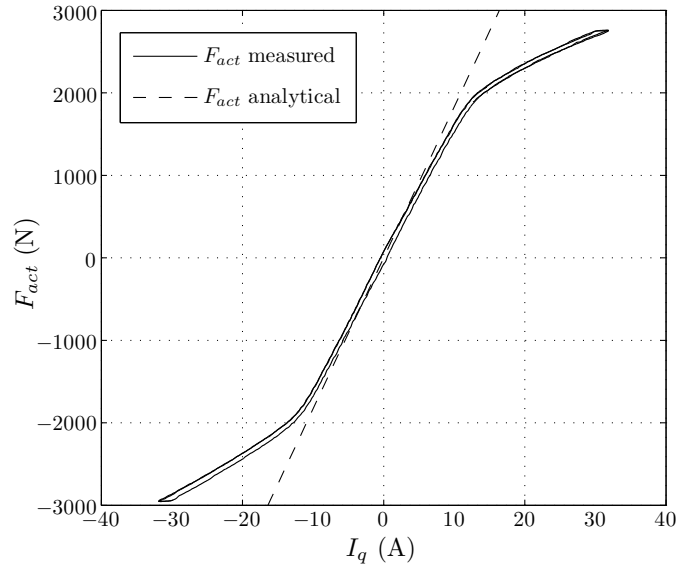


Figure 7.13: Measured active force versus RMS quadrature current together with analytical prediction.

7.2.4 The active force

The developed output force as a function of the RMS quadrature phase current, I_q , is measured. The response is shown in Fig. 7.13 together with the characteristic of the analytical model which assumes a pure linear response. The measured response is linear up to a force of $F_{act} = 2$ kN, which is twice the rated force, at a rate of $K_i = 161$ N/A compared to 181 N/A predicted with the analytical model. This difference has the same cause as the difference in the emf waveform shown in Fig. 7.8. Beyond the force of 2 kN, saturation due to the armature reaction decreases this rate to 45 N/A. Due to the magnetic hysteresis of the soft-magnetic material, the force characteristic inhibits a hysteresis of ± 75 N.

The response to a step force command of 500 N is measured to determine the bandwidth of the actuator force. The response is shown in Fig. 7.14 together with the 10 % margin of the final value. The response remains within this margin after 8 ms, resulting in a bandwidth of around 125 Hz. The overshoot is partly caused by the relatively low inductance of the actuator ($L_s = 1.1$ mH), causing an overshoot in the current control loop of the inverter, and partly by the finite stiffness of the measurement setup. However, for the given application, a sufficient bandwidth is obtained.

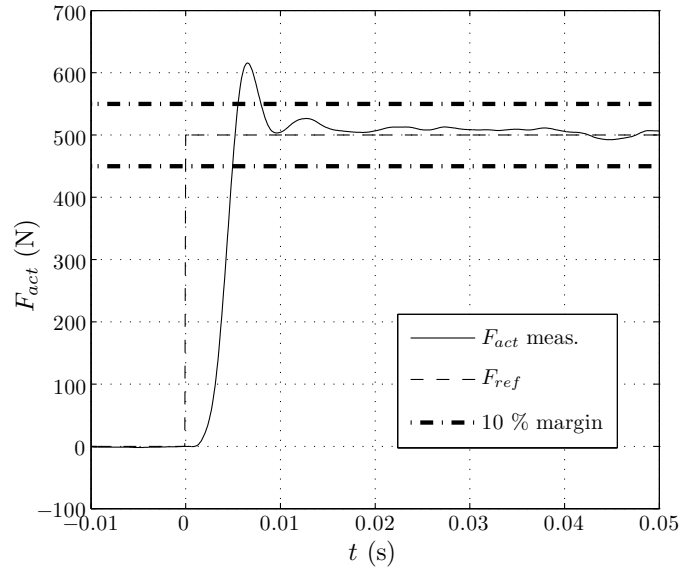


Figure 7.14: Step response of the active force.

7.3 Quarter car test setup

This section describes the quarter car test setup, together with the control of the actuation system for performing prescribed road vibrations. The performance of the test setup is identified and verified with the two-DoF quarter car model.

7.3.1 Description of the setup

To verify the performance of the active suspension system and the developed control algorithms, a quarter car test setup is built. This setup shown in Fig. 7.15 represents the vertical dynamics of a single corner of the BMW 530i on full scale. Three vertically aligned moving masses can be distinguished, the mass of the road actuation, M_r , with position, z_r , the unsprung mass, M_u , with position, z_u , and the quarter sprung mass, M_s , with position, z_s .

The mass of the road actuation is coupled to the fixed world via a mechanical spring, $k_r = 29$ kN/m, for gravitation compensation of the total setup. In parallel, the industrial TPMA, used for verification of the prototype in Section 7.2, provides the road vibrations by applying the proper force F_{ra} , further referred as road actuator. The mass of the road actuation and the unsprung mass are connected via a mechanical spring representing the tire stiffness. The sprung and unsprung mass are coupled via the suspension strut. A closer view of to the unsprung mass is shown in Fig. 7.16.

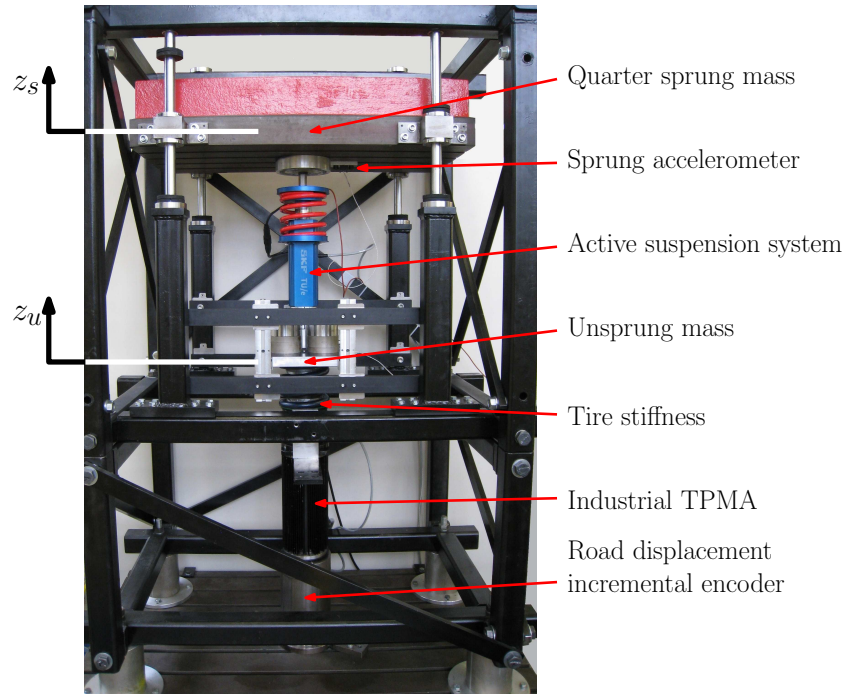


Figure 7.15: Quarter car setup including active suspension

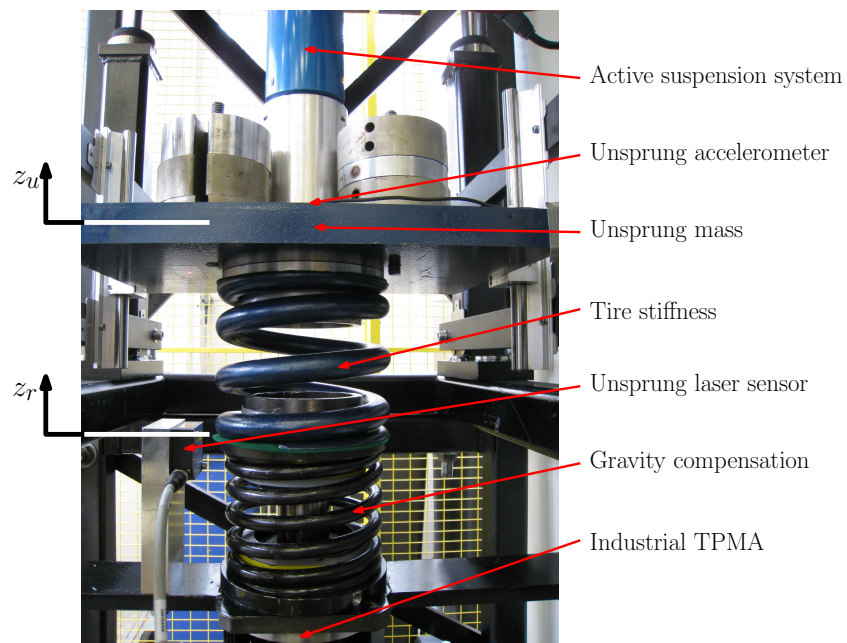


Figure 7.16: Detailed side view of the quarter car setup.

Five sensors are installed, the incremental encoder of the industrial TPMA measures the road position, z_r , the laser sensor attached to the suspension system measures the suspension travel, Δ_z , a Kistler 8330A3 (3g) accelerometer measures the sprung acceleration, a_s , the unsprung acceleration, a_u , is measured using a Kistler 8305B50 (50g) accelerometer and finally, the absolute unsprung position, z_u , is measured using the same laser sensor as for the suspension travel. From this sensor set, only three inputs are used for control of the active suspension, the sprung and unsprung acceleration and the suspension travel, (a_s, a_u, Δ_z) , as explained in Section 5.8.

The quarter car setup has two inputs, the force of the active suspension system, F_{act} , and the force of the road actuator, F_{ra} . The dynamics of the setup can be described using the following set of differential equations

$$M_{s,q}a_s = -k_a(z_s - z_u) - d_a(v_s - v_u) + F_{act}, \quad (7.3)$$

$$M_u a_u = k_a(z_s - z_u) + d_a(v_s - v_u) - F_{act} - k_t(z_u - z_r), \quad (7.4)$$

$$M_r a_r = k_t(z_u - z_r) - k_r z_r + F_{ra}. \quad (7.5)$$

Based upon this set of equations, the control of the road actuation system is designed.

7.3.2 Control of road actuation

The control structure for the road actuator is shown in Fig. 7.17. A loop shaping controller with notches, $C_{r,ff}$, is used to control the road actuator which should follow a given reference road profile, $z_{r,ref}$. Since forces from the active suspension system disturb the road input, feed forward control, $C_{r,ff}$, is applied to counteract these forces and to guarantee a correct road profile. Fig. 7.18 shows the open loop transfer function from F_{ra} to z_r not considering disturbance forces from the active suspension system, $F_{act} = 0$. Notable are the 1.45 Hz resonance of the sprung mass and the 33.5 Hz resonance of the road actuator mass, M_r . A loop shaping feedback controller with notches, $C_{r,fb}$, is therefore designed to obtain a closed loop bandwidth of 30 Hz. The feed forward force is determined from the transfer function from F_{act} to the reaction force on the mass M_r , denoted by $F_{ra,act} = M_r a_r$. This transfer function can be derived using the differential equations of Section 7.3.1. The feedback and feed forward controller are both listed in Appendix C.1.

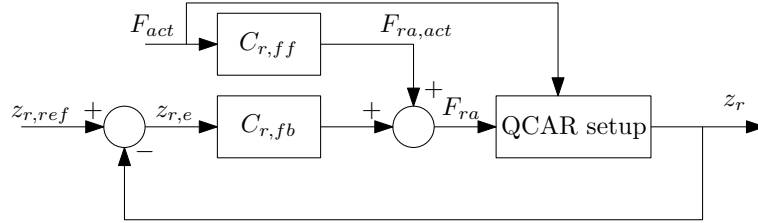
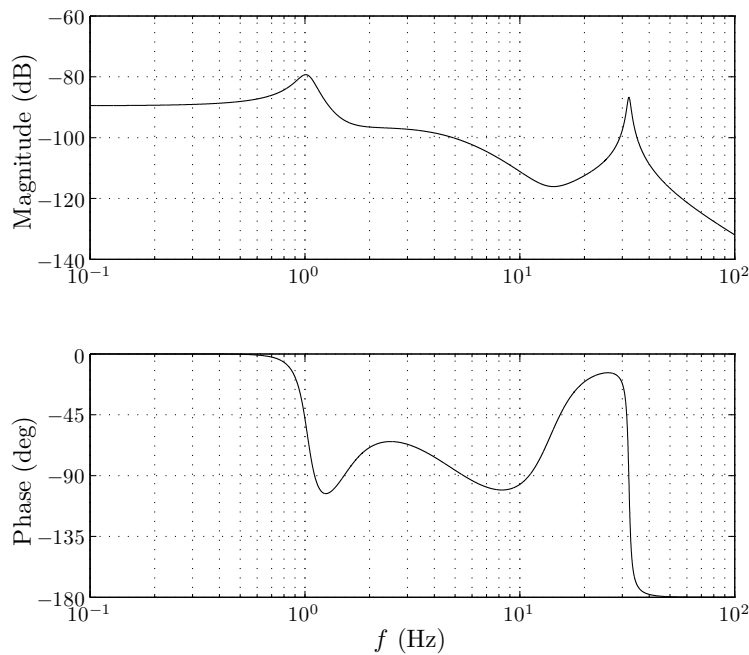


Figure 7.17: Control scheme for the road actuator.

Figure 7.18: Open loop transfer function of F_{ra}/z_r for $F_{act} = 0$.

7.3.3 Identification

To validate the performance of the quarter car test setup, the power spectral density of the road displacement, sprung and unsprung acceleration and suspension travel are measured and compared with the simulation model. The used suspension system in the simulations and the measurements is the passive BMW suspension system. A smooth road profile is used for both cases and the resulting PSD spectra are shown in Fig. 7.19. The road input signal is followed up to 30 Hz, which is sufficient since the human sensitivity to vibrations is dominant up to 12 Hz. Furthermore, the sprung acceleration, unsprung acceleration and suspension travel have a very good agreement up to 30 Hz. The small differences are caused by friction in the bearings and setup misalignment. Furthermore, transmission of vibrations through the construction of the test setup causes

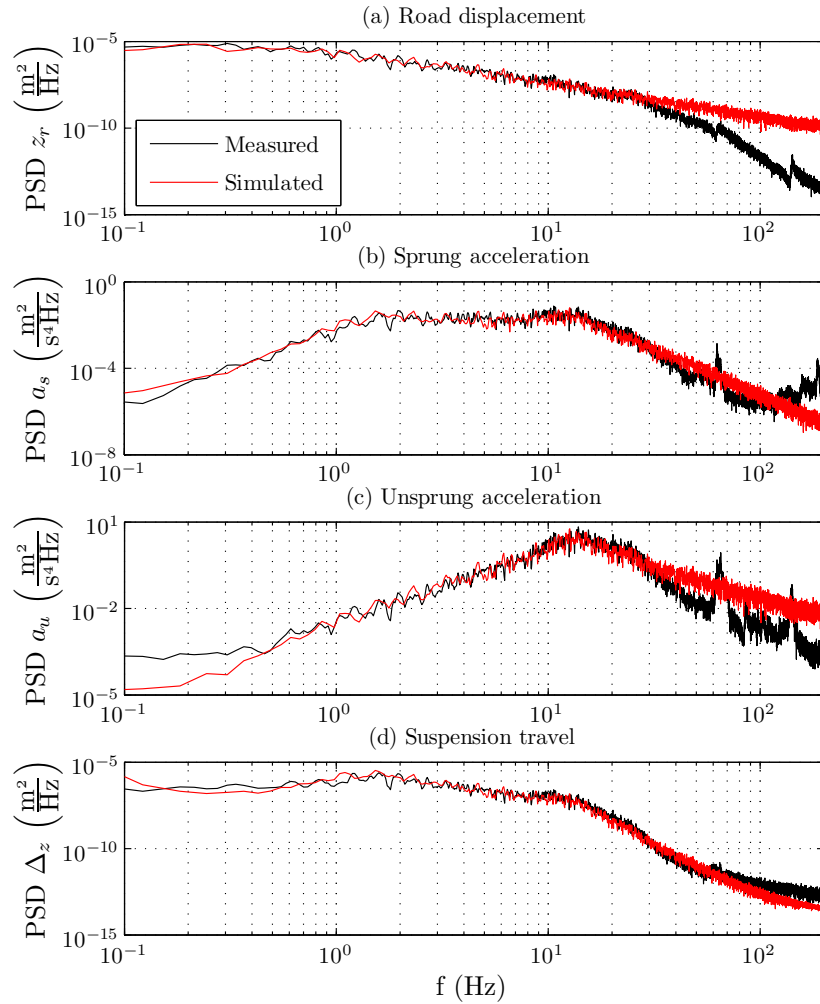


Figure 7.19: Power spectral densities (PSDs) of the road displacement, sprung and unsprung accelerations and suspension travel simulated and measured on the quarter car test setup.

higher measured accelerations. Figure 7.19 also shows resonances at 64.5 Hz and 141 Hz, these are parasitic resonances of the gravity compensation spring, k_r , tire spring, k_t , and suspension spring, k_p , respectively. Since these resonances are outside the region of interest, the setup is considered representative for the vertical dynamics of a vehicle corner.

7.4 Robust control of the vehicle corner

Control of active suspension systems dates back from the 1970's when the computational performance of micro-controllers was developing rapidly. Ever since, numerous papers have been written on the control of active suspension systems. They can be classified according to the applied control strategy. The most commonly used strategies are skyhook [77, 88], optimal control (LQR/LQG) [110, 149], robust control (H_∞ and μ -synthesis) [96, 162], fuzzy logic [130] and adaptive control [23].

Skyhook damping is based on connecting the sprung mass to a virtual inertial reference frame with a skyhook damper. This reduces the body accelerations but increases the tire forces and hence, an additional virtual damper is introduced which connects the wheel with the ground, referred as groundhook damping. As such, a trade-off is obtained between comfort and handling. This method is favorable due to its simplicity and low computational requirements. The use of optimal control requires the exact knowledge of the systems parameters and measurement of the full state. This technique is therefore only 'optimal' in case the systems behavior is linear and variations in parameters are small. Furthermore, the full state is not observable and therefore, state estimation is required which deteriorates the performance. Evenmore, the stability cannot be guaranteed using a state estimator [36]. A fuzzy logic controller determines the control force based upon a set of rules. This control algorithm is preferable for systems with a high level of uncertainty. The downside of this method is that stability and performance cannot be guaranteed and trial and error is necessary to consider proper functioning under all conditions. Robust control has the capability of including a certain degree of uncertainty or parameter variations. Furthermore, the performance can be defined in the frequency domain using weighting filters. The downside of this method is its complexity and the high order of controllers which is computational expensive. Adaptive control can be applied for all the previous control structure in which the parameter of the controller depend on the road conditions, vehicle state and driver inputs.

The vertical behavior of a vehicle can be estimated using the quarter car model with a certain degree of variation in sprung mass, tire pressure and damping ratio of the suspension system. Furthermore, the body acceleration and dynamic tire load should be reduced in different frequency bands. To guarantee stability and performance in a broad range of operating conditions, a robust control scheme is preferable. Although an H_∞ -controller provides more stability and performance with respect to plant or system variations, the actual performance is less compared to an optimal controller for the nominal plant. Furthermore, the variations in inputs (road disturbances and driver inputs) are large and in that respect, it is more beneficial to consider adaptive control to provide a higher level of performance under any conditions. However, this thesis considers the performance of an H_∞ -controller as a benchmark result for future development of control strategies.

Table 7.1: Uncertainties of the quarter car model.

Parameter	Symb.	Type	Nom. value	RMS Deviation
Quarter sprung mass	M_{qs}	Parametric	395.3 kg	-10.8/+19 %
Tire stiffness	k_t	Parametric	340 kN/m	± 8.8 %
Damping coefficient	d_a	Parametric	1450 Ns/m	-37.9/+17.24 %
Sprung acc.	a_s	Sensor noise	0 m/s ²	± 0.024 m/s ²
Unsprung acc.	a_u	Sensor noise	0 m/s ²	± 0.178 m/s ²
Suspension travel	Δ_z	Sensor noise	0 m	± 0.002 m

7.4.1 Parameter variation

To improve the comfort and handling of the vehicle, the force of the suspension system has to be controlled based upon the sensor inputs. The vertical dynamics of one vehicle corner are considered which govern the dynamic equations given in Section 5.5. However, the parameters of the vehicle corner are not fixed. The vehicle mass changes due to additional passengers, loading or fuel. Furthermore, the tire pressure and stiffness can vary and the damping ratio varies dependent on velocity and temperature. In Table 7.1, the percentual variations of the three parameters are listed together with their nominal values. These variations are included as a parametric uncertainty, hence, the parameter can have any value in the given set defined by its minimum and maximum. Additionally, sensor measurements are not considered ideal and contain a certain noise level as depicted in Table 7.1.

7.4.2 Robust control structure

The quarter car model described by the differential equations (5.5)-(5.6) with the nominal parameters given in Tables 5.1 and 7.1 is considered to be the nominal plant, $G(j\omega)$. This multi-input-multi-output (MIMO) system has two inputs, the road displacement, z_r , and the actuator force, F_{act} . The four considered outputs are the sprung, a_s , and unsprung acceleration, a_u , the suspension travel, Δ_z , and the tire compression, z_t . The variations in the parameters mentioned in the previous section are modeled as a parametric uncertainty, indicated by the Δ_p -block in Fig. 7.20. Furthermore, dynamic uncertainty (uncertainty defined in the frequency domain) is added since the model assumes ideal masses, springs and dampers which leads to a description which is only valid for relatively low frequencies. This dynamic uncertainty is defined as a multiplicative uncertainty, $G_p = G(I + W_{un}\Delta_I)$, as shown in Fig. 7.20. These two types of uncertainties together with the nominal plant define the set of perturbed plants, G_p .

The total robust control structure is illustrated in Fig. 7.21 where the uncertain plant, G_p , has two inputs and four outputs. As was explained in Section 5.8, only three outputs are fed to the controller, the sprung and unsprung acceleration and the suspension travel, together with an added noise level indicated

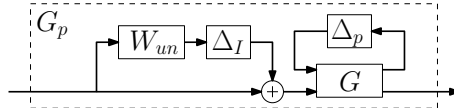


Figure 7.20: The uncertain plant (G_p) with parametric uncertainty, Δ_p , and unmodeled dynamics as input uncertainty.

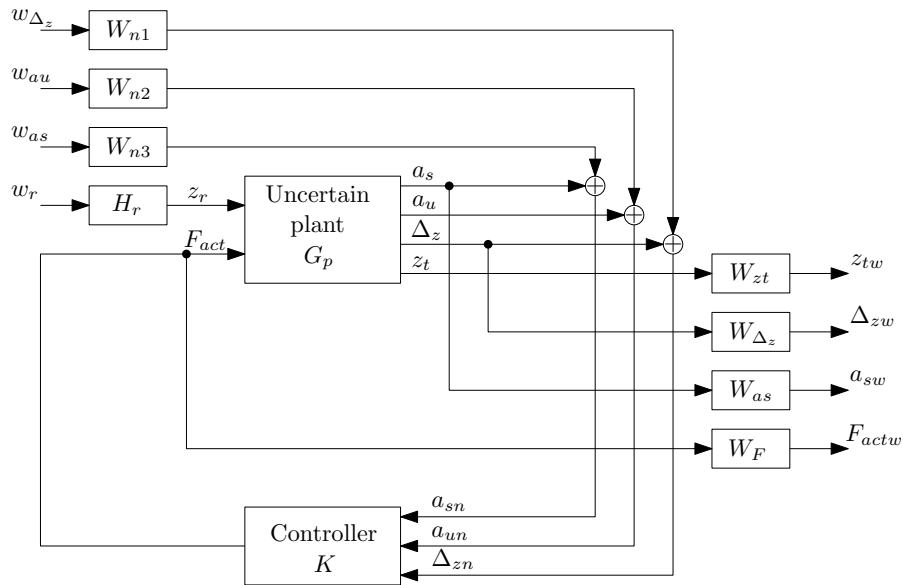


Figure 7.21: Block diagram of the robust control scheme including the various weighting filters.

by W_{n1} , W_{n2} and W_{n3} as presented in Table 7.1. This linear controller K , calculates the required actuator force which is fed to the perturbed plant. The controlled outputs, a_s and z_t , have their own frequency dependent weighting filter, W_{zt} and W_{a_s} , to emphasize the performance in a certain frequency band. The constraints on the suspension travel and actuator force both have their frequency dependent weighting W_z and W_F . Each of the weighting filters are described in the following section.

7.4.3 Weighting functions

The normalized weighting filters are shown in Fig. 7.22 and are listed in Appendix C.2. Each of them is explained in the following sections.

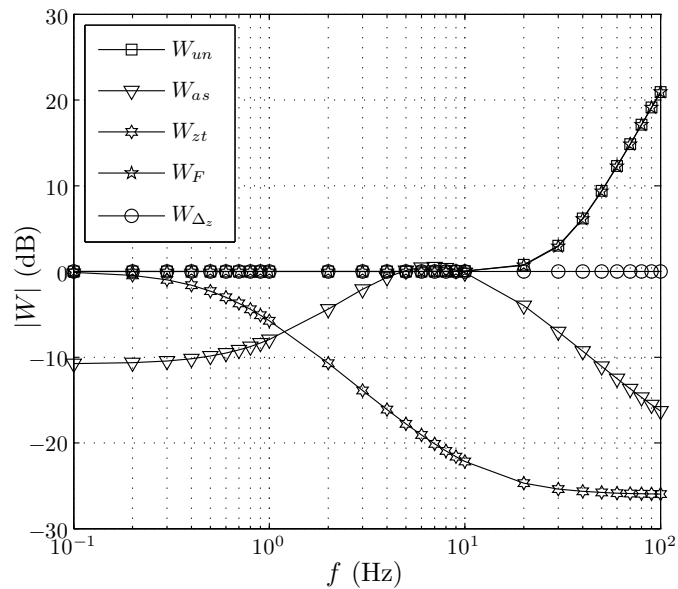


Figure 7.22: Magnitude of the various weighting filters illustrated in Figs. 7.20 and 7.21.

Unmodeled dynamics

The quarter car model derived in Section 5.5 assumes ideal masses, springs and dampers. These assumptions are general valid at low frequencies. However, the springs have their own resonance frequencies since the individual coils start resonating around 64.5 Hz. Therefore, the system has unmodeled dynamics which are included in a form of uncertainty using a high pass weighting filter. This filter has its first zero at 30 Hz, since vertical body dynamics are generally limited to this frequency. Additionally, a pole is added at 400 Hz to limit the gain at higher frequencies.

Dynamic tire compression

On a vehicle corner level, handling can be defined as the minimization of the dynamic tire compression. Due to tire relaxation effects, a rolling tire needs a certain traveling distance to generate a certain side force after a change in vertical load. Therefore, the dynamic compression should be minimized during cornering. Due to the necessary travel distance and corresponding time the tire needs to develop this side force, it is only necessary to ensure minimization of the low frequent dynamic tire compression. Therefore, a low pass filter is used to emphasize this performance objective.

Sprung acceleration

Comfort is, generally, defined as the level of body accelerations within the frequency band where humans are sensitive to. This frequency weighting is defined by the ISO 2631-1 standard as explained in Section 5.7.2. A second order approximation is used to reduce the order of this weighting filter and the resulting controller.

Suspension travel

For the suspension travel, it is important that irrespective of the road conditions, the maximum suspension travel does not exceed the limited stroke. Furthermore, to make a fair comparison with respect to the passive suspension, the maximum travel should be equal to the passive suspension travel under similar road conditions. Since no frequency dependent information is given regarding the suspension travel, the weighting function is described as a proportional gain.

Actuator force

High frequent actuator forces excite chassis resonances which makes the suspension system harsh. Furthermore, high frequent actuation increases eddy current losses in the permanent magnets, coils and soft-magnetic material. Therefore, a high pass filter is used to penalize these frequencies. The magnitude of the pass band penalizes the average actuator force which should not be beyond 1 kN regarding thermal limitations.

7.4.4 Controller synthesis

For controller synthesis and robustness analysis, the total block diagram shown in Fig. 7.21 is simplified to the block scheme of Fig. 7.23(a). It consists of the generalized plant, G_g , which consists of the nominal plant, G , together with the various weighting filters. The parametric and dynamic uncertainties are extracted and written as a diagonal structure uncertainty, Δ , examples of how to extract the structured uncertainty are given in [133]. The block scheme is completed with the controller, K , which calculates the controlled input, $u = F_{act}$, from the measured outputs, $v = [a_{sn}, a_{un}, \Delta_{zn}]^T$.

If the controller, K , is given, the block scheme of Fig. 7.23(a) can be transformed into the $N\Delta$ structure of Fig. 7.23(b) with N given by the lower fractional transformation of G_g and K

$$N = F_l(G_g, K) = G_{g11} + G_{g12}K(I - G_{g22}K)^{-1}G_{g21}. \quad (7.6)$$

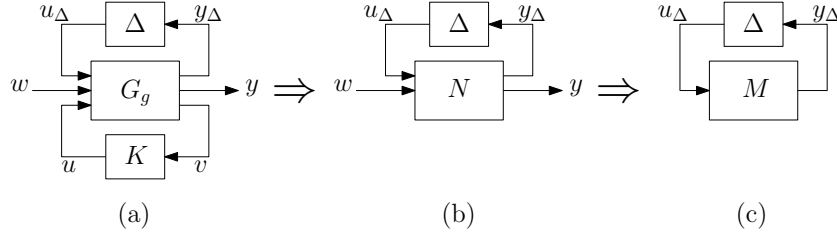


Figure 7.23: (a) Block diagram for the analysis of robustness and performance, (b) the $N\Delta$ structure and (c) the $M\Delta$ structure.

The transfer function from the exogenous inputs w to the exogenous outputs y are given by the upper fractional transformation of N and Δ

$$F_u(N, \Delta) = N_{22} + N_{21}\Delta(I - N_{11}\Delta)^{-1}N_{12}. \quad (7.7)$$

Nominal stability is guaranteed if N is stable for $\Delta = 0$. Robust stability is guaranteed if F_u is stable for all perturbations. Given that N is stable, instability can only occur if $(I - N_{11}\Delta)$ is singular. Hence, robust stability can be guaranteed if the $M\Delta$ structure of Fig. 7.23(c) is stable where $M = N_{11}$. Using the aforementioned $N\Delta$ structure, a controller can be analyzed and synthesized using μ -synthesis and DK-iteration. A detailed treatment of this algorithm is beyond the scope of the thesis and can be found in [37, 126, 127, 133, 138]. It is, however, worth mentioning that this DK-iteration is a minimization problem and this algorithm does not guarantee convergence towards a global or even local minimum [138] and requires proper scaling of the generalized plant.

By varying the amplitude of each weighting filter, comfort or handling can be emphasized ensuring suspension travel and actuator force remain within the limit. Hence, depending on the emphasize, a different controller is obtained. In total, a set of eleven controllers are designed emphasizing either comfort (controller 1), handling (controller 11) or a compromise between both (controllers 2-10). The simulated performance improvement compared to the passive BMW suspension for each of the controllers is shown in Fig. 7.24. Furthermore, the fail-safe performance of the active suspension is shown (the actuator is inactive), hence only the mechanical spring and eddy current damping are apparent. This operating point is 17 % more comfortable but has an increased dynamic tire load, and is therefore worse in handling. Depending on the selected controller, the ISO weighted acceleration can be reduced up to 60 % (better comfort). On the other hand, the dynamic tire load can be reduced up to 20 % (better handling). The reduction in comfort is limited by the maximum suspension travel whilst the reduction in handling is limited by the RMS actuator force of 1 kN (due to thermal limitations).

The disadvantage of robust control and H_∞ -controllers is the high order of the synthesized controllers. The order is equal to the order of the generalized plant G_g which is the sum of the orders of the nominal plant, the dynamic uncertainty and

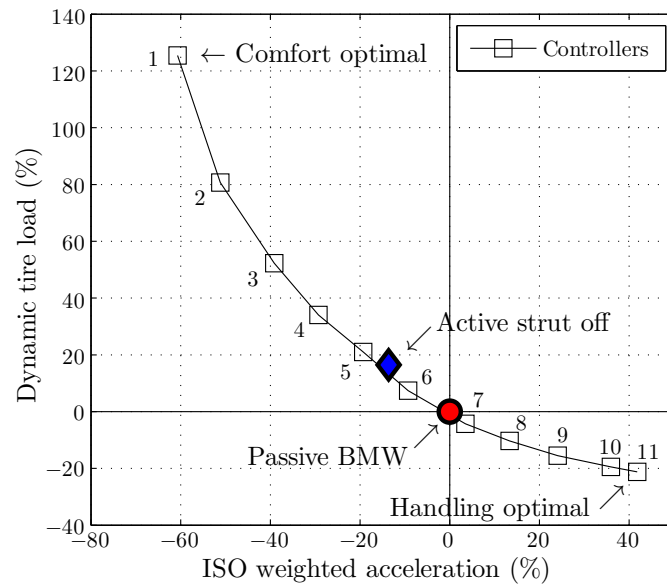


Figure 7.24: Simulated performance of the developed controllers and the active strut, the inactive strut and the passive BMW suspension.

all the input and output weighting filters. The resulting order is between 12 and 16 which might give numerical instability, especially for a low sampling frequency. In that case, a controller order reduction should be applied. However, stability cannot be guaranteed anymore.

7.5 Experimental verification on the quarter car test setup

The controllers are implemented on a dSpace system operating at a sampling frequency of 10 kHz. The measurements are conducted for the smooth and rough road as input. First, the passive BMW suspension is installed on the setup which provides the benchmark measurement. Second, the active suspension is installed and measurements were performed when the actuator was inactive, giving the performance of the fail-safe operation. Finally, the performance due to each of the eleven controllers is measured individually. Note that the rough road could only be performed at 50 % of its amplitude due to limitations of the road actuation system. However, this road it still significantly worse than the smooth road.

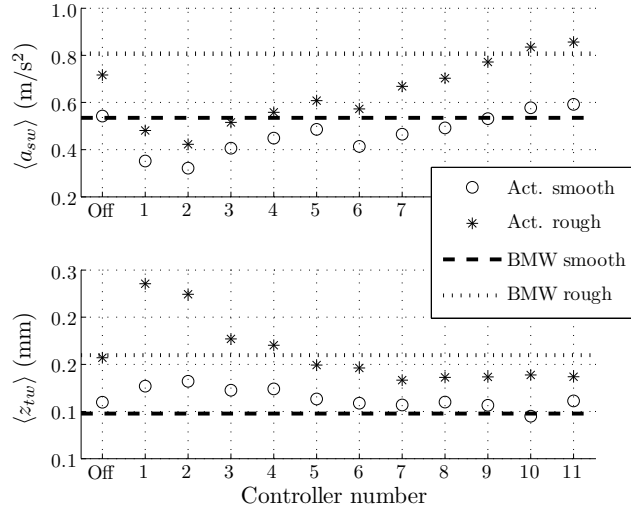


Figure 7.25: Measured average weighted sprung acceleration, $\langle a_{sw} \rangle$ and dynamic tire load, $\langle z_{tw} \rangle$ for the various controllers together with the passive performance (dashed lines).

7.5.1 Performance on a stochastic road

The sprung acceleration and the dynamic tire load were recorded during a time span of two minutes on the smooth and rough road, respectively. The measurements were filtered using the corresponding performance weighting filters, W_{as} and W_{zt} , for the sprung acceleration and the dynamic tire load. Consequently, the RMS values were taken which are shown in Fig. 7.25. The benchmark values of the BMW suspension system are indicated using dashed lines.

It can be observed that for the smooth and rough road, the average weighted sprung acceleration decreases for reduced controller number as expected. However, the weighted sprung acceleration is not monotonically decreasing for decreasing controller number. This is due to static friction of the active suspension system and static friction in the linear bearings of the quarter car setup. When this effect is included in the simulations, a similar non-monotonically increasing trend is observed. This proves that static friction is the origin of the non-monotonic decrement in body acceleration.

The best performance in comfort is obtained using controller 2 with an improvement of 39.8 % and 47.7 % compared to the passive BMW suspension system for the smooth and rough road, respectively. The performance gain is better on the rough road since static friction is of less influence due to the higher velocities.

Considering the reduction in dynamic tire load for the smooth road, only controller number 10 gives a reduction of 2.8 %. For the rough road, the improvement of 16.6 % is significantly better. Again, this difference can be accounted to static

friction in the quarter car test setup. The linear guiding of the unsprung and sprung mass is overdetermined hereby increasing the normal force on the bearings in case of a misalignment. Additionally, compression of the tire spring results in rotation forces on the sprung mass and the bearings.

A more detailed information on the performance of the active suspension system is obtained from the PSD distribution. In Fig. 7.26, the PSD distributions of the relevant variables are shown for controller number 2 on the rough road. The distributions are shown for the measured and simulated active suspension and the measured passive BMW suspension. It can be observed that the weighted sprung acceleration is significantly reduced within the frequency band of interest. However, the wheel hop frequency cannot be reduced since it is an invariant frequency for the actuator. On the other hand, the dynamic tire load is increased below 0.6 Hz (area of interest) and around the wheel hop frequency. Around the bounce frequency, the dynamic tire load is reduced, giving a better handling and comfort around this frequency. The suspension travel and the road displacement are close for the passive and active case, indicating that similar conditions are present, and a fair comparison is made. The PSD distribution of the actuator force indicates that a significant amount of force is generated around the wheel hop frequency which does not have any influence on the sprung acceleration (invariant point). Suppression of this frequency might lower the total power consumption, however proper filtering is difficult since it would lead to phase shift of the neighboring variant frequencies.

7.5.2 Force and power consumption

Furthermore, the output of the controller or actuator force is recorded, and the total power supplied to the actuator is determined from the measured phase currents and voltages. The average values over the measurement of two minutes are shown in Fig. 7.27 for each controller. The highest actuator forces are required for minimization of the tire load while the highest power demand is necessary for optimal comfort. The average force necessary for controller number 10, on a rough road, is around 500 N. Note that the controller was designed to not exceed the RMS force of 1 kN, however, only 50 % of the rough road could be simulated on the quarter car setup. The power demand for controller number two is 110 W. Since improving comfort requires a significantly more amount of mechanical energy compared to improving handling, which requires relatively static forces, the total power consumption is higher. However, on overall the power consumption of each controller is relatively low, especially compared to a hydraulic system, requiring several kW for the total car.

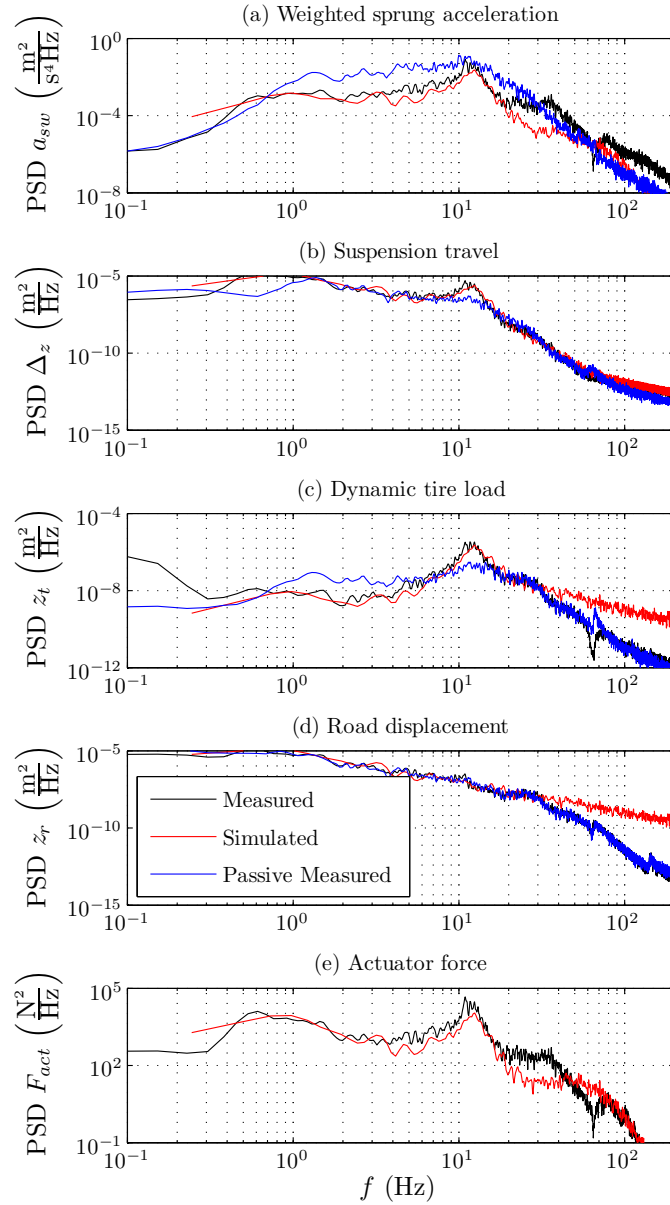


Figure 7.26: Measured and simulated PSDs of the performance of controller 2 compared with the performance of the passive suspension on the rough road.

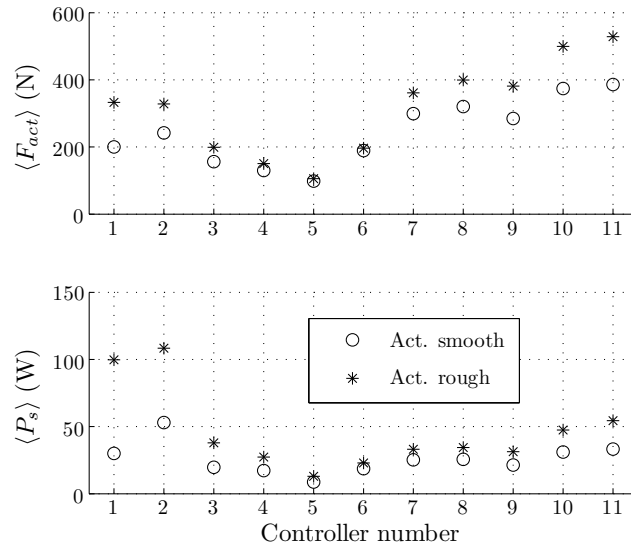


Figure 7.27: Measured average force and power consumption for the various controllers.

7.5.3 Performance on a deterministic road profile

A more intuitive performance evaluation is obtained when considering a deterministic road profile. Therefore, the response to a speed bump as road input is measured. Since for this situation, comfort is of importance, controller number 2 is considered, since it gives the best performance in reducing the sprung acceleration. The measured and simulated response for the active suspension system is shown in Fig. 7.28 together with the measured response of the passive BMW suspension. A significant reduction of 54.86 % in the sprung acceleration is obtained. Investigating the suspension travel, the absorption of the bump together with the gradual decay is clearly visible. A behavior which, the passive BMW suspension, is not able to provide. An equivalent behavior is observed for the actuator force where besides the gradual decay, the wheel hop resonance is again significantly present. Although the controller tries to suppress this frequency, it is still visible in the sprung acceleration. The peak power consumption reaches 884 W, however the average power consumption is only 87.5 W considering this speed bump appears with a 50 % duty cycle.

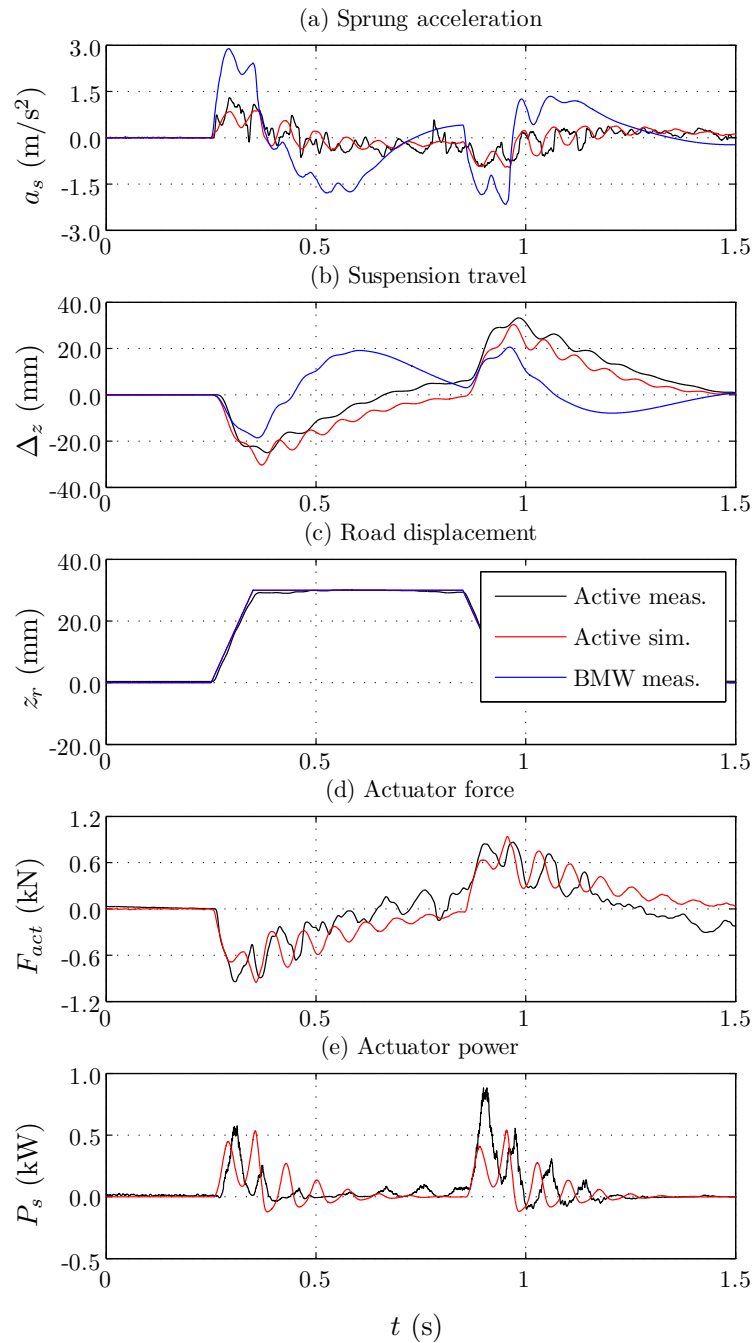


Figure 7.28: Measured and simulated performance of controller number two compared with the performance of the measured inactive suspension on a speed bump on the quarter car test setup.



Figure 7.29: Installation of the active suspension system within the BMW 530i.

7.6 Experimental verification on the BMW 530i

The active suspension system is installed as a front suspension underneath the BMW 530i as shown in Fig. 7.29. The power electronics together with the dSpace system are installed in the trunk of the vehicle. The same sensor set as for the quarter car setup is applied on the front left and right corner. For correct performance of this suspension system on a vehicle level, full car control should be developed and additional vehicle dynamics should be measured such as yaw rate, pitch rate and vehicle speed. However, it is still possible to perform preliminary tests to evaluate the performance of the system.

7.6.1 Comfort

The first test undertaken is the vehicle driving over a speed bump situated on the left side of the vehicle with dimensions as given in Section 5.6 with 25 km/h. Since this situation should improve the comfort, controller number two is selected which gave the best performance for the experimental verification on the quarter car test setup. The response of the front left body acceleration for the passive case (fail-safe mode) and the active case are shown in Fig. 7.30. It can be observed that the peak acceleration is significantly reduced from 9 to 4 m/s². However, an additional resonance is observed for the active case. This resonance can be accounted to the stick-slip friction of the suspension system. This is the major disadvantage and performance limitation of the MacPherson topology in the combination with an active suspension. This could be minimized by considering side-force cancelation using a special coil spring geometry [101].

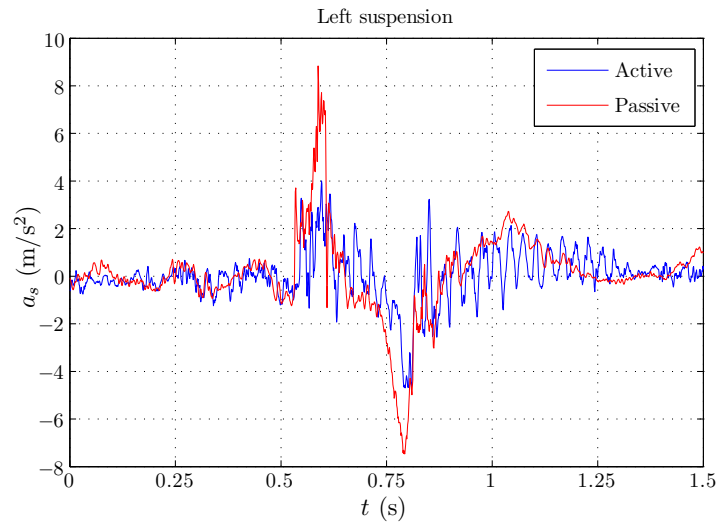


Figure 7.30: Measured body acceleration while the vehicle drives over the speed bump for the passive and active suspension system.

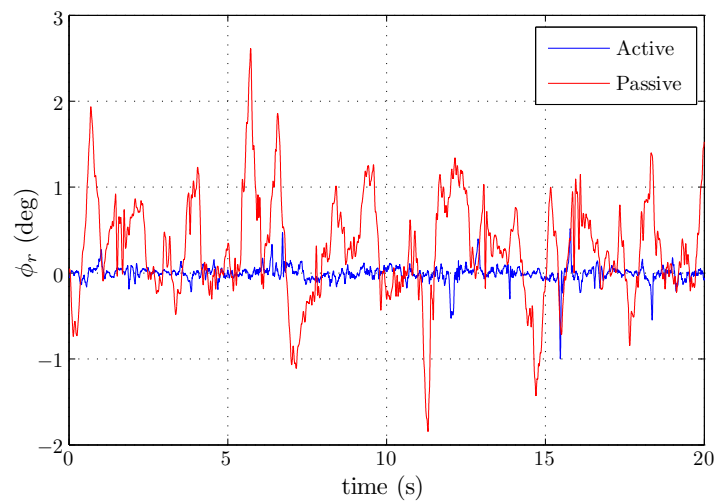


Figure 7.31: Measured differential suspension deflection while the vehicle drives over the TU/e terrain for the passive and active suspension system.

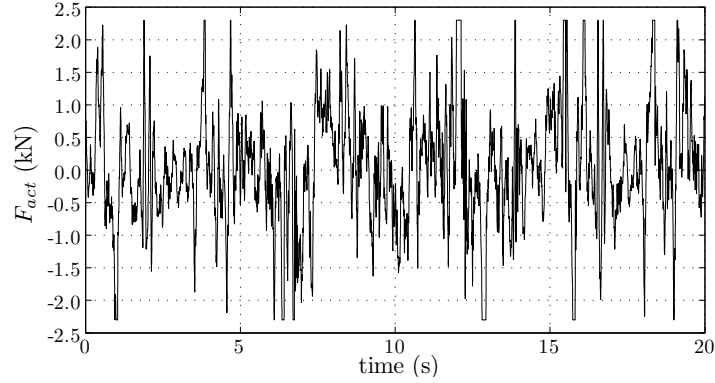


Figure 7.32: Force command of the front left actuator while the vehicle drives over the TU/e terrain for minimization of the differential suspension deflection shown in Fig. 7.31.

7.6.2 Handling

The second test is performed while driving on the terrain of the Eindhoven University of Technology (TU/e). The objective of the test is to improve the handling of the BMW 530i. Since this objective requires the highest actuator forces, this test shows the high performance of the active suspension system. However, yaw rate, yaw angle or lateral acceleration could not be measured using the current sensor set on the vehicle. Alternatively, the roll angle in degrees, ϕ_r , is minimized, which is derived using the left and right suspension travel as

$$\phi_r = \frac{180}{\pi} \arctan \left(\frac{\Delta_{zl} - \Delta_{zr}}{T_w} \right), \quad (7.8)$$

where T_w is the track width of the vehicle, given in Table 5.1, and Δ_{zl} and Δ_{zr} are the suspension travel of the front left and right corner, respectively. A PD controller is used for minimization of the roll angle, ϕ_r . In Fig. 7.31, the roll angle is shown during the test track for the passive (fail-safe mode) and active case. It can be observed that the roll angle is reduced significantly, from a maximum of 2.65 degrees for the passive case to a maximum of 1 degree for the active case. The required actuator force is shown in Fig. 7.32. It should be noted that the maximum force was limited to 2300 N during this test. This control strategy creates a very stiff suspension and the responsiveness of a steering command is improved, as was experienced during driving. However, the stability is reduced after cornering since this the suspension is no longer independent and front traction is reduced, leading to a slight increase in understeer. Although this is by no means an optimized control strategy to improve stability, since only the roll angle is minimized, it still illustrates the high performance and potential of the active suspension system. Future development of efficient full-car control strategies is however still necessary.

7.7 Summary and conclusions

In this chapter, the novel proof of principle is realized and tested. The designed prototype of the active suspension system is manufactured. The quasi-Halbach array is constructed from a combination of axially magnetized ring magnets and segmented parallel magnetized ring magnets. The semi-analytical model is verified by magnetic field measurements both the permanent magnet array and armature.

Induced electromotive forces (emf) at various speeds and their phase shift due to the eddy current damping are measured. This phase shift is essential for a stator current commutation that maximizes force per Ampère. The total cogging is measured to be within specifications. The measured damping ratio is within 85 % of the calculated value due to lead wires, etc, which still guarantees fail-safe operation. The force versus current characteristic is measured to be linear up to 2 kN (twice the rated force) and is within 87 % of the predicted response. Furthermore, the excellent performance of this active suspension system has been illustrated by a settling time of only 8 ms when a step in the force command is given, hence the bandwidth is approximately 125 Hz.

A full scale quarter car test setup is constructed together with a 30 Hz bandwidth electromagnetic road actuation system. In this setup, the tire is represented by an equivalent spring stiffness and unsprung mass. System identification of the setup corresponds with the simulations within the frequency band of interest. For the vehicle corner, a robust controller is considered to improve both comfort and handling. Parameter variation in sprung mass, tire pressure and damping are included as well as sensor noise. Performance specifications are incorporated using frequency dependent weighting filters. Using DK-iteration, a set of controllers are synthesized for either comfort or handling.

These controllers are experimentally verified on the quarter car test setup. First, stochastic road profiles are considered. Dependent on the chosen controller, an improvement of 40 % and 48 % is achieved compared to the passive BMW suspension on a smooth and rough road, respectively. An improvement of 3 % and 17 % in handling is obtained. The improvements on a rough road are better since static friction of the actuator and quarter car setup are of less influence. Second, comfort on a speed bump is improved by approximately 55 %. The power consumption is in the order of 100 W, which is significantly less than commercially available hydraulic active suspension systems.

The active suspension system is installed in the front of the BMW 530i. During a test drive, solely consisting of a speed bump, the peak acceleration is decreased by 55 % compared to the passive case. Furthermore, a test drive on the TU/e terrain with high speed cornering is undertaken to minimize roll. Hereby is measured that the roll angle is decreased from 2.65 degrees to approximately 1 degree. This has indicated the active suspension system potential under extreme driving conditions.

Part III

Closing

Chapter 8

Conclusions and Recommendations

A generalized harmonic modeling technique for 2D electromagnetic problems has been the main contribution of Part I of this thesis. Consequently, Part II shows that a direct-drive electromagnetic active suspension system is a suitable technology to improve both handling and comfort of a passenger car. From this thesis, the main scientific contributions have been extracted and are listed in this chapter. The research contained in this thesis also highlighted some problems and future challenges, these have been summarized in recommendations for development and future research.

8.1 Conclusions of Part I

8.1.1 Generic harmonic modeling technique

The generic formulation of the magnetic field distribution for 2D electromagnetic problems combines and integrates prior-art and has completed the unsolved cases into a single framework. As such, problems in the 2D Cartesian, polar or axisymmetric coordinate system have been divided into orthogonal regions. These regions need to be either periodic or non-periodic. The electromagnetic sources, i.e. permanent magnets and phase currents, have to be described by means of a Fourier series. In the specific case that the source is situated in a non-periodic region, imaging of the source has to be applied to obtain the complete description of the Fourier series. In this way, a generic solution for each type of region has been obtained by solving the Poisson equation in terms of the magnetic vector

potential for the various coordinate systems. Applying the various boundary conditions gives a set of linear equations which are solved using the singular value decomposition.

Accuracy of the magnetic field distribution due to harmonic truncation has been researched. The optimal number of harmonics for non-periodic regions is derived as a ratio of the number of harmonics for periodic regions (see Chapter 2). The presented generic formulation is verified with FEA using various examples in the different coordinate systems. The inaccuracies within these examples are all related to the harmonic truncations. They are particularly apparent at the corner points of the sources and non-periodic regions. Using this modeling technique, an accuracy is obtained within 5 % given that the soft-magnetic materials are not highly saturated.

This harmonic modeling technique can be applied to a large class of electromagnetic problems. The unified formulation allows this framework to be implemented in a software environment, where the boundary condition matrices are automatically generated. This facilitates the automated use of this technique to complex electromagnetic problems for research, analysis, design and optimization.

8.1.2 Modeling of slotted TPMAs

The developed generic harmonic modeling technique has been successfully applied to three phase slotted TPMAs. Further, this method allows for inclusion of regions with Neumann boundary conditions, hence the slotted structure and resulting fringing fields have been included. This provides a very accurate field solution in the airgap, as well as in the slot openings and permanent magnets. Due to the automatic creation of the boundary condition matrices, many topologies and configurations have been considered.

Although the method only considers the field solution in low-permeability regions, a method is provided to determine the average flux density in the soft-magnetic regions. Further, accurate calculation methods for the emf waveforms, synchronous inductances and force profiles have been provided which all include the position dependency and ripples due to the slotted stator. The calculation time for each of the methods is in the order of milliseconds and provide an accuracy within 5 %.

Finally, copper losses are calculated in combination with coil and magnet temperatures. These have been estimated using a thermal equivalent circuit for both internal and external magnet topologies (IMT and EMT) which is iteratively solved. The obtained worst-case magnet and coil temperatures have been determined within 10 % accuracy compared to FEA.

8.1.3 Integration of eddy current damping

For applications requiring additional passive damping, the integration of eddy current damping within a tubular actuator has been considered. The level of damping in a tubular actuator can be enhanced using solid steel instead of laminations which is furthermore beneficial from a manufacturing point of view. Measurements have shown that the use of solid steel improves the amount of eddy current damping by a factor 350. However, the characteristic is highly non-linear and might still be insufficient for certain applications. Therefore, alternative methods for the enhancement of the eddy current damping have been investigated. The insertion of conductive rings in the slot openings provided the highest increase in damping without a concession of the initial actuator design and hence, performance. The method of integration of the conductive rings within the tubular actuator has been patented.

Determination of the enhanced passive damping characteristic by means of FEA is very time consuming. Therefore, a method for calculation of the dynamic damping characteristic has been proposed based upon the determination of the electrical pole of the conductive rings. This method requires the calculation of the resistance and synchronous inductance of these conductive rings and enables the reuse of the proposed generic harmonic modeling technique. The technique allows for investigation of the ripple of the damping force, velocity dependency and even temperature dependency. The most linear damping characteristic is obtained using quasi-Halbach magnetization due to the low inductance of the rings. An agreement within 10 % is obtained compared to FEA, while the largest discrepancy is attributed to axial magnetized topologies, since the dependency of the ring inductance on the relative position is not included. This method is significantly faster than transient FEA and more suitable for the design and material selection of the conductive rings.

8.2 Conclusions of Part II

8.2.1 Direct-drive fail-safe active suspension system

The developed active suspension system consists of a mechanical coil spring for gravity compensation in parallel with a tubular permanent magnet actuator. This direct-drive tubular actuator is capable of four-quadrant operation, hence can provide active vertical force or regenerate power. Additionally, a fail-safe passive damping ratio has been integrated to ensure system functionality in case of a power breakdown. The system has been designed to be a retrofit for a BMW 530i, and should therefore be compact and provide a continuous force of 1 kN (required actuator force density is 755 kN/m^3). The passive spring and specified damper characteristic have been selected such that a similar behavior as the original pas-

sive suspension is obtained. The damping characteristic is symmetric in bound and rebound due to use of the eddy current damping. Regarding the efficiency, the system is designed to operate on a high voltage dc bus (340 Vdc) instead of the common 12-14 Vdc.

8.2.2 Automated optimization and design

The developed fast semi-analytical framework for modeling of TPMAs has been an essential asset in two individual constrained non-linear optimization routines to obtain the active suspension electromagnetic design. First, the actuator force density need to exceed 755 kN/m^3 , where maximum outer radius, inner radius, temperature, force ripple and average magnetic flux density in the soft-magnetic material are constrained. Second, copper losses have been minimized for the topologies that exceeded the minimal required force density. This resulted in the most optimized topology being the EMT using a singular winding configuration with quasi-Halbach magnetization and four poles per three slots using cobalt iron as soft-magnetic material. Further, both specifically designed aluminium conductive rings and eddy-currents in the soft-magnetic material give the required initial damping coefficient of 1600 Ns/m . It needs noting that, only for the calculation of the eddy-current damping in the solid soft-magnetic material, FEA has been used. Further, this particular magnetization topology has the most linear damping ratio characteristic due to the low inductance of the rings. Finally, the number of turns per coil has been determined to match the specifications of the inverter.

8.2.3 Control and experimental verification

A first-in-the-world direct-drive electromagnetic active suspension prototype with integrated passive damping has been manufactured. Measurements of the magnetic field distribution due to the permanent magnets and armature reaction have been used to verify the accuracy of the proposed semi-analytical harmonic modeling technique. The emf waveforms and cogging forces have been determined to be according to the calculations, respectively 80 Vs/m and 28 N peak. The obtained damping characteristic is 11 % lower than predicted due to changes in the design for lead wires and isolation, however, a fail-safe operation is still obtained. The force constant has been measured to be linear up to 2 kN , twice the rated force, and a peak force of 3 kN has been reached with a bandwidth of approximately 125 Hz .

A full scale quarter car test setup has been developed for verification of the control and performance of the active suspension system on a corner level. Random road vibrations have been applied by electromagnetic actuation to obtain a spectrum up to 30 Hz . A robust control scheme has been considered to control the active suspension system incorporating parameter variation in the sprung mass, tire stiffness and damping characteristic. Weighting filters have been designed to

emphasize either comfort or handling in a certain frequency band and to limit the actuator force and suspension travel. Finally, a set of controllers has been synthesized for either improving comfort or handling or a combination of both. The performance of this set of controllers in combination with the active suspension system has been experimentally verified on the full scale quarter car test setup. The passive response of the active system has been measured to be within 15 % of the original passive suspension. Furthermore, an improvement of 48 % in comfort and 17 % in handling has been obtained on a random road at the expense of a power consumption of 110 W and 55 W, respectively. Even more, a reduction of 55 % in body acceleration on a speed bump has been achieved. The extensive test results have proved that this solution provides an improvement in comfort and handling at the expense of a relatively low power consumption.

To prove the full functionality on a vehicle level, the active suspension system has been installed as a front suspension in the BMW 530i. Again, a reduction of 55 % in body acceleration has been obtained while driving over a speed bump. Additionally, a decrease from 2.35 degrees to 1 degree in differential body deflection has been obtained during a test drive with high speed cornering.

8.3 Thesis contributions

The main contributions and output of the thesis can be summarized as

- *The development of a generalized harmonic modeling technique for 2D electromagnetic problems.* Rather than solving a particular problem, this framework provides a general solution applicable to a broad class of electromagnetic actuators and devices.
- *The application of the harmonic modeling technique to slotted tubular permanent magnet actuators.* The technique is applied to internal and external magnet topologies, radial, axial and quasi-Halbach magnetization. Besides the conventional winding configurations, a singular winding configuration is considered, offering a better force per power ratio. The fringing fields and resulting harmonics in the emf and force waveform due to the slotting effect are included within a small computation time.
- *The integration and enhancement of the eddy current damping in tubular permanent magnet actuators using conductive rings in the slot openings.* A means of modeling the resulting dynamic damping characteristic is proposed.
- *A direct-drive electromagnetic active suspension system is designed with integrated fail-safe damping.* The system comprises a coilover consisting of a mechanical spring in parallel with a tubular permanent magnet actuator with integrated passive eddy current damping. The integrated damping is

realized using solid steel and additional conductive rings in the slot openings. This novel integration of actuator and damper is patented in [66]. The final design is obtained by means of automated optimization and design using the developed semi-analytical framework.

- *Experimental verification of the electromagnetic active suspension system on a full scale quarter car test setup.* The stand-alone suspension strut is experimentally verified as well as the developed robust controllers on the quarter car test setup. The comfort and handling of the vehicle corner are improved at the expense of a low power consumption.
- *Experimental verification of the electromagnetic active suspension system on a vehicle level.* Experimental verification of the electromagnetic suspension system on a vehicle level proved the feasibility of practical implementation and applicability for automotive applications.

8.4 Recommendations for future work

8.4.1 Harmonic modeling including high permeability regions

The proposed semi-analytical method assumes an infinite permeability of the soft-magnetic material. This requires the prediction of the magnetic flux density in the soft-magnetic regions as discussed in Chapter 3. Including the high permeability regions would lead to an improvement of this generic modeling technique. As already suggested, in case the region is periodic, a finite permeability can be included. However, in case a distribution of several regions exists in the tangential direction, the soft-magnetic regions are assumed to have an infinite permeability. The spatial frequencies of the surrounding regions are, therefore, chosen such that the Neumann boundary condition at the tangential borders is satisfied. In case a finite permeability is included, a continuous boundary condition should be applied. This boundary condition can only be satisfied by altering the spatial frequencies or eigenvalues. In case two regions are considered, this boundary condition results in a non-linear equation in terms of the eigenvalues. This equation can be solved iteratively using a Newton-Raphson method as for example considered in [143]. In case more than two regions are considered, a set of non-linear equations has to be solved making this method very time consuming and numerically unstable. However, alterations on this theme could lead to a feasible and suitable solution for problems including high permeability regions.

8.4.2 Harmonic modeling of 3D problems

Since the advantage of a 3D (semi-) analytical modeling technique compared to a numerical technique is even more significant, the extension of this technique to 3D problems is of great scientific contribution. Several publications are already considering the harmonic modeling for 3D geometries, e.g. the work of Meessen on the 3D effects of segmented cylindrical quasi-Halbach arrays in [107] and the work of Gysen on the 3D modeling of skewed permanent magnet arrays in the cylindrical coordinate system [62]. However, a more greater challenge is the incorporation of non-periodic regions surrounded by Neumann boundary conditions. This requires a two-dimensional correlation technique in which numerical implementation becomes a bottleneck. The work of Theodoulidis describes the 3D field solution over a rectangular conductive wedge in Cartesian coordinates, however only a single wedge is considered [144].

8.4.3 Revision of specifications for the active suspension system

The developed prototype in this thesis together with the developed control algorithms provide feedback on the previously defined specifications for the active suspension system. Depending on the required performance and functionality, the specifications might be increased or even decreased. This might give the opportunity to reduce the actuator volume, or amount of permanent magnets, hereby decreasing the cost. Additionally, more tests have to be performed to have more detailed information about the thermal specifications, like environment temperature and convection at the vehicle corner under different driving conditions.

8.4.4 Full vehicle control

The system is initially installed in the front suspension system of the BMW 530i. However, in order to fully employ the benefit of the active suspension system, the rear suspension has to be equipped with active suspension as well. Additionally, the development of full vehicle control is essential in order to minimize roll, pitch, and to control yaw moment. Furthermore, the use of different sensor sets, including the input from load sensing hub bearing units developed by SKF can further improve the performance of the full suspension system [30].

8.4.5 Alternative functionalities or applications

The developed system has a high bandwidth, opening the opportunity to investigate other functionalities like road noise [128] or engine noise cancelation. Alternatively, the fail-safe function can be obtained by other means, increasing the efficiency of the actuator. This might lead to a more regenerative system, although for passenger cars, the amount of regenerative power is limited. Furthermore, the developed system could be used to investigate the durability of vehicle components under heavy vibrations and resonances.

Additionally, this system can be scaled to any passenger car, commercial vehicle, or even maritime and aviation applications. Furthermore, the tubular actuator technology could be used in 6-DoF flight simulators (e.g. the SIMONA Research Simulator of the TUDelft [132]) to replace the hydraulic actuators to obtain a higher bandwidth. This provides a wider spectra of vibrations or motion profiles to be applied, hence improves the simulation of real-life behavior.

Appendix A

Correlation functions

The correlation functions used in the combined Neumann and continuous boundary conditions of Section 2.7.4 are written as

$$\varepsilon_s^{k,j\nu}(m, n) = \frac{2m\tau_k^2 [\sin(w_n^k \Delta) - \cos(m\pi) \sin(w_n^k (\Delta + \tau_{j\nu}))]}{\pi(m^2\tau_k^2 - n^2\tau_{j\nu}^2)}, \quad (\text{A.1})$$

$$\varepsilon_c^{k,j\nu}(m, n) = \frac{2m\tau_k^2 [\cos(w_n^k \Delta) - \cos(m\pi) \cos(w_n^k (\Delta + \tau_{j\nu}))]}{\pi(m^2\tau_k^2 - n^2\tau_{j\nu}^2)}, \quad (\text{A.2})$$

$$\eta_s^{k,j\nu}(m, n) = \frac{2n\tau_k\tau_{j\nu} [\cos(m\pi) \cos(w_n^k (\Delta + \tau_{j\nu})) - \cos(w_n^k \Delta)]}{\pi(m^2\tau_k^2 - n^2\tau_{j\nu}^2)}, \quad (\text{A.3})$$

$$\eta_c^{k,j\nu}(m, n) = \frac{2n\tau_k\tau_{j\nu} [\sin(w_n^k \Delta) - \cos(m\pi) \sin(w_n^k (\Delta + \tau_{j\nu}))]}{\pi(m^2\tau_k^2 - n^2\tau_{j\nu}^2)}, \quad (\text{A.4})$$

$$\kappa_s^{k,j\nu}(m, n) = \frac{sm\tau_k\tau_{j\nu} [\sin(w_n^k \Delta) - \cos(m\pi) \sin(w_n^k (\Delta + \tau_{j\nu}))]}{\pi(m^2\tau_k^2 - n^2\tau_{j\nu}^2)}, \quad (\text{A.5})$$

$$\kappa_c^{k,j\nu}(m, n) = \frac{sn\tau_{j\nu}^2 [\cos(m\pi) \cos(w_n^k (\Delta + \tau_{j\nu})) - \cos(w_n^k \Delta)]}{\pi(m^2\tau_k^2 - n^2\tau_{j\nu}^2)}, \quad (\text{A.6})$$

$$\kappa_0^{k,j\nu}(n) = \frac{s [\cos(w_n^k \Delta) - \cos(w_n^k (\Delta + \tau_{j\nu}))]}{n\pi}, \quad (\text{A.7})$$

$$\zeta_s^{k,j\nu}(m, n) = \frac{sm\tau_k\tau_{j\nu} [\cos(w_n^k\Delta) - \cos(m\pi) \cos(w_n^k(\Delta + \tau_{j\nu}))]}{\pi(m^2\tau_k^2 - n^2\tau_{j\nu}^2)}, \quad (\text{A.8})$$

$$\zeta_c^{k,j\nu}(m, n) = \frac{sn\tau_{j\nu}^2 [\sin(w_n^k\Delta) - \cos(m\pi) \sin(w_n^k(\Delta + \tau_{j\nu}))]}{\pi(m^2\tau_k^2 - n^2\tau_{j\nu}^2)}, \quad (\text{A.9})$$

$$\zeta_0^{k,j\nu}(n) = \frac{s [\sin(w_n^k(\Delta + \tau_{j\nu})) - \sin(w_n^k\Delta)]}{n\pi}, \quad (\text{A.10})$$

with $\Delta = \Delta_{j\nu} - \Delta_k$. The variable $s = 1$ when region k has periodic boundary conditions in the tangential direction and $s = 2$ when region k has Neumann boundary conditions in the tangential direction. If $m\tau_k = n\tau_{j\nu}$, the correlation functions are given by

$$\varepsilon_s^{k,j\nu}(m, n) = \cos\left(\frac{n\pi\Delta}{\tau_k}\right), \quad \kappa_s^{k,j\nu}(m, n) = \frac{s\tau_{j\nu}}{2\tau_k} \cos\left(\frac{n\pi\Delta}{\tau_k}\right), \quad (\text{A.11})$$

$$\varepsilon_c^{k,j\nu}(m, n) = -\sin\left(\frac{n\pi\Delta}{\tau_k}\right), \quad \kappa_c^{k,j\nu}(m, n) = \frac{s\tau_{j\nu}}{2\tau_k} \sin\left(\frac{n\pi\Delta}{\tau_k}\right), \quad (\text{A.12})$$

$$\eta_s^{k,j\nu}(m, n) = \sin\left(\frac{n\pi\Delta}{\tau_k}\right), \quad \zeta_s^{k,j\nu}(m, n) = \frac{s\tau_{j\nu}}{2\tau_k} \sin\left(\frac{n\pi\Delta}{\tau_k}\right), \quad (\text{A.13})$$

$$\eta_c^{k,j\nu}(m, n) = \cos\left(\frac{n\pi\Delta}{\tau_k}\right), \quad \zeta_c^{k,j\nu}(m, n) = \frac{s\tau_{j\nu}}{2\tau_k} \cos\left(\frac{n\pi\Delta}{\tau_k}\right). \quad (\text{A.14})$$

Appendix B

Boundary condition matrices for TPMAs

The boundary condition matrices solve the unknown coefficients for the magnetic field solution of the TPMA. The solutions are used in Chapters 3, 4 and 6. The vector of N_k truncated spatial harmonics for each region k is defined as

$$\mathbf{w}^k = [w_1^k, w_2^k, \dots, w_{N_k}^k]. \quad (\text{B.1})$$

For simplification of notation, the following matrices are introduced

$$\begin{aligned}
 \mathbf{C}_1 &= \text{diag} \left(\mathcal{I}_0 \left(\mathbf{w}^I R_r \right) \right), & \mathbf{C}_2 &= \text{diag} \left(\mathcal{K}_0 \left(\mathbf{w}^I R_r \right) \right), \\
 \mathbf{C}_3 &= \text{diag} \left(\mathcal{I}_1 \left(\mathbf{w}^I R_r \right) \right), & \mathbf{C}_4 &= \text{diag} \left(\mathcal{K}_1 \left(\mathbf{w}^I R_r \right) \right), \\
 \mathbf{C}_5 &= \text{diag} \left(U \left(\mathcal{I}_0 \left(\mathbf{w}^{II} R_r \right), P \right) \right), & \mathbf{C}_6 &= \text{diag} \left(U \left(\mathcal{K}_0 \left(\mathbf{w}^{II} R_r \right), P \right) \right), \\
 \mathbf{C}_7 &= \text{diag} \left(U \left(\mathcal{I}_1 \left(\mathbf{w}^{II} R_r \right), P \right) \right), & \mathbf{C}_8 &= \text{diag} \left(U \left(\mathcal{K}_1 \left(\mathbf{w}^{II} R_r \right), P \right) \right), \\
 \mathbf{C}_9 &= \text{diag} \left(\mathcal{I}_0 \left(\mathbf{w}^I R_m \right) \right), & \mathbf{C}_{10} &= \text{diag} \left(\mathcal{K}_0 \left(\mathbf{w}^I R_m \right) \right), \\
 \mathbf{C}_{11} &= \text{diag} \left(\mathcal{I}_1 \left(\mathbf{w}^I R_m \right) \right), & \mathbf{C}_{12} &= \text{diag} \left(\mathcal{K}_1 \left(\mathbf{w}^I R_m \right) \right), \\
 \mathbf{C}_{13} &= \text{diag} \left(U \left(\mathcal{I}_0 \left(\mathbf{w}^{II} R_m \right), P \right) \right), & \mathbf{C}_{14} &= \text{diag} \left(U \left(\mathcal{K}_0 \left(\mathbf{w}^{II} R_m \right), P \right) \right), \\
 \mathbf{C}_{15} &= \text{diag} \left(U \left(\mathcal{I}_1 \left(\mathbf{w}^{II} R_m \right), P \right) \right), & \mathbf{C}_{16} &= \text{diag} \left(U \left(\mathcal{K}_1 \left(\mathbf{w}^{II} R_m \right), P \right) \right), \\
 \mathbf{C}_{17} &= \text{diag} \left(\mathcal{I}_0 \left(\mathbf{w}^I R_i \right) \right), & \mathbf{C}_{18} &= \text{diag} \left(\mathcal{K}_0 \left(\mathbf{w}^I R_i \right) \right), \\
 \mathbf{C}_{19} &= \text{diag} \left(\mathcal{I}_1 \left(\mathbf{w}^I R_i \right) \right), & \mathbf{C}_{20} &= \text{diag} \left(\mathcal{K}_1 \left(\mathbf{w}^I R_i \right) \right),
 \end{aligned}$$

$$\begin{aligned}
\mathbf{C}_{21} &= \text{diag} \left(U \left(\mathcal{I}_0 \left(\mathbf{w}^{\text{IV}} R_i \right), S \right) \right), & \mathbf{C}_{22} &= \text{diag} \left(U \left(\mathcal{K}_0 \left(\mathbf{w}^{\text{IV}} R_i \right), S \right) \right), \\
\mathbf{C}_{23} &= \text{diag} \left(U \left(\mathcal{I}_1 \left(\mathbf{w}^{\text{IV}} R_i \right), S \right) \right), & \mathbf{C}_{24} &= \text{diag} \left(U \left(\mathcal{K}_1 \left(\mathbf{w}^{\text{IV}} R_i \right), S \right) \right), \\
\mathbf{C}_{25} &= \text{diag} \left(U \left(\mathcal{I}_0 \left(\mathbf{w}^{\text{IV}} R_t \right), S \right) \right), & \mathbf{C}_{26} &= \text{diag} \left(U \left(\mathcal{K}_0 \left(\mathbf{w}^{\text{IV}} R_t \right), S \right) \right), \\
\mathbf{C}_{27} &= \text{diag} \left(U \left(\mathcal{I}_1 \left(\mathbf{w}^{\text{IV}} R_t \right), S \right) \right), & \mathbf{C}_{28} &= \text{diag} \left(U \left(\mathcal{K}_1 \left(\mathbf{w}^{\text{IV}} R_t \right), S \right) \right), \\
\mathbf{C}_{29} &= \text{diag} \left(U \left(\mathcal{I}_0 \left(\mathbf{w}^{\text{IV}} R_c \right), S \right) \right), & \mathbf{C}_{30} &= \text{diag} \left(U \left(\mathcal{K}_0 \left(\mathbf{w}^{\text{IV}} R_c \right), S \right) \right), \\
\mathbf{C}_{31} &= \text{diag} \left(U \left(\mathcal{I}_1 \left(\mathbf{w}^{\text{IV}} R_c \right), S \right) \right), & \mathbf{C}_{32} &= \text{diag} \left(U \left(\mathcal{K}_1 \left(\mathbf{w}^{\text{IV}} R_c \right), S \right) \right),
\end{aligned} \tag{B.2}$$

where $U(\mathbf{v}, P)$ gives P tiling copies of the vector \mathbf{v} and $\text{diag}(\mathbf{v})$ is the diagonal matrix with the elements of vector \mathbf{v} . The unknown coefficients $a_n^k, b_n^k, c_n^k, d_n^k$ and constants B_0^k are listed in the unknown vector \mathbf{X} . The set of boundary conditions can therefore be written as

$$\mathbf{E}\mathbf{X} = \mathbf{Y}, \tag{B.3}$$

and hence, the unknown coefficients are obtained by inversion of the matrix \mathbf{E} as

$$\mathbf{X} = \mathbf{E}^{-1}\mathbf{Y}. \tag{B.4}$$

using the singular value decomposition. The vectors \mathbf{X}, \mathbf{Y} and matrix \mathbf{E} are defined for radial, quasi-Halbach and axial magnetization in the following sections. The unknown constants in the magnetic vector potential formulation, A_0^k , are solved in the final Section.

B.1 Radial magnetization

The unknown coefficients a_n^k are written as a vector

$$\mathbf{a}^k = [a_1^k, a_2^k, \dots, a_{N_k}^k], \tag{B.5}$$

with similar expressions for $\mathbf{b}^k, \mathbf{c}^k$ and \mathbf{d}^k . For periodic regions k , the constant $\mathbf{B}_0^k = 0$ since it would lead to a net flux in the tangential direction which violates the conservation of flux. In case a region j consists of several subregions $j\nu$ for $\nu = 1, \dots, \mathcal{V}$, the unknown coefficients are written as augmented vectors for each subregion as

$$\mathbf{a}^j = [a_1^{j1}, a_2^{j1}, \dots, a_{N_j}^{j1}, a_1^{j2}, a_2^{j2}, \dots, a_{N_j}^{j2}, \dots, a_1^{j\mathcal{V}}, a_2^{j\mathcal{V}}, \dots, a_{N_j}^{j\mathcal{V}}], \tag{B.6}$$

with similar expressions for \mathbf{b}^j and \mathbf{B}_0^j . Subregions have Neumann boundary conditions in the tangential direction and therefore, $\mathbf{c}^j = 0$ and $\mathbf{d}^j = 0$. The total vector of unknowns for radial magnetization \mathbf{X} is then given by

$$\mathbf{X} = [\mathbf{a}^{\text{I}}, \mathbf{b}^{\text{I}}, \mathbf{c}^{\text{I}}, \mathbf{d}^{\text{I}}, \mathbf{a}^{\text{II}}, \mathbf{b}^{\text{II}}, \mathbf{c}^{\text{II}}, \mathbf{d}^{\text{II}}, \mathbf{a}^{\text{IV}}, \mathbf{b}^{\text{IV}}, \mathbf{B}_0^{\text{IV}}, \mathbf{a}_n^{\text{V}}, \mathbf{b}_n^{\text{V}}, \mathbf{B}_0^{\text{V}}]^T. \tag{B.7}$$

Furthermore, define the correlation matrix $\boldsymbol{\varepsilon}_s^{k,j}$ as

$$\boldsymbol{\varepsilon}_s^{k,j} = [\boldsymbol{\varepsilon}_s^{k,j1}, \boldsymbol{\varepsilon}_s^{k,j2}, \dots, \boldsymbol{\varepsilon}_s^{k,j\mathcal{V}}]^T, \quad (\text{B.8})$$

with each matrix $\boldsymbol{\varepsilon}_s^{k,j\nu}$ written as

$$\boldsymbol{\varepsilon}_s^{k,j\nu} = \begin{bmatrix} \varepsilon_s^{k,j\nu}(1,1) & \varepsilon_s^{k,j\nu}(1,2) & \dots & \varepsilon_s^{k,j\nu}(1,N_k) \\ \varepsilon_s^{k,j\nu}(2,1) & \varepsilon_s^{k,j\nu}(2,2) & \dots & \varepsilon_s^{k,j\nu}(2,N_k) \\ \vdots & \vdots & \ddots & \vdots \\ \varepsilon_s^{k,j\nu}(N_j,1) & \varepsilon_s^{k,j\nu}(N_j,2) & \dots & \varepsilon_s^{k,j\nu}(N_j,N_k) \end{bmatrix}. \quad (\text{B.9})$$

The correlation matrix $\boldsymbol{\varepsilon}_c^{k,j}$ is obtained in a similar manner. Furthermore, define the correlation matrix $\boldsymbol{\kappa}_c^{k,j}$ as

$$\boldsymbol{\kappa}_c^{k,j} = [\boldsymbol{\kappa}_c^{k,j1}, \boldsymbol{\kappa}_c^{k,j2}, \dots, \boldsymbol{\kappa}_c^{k,j\mathcal{V}}], \quad (\text{B.10})$$

with each matrix $\boldsymbol{\kappa}_c^{k,j\nu}$ written as

$$\boldsymbol{\kappa}_c^{k,j\nu} = \begin{bmatrix} \kappa_c^{k,j\nu}(1,1) & \kappa_c^{k,j\nu}(2,1) & \dots & \kappa_c^{k,j\nu}(N_j,1) \\ \kappa_c^{k,j\nu}(1,2) & \kappa_c^{k,j\nu}(2,2) & \dots & \kappa_c^{k,j\nu}(N_j,2) \\ \vdots & \vdots & \ddots & \vdots \\ \kappa_c^{k,j\nu}(1,N_k) & \kappa_c^{k,j\nu}(2,N_k) & \dots & \kappa_c^{k,j\nu}(N_j,N_k) \end{bmatrix}. \quad (\text{B.11})$$

The correlation matrix $\boldsymbol{\zeta}_c^{k,j\nu}$ is obtained in a similar manner. The correlation matrix $\boldsymbol{\kappa}_0^{k,j}$ is written as

$$\boldsymbol{\kappa}_0^{k,j} = \begin{bmatrix} \kappa_0^{k,j1}(1) & \kappa_0^{k,j2}(1) & \dots & \kappa_0^{k,j\mathcal{V}}(1) \\ \kappa_0^{k,j1}(2) & \kappa_0^{k,j2}(2) & \dots & \kappa_0^{k,j\mathcal{V}}(2) \\ \vdots & \vdots & \ddots & \vdots \\ \kappa_0^{k,j1}(N_k) & \kappa_0^{k,j2}(N_k) & \dots & \kappa_0^{k,j\mathcal{V}}(N_k) \end{bmatrix}. \quad (\text{B.12})$$

The correlation matrix $\boldsymbol{\zeta}_0^{k,j}$ is again obtained in a similar manner. The source term vector of region II, $\mathbf{G}_{ps}^{\text{II}}$ is given by

$$\mathbf{G}_{ps}^{\text{II}} = [\mathcal{G}_{ps1}^{\text{II}}(R_m), \mathcal{G}_{ps2}^{\text{II}}(R_m), \dots, \mathcal{G}_{psN}^{\text{II}}(R_m)]^T. \quad (\text{B.13})$$

with similar equations for $\mathbf{G}_{pc}^{\text{II}}$, $\mathbf{G}_{qs}^{\text{II}}$ and $\mathbf{G}_{qc}^{\text{II}}$. The current density vector for region IV (only considered for the calculation of the ring inductance in Section 4.3.3) and V (only considered when armature reaction is included) is written as

$$\mathbf{J}_{l0}^j = [\mathbf{J}_{l0}^{j1}, \mathbf{J}_{l0}^{j2}, \dots, \mathbf{J}_{l0}^{jS}]^T. \quad (\text{B.14})$$

$$\begin{array}{cccccccc}
\mathbf{C}_{33} & \mathbf{0} & \mathbf{0} & \mathbf{0} & \mathbf{0} & \mathbf{0} & \mathbf{0} & \mathbf{0} \\
\mathbf{0} & -\mathbf{C}_{33} & \mathbf{0} & \mathbf{0} & \mathbf{0} & \mathbf{0} & \mathbf{0} & \mathbf{0} \\
\mathbf{0} & \mu_r \mathbf{C}_{34} & \mathbf{0} & \mathbf{0} & \mathbf{0} & \mathbf{0} & \mathbf{0} & \mathbf{0} \\
\mu_r \mathbf{C}_{34} & \mathbf{0} & \mathbf{0} & \mathbf{0} & \mathbf{0} & \mathbf{0} & \mathbf{0} & \mathbf{0} \\
\mathbf{0} & \mathbf{0} & \mathbf{0} & \mathbf{0} & \mathbf{0} & \mathbf{0} & \mathbf{0} & \mathbf{0} \\
\mathbf{0} & \mathbf{0} & \mathbf{0} & \mathbf{0} & \mathbf{0} & \mathbf{0} & \mathbf{0} & \mathbf{0} \\
\mathbf{0} & \mathbf{0} & -\mathbf{C}_{23} & -\mathbf{C}_{24} & \mathbf{0} & \mathbf{0} & \mathbf{0} & \mathbf{0} \\
\mathbf{0} & \mathbf{0} & -\boldsymbol{\kappa}_c^{I,IV} \mathbf{C}_{21} & \boldsymbol{\kappa}_c^{I,IV} \mathbf{C}_{22} & -\boldsymbol{\kappa}_0^{I,IV} & \mathbf{0} & \mathbf{0} & \mathbf{0} \\
\mathbf{0} & \mathbf{0} & -\boldsymbol{\zeta}_c^{I,IV} \mathbf{C}_{21} & \boldsymbol{\zeta}_c^{I,IV} \mathbf{C}_{22} & -\boldsymbol{\zeta}_0^{I,IV} & \mathbf{0} & \mathbf{0} & \mathbf{0} \\
\mathbf{0} & \mathbf{0} & \mathbf{C}_{27} & \mathbf{C}_{28} & \mathbf{0} & -\mathbf{C}_{27} & -\mathbf{C}_{28} & \mathbf{0} \\
\mathbf{0} & \mathbf{0} & \mathbf{C}_{25} & -\mathbf{C}_{26} & \mathbf{0} & -\mathbf{C}_{25} & \mathbf{C}_{26} & \mathbf{0} \\
\mathbf{0} & \mathbf{0} & \mathbf{0} & \mathbf{0} & \mathbf{I} & \mathbf{0} & \mathbf{0} & -\mathbf{I} \\
\mathbf{0} & \mathbf{0} & \mathbf{0} & \mathbf{0} & \mathbf{0} & \mathbf{C}_{29} & -\mathbf{C}_{30} & \mathbf{0} \\
\mathbf{0} & \mathbf{0} & \mathbf{0} & \mathbf{0} & \mathbf{0} & \mathbf{0} & \mathbf{0} & \mathbf{I}
\end{array} \Bigg), \quad (\text{B.20})$$

with the matrices \mathbf{C}_{33} and \mathbf{C}_{34} given by

$$\mathbf{C}_{33} = \begin{cases} \mathbf{C}_3 & \text{for IMT,} \\ \mathbf{C}_4 & \text{for EMT,} \end{cases} \quad (\text{B.21})$$

$$\mathbf{C}_{34} = \begin{cases} \mathbf{C}_1 & \text{for IMT,} \\ -\mathbf{C}_2 & \text{for EMT,} \end{cases} \quad (\text{B.22})$$

and the vector \mathbf{Y} is given by

$$\mathbf{Y} = \begin{bmatrix} \mathbf{0} \\ \mathbf{0} \\ -\mu_0 \mathbf{M}_{qs}^{\text{II}} \\ -\mu_0 \mathbf{M}_{qc}^{\text{II}} \\ -\mathbf{G}_{ps}^{\text{II}} \\ -\mathbf{G}_{pc}^{\text{II}} \\ -\mathbf{G}_{qs}^{\text{II}} + \mu_0 \mathbf{M}_{qs}^{\text{II}} \\ -\mathbf{G}_{qc}^{\text{II}} + \mu_0 \mathbf{M}_{qc}^{\text{II}} \\ \mathbf{0} \\ -\mu_0 R_i \boldsymbol{\kappa}_0^{I,IV} \mathbf{J}_{l_0}^{\text{IV}} \\ -\mu_0 R_i \boldsymbol{\zeta}_0^{I,IV} \mathbf{J}_{l_0}^{\text{IV}} \\ \mathbf{0} \\ \mathbf{0} \\ \mu_0 R_t (\mathbf{J}_{l_0}^{\text{IV}} - \mathbf{J}_{l_0}^{\text{V}}) \\ \mathbf{0} \\ \mu_0 \mathbf{J}_{l_0}^{\text{V}} R_c \end{bmatrix}. \quad (\text{B.23})$$

B.3 Axial magnetization

Since the permanent magnets consist of separate, non-periodic, regions, with Neumann boundary conditions in the tangential direction, equation (B.6) should be used instead of equation (B.5) to define the unknown vector for subregions $\Pi_{j\nu}$. Additionally, the coefficients \mathbf{c}^{II} and \mathbf{d}^{II} are equal to zero. Furthermore, each subregion $\Pi_{j\nu}$ for $\nu = 1 \dots P$ has now a constant $B_0^{j\nu}$. However, the unknown vector \mathbf{B}_0^{II} only contains the $P - 1$ constants

$$\mathbf{B}_0^{\text{II}} = \left[B_0^{\text{II}1}, B_0^{\text{II}2}, \dots, B_0^{\text{II}(P-1)} \right]. \quad (\text{B.24})$$

The final constant $B_0^{\text{II}P}$ can be calculated from the other constants as

$$B_0^{\text{II}P} = - \sum_{\nu=1}^{P-1} B_0^{\text{II}\nu}, \quad (\text{B.25})$$

since the total sum of these constants should be zero. This results from applying Ampère's law, equation (2.106) at $r = R_m$. The total vector of unknowns is then given by

$$\mathbf{X} = \left[\mathbf{a}^{\text{I}}, \mathbf{b}^{\text{I}}, \mathbf{c}^{\text{I}}, \mathbf{d}^{\text{I}}, \mathbf{a}^{\text{II}}, \mathbf{b}^{\text{II}}, \mathbf{B}_0^{\text{II}}, \mathbf{a}^{\text{III}}, \mathbf{c}^{\text{III}}, \mathbf{a}^{\text{IV}}, \mathbf{b}^{\text{IV}}, \mathbf{B}_0^{\text{IV}}, \mathbf{a}_n^{\text{V}}, \mathbf{b}_n^{\text{V}}, \mathbf{B}_0^{\text{V}} \right]^T, \quad (\text{B.26})$$

for IMT and

$$\mathbf{X} = \left[\mathbf{a}^{\text{I}}, \mathbf{b}^{\text{I}}, \mathbf{c}^{\text{I}}, \mathbf{d}^{\text{I}}, \mathbf{a}^{\text{II}}, \mathbf{b}^{\text{II}}, \mathbf{B}_0^{\text{II}}, \mathbf{b}^{\text{III}}, \mathbf{d}^{\text{III}}, \mathbf{a}^{\text{IV}}, \mathbf{b}^{\text{IV}}, \mathbf{B}_0^{\text{IV}}, \mathbf{a}_n^{\text{V}}, \mathbf{b}_n^{\text{V}}, \mathbf{B}_0^{\text{V}} \right]^T, \quad (\text{B.27})$$

for EMT. Define the vector of magnetization as

$$\mathbf{M}_{q0}^{\text{II}} = \left[\mathbf{M}_{q0}^{\text{II}1}, \mathbf{M}_{q0}^{\text{II}2}, \dots, \mathbf{M}_{q0}^{\text{II}P} \right]^T. \quad (\text{B.28})$$

Furthermore, define the matrices \mathbf{K}_1 and \mathbf{K}_2 as

$$\mathbf{K}_1 = \begin{bmatrix} \frac{1}{\mathbf{w}^{\text{I}}} (\cos(\mathbf{w}^{\text{I}} (\Delta_{\text{I}1} + \tau_{mz})) - \cos(\mathbf{w}^{\text{I}} (\Delta_{\text{II}1} + \tau_p))) \\ \frac{1}{\mathbf{w}^{\text{I}}} (\cos(\mathbf{w}^{\text{I}} (\Delta_{\text{I}2} + \tau_{mz})) - \cos(\mathbf{w}^{\text{I}} (\Delta_{\text{II}2} + \tau_p))) \\ \vdots \\ \frac{1}{\mathbf{w}^{\text{I}}} (\cos(\mathbf{w}^{\text{I}} (\Delta_{\text{I}(P-1)} + \tau_{mz})) - \cos(\mathbf{w}^{\text{I}} (\Delta_{\text{II}(P-1)} + \tau_p))) \end{bmatrix}, \quad (\text{B.29})$$

$$\mathbf{K}_2 = \begin{bmatrix} \frac{1}{\mathbf{w}^{\text{I}}} (\sin(\mathbf{w}^{\text{I}} (\Delta_{\text{I}1} + \tau_{mz})) - \sin(\mathbf{w}^{\text{I}} (\Delta_{\text{II}1} + \tau_p))) \\ \frac{1}{\mathbf{w}^{\text{I}}} (\sin(\mathbf{w}^{\text{I}} (\Delta_{\text{I}2} + \tau_{mz})) - \sin(\mathbf{w}^{\text{I}} (\Delta_{\text{II}2} + \tau_p))) \\ \vdots \\ \frac{1}{\mathbf{w}^{\text{I}}} (\sin(\mathbf{w}^{\text{I}} (\Delta_{\text{I}(P-1)} + \tau_{mz})) - \sin(\mathbf{w}^{\text{I}} (\Delta_{\text{II}(P-1)} + \tau_p))) \end{bmatrix}, \quad (\text{B.30})$$

note that elementary multiplication and division are performed to construct the matrices \mathbf{K}_1 and \mathbf{K}_2 . Define the vectors $\mathbf{t}_1, \dots, \mathbf{t}_4$ as

$$\mathbf{t}_1 = -\cos\left(\frac{\mathbf{w}^{\text{II}}}{\tau_{mz}}\right) \frac{(R_m \mathcal{I}_1(\mathbf{w}^{\text{II}} R_m) - R_r \mathcal{I}_1(\mathbf{w}^{\text{II}} R_r))}{\mathbf{w}^{\text{II}}}, \quad (\text{B.31})$$

$$\mathbf{t}_2 = \frac{(R_m \mathcal{I}_1(\mathbf{w}^{\text{II}} R_m) - R_r \mathcal{I}_1(\mathbf{w}^{\text{II}} R_r))}{\mathbf{w}^{\text{II}}}, \quad (\text{B.32})$$

$$\mathbf{t}_3 = -\cos\left(\frac{\mathbf{w}^{\text{II}}}{\tau_{mz}}\right) \frac{(R_m \mathcal{K}_1(\mathbf{w}^{\text{II}} R_m) - R_r \mathcal{K}_1(\mathbf{w}^{\text{II}} R_r))}{\mathbf{w}^{\text{II}}}, \quad (\text{B.33})$$

$$\mathbf{t}_4 = \frac{(R_m \mathcal{K}_1(\mathbf{w}^{\text{II}} R_m) - R_r \mathcal{K}_1(\mathbf{w}^{\text{II}} R_r))}{\mathbf{w}^{\text{II}}}, \quad (\text{B.34})$$

where again elementary multiplication and division are performed to construct the vectors $\mathbf{t}_1, \dots, \mathbf{t}_4$. Consequently, the matrices T_{12} and T_{34} can be built up as

$$\mathbf{T}_{12} = \begin{bmatrix} \mathbf{t}_1 & \mathbf{t}_2 & \mathbf{0} & \mathbf{0} & \cdots & \mathbf{0} \\ \mathbf{0} & \mathbf{t}_1 & \mathbf{t}_2 & \mathbf{0} & \cdots & \mathbf{0} \\ \vdots & \vdots & \vdots & \vdots & \ddots & \vdots \\ \mathbf{0} & \cdots & \mathbf{0} & \mathbf{0} & \mathbf{t}_1 & \mathbf{t}_2 \end{bmatrix}, \quad \left. \begin{array}{l} \\ \\ \\ \end{array} \right\} (P-1) \text{ rows} \quad (\text{B.35})$$

$$\mathbf{T}_{34} = \begin{bmatrix} \mathbf{t}_3 & \mathbf{t}_4 & \mathbf{0} & \mathbf{0} & \cdots & \mathbf{0} \\ \mathbf{0} & \mathbf{t}_3 & \mathbf{t}_4 & \mathbf{0} & \cdots & \mathbf{0} \\ \vdots & \vdots & \vdots & \vdots & \ddots & \vdots \\ \mathbf{0} & \cdots & \mathbf{0} & \mathbf{0} & \mathbf{t}_3 & \mathbf{t}_4 \end{bmatrix}, \quad \left. \begin{array}{l} \\ \\ \\ \end{array} \right\} (P-1) \text{ rows} \quad (\text{B.36})$$

Additionally, define δ as

$$\delta = \frac{R_m^2 - R_r^2}{2}, \quad (\text{B.37})$$

which is used to construct the matrix \mathbf{G}_1 as

$$\mathbf{G}_1 = \begin{bmatrix} -\delta & \delta & 0 & \cdots & 0 \\ 0 & -\delta & \delta & \cdots & 0 \\ \vdots & \vdots & \vdots & \ddots & \vdots \\ 0 & \cdots & 0 & -\delta & \delta \\ 0 & \cdots & 0 & 0 & -\delta \end{bmatrix}. \quad \left. \begin{array}{l} \\ \\ \\ \end{array} \right\} (P-1) \text{ rows} \quad (\text{B.38})$$

$\xrightarrow{\hspace{10em}}$
 $(P-1) \text{ columns}$

Additionally, the matrix \mathbf{G}_2 can be constructed as

$$\mathbf{G}_2 = \begin{bmatrix} 0 & 0 & 0 & \cdots & 0 \\ \vdots & \vdots & \vdots & \ddots & \vdots \\ 0 & 0 & 0 & \cdots & 0 \\ -\delta & -\delta & -\delta & \cdots & -\delta \end{bmatrix}, \quad \begin{array}{l} \downarrow \\ (P-1) \text{ rows} \end{array} \quad (\text{B.39})$$

$\xrightarrow{\hspace{10em}}$
 $(P-1) \text{ columns}$

The boundary condition matrix \mathbf{E} for axial magnetization is constructed as

$$\mathbf{E} = \begin{bmatrix} 0 & 0 & 0 & 0 & -\mathbf{C}_7 & -\mathbf{C}_8 & 0 \\ 0 & 0 & 0 & 0 & -\kappa_c^{\text{III,II}} \mathbf{C}_5 & \kappa_c^{\text{III,II}} \mathbf{C}_6 & \kappa_0^{\text{III,II}} \\ 0 & 0 & 0 & 0 & -\zeta_c^{\text{III,II}} \mathbf{C}_5 & \zeta_c^{\text{III,II}} \mathbf{C}_6 & \zeta_0^{\text{III,II}} \\ \varepsilon_s^{\text{I,II}} \mathbf{C}_{11} & \varepsilon_s^{\text{I,II}} \mathbf{C}_{12} & -\varepsilon_c^{\text{I,II}} \mathbf{C}_{11} & -\varepsilon_c^{\text{I,II}} \mathbf{C}_{12} & -\mathbf{C}_{15} & -\mathbf{C}_{16} & 0 \\ 0 & 0 & \mu_r \mathbf{C}_9 & -\mu_r \mathbf{C}_{10} & -\kappa_c^{\text{I,II}} \mathbf{C}_{13} & \kappa_c^{\text{I,II}} \mathbf{C}_{14} & \kappa_0^{\text{I,II}} \\ \mu_r \mathbf{C}_9 & -\mu_r \mathbf{C}_{10} & 0 & 0 & -\zeta_c^{\text{I,II}} \mathbf{C}_{13} & \zeta_c^{\text{I,II}} \mathbf{C}_{14} & \zeta_0^{\text{I,II}} \\ R_m \mathbf{K}_1 \mathbf{C}_{11} & R_m \mathbf{K}_1 \mathbf{C}_{12} & R_m \mathbf{K}_2 \mathbf{C}_{11} & R_m \mathbf{K}_2 \mathbf{C}_{12} & \mathbf{T}_{12} & \mathbf{T}_{34} & \mathbf{G}_1 + \mathbf{G}_2 \\ \varepsilon_s^{\text{I,IV}} \mathbf{C}_{19} & \varepsilon_s^{\text{I,IV}} \mathbf{C}_{20} & -\varepsilon_c^{\text{I,IV}} \mathbf{C}_{19} & -\varepsilon_c^{\text{I,IV}} \mathbf{C}_{20} & 0 & 0 & 0 \\ 0 & 0 & \mathbf{C}_{17} & -\mathbf{C}_{18} & 0 & 0 & 0 \\ \mathbf{C}_{17} & -\mathbf{C}_{18} & 0 & 0 & 0 & 0 & 0 \\ 0 & 0 & 0 & 0 & 0 & 0 & 0 \\ 0 & 0 & 0 & 0 & 0 & 0 & 0 \\ 0 & 0 & 0 & 0 & 0 & 0 & 0 \\ 0 & 0 & 0 & 0 & 0 & 0 & 0 \\ 0 & 0 & 0 & 0 & 0 & 0 & 0 \\ 0 & 0 & 0 & 0 & 0 & 0 & 0 \end{bmatrix},$$

$$\begin{bmatrix} \varepsilon_s^{\text{III,II}} \mathbf{C}_{33} & -\varepsilon_c^{\text{III,II}} \mathbf{C}_{33} & 0 & 0 & 0 & 0 & 0 & 0 \\ 0 & \mu_r \mathbf{C}_{34} & 0 & 0 & 0 & 0 & 0 & 0 \\ \mu_r \mathbf{C}_{34} & 0 & 0 & 0 & 0 & 0 & 0 & 0 \\ 0 & 0 & 0 & 0 & 0 & 0 & 0 & 0 \\ 0 & 0 & 0 & 0 & 0 & 0 & 0 & 0 \\ 0 & 0 & 0 & 0 & 0 & 0 & 0 & 0 \\ -R_r \mathbf{K}_1 \mathbf{C}_{33} & R_r \mathbf{K}_2 \mathbf{C}_{33} & 0 & 0 & 0 & 0 & 0 & 0 \\ 0 & 0 & -\mathbf{C}_{23} & -\mathbf{C}_{24} & 0 & 0 & 0 & 0 \\ 0 & 0 & -\kappa_c^{\text{I,IV}} \mathbf{C}_{21} & \kappa_c^{\text{I,IV}} \mathbf{C}_{22} & -\kappa_0^{\text{I,IV}} & 0 & 0 & 0 \\ 0 & 0 & -\zeta_c^{\text{I,IV}} \mathbf{C}_{21} & \zeta_c^{\text{I,IV}} \mathbf{C}_{22} & -\zeta_0^{\text{I,IV}} & 0 & 0 & 0 \\ 0 & 0 & \mathbf{C}_{27} & \mathbf{C}_{28} & 0 & -\mathbf{C}_{27} & -\mathbf{C}_{28} & 0 \\ 0 & 0 & \mathbf{C}_{25} & -\mathbf{C}_{26} & 0 & -\mathbf{C}_{25} & \mathbf{C}_{26} & 0 \\ 0 & 0 & 0 & 0 & \mathbf{I} & 0 & 0 & -\mathbf{I} \\ 0 & 0 & 0 & 0 & 0 & \mathbf{C}_{29} & -\mathbf{C}_{30} & 0 \\ 0 & 0 & 0 & 0 & 0 & 0 & 0 & \mathbf{I} \end{bmatrix}, \quad (\text{B.40})$$

with the matrices \mathbf{C}_{33} and \mathbf{C}_{34} given by

$$\mathbf{C}_{33} = \begin{cases} \mathbf{C}_3 & \text{for IMT,} \\ \mathbf{C}_4 & \text{for EMT,} \end{cases} \quad (\text{B.41})$$

$$\mathbf{C}_{34} = \begin{cases} \mathbf{C}_1 & \text{for IMT,} \\ -\mathbf{C}_2 & \text{for EMT,} \end{cases} \quad (\text{B.42})$$

and \mathbf{Y} is given by

$$\mathbf{Y} = \begin{bmatrix} \mathbf{0} \\ \mathbf{0} \\ -\mu_0 \kappa_0^{\text{III,II}} \mathbf{M}_{q0}^{\text{II}} \\ -\mu_0 \zeta_0^{\text{III,II}} \mathbf{M}_{q0}^{\text{II}} \\ \mathbf{0} \\ \mathbf{0} \\ -\mu_0 \kappa_0^{\text{I,II}} \mathbf{M}_{q0}^{\text{II}} \\ -\mu_0 \zeta_0^{\text{I,II}} \mathbf{M}_{q0}^{\text{II}} \\ \mathbf{0} \\ \mathbf{0} \\ -\mu_0 R_i \kappa_0^{\text{I,IV}} \mathbf{J}_{l0}^{\text{IV}} \\ -\mu_0 R_i \zeta_0^{\text{I,IV}} \mathbf{J}_{l0}^{\text{IV}} \\ \mathbf{0} \\ \mathbf{0} \\ \mu_0 R_t (\mathbf{J}_{l0}^{\text{IV}} - \mathbf{J}_{l0}^{\text{V}}) \\ \mathbf{0} \\ \mu_0 \mathbf{J}_{l0}^{\text{V}} R_c \end{bmatrix}. \quad (\text{B.43})$$

B.4 Continuity of the magnetic vector potential

This section gives the solution of the constants A_0^k of the magnetic vector potential formulation for each region k . This solution is necessary to calculate the induced flux linkage in the conductive rings and the ring inductance, as described in Chapter 4. For periodic regions, the constant A_0^k is zero since it would lead to a net flux in the tangential direction which is incorrect from a physical point of view. Hence, the constant only has to be determined in the slot openings (region IV). A similar calculation can be performed for the regions V and II in case of axial magnetization but it is irrelevant for the content of the thesis. Since the magnetic vector potential formulation in the airgap is known, the constants $A_0^{\text{IV}\nu}$ can be determined by applying the continuity of the magnetic vector potential at $r = R_i$ over the width of the slot opening. The average value of magnetic vector potential in the airgap A_l^{I} at the radius $r = R_i$ over the width of the slot opening is obtained as

$$A_{l0}^{\text{IV}\nu}(R_i) = \frac{1}{\tau_o} \int_{\Delta^{\text{IV}\nu}}^{\Delta^{\text{IV}\nu} + \tau_o} A_l^{\text{I}}(R_i, q) dq, \quad (\text{B.44})$$

which can be evaluated as

$$\begin{aligned}
A_{l_0}^{\text{IV}\nu}(R_i) &= \frac{1}{\tau_o} \sum_{n=1}^{N_i} \frac{1}{(w_n^{\text{I}})^2} (a_n^{\text{I}} \mathcal{I}_1(w_n^{\text{I}} R_i) + b_n^{\text{I}} \mathcal{K}_1(w_n^{\text{I}} R_i)) \\
&\quad \times [\sin(w_n^{\text{I}} (\Delta^{\text{IV}\nu} + \tau_o)) - \sin(w_n^{\text{I}} \Delta^{\text{IV}\nu})] \\
&- \frac{1}{\tau_o} \sum_{n=1}^{N_i} \frac{1}{(w_n^{\text{I}})^2} (c_n^{\text{I}} \mathcal{I}_1(w_n^{\text{I}} R_i) + d_n^{\text{I}} \mathcal{K}_1(w_n^{\text{I}} R_i)) \\
&\quad \times [\cos(w_n^{\text{I}} (\Delta^{\text{IV}\nu} + \tau_o)) - \cos(w_n^{\text{I}} \Delta^{\text{IV}\nu})]. \tag{B.45}
\end{aligned}$$

Given the equation for $A_{l_0}^{\text{IV}\nu}(p)$, (2.53) in Section 2.6.3, the constant $A_0^{\text{IV}\nu}$ can be calculated as

$$A_0^{\text{IV}\nu} = R_i A_{l_0}^{\text{IV}\nu}(R_i) + \mu_0 J_{l_0}^{\text{IV}\nu} \frac{R_i^2}{3} - B_0^{\text{IV}\nu} \frac{R_i}{2}. \tag{B.46}$$

Appendix C

Controllers and weighting filters

C.1 Road actuation

The feedback loop shaping controller for the road actuation can be written in the Laplace domain, with $s = j\omega$, as

$$C_{r,fb} = \underbrace{1.3e6}_{\text{Gain}} \underbrace{\frac{\frac{1}{(2\pi 1.45)^2} s^2 + \frac{0.66}{2\pi 1.45} s + 1}{(2\pi)^2 s^2 + \frac{1}{2\pi} s + 1}}_{\text{Notch 1}} \underbrace{\frac{\frac{1}{(2\pi 33.9)^2} s^2 + \frac{0.22}{2\pi 33.9} s + 1}{(2\pi 12)^2 s^2 + \frac{2}{2\pi 12} s + 1}}_{\text{Notch 2}} \underbrace{\frac{\frac{1}{2\pi 4} + 1}{\frac{1}{2\pi 45} + 1}}_{\text{Lead filter}}. \quad (\text{C.1})$$

The feed forward for the road actuation is given by

$$C_{r,ff} = \frac{F_{act}}{F_{r,act}} = \frac{F_{act}}{M_r z_r s^2}, \quad (\text{C.2})$$

$$= \frac{-k_t M_s s^2}{k_a k_t + d_a k_t s + (k_t M_s + k_a (M_s + M_u)) s^2 + d_a (M_s + M_u) s^3 + M_s M_u s^4}. \quad (\text{C.3})$$

C.2 Weighting filters

The various weighting filters applied for the design of the robust controllers in the Laplace domain, with $s = j\omega$, can be listed as

$$W_{un} = \frac{\frac{1}{(2\pi 30)^2} s^2 + \frac{\sqrt{2}}{2\pi 30} s + 1}{\frac{1}{(2\pi 400)^2} s^2 + \frac{\sqrt{2}}{2\pi 400} s + 1}, \quad (\text{C.4})$$

$$W_{as} = w_{as} \frac{86.51s + 546.1}{s^2 + 82.17s + 1892}, \quad (\text{C.5})$$

$$W_{zt} = w_{zt} \frac{\frac{1}{2\pi 12} s + 1}{\frac{1}{2\pi 0.6} s + 1}, \quad (\text{C.6})$$

$$W_F = w_F \frac{\frac{1}{(2\pi 30)^2} s^2 + \frac{\sqrt{2}}{2\pi 30} s + 1}{\frac{1}{(2\pi 200)^2} s^2 + \frac{\sqrt{2}}{2\pi 200} s + 1}, \quad (\text{C.7})$$

$$W_{\Delta_z} = w_{\Delta_z}, \quad (\text{C.8})$$

with w_{as} , w_{zt} , w_F and w_{Δ_z} gains which are tuned to enforce either comfort or handling and to suppress the actuator force and suspension travel, respectively.

Bibliography

- [1] Ackermann, B. and Sottek, R. [1995], ‘Analytical modeling of the cogging torque in permanent magnet motors’, *Electrical Engineering* **78**(2), 117–125.
- [2] Akoun, G. and Yonnet, J. P. [1984], ‘3D analytical calculation of the forces exerted between two cuboidal magnets’, *IEEE Transactions on Magnetics* **20**(5), 1962–1964.
- [3] Alonso, M. and Comas, A. [2008], ‘Thermal model of a twin-tube cavitating shock absorber’, *Proc. IMechE Part D: J. Automobile Engineering* **222**(4), 1955–1964.
- [4] Alwash, J. H. H. [1972], Analysis and design of linear induction machines, PhD thesis, University of London.
- [5] Amati, N., Tonoli, A., Canova, A., Cavalli, F. and Padovani, M. [2007], ‘Dynamic behavior of torsional eddy-current dampers: Sensitivity of the design parameters’, *IEEE Transactions on Magnetics* **43**(7), 3266–3277.
- [6] Andr n, P. [2006], ‘Power spectral density approximations of longitudinal road profiles’, *Int. J. of Vehicle Design* **40**(1/2/3), 2–14.
- [7] Baber, J., Kolodko, J., Noel, T., Parent, M. and Vlacic, L. [2005], ‘Cooperative autonomous driving: intelligent vehicles sharing city roads’, *IEEE Robotics Automation Magazine* **12**(1), 44–49.
- [8] Bankestrom, J. [1996], ‘Load sensing bearing’, U.S. Patent 5,503,030.
- [9] Bastow, D., Howard, G. and Whitehead, J. P. [2004], *Car Suspension and Handling, 4th edition*, SAE International, U.S.A.
- [10] Bazaraa, M. S., Sherali, H. D. and Shetty, C. M. [1993], *Nonlinear Programming: Theory and Algorithms*, John Wiley and Sons, U.S.A.
- [11] Benson, A. J. [1998], *Motion Sickness*, Stellman JM, et al, eds. Encyclopedia of occupational health and safety. 4th ed., Switzerland.

- [12] Bertotti, G. [1998], *Hysteresis in Magnetism*, Academic Press, U.S.A.
- [13] Blom, R. E. A., Vissers, J. P. M., Merks, L. L. F. and Pinxteren, M. [2009], Flat plank tyre tester, user's manual, Technical report, Eindhoven University of Technology.
- [14] Bodie, M. O. and Hac, A. [2000], 'Closed loop yaw control of vehicles using magneto-rheological dampers', *Society of Automotive Engineers - 2000-01-0107*.
- [15] Bose Corp. [n.d.], 'Active suspension system', <http://www.bose.com>.
- [16] Boules, N. [1984], 'Two-dimensional field analysis of cylindrical machines with permanent magnet excitation', *IEEE Transactions on Industry Applications* **20**(5), 1267–1277.
- [17] Boules, N. [1985], 'Prediction of no-load flux density distribution in permanent magnet machines', *IEEE Transactions on Industry Applications* **21**(4), 633–643.
- [18] Brockhaus Messtechnik GmbH [n.d.], <http://www.brockhaus.net>.
- [19] Brown, S. and Holweg, E. [2004], Smart electro-mechanical actuation for drive-by-wire applications, in 'Convergence International Congress & Exposition On Transportation Electronics', Detroit, MI, USA, pp. 1–6.
- [20] Bruscella, B., Rouillard, V. and Sek, M. [1999], 'Analysis of road profile surfaces', *Journal of Sound and Vibration* **125**(1), 55–59.
- [21] Cain, G. and Meyer, G. H. [2006], *Separation of variables for partial differential equations : an eigenfunction approach*, Chapman & Hall/CRC, U.K.
- [22] Canova, A. and Vusini, B. [2005], 'Analytical modeling of rotating eddy-current couplers', *IEEE Transactions on magnetics* **41**(1), 24–35.
- [23] Cao, J., Liu, H., Li, P. and Brown, D. J. [2008], 'State of the art in vehicle active suspension adaptive control systems based on intelligent methodologies', *IEEE Transactions on Intelligent Transportation Systems* **9**(3), 392–405.
- [24] Carpenter, C. J. [1959], 'Surface-integral methods of calculating forces on magnetized iron parts', *Proceedings of the IEE - Part C: Monographs* **107**(11), 19–28.
- [25] Chan, C., Bouscayrol, A. and Chen, K. [2010], 'Electric, hybrid, and fuel-cell vehicles: Architectures and modeling', *Vehicular Technology, IEEE Transactions on* **59**(2), 589–598.

- [26] Cheng, Y., Espanet, C., Trigui, R., Bouscayrol, A. and Cui, S. [2010], Design of a permanent magnet electric variable transmission for hev applications, *in* 'IEEE Vehicle Power and Propulsion Conference, VPPC 2010', Lille, France, pp. 1–5.
- [27] Clark, R., Jewell, G., Forrest, S., Rens, J. and Mearky, C. [2005], 'Design features for enhancing the performance of electromagnetic valve actuation systems', *IEEE Transactions on Magnetics* **41**(3), 1163–1168.
- [28] Coulomb, J. [1983], 'A methodology for the determination of global electromechanical quantities from a finite element analysis and its application to the evaluation of magnetic forces, torques and stiffness', *IEEE Transactions on Magnetics* **19**(6), 2514–2519.
- [29] Coulomb, J. and Meunier, G. [1984], 'Finite element implementation of virtual work principle for magnetic or electric force and torque computation', *IEEE Transactions on Magnetics* **20**(5), 1894–1896.
- [30] de Bruijn, E., Gerard, M., Corno, M., Verhaegen, M. and Holweg, E. [2010], On the performance increase of wheel deceleration control through force sensing, *in* 'IEEE International Conference on Control Applications, CCA 2010', Yokohama, Japan, pp. 161–166.
- [31] Delphi Automotive LLP [2006], 'Audi R8 features Delphi's revolutionary MagneRide semi-active suspension', http://delphi.com/news/pressReleases/pressReleases_2006/pr_2006-11_30_001.
- [32] Dixon, J. C. [1996], *Tires, Suspension and Handling*, Cambridge University Press, U.K.
- [33] Dixon, J. C. [1999], *The Shock Absorber Handbook*, Society of Automotive Engineers, Inc., U.S.A.
- [34] Dodds, C. J. and Robson, J. D. [1973], 'The description of road surface roughness', *Journal of Sound and Vibration* **31**(2), 175–183.
- [35] Doležel, I., Karban, P. and Šolin, P. [2009], *Integral Methods in Low-Frequency Electromagnetics*, John Wiley and Sons, U.S.A.
- [36] Doyle, J. C. [1978], 'Guaranteed margins for lqg regulators', *IEEE Transactions on Automatic Control* **AC-23**(4), 756–757.
- [37] Doyle, J. C. [1983], Synthesis of robust controllers and filters, *in* 'Proceedings of the IEEE Conference on Decision and Control', San Antonio, TA, USA, pp. 109–114.
- [38] Driscoll, T. A. and Trefethen, L. N. [2002], *Schwarz-Christoffel Mapping*, Cambridge University Press, U.K.

- [39] Dubas, F. and Espanet, C. [2009], ‘Analytical solution of the magnetic field in permanent-magnet motors taking into account slotting effect: No-load vector potential and flux density calculation’, *IEEE Transactions on Magnetics* **45**(5), 2097–2109.
- [40] Eastham, J. F. and Alwash, J. H. [1972], ‘Transverse-flux tubular motors’, *IEE Proceedings* **112**(12), 1709–1718.
- [41] Ebrahimi, B., Khamesee, M. B. and Golnaraghi, F. [2008], ‘Design and modeling of a magnetic shock absorber based on eddy current effect’, *Journal of Sound and Vibration* **315**(4-5), 875–889.
- [42] Ebrahimi, B., Khamesee, M. B. and Golnaraghi, F. [2009a], ‘Eddy current damper feasibility in automobile suspension: modeling, simulation and testing’, *Smart Materials and Structures* **18**(1), 1–12.
- [43] Ebrahimi, B., Khamesee, M. B. and Golnaraghi, F. [2009b], ‘A novel eddy current damper: theory and experiment’, *Journal of Physics D: Applied physics* **42**(7), 1–6.
- [44] Ebrahimi, B., Khamesee, M. B. and Golnaraghi, F. [2010], ‘Permanent magnet configuration in design of an eddy current damper’, *Microsystem Technologies* **16**(1-2), 19–24.
- [45] Ebrahimi, B., Khamesee, M. and Golnaraghi, F. [2009c], Design of a hybrid electromagnetic/hydraulic damper for automotive suspension systems, *in* ‘International Conference on Mechatronics and Automation, ICMA 2009’, Waterloo, ON, Canada, pp. 3196–3200.
- [46] Encica, L. [2008], Space-mapping optimization applied to the design of a novel electromagnetic actuator for active suspension, PhD thesis, Eindhoven University of Technology.
- [47] Encica, L., Paulides, J. J. H. and Lomonova, E. A. [2009], Space-mapping optimization in electromechanics: an overview of algorithms and applications, *in* ‘COMPEL: The International Journal for Computation and Mathematics in Electrical and Electronic Engineering’, Vol. 28, pp. 1216–1226.
- [48] Encica, L., Paulides, J. J. H., Lomonova, E. A., Vandenput, A. J. A. and Leeuwen, B. G. [2008], ‘Spring, assembly of springs, assembly of a spring and a damper, as well as a vehicle comprising a spring’, WIPO Patent Application WO/2008/004871.
- [49] Evers, W. [2010], Improving driver comfort in commercial vehicles, Modeling and control of a low-power active cabin suspension system, PhD thesis, Eindhoven University of Technology.
- [50] Evers, W., Teerhuis, A., Knaap, A. v. d., Besselink, I. J. M. and Nijmeijer, H. [2011], ‘The electromechanical low-power active suspension: Modeling, control, and prototype testing’, *Journal of Dynamic Systems, Measurement, and Control* **133**(4), 1–9.

- [51] Frank, L. H., Casali, J. G. and Wierwill, W. W. [1988], 'Effects of visual display and motion system delays on operator performance and uneasiness in a driving simulator', *Human Factors* **30**(2), 201–217.
- [52] Furlani, E. P. [2001], *Permanent Magnet and Electromechanical devices*, Academic Press, U.S.A.
- [53] Gahlinger, P. M. [1999], 'Motion sickness - how to help your patients avoid travel travail', *Postgraduate Medicine Online* **106**(4), 451–465.
- [54] Gerard, M. and Verhaegen, M. [2009], Global and local chassis control based on load sensing, in 'American Control Conference, ACC 2009', St. Louis, MO, pp. 677–682.
- [55] Gu, Q. and Gao, H. [1985], 'Air gap field for PM electric machines', *Electric Power Components and Systems* **10**(5 & 6), 459–470.
- [56] Guo, S., Li, S. and Yang, S. [2006], Semi-active vehicle suspension systems with magnetorheological dampers, in 'IEEE International Conference on Vehicular Electronics and Safety', Beijing, China, pp. 403–406.
- [57] Gysen, B. L. J., Gibson, S., Clark, R. E. and Jewell, G. W. [2008], 'High temperature permanent magnet actuator for fail-safe applications', *IEEE Transactions on Industry Applications* **128-D**(10), 1198–1202.
- [58] Gysen, B. L. J., Ilhan, E., Meessen, K. J., Paulides, J. J. H. and Lomonova, E. A. [2010], 'Modeling of flux switching permanent magnet machines with Fourier analysis', *IEEE Transactions on Magnetics* **46**(6), 1499–1502.
- [59] Gysen, B. L. J., Janssen, J. L. G., Paulides, J. J. H. and Lomonova, E. A. [2009], 'Design aspects of an active electromagnetic suspension system for automotive applications', *IEEE Transactions on Industry Applications* **45**(5), 1589–1597.
- [60] Gysen, B. L. J., Meessen, K. J., Paulides, J. J. H. and Lomonova, E. A. [2009], Computational analysis of fringing fields and forces in the cylindrical coordinate system, in 'Proceedings of the 17th Conference on the Computation of Electromagnetic Fields, COMPUMAG 2009', Florianopolis, Brasil, pp. 769–770.
- [61] Gysen, B. L. J., Meessen, K. J., Paulides, J. J. H. and Lomonova, E. A. [2010], 'General formulation of the electromagnetic field distribution in machines and devices using Fourier analysis', *IEEE Transactions on Magnetics* **46**(1), 39–52.
- [62] Gysen, B. L. J., Meessen, K. J., Paulides, J. J. H. and Lomonova, E. A. [2011], '3D analytical and numerical modeling of tubular actuators with skewed permanent magnets', *IEEE Transactions on Magnetics* **47**(9), 2200–2212.

- [63] Gysen, B. L. J., Paulides, J. J. H., Encica, L. and Lomonova, E. A. [2009], Slotted tubular permanent magnet actuator for active suspension systems, *in* 'The 7th International Symposium on Linear Drives for Industry Applications, LDIA 2009', Incheon, South Korea, pp. 292–295.
- [64] Gysen, B. L. J., Paulides, J. J. H. and Lomonova, E. A. [2011a], Direct-drive electromagnetic active suspension system with integrated eddy current damping for automotive applications, *in* 'The 8th International Symposium on Linear Drives for Industry Applications, LDIA 2011', Eindhoven, The Netherlands, pp. 1–4.
- [65] Gysen, B. L. J., Paulides, J. J. H. and Lomonova, E. A. [2011b], Dynamic analysis and optimization of tubular eddy current dampers, *in* 'IEEE International Magnetics Conference, Intermag 2011', Taipei, Taiwan, pp. 1–4.
- [66] Gysen, B. L. J., Paulides, J. J. H., Lomonova, E. A., Encica, L. and Leeuwen, B. G. v. [2009], 'Electromagnetic actuator with integrated passive damper', WIPO Patent Application WO/2010/136049.
- [67] Gysen, B. L. J., Paulides, J. J. H., Lomonova, E. A. and Vandenput, A. J. A. [2008a], 'Analytical and numerical techniques for solving Laplace and Poisson equations in a tubular permanent magnet actuator: Part I. Semi-analytical framework', *IEEE Transactions on Magnetics* **44**(7), 1751–1760.
- [68] Gysen, B. L. J., Paulides, J. J. H., Lomonova, E. A. and Vandenput, A. J. A. [2008b], 'Analytical and numerical techniques for solving Laplace and Poisson equations in a tubular permanent magnet actuator: Part II. Schwarz-Christoffel mapping', *IEEE Transactions on Magnetics* **44**(7), 1761–1767.
- [69] Gysen, B. L. J., Sande, T. P. J. v. d., Paulides, J. J. H. and Lomonova, E. A. [2011], 'Efficiency of a regenerative direct-drive electromagnetic active suspension', *IEEE Transactions on Vehicular Technology* **60**(4), 1384–1393.
- [70] Hague, B. [1929], *Electromagnetic Problems in Electrical Engineering*, Oxford University Press, U.K.
- [71] Hameyer, K. and Belmans, R. [1996], 'Design and optimization of electrotechnical devices', *Journal of Engineering Design* **7**(3), 235–249.
- [72] Hameyer, K., Driessen, J., de Gerssem, H. and Belmans, R. [1999], 'The classification of couples field problems', *IEEE Transactions on Magnetics* **35**(3), 1618–1621.
- [73] Hanselman, D. [2003], *Brushless permanent magnet motor design*, The Writer's Collective, U.S.A.
- [74] Hendershot, J. R. and Miller, T. J. E. [1994], *Design of brushless permanent-magnet motors*, Oxford University Press Inc., U.S.A.

- [75] Hewitt, E. and Hewitt, R. [1979], ‘The Gibbs-Wibraham phenomenon: An episode in Fourier analysis’, *Archive for History of Exact Sciences* **21**, 129–160.
- [76] Hrovat, D. [1988], ‘Influence of unsprung weight on vehicle ride quality’, *Journal of Sound and Vibration* **124**(3), 497–516.
- [77] Hrovat, D. [1997], ‘Survey of advanced suspension developments and related optimal control applications’, *Automatica* **33**(10), 1781–1817.
- [78] Hughes, A. and Miller, T. J. E. [1977], ‘Analysis of fields and inductances in air-cored and iron-cored synchronous machines’, *Proceedings of the Institution of Electrical Engineers* **124**(2), 121–126.
- [79] Hundal, M. S. [1977], ‘Impact absorber with two-stage variable area orifice hydraulic damper’, *Journal of Sound and Vibration* **50**(2), 195–202.
- [80] ISO [1995], ISO8608:1995:Mechanical vibration-Road surface profiles-Reporting of measured data, Technical report, International Organization for Standardization, Geneva - Switzerland.
- [81] Jansen, J. W., Lierop, C. M. M. v., Lomonova, E. A. and Vandenput, A. J. A. [2007], ‘Modeling of magnetically levitated planar actuators with moving magnets’, *IEEE Transactions on Magnetics* **43**(1), 15–25.
- [82] Jansen, J. W., Lomonova, E. A. and Rovers, J. M. M. [2009], ‘Effects of eddy currents due to a vacuum chamber wall in the airgap of a moving-magnet linear actuator’, *Journal of Applied Physics* **105**(7), 07F111–1–3.
- [83] Janssen, J. L. G. [2006], Design of active suspension using electromagnetic devices, Master’s thesis, Eindhoven University of Technology.
- [84] Janssen, J. L. G., Paulides, J. J. H., Encica, L. and Lomonova, E. [2008], Analytical modeling of permanent magnets on a soft magnetic support for a suspension system, in ‘International Conference on Electrical Machines and Systems, ICEMS 2008’, Wuhan, China, pp. 3825–3830.
- [85] Janssen, J. L. G., Paulides, J. J. H., Gysen, B. L. J., Meessen, K. J., Encica, L. and Lomonova, E. A. [2009], Separation of the cogging force components in a tubular permanent magnet actuator using FEM, in ‘Proceedings of the 2009 FLUX Users Conference’, Autrans, France, pp. 1–7.
- [86] Janssen, J. L. G., Paulides, J. J. H. and Lomonova, E. A. [2009], ‘Three-dimensional analytical field calculation of pyramidal-frustum shaped permanent magnets’, *IEEE Transactions on Magnetics* **45**(10), 4628–4631.
- [87] Jones, W. [2005], ‘Easy ride: Bose corp. uses speaker technology to give cars adaptive suspension’, *IEEE Spectrum* **42**(5), 12–14.
- [88] Karnopp, D. C. [1995], ‘Active and semi-active vibration isolation’, *Journal of Mechanical Design* **117**(B), 177–185.

- [89] Karnopp, D. C. and Heess, G. [1991], ‘Electronically controllable vehicle suspensions’, *Vehicle System Dynamics* **20**(3-4), 207–217.
- [90] Kim, C. and Ro, P. I. [2000], ‘Reduced-order modelling and parameter estimation for a quarter-car suspension system’, *Proceedings of the Institution of Mechanical Engineers* **214**(Part D), 851–864.
- [91] Kim, U. and Lieu, D. K. [1998], ‘Magnetic field calculation in permanent magnet motors with rotor eccentricity: With slotting effect considered’, *IEEE Transactions on Magnetics* **34**(4), 2253–2266.
- [92] Knutson, D. [1991], ‘Selection and design of electrohydraulic valves for electronically-controlled automotive suspension systems’, *Society of Automotive Engineers - 912500*.
- [93] Krop, D. C. J., Lomonova, E. A. and Vandenput, A. J. A. [2008], ‘Application of Schwarz-Christoffel mapping to permanent-magnet linear motor analysis’, *IEEE Transactions on Magnetics* **44**(3), 352–359.
- [94] Kruczek, A. and Stribrsky, A. [2004], A full-car model for active suspension - some practical aspects, in ‘Proceedings of the IEEE International Conference on Mechatronics, ICM 2004’, pp. 41 – 45.
- [95] Lackner, J. R. [2003], ‘Motion sickness’, *Encyclopedia of Neuroscience, 3rd edition, CD-ROM version, G. Adelman, B. Smith (eds)*. **106**(4), 451–465.
- [96] Lauwerys, C., Swevers, J. and Sas, P. [2005], ‘Robust linear control of an active suspension on a quarter car test-rig’, *Control engineering practice* **13**, 577–586.
- [97] Lee, S. W., Jones, W. R. and Campbell, J. J. [1971], ‘Convergence of numerical solutions of iris-type discontinuity problems’, *Microwave Theory and Techniques, IEEE Transactions on* **19**(6), 528–536.
- [98] Levant Power Corporation [n.d.], <http://www.levantpower.com>.
- [99] Lindh, P. M., Jussila, H. K., Niemela, M., Parviainen, A. and Pyrhonen, J. [2009], ‘Comparison of concentrated winding permanent magnet motors with embedded and surface-mounted rotor magnets’, *IEEE Transactions on Magnetics* **45**(5), 2085–2089.
- [100] Lion, A. and Loose, S. [2002], ‘A thermomechanically couple model for automotive shock absorbers: Theory, experiments and vehicle simulations on test tracks’, *Vehicle System Dynamics* **37**(4), 241–261.
- [101] Liu, J., Zhuang, D. J., Yu, F. and Lou, L. M. [2008], ‘Optimized design for a macpherson strut suspension with side load springs’, *International Journal of Automotive Technology* **9**(1), 29–35.
- [102] Liu, Z. J. and Li, J. T. [2007], ‘Analytical solution of air-gap field in permanent-magnet motors taking into account the effect of pole transition over slots’, *IEEE Transactions on Magnetics* **43**(10), 3872–3883.

- [103] MacPherson, E. [1947], ‘Vehicle wheel suspension system’, U.S. Patent 2,624,592.
- [104] Marinescu, M. and Marinescu, N. [1992], ‘New concept of permanent magnet excitation for electrical machines: analytical and numerical computation’, *IEEE Transactions on Magnetics* **28**(2), 1390–1393.
- [105] Martins, I., Esteves, J., Marques, G. D. and da Silva, F. P. [2006], ‘Permanent-magnets linear actuators applicability in automobile active suspensions’, *IEEE Transactions on Vehicular Technology* **55**(1), 86–94.
- [106] Meessen, K. J., Gysen, B. L. J., Paulides, J. J. H. and Lomonova, E. A. [2008], ‘Halbach permanent magnet shape selection for slotless tubular actuators’, *IEEE Transactions on Magnetics* **44**(11), 4305–4308.
- [107] Meessen, K. J., Gysen, B. L. J., Paulides, J. J. H. and Lomonova, E. A. [2010], ‘Three-dimensional magnetic field modeling of a cylindrical Halbach array’, *IEEE Transactions on Magnetics* **46**(6), 1733–1736.
- [108] Meessen, K. J., Paulides, J. J. H. and Lomonova, E. A. [2010], ‘Analysis of 3-D effects in segmented cylindrical quasi-Halbach magnet arrays’, *IEEE Transactions on Magnetics* **47**(4), 727–733.
- [109] Melcher, J. R. [1981], *Continuum Electromechanics*, MIT Press, U.S.A.
- [110] Michelberg, P., Palkovics, L. and Bokor, J. [1993], ‘Robust design of active suspension system’, *International Journal of Vehicle Design* **14**(2/3), 145–165.
- [111] Micro-Epsilon Messtechnik [n.d.], <http://www.micro-epsilon.com>.
- [112] Mishkin, E. [1954], ‘Theory of the squirrel-cage induction machine derived directly from Maxwell’s field equations’, *Quarterly Journal of Mechanics and Applied Mathematics* **7**(4), 472–487.
- [113] Münster, M., Mair, U., Gilsdorf, H., Thoma, A., Müller, C., Hippe, M. and Hoffmann, J. [2009], ‘Electromechanical active body control’, *ATZ worldwide* pp. 44–49.
- [114] Ostovic, V. [1989], *Dynamics of saturated electric machines*, Springer-Verlag, U.S.A.
- [115] Overboom, T. T., Smeets, J. P. C., Jansen, J. W. and Lomonova, E. A. [2011], Semi-analytical modeling of a linear induction motor including primary slotting, in ‘IEEE Int. Electric Machines and Drives Conference, ISEF 2011’, Vol. accepted, Madeira, Spain, pp. 1–2.
- [116] Pacejka, H. B. [2006], *Tyre and vehicle dynamics*, Butterworth-Heinemann, The Netherlands.

- [117] Pahner, U., Mertens, R., de Gersem, H., Belmans, R. and Hameyer, K. [1998], ‘A parametric finite element environment tuned for numerical optimization’, *IEEE Transactions on Magnetics* **34**(5), 2936–2939.
- [118] Paulides, J. J. H., Gysen, B. L. J., Meessen, K. J., Tang, Y. and Lomonova, E. A. [2011], ‘Influence of multiple air-gaps on the performance of coreless electrical machines with Halbach magnetization’, *IEEE Transactions on Magnetics* **47**(10), 1–4.
- [119] Paulides, J. J. H., Meessen, K. J. and Lomonova, E. A. [2008], ‘Eddy-current losses in laminated and solid steel stator back iron in a small rotary brushless permanent-magnet actuator’, *IEEE Transactions on Magnetics* **44**(11), 4373–4376.
- [120] Prokop, G. and Sharp, R. S. [1995], ‘Performance enhancement of limited-bandwidth active automotive suspensions by road preview’, *IEE Proceedings - Control Theory and Applications* **142**(2), 140–148.
- [121] Pyrhönen, J., Jokinen, T. and Hrabovcová, V. [2008], *Design of rotating electrical machines*, John Wiley and Sons, U.K.
- [122] Raine, J. K. and Henderson, R. J. [1997], ‘A two-degree-of-freedom ambulance stretcher suspension Part 1: system overview’, *Proc. Inst. Mech. Eng.* **212 Part D**, 93–102.
- [123] Regan, E. C. and Price, K. R. [1994], ‘The frequency of occurrence and severity of side-effects of immersion virtual reality’, *Aviation, Space, and Environmental Medicine* **65**(6), 527530.
- [124] Roters, H. C. [1941], *Electromagnetic Devices*, John Wiley and Sons, U.S.A.
- [125] Sagawa, M., Fujimura, S., Togawa, N., Yamamoto, H. and Matsuura, Y. [1984], ‘New material for permanent magnets on a base of nd and fe’, *Journal of Applied Physics* **55**(6), 2083–2087.
- [126] Sande, T. P. J. v. d., Gysen, B. L. J., Besselink, I. J. M., Paulides, J. J. H., Lomonova, E. A. and Nijmeijer, H. [2011a], ‘Robust control of a direct-drive electromagnetic active suspension system’, *Mechatronics* (submitted).
- [127] Sande, T. P. J. v. d., Gysen, B. L. J., Besselink, I. J. M., Paulides, J. J. H., Lomonova, E. A. and Nijmeijer, H. [2011b], Robust control of a direct-drive electromagnetic active suspension system, in ‘The 8th International Symposium on Linear Drives for Industry Applications, LDIA 2011’, Eindhoven, The Netherlands, pp. 1–4.
- [128] Sas, P. and Dehandschutter, W. [1999], ‘Active structural and acoustic control of structure-borne road noise in a passenger car’, *Noise & Vibration Worldwide* **30**(5), 17–27.

- [129] Schmeitz, A. J. C. [2004], A semi-empirical three-dimensional model of the pneumatic tyre rolling over arbitrarily uneven road surfaces, PhD thesis, Delft University of Technology.
- [130] Sharkawy, A. B. [2005], ‘Fuzzy and adaptive fuzzy control for the automobiles active suspension system’, *Vehicle system dynamics* **43**(11), 795–806.
- [131] Silvester, J. C. and Ferrari, R. L. [1990], *Finite Elements for Electrical Engineers*, Cambridge University Press, U.S.A.
- [132] SIMONA Research Simulator [n.d.], <http://www.simona.tudelft.nl>.
- [133] Skogestad, S. and Postlethwaite, I. [2005], *Multivariable Feedback Control*, John Wiley and Sons, U.K.
- [134] Smart, L. J., Stoffregen, T. A. and Bardy, B. G. [2002], ‘Visually induced motion sickness predicted by postural instability’, *Human Factors* **44**(3), 451–465.
- [135] Smythe, W. R. [1939], *Static and Dynamic Electricity*, McGraw-Hill, U.S.A.
- [136] Sodano, H. A. and Bae, J. [2004], ‘Eddy current damping in structures’, *The Shock and Vibration Digest* **36**(6), 469–478.
- [137] Sodano, H. A., Bae, J., Inman, D. J. and Belvin, W. K. [2006], ‘Improved concept and model of eddy current damper’, *Transactions of the ASME* **128**(3), 294–302.
- [138] Stein, G. and Doyle, J. C. [1991], ‘Beyond singular values and loopshapes’, *AIAA Journal of Guidance and Control* **14**(1), 5–16.
- [139] Stichting BOVAG-RAI Mobiliteit [2010-2011], Mobility in figures, Cars 2010/2011, Technical report, Amsterdam, The Netherlands.
- [140] Strassberger, M. and Guldner, J. [2004], ‘BMW’s dynamic drive: an active stabilizer bar system’, *IEEE Control Systems* **24**(4), 28–29, 107.
- [141] Tedea-Huntleigh Electronics Co LTD [n.d.], <http://www.tedea-huntleigh.com>.
- [142] Tegopoulos, J. A. and Kriezis, E. E. [1985], *Eddy Currents in Linear Conducting Media*, Elsevier Science Publishers B.V., U.S.A.
- [143] Theodoulidis, T. and Bowler, J. [2005], ‘Eddy-current interaction of a long coil with a slot in a conductive plate’, *IEEE Transactions on Magnetics* **41**(4), 1238–1247.
- [144] Theodoulidis, T. and Bowler, J. [2010], ‘Interaction of an eddy-current coil with a right-angled conductive wedge’, *IEEE Transactions on Magnetics* **46**(4), 1034–1042.

- [145] Tims, H. E. [2005], Vehicle Active Suspension System Sensor Reduction, PhD thesis, University of Texas, Austin.
- [146] Tonoli, A. [2007], ‘Dynamic characteristics of eddy current dampers and couplers’, *Journal of Sound and Vibration* **301**(3-5), 576–591.
- [147] Trumper, D. L., Kim, W. and Williams, M. E. [1996], ‘Design and analysis framework for linear permanent-magnet machines’, *IEEE Transactions on Industry Applications* **32**(2), 371–379.
- [148] Vacuumschmelze GmbH & Co. KG [n.d.], <http://www.vacuumschmelze.de>.
- [149] Venhovens, P. [1994], Optimal control of vehicle suspensions, PhD thesis, Delft University of Technology.
- [150] Venkataraman, P. [2001], *Applied Optimization with MATLAB Programming*, Wiley-Interscience, U.S.A.
- [151] Vos, R., Besselink, I. J. M. and Nijmeijer, H. [2010], Influence of in-wheel motors on the ride comfort of electric vehicles, in ‘International Symposium on Advanced Vehicle Control’, Loughborough, United Kingdom, pp. 835–840.
- [152] Wal, M. v. d., Philips, P. and Jager, B. D. [1998], ‘Actuator and sensor selection for an active vehicle suspension aimed at robust performance’, *International Journal of Control* **70**(5), 703–720.
- [153] Wang, J. and Howe, D. [2004], ‘Design optimization of radially magnetized, iron-cored, tubular permanent-magnet machines and drive systems’, *IEEE Transactions on Magnetics* **40**(5), 3262–3277.
- [154] Wang, J. and Howe, D. [2005], ‘Tubular modular permanent-magnet machines equipped with quasi-Halbach magnetized magnets-Part I: magnetic field distribution, EMF, and thrust force’, *IEEE Transactions on Magnetics* **41**(9), 2470–2478.
- [155] Wang, J., Howe, D. and Jewell, G. W. [2003a], ‘Fringing in tubular permanent-magnet machines: Part I. magnetic field distribution, flux linkage, and thrust force’, *IEEE Transactions on Magnetics* **39**(6), 3507–3516.
- [156] Wang, J., Howe, D. and Jewell, G. W. [2003b], ‘Fringing in tubular permanent-magnet machines: Part II. cogging force and its minimization’, *IEEE Transactions on Magnetics* **39**(6), 3517 – 3522.
- [157] Wang, J., Jewell, G. W. and Howe, D. [1999], ‘A general framework for the analysis and design of tubular linear permanent magnet machines’, *IEEE Transactions on Magnetics* **35**(3), 1986–2000.
- [158] Wang, J., Wang, W. and Atallah, K. [2011], ‘A linear permanent-magnet motor for active vehicle suspension’, *IEEE Transactions on Vehicular Technology* **60**(1), 55–63.

- [159] Wang, J., Wang, W., Atallah, K. and Howe, D. [2008], Comparative studies of linear permanent magnet motor topologies for active vehicle suspension, in 'IEEE Vehicle Power and Propulsion Conference, VPPC 2008', pp. 1–6.
- [160] Williamson, S. [1976], 'The anisotropic layer theory of induction machines and induction devices', *IMA Journal of Applied Mathematics* **17**(1), 69–84.
- [161] Wright, P. G. and Williams, D. A. [1989], 'The case of an irreversible active suspension system', *SAE Transaction* **6**, 83–87.
- [162] Yamashita, M., Fujimori, K., Hayakawa, K. and Kimura, H. [1994], 'Application of h_∞ control to active suspension system', *Automatica* **30**(11), 1717–1729.
- [163] Yoo, Y., Lee, G. C. H. and Jones, S. A. [1997], 'Vection, compensatory sway, and simulator sickness', *Advances in occupational ergonomics and safety, B. Dos and W. Karowski (Eds.)* pp. 589–592.
- [164] Zarko, D., Ban, D. and Lipo, T. A. [2006], 'Analytical calculation of magnetic field distribution in the slotted air gap of a surface permanent-magnet motor using complex relative air-gap permeance', *IEEE Transactions on Magnetics* **42**(7), 1828–1837.
- [165] Zhu, Z. Q. and Chen, J. T. [2010], 'Advanced flux-switching permanent magnet brushless machines', *IEEE Transactions on Magnetics* **46**(6), 1447–1453.
- [166] Zhu, Z. Q. and Howe, D. [1993a], 'Instantaneous magnetic field distribution in brushless permanent magnet DC motors. Part II. Armature-reaction field', *IEEE Transactions on Magnetics* **29**(1), 136–142.
- [167] Zhu, Z. Q. and Howe, D. [1993b], 'Instantaneous magnetic field distribution in brushless permanent magnet DC motors. Part III. Effect of stator slotting', *IEEE Transactions on Magnetics* **29**(1), 143–151.
- [168] Zhu, Z. Q. and Howe, D. [1993c], 'Instantaneous magnetic field distribution in brushless permanent magnet DC motors. Part IV. Magnetic field on load', *IEEE Transactions on Magnetics* **29**(1), 152–158.
- [169] Zhu, Z. Q., Howe, D., Bolte, E. and Ackermann, B. [1993], 'Instantaneous magnetic field distribution in brushless permanent magnet DC motors. Part I. Open-circuit field', *IEEE Transactions on Magnetics* **29**(1), 124–135.
- [170] Zhu, Z. Q., Pang, Y., Howe, D., Iwasaki, S., Deodhar, R. and Pride, A. [2005], 'Analysis of electromagnetic performance of flux-switching permanent-magnet machines by nonlinear adaptive lumped parameter magnetic circuit model', *IEEE Transactions on Magnetics* **41**(11), 4277–4287.

Samenvatting

Generalized Harmonic Modeling Technique for 2D Electromagnetic Problems

Applied to the Design of a Direct-Drive Active Suspension System

De introductie van permanente magneten heeft de prestatie en efficiëntie van geavanceerde actuatiesystemen significant verbeterd. De vraag naar deze systemen in de industrie is groeiende en de specificaties worden steeds uitdagender. Nauwkeurige en snelle modellering van de elektromagnetische fenomenen is daarom noodzakelijk om gedurende de ontwerpfase, het optimaliseren van verschillende topologieën mogelijk te maken.

Deze thesis presenteert een methodologie voor het ontwerpen en analyseren van tweedimensionale elektromagnetische problemen gebaseerd op harmonische modellering. Daarvoor is de bestaande modellering uitgebreid en universeel gemaakt om een methode te creëren die toegepast kan worden in bijna elk probleem in het Cartesisch, polair en axisymmetrisch coördinatenstelsel. Deze generalisatie biedt de mogelijkheid voor het automatisch oplossen van gecompliceerde randvoorwaardeproblemen binnen een zeer korte rekentijd. Deze methode kan daarom niet alleen voor klassieke machines worden toegepast maar ook voor meer geavanceerde en gecompliceerde elektromagnetische actuatiesystemen.

Deze nieuwe ontwikkelde methodologie is uitvoerig gedemonstreerd voor getande lineaire cilindrische permanent magneet actuatoren. Daardoor kunnen vele topologieën, magnetisatie- en windingconfiguraties geanalyseerd worden. Verder zijn er nauwkeurige methodes voor krachtprofielen, emk golfvormen en synchrone inducties gepresenteerd. De rimpel op de golfvorm ten gevolge van de getande stator is inbegrepen en de resultaten liggen binnen 5 % van de niet-lineaire eindige element resultaten.

Verder is er een unieke oplossing voor passieve demping geïntegreerd binnen de cilindrische permanent magneet actuator op basis van wervelstroomdemping. Deze is verkregen door de invoering van geleidende ringen in de tandopeningen van de stator om een dempingskracht te leveren zonder te compromitteren op de prestatie van de cilindrische actuator. Dit vernieuwende idee van het integreren

van geleidende ringen is vastgelegd in een patent. Een methode is gepresenteerd om de demping tengevolge van de geleidende ringen uit te rekenen waarin de afhankelijkheden in positie, snelheid en temperatuur zijn aangetoond.

De ontwikkelde methodologie is toegepast op het ontwerp en de optimalisatie van een direct aangedreven elektromagnetisch actief veersysteem voor personeelauto's. Deze innovatieve oplossing is een alternatief voor huidige toegepaste hydraulische en pneumatische actieve veersystemen ten behoeve van de verbetering in comfort en wegligging van een voertuig. Het elektromagnetische systeem biedt een verbeterde bandbreedte die typisch 20 maal hoger ligt tezamen met een energieverbruik dat ongeveer vijfmaal lager ligt. Op deze manier elimineert het voorgestelde systeem twee van de grootste nadelen die een commerciële doorbraak van actieve veersystemen hebben voorkomen.

Het direct aangedreven elektromagnetisch actief veersysteem bestaat uit een spiraalveer parallel aan een cilindrische permanent magneet actuator met geïntegreerde wervelstroomdemping. De spiraalveer draagt de geveerde massa terwijl de cilindrische actuator energie omzet in direct aangedreven verticale krachten, ofwel energie regenereert. De toegepaste cilindrische actuator is ontworpen gebruikmakende van een niet-lineair optimalisatiealgoritme in combinatie met de ontwikkelde analytische methodologie. Dit verzekert het ontwerp met de hoogste krachtdichtheid tezamen met een laag energieverbruik. In het geval dat het vermogen wegvallt creëert de geïntegreerde wervelstroomdemping in de tandopeningen van de cilindrische actuator, tezamen met de spiraalveer, een passief veersysteem en garandeert een faalveilige werking.

Om de prestatie van het conceptueel nieuwe elektromagnetische veersysteem te valideren is er een prototype gerealiseerd en een testopstelling ontwikkeld die de verticale voertuigdynamica representeert van een kwart voertuig, een BMW 530i. Daarnaast zijn er regelalgoritmes ontworpen voor het actief veersysteem ter verbetering van het comfort en de wegligging. Uiteindelijk is het veersysteem in de voorophanging van een BMW 530i geïnstalleerd. Uitvoerige experimentele testen zowel in het lab als op de weg hebben de capaciteit van het nieuwe direct-aangedreven elektromagnetisch actief veersysteem aangetoond. Bovendien demonstreert het de toepasbaarheid van de ontwikkelde analytische methodologie voor het ontwerpen en optimaliseren van elektromagnetische actuatoren.

Acknowledgements

Although a PhD candidate is generally considered to be a solitary person behind books or a desktop, this thesis is the result of great team work!

First of all, my sincere gratitude goes to prof. André Vandenput for giving me the opportunity to work as a PhD student within his group. His attitude and decency was an inspiration for me and it was nice to have a Belgian colleague. Additionally, I would like to thank prof. Elena Lomonova for her guidance, effort and sometimes long discussions. You opened many doors for me and ‘tuned my vector’ in the right direction, not only professionally, but also personally.

I wish to thank Johan, my closest supervisor, who was my right hand during the whole project. Your positive attitude, support and practical experience gave me more confidence that ‘things will work out right’. You taught me how to behave among Dutch people, handle their jokes and to become more positive and open.

Many thanks go to my officemates, Koen, Jeroen and Davy. You guys made the life of a PhD not all that boring. Thank you for all the inside jokes, ball games and sometimes nonsense that was going on in IM 0.02, we had a terrific time. Also my appreciations for absorbing the sound of my ‘repetitive’ music. In extend, I especially would like to thank Koen, for the scientific discussions we had on harmonic modeling, considering problems from both angles solved things more efficiently.

Furthermore, my gratitude goes to Marijn for his tremendous work on all the experimental setups involved in this thesis. This work could not have been obtained without your help, patience and practical way of solving many unforeseen problems. I admit I was a demanding person sometimes and I truly appreciate your long hours of work as well as our pleasant conversations.

Additional thanks go the GTD (Gemeenschappelijke Technische Dienst) workshop of the TU/e. In particular to Jovita Moerel, Erwin Dekkers and Rene Henselmans for their impressive work in manufacturing the prototypes. Many fruitful discussions have given me more knowledge how to go from idea to technical drawing to realization. For years it was my weekly escape from the office to visit the GTD and have a cup of coffee.

My sincere thanks to SKF ADC, who not only supported this project but also had the confidence and belief in the EPE group and myself to invest in this project. The input from the industrial side was very valuable and kept me sharp in realizing a working prototype. Special thanks go to Lex Molenaar, Bernie van Leeuwen, Edward Holweg, Raimond Breuker and Igor Dorrestijn.

I had the opportunity to work with many students who made it a very dynamic project. Many thanks go to Tom, Dave, Araz, Chaim, Banu and Esin. Furthermore, my gratitude goes to the supervision of these student projects from external groups, in particular to the Dynamics and Control group, Control Systems group, Fontys Hogeschool and Institute of Electrical Machines (RWTH Aachen University). Additionally, I would like to thank all my colleagues from the EPE group, for the great working atmosphere, it is one of the reasons why I still will be active within the EPE group in the future.

Ten slotte wil ik mijn familie, vriendengroep uit Wèzent en mijn vriendin bedanken voor hun steun gedurende deze jaren. Jullie gaven me het zelfvertrouwen, de nodige afleiding en ‘fieskes’, en brachten mijn gedachten even op iets anders. Mijn grootste dank en respect gaat uit naar mijn ouders voor hun liefdevolle hulp, begeleiding en steun gedurende mijn gehele studie.

Merci!

Bart Gysen, August 2011

Curriculum Vitae

Bart Gysen was born on January 3th 1984 in Bilzen, Belgium. He received his B.Sc. degree and M.Sc. degree in Electrical Engineering from the Eindhoven University of Technology, in August 2005 and August 2007, respectively. From September 2007 until October 2011, he worked as a PhD student in the group of Electromechanics and Power Electronics at the Electrical Engineering department of the Eindhoven University of Technology. His research topic was the design of an electromagnetic active suspension systems for automotive applications which has led to this thesis. The developed electromagnetic active suspension system was one of the four nominees for the ATC automotive innovation award 2011. Since November 2011 he started his industrial career at Prodrive in Son and continued his scientific career as a part-time assistant professor in the group of Electromechanics and Power Electronics.